MICROCOPY RESOLUTION TEST CHART

NATIONAL BUREAU OF STANDARDS-1963-A
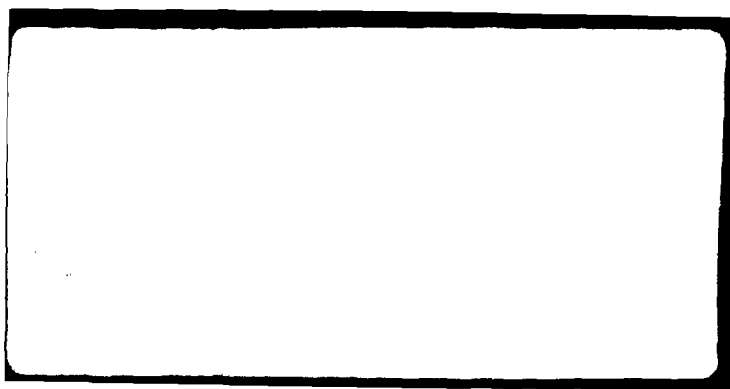
NUMERICAL SOLUTION OF LAMINAR AND
TURBULENT BOUNDARY LAYER EQUATIONS
INCLUDING TRANSITION, AND
EXPERIMENTAL STUDY OF A FLAT PLATE
WITH A BLUNT FIN AT INCIDENCE

THESIS

Alice J. Chen
Captain, USAF

AFIT/GAE/ENY/86M-1

SELECTED

OCT 2 1986

A

NUMERICAL SOLUTION OF LAMINAR AND TURBULENT
BOUNDARY LAYER EQUATIONS INCLUDING TRANSITION, AND
EXPERIMENTAL STUDY OF A FLAT PLATE WITH A
BLUNT FIN AT INCIDENCE

THESIS

Presented to the Faculty of the School of Engineering

of the Air Force Institute of Technology

Air University

In Partial Fulfillment of the

Requirements for the Degree of

Master of Science in Aeronautical Engineering

Alice J. Chen, B.S.

Captain, USAF

March 1986

Acknowledgments

In performing the modification of the numerical code, and conducting the experimentation, I have had a great deal of assistance from others.

I am deeply indebted to my thesis advisor, Maj James K. Hodge, and I would like to thank him for his knowledge, guidance, and trans-Atlantic assistance throughout the scope of this entire project.

I would like to thank my VKI project advisor, Prof John F. Wendt, for his guidance and advice on my project and experimental research techniques in general. I wish to thank Prof Tony Arts for giving his time to answer my many questions concerning thin film gages and halting his testing schedule so that I could use his equipment for my tests. I wish to express my sincere appreciation to Mr. Roger Conniasselle, the chief technical engineer of the VKI High Speed Department for his assistance and expertise, and also "merci beaucoup" to Mr. Oscar Opalvens who performed a seemingly endless amount of model changes without complaint. I also thank Eric Abriat for lending me his plotting program. I also wish to express my appreciation to Mr. J.C. Lobet for his assistance and his team for developing the many photographs that I required.

Last, but certainly not least, I wish to thank my husband, Bob, for his support and guidance even though we were separated by the Atlantic Ocean.

Alice J. Chen

Contents

List of Figures

List of Tables

List of Symbols

a	Speed of sound
A	Rake orientation angle
A	Van Driest damping parameter
A^+	Nondimensional Van Driest damping parameter
AOS	Chapman damping parameter
AOS^+	Nondimensional Chapman parameter
$A*/\beta$	Calibration constant for the electrical analog
C	Electrical capacitance
C'	Distributed electrical capacitance per unit length
c_f	Skin friction coefficient
cp	Specific heat capacity at constant pressure
d	Derivative symbol
d	Diameter of fin leading edge
EPS	Maximum error allowed for computer code
H	Total enthalpy
h	Static enthalpy
h	Height of fin
h	Number of stages of arithmetically increasing components in the analog circuit
HC	Heat transfer coefficient
HREF	Reference heat transfer coefficient
H.O.T.	Higher order terms
I	Number of spatial node points in X or ξ direction
i	Node point in X or ξ direction

i	Electrical current	
J	Number of spatial node points in Y or η direction	
j	Node point in Y or η direction	
k	Conductivity	
k_T	Turbulent conductivity	
K	von Karman's constant	
L	Flat plate length	
l	Separation distance ahead of the fin leading edge	
l	Turbulent length scale, mixing length	
lo	Outer region mixing length	
Lm	Mixing length parameter	
Lm_C	Chapman's mixing length parameter	
Lm_{VD}	Van Driest's mixing length parameter	
M	Mach number	
M_∞	Freestream Mach number	
n	Number of stages in an identical component analog circuit	
P	Static pressure	
Po	Stagnation pressure	
Pr	Prandtl number	
Pr_T	Turbulent Prandtl number	
Q	Cumulative heating	
q	Heat rate	
q_W	Heat rate at the wall	

R	Gas constant for air
R	Electrical resistance
RREF	Thin film resistance at temperature TREF
r	Recovery factor
r	Radial distance in the H-3 tunnel
r'	Distributed electrical resistance per unit length
Re	Reynolds Number per unit length
Rex	Local Reynolds Number, based on x distance downstream of the leading edge of the plate
s	Laplace variable
St	Stanton Number
T	Static temperature
Ta	Ambient temperature
T_{AW}	Adiabatic wall temperature
TF	Reference temperature for theoretical Stanton number calculation
T_∞	Freestream temperature
To	Stagnation temperature
TREF	Reference temperature, usually ambient
t	Time
U	Dorodnitsyn's transformation of streamwise flow velocity
u	Streamwise flow velocity
U^+	Nondimensional turbulent velocity scale
U_τ	Friction velocity

V	Dorodnitsyn's transformation of normal flow velocity
V	Electrical voltage
VOUT	Output voltage from analog circuit
VREF	Initial thin film voltage, taken at Ta
v	Normal flow velocity
ΔV	Film output voltage
X	Dorodnitsyn's transformation of streamwise spatial coordinate
x	Streamwise spatial coordinate
x	Streamwise direction in wind tunnel
$x_{T,I}$	Initial location of transition zone
$x_{T,F}$	Final location of transition zone
Y	Dorodnitsyn's transformation of normal spatial coordinate
y	Normal spatial coordinate
Y^+	Nondimensional turbulent scale
α	Flat plate incidence angle, pitch up is positive
α	Thermal diffusivity
α_R	Film temperature coefficient of resistance
$\alpha*$	Clauser model factor to account for low Reynolds Number
β	Chapman's length scale
Γ	Transition parameter
γ	Specific heat ratio

Δ	Delta difference of some quantity
δ	Boundary layer thickness
$\delta*$	Kinematic displacement thickness
η	Transformed Y in the computational plane
Θ	Normalized streamwise coordinate in transition zone
Θ	Shock angle
Θs	Numerical stability constant
μ	Dynamic viscosity
μ_T	Turbulent viscosity
ξ	Transformed X in the computational plane
ρ	Density
σ	Intermittency parameter
Ξ	Extent of transition
$\emptyset$	Delta wing incidence angle
∂	Partial derivative symbol
Ω	Delta wing sweep angle

Superscripts

n	Time level
s	Iteration level
#	Dimensional quantity
*	Laplace transformed variable
'	Mass averaged variable-fluctuation
~	Mass averaged variable-mean
"	Time averaged variable-fluctuation
-	Time averaged variable-mean

Subscripts

e	Edge condition
i,j	Spatial node point
∞	Freestream condition
o	Stagnation property

Abstract

This study combines the techniques of computational fluid dynamics and experimentation.

An unsteady laminar boundary layer code was shown to be more efficient when modified to solve the momentum and energy equations using Thomas' algorithm instead of optimized successive over-relaxation (SOR). A steady eddy viscosity turbulence model was then added to the code: two models for the inner region, Van Driest and Chapman, and two models for the outer region, a mixing length and Clauser were used. The computer code was verified against theoretical and experimental data from the literature. The code shows excellent results for laminar flow and each of the models showed very good agreement with turbulent experimental data.

The experimental study was conducted in a Mach 6 blowdown wind tunnel. Oil flow, sublimation, liquid crystals, and thin film gages were used to examine the flow structure and heat transfer on a flat plate. The heat transfer rates from these gages were lower than from the liquid crystals. The viscid-inviscid interaction flow region of flow past a blunt fin mounted on the flat plate was examined using the same flow visualization methods and possible flow interaction models are presented. Striation heating appeared when the fin incidence was 40° and the sweep was 60 or 75°.

The numerical and experimental techniques of this study were then merged. The heat transfer results from the flat plate experiment were compared with results from the computer code and were found to be in good agreement.

I. Introduction

This research effort, as well as this report based on it, consists of three main parts; a computational part, an experimental part, and a comparison between experimental data obtained and results from the computer program. The computational part was completed at the Air Force Institute of Technology (AFIT), Wright-Patterson Air Force Base, Ohio, while the experimental part was completed at the von Karman Institute for Fluid Dynamics (VKI), Rhode-Saint-Genese, Belgium. The experimental research was sponsored by HQ USAF, AFIT, VKI, and the Flight Dynamics Laboratory at Wright-Patterson Air Force Base, Ohio.

The computational effort consisted of modifying an unsteady laminar boundary layer code to a turbulent boundary layer code. The computational effort originally consisted of adding an unsteady turbulence model (38) to the unsteady laminar boundary layer code. However, due to time limitations, only a steady eddy viscosity turbulence model was added. Two models for the turbulent length scale were included, the Van Driest model and the Chapman model. The theory and results of these two models were compared with one another. Two models for the turbulent viscosity in the outer region are also examined; the mixing length model and Clauser's formulation of the mixing length model. A transition (laminar to turbulent) model was also included in the modification of the boundary layer code.

The experimental effort consisted of the study of a sharp nosed flat plate at zero degrees angle of attack. Heat transfer measurements were taken to determine the location of transition and turbulence. A swept blunt fin at incidence was placed on the flat plate and studied using flow visualization. This configuration was chosen due to its similarity to the configuration of the NASA Space Shuttle side fuselage and blunt fin. The Shuttle experiences high heat transfer rates on its side fuselage during re-entry, so the experimental effort originally was envisioned to concentrate on examining heat transfer rates on the flat plate on the expansion side of the blunt fin in laminar flow. Flight data has shown the existence of laminar flow on the Shuttle during many flight regimes including re-entry. Due to time limitations, only flow visualization tests were completed for this configuration. Effects of fin incidence and sweep angle are examined and possible models for the flow interaction region are suggested. Previous studies at VKI have examined this configuration on the expansion side (14), the compression side (15), (53), and the impingement portion (1) of the fin during turbulent flow.

The third part of this study ties the first and the second portions of this study together. Although computational fluid dynamics has recently become more important in determining flow properties about flight

vehicles, it can never exist without experimental data. As each computer code becomes developed, it must be verified for accuracy using experimental data. The third portion of this thesis blends a portion of the separate computational and experimental efforts by verifying the computer code using some of the experimental results from this study.

II. Computational Effort

2.1 Introduction

The computational aspect of this research dealt with the modification of an unsteady compressible laminar boundary layer code to a compressible turbulent boundary layer code. Time limitations caused only a steady turbulence model to be added to the code. A transition to turbulence model was also included. The applicable portions of the laminar boundary layer code are described in a later section.

Three major modifications were made to the original program. The momentum and energy equations were originally solved by the program using optimized successive over-relaxation. This was changed to take advantage of the diagonal dominance inherent in the finite differencing. Thomas' algorithm, which is a tridiagonal solver, was modified to a quad-diagonal solver. The momentum and energy equations were solved using this quad-diagonal solver.

The second major modification was the inclusion of the Cebeci-Smith turbulence model. Prandtl's mixing length theorem was used which included the Van Driest model for the turbulent length scale in the inner region. The Chapman model was also used for the inner region length scale and the differences between the two models are examined. For the outer region, two different models were examined and compared: a mixing length model and the Clauser model.

The third major modification was the addition of a transition to turbulence model. Given the location of the beginning of transition and the end of transition (fully turbulent), the model uses an exponential distribution to match the turbulent viscosity between the two regions.

2.2 Governing Equations

The Navier-Stokes equations for a viscous compressible flow are simplified using normal boundary layer assumptions. That is, gradients perpendicular to the surface are much larger than gradients parallel to the surface. The terms of the order of magnitude of the inverse square of the characteristic Reynolds number are neglected. The resulting boundary layer equations in conservative form are:

continuity

$$\frac{\partial \rho}{\partial t} + \frac{\partial \rho u}{\partial x} + \frac{\partial \rho v}{\partial Y} = 0 \qquad (2.1)$$

x-momentum

$$\frac{\partial \rho u}{\partial t} + \frac{\partial \rho u u}{\partial x} + \frac{\partial \rho u v}{\partial Y} = - \frac{\partial P}{\partial x} + \frac{\partial}{\partial Y}\left[\mu \frac{\partial u}{\partial Y}\right] \qquad (2.2)$$

Y-momentum

$$\frac{\partial P}{\partial Y} = 0 \qquad (2.3)$$

energy

$$\frac{\partial \rho\# H\#}{\partial t\#} + \frac{\partial \rho\# u\# H\#}{\partial x\#} + \frac{\partial \rho\# v\# H\#}{\partial Y\#} = \frac{\partial P\#}{\partial t\#} + \frac{\partial}{\partial Y\#}\left[k\# \frac{\partial T\#}{\partial Y\#}\right]$$

$$+ \frac{\partial}{\partial Y\#}\left[\mu\# u\# \frac{\partial u\#}{\partial Y\#}\right] \qquad (2.4)$$

These equations have boundary conditions at the edge of the boundary layer and at the wall.

2.2.1 Time and Mass-Weighted Averaging

In order to obtain the governing equations for turbulent flows, it is convenient to replace the instantaneous quantities in the equations by their mean and fluctuating quantities. A combination of conventional time averaging and mass-weighted averaging will be used as outlined in Cebeci and Smith (7:49-55).

The time averaged variables are defined as follows:

$$\rho = \bar{\rho} + \rho^{\circ}$$

$$\qquad (2.5)$$

$$P = \bar{P} + P^{\circ}$$

where $\bar{\rho}$ and $\bar{P}$ are the time averages of the bulk density and pressure, respectively, and ρ° and P° are the superimposed density and pressure fluctuations, respectively. The time average or "mean" of any quantity, $q(t)$, is defined by

$$\bar{q(t)} = \lim_{\Delta t \to \infty} \frac{1}{\Delta t} \int_{t_o}^{t_o+\Delta t} q(t)\, dt \qquad (2.6)$$

where ∞, as defined by Cebeci and Smith (7:49), is taken to mean

"a time that is long compared to the reciprocal of the predominant frequencies in the spectrum of q; in wind tunnel experiments, averaging times of a few seconds to a minute are usual."

For a fluctuating quantity $q''(t)$, the mean is zero by definition, ie.,

$$\overline{q''(t)} = 0 \tag{2.7}$$

therefore,

$$\overline{\rho''} = 0$$
$$\tag{2.8}$$
$$\overline{P''} = 0$$

The mass-weighted variables are defined as follows:

$$u = \tilde{u} + u'$$

$$v = \tilde{v} + v'$$

$$H = \tilde{H} + H' \tag{2.9}$$

$$T = \tilde{T} + T'$$

A mass-weighted mean quantity is defined as:

$$\tilde{q} = \frac{\overline{\rho q}}{\overline{\rho}} \tag{2.10}$$

where the bar denotes conventional time averaging and the tilde denotes mass-weighted averaging. A consequence of combining the time and mass-weighted averaging is that

$$\overline{\rho u'} = 0$$

$$\overline{\rho v'} = 0$$

$$\overline{\rho H'} = 0 \qquad\qquad (2.11)$$

$$\overline{\rho T'} = 0$$

Applying the mass-weighted averaging on the boundary layer equations and then taking the mean, results in a complicated set of equations. An order of magnitude analysis can be used to determine which terms are small enough that they may be neglected. An assumption used in the averaging technique is that fluctuations in the transport properties μ and k are ignored. Since the temperature is allowed to fluctuate, this is an important assumption since μ and k are both functions of the temperature. Details of the averaging are described in Appendix A. The order of magnitude analysis used in this study parallels the analysis in Cebeci and Smith (7:71-78). The resulting set of boundary layer equations for turbulent flow are:

continuity

$$\frac{\partial \overline{\rho}}{\partial t} + \frac{\partial \overline{\rho}\,\overline{u}}{\partial x} + \frac{\partial \overline{\rho}\,\widetilde{v}}{\partial Y} = 0 \qquad\qquad (2.12)$$

x-momentum

$$\frac{\partial \overline{\rho}\,\overline{u}}{\partial t} + \frac{\partial \overline{\rho}\,\overline{u}\,\overline{u}}{\partial x} + \frac{\partial \overline{\rho}\,\overline{u}\,\widetilde{v}}{\partial Y} + \frac{\partial \overline{\rho}\,\overline{u'v'}}{\partial Y} = -\frac{\partial \overline{P}}{\partial x}$$

$$+ \frac{\partial}{\partial Y}\left[\mu \; \frac{\partial \overline{u}}{\partial Y} \right] \qquad\qquad (2.13)$$

Y-momentum

$$\frac{\partial \bar{P}}{\partial Y} = 0 \qquad (2.14)$$

energy

$$\frac{\partial \bar{\rho}\bar{H}}{\partial t} + \frac{\partial \bar{\rho}\bar{u}\bar{H}}{\partial x} + \frac{\partial \bar{\rho}\bar{v}\tilde{H}}{\partial Y} + \frac{\partial \overline{\bar{\rho}v'H'}}{\partial Y} = \frac{\partial \bar{P}}{\partial t}$$

$$+ \frac{\partial}{\partial Y}\left[\frac{k}{cp}\frac{\partial \bar{H}}{\partial Y}\right] + \frac{\partial}{\partial Y}\left[\left[\mu - \frac{k}{cp}\right]\frac{\partial}{\partial Y}\left(1/2\ \overline{\bar{u}\bar{u}}\right)\right] \qquad (2.15)$$

These eqns (2.12), (2.13), (2.14), and (2.15) are similar to the corresponding original eqns, (2.1), (2.2), (2.3) and (2.4), except for an additional term in the x-momentum equation and one in the energy equation. The additional term in the momentum equation, is called the Reynold's stress. These two additional terms from the momentum and energy equations are listed in eqns (2.16) and (2.17) and must be defined before the governing equations can be solved.

Reynold's stress term $\qquad -\overline{\bar{\rho}u'v'}$ $\qquad\qquad$ (2.16)

energy transport term $\qquad \overline{\rho v'H'}$ $\qquad\qquad$ (2.17)

Note the last two terms in the energy eqn (2.4) are the same as the last two terms in eqn (2.15), just rewritten in another form.

2.2.2 Closure Equations

Before the continuity, momentum, and energy equations, (2.12), (2.13), (2.14) and (2.15), can be solved, two more equations are needed for complete closure of the set of equations. Boussinesq (3:221) suggested that the apparent turbulent shear stresses might be related to the rate of mean strain through an apparent scalar turbulent or "eddy" viscosity. For the Reynold's stress term, eqn (2.16), the Boussinesq assumption gives

$$-\overline{\rho\#u\#'v\#'} = \mu_T\# \frac{\partial u\#}{\partial Y\#} \qquad (2.18)$$

where $\mu_T\#$ is a turbulent viscosity which will be defined later. The second closure equation (3:225; 7:239) uses a form of the Reynold's analogy which is based on the similarity between the transport of heat and momentum. Combining the Boussinesq assumption and Reynolds analogy:

$$\overline{\rho\#cp\#v\#'T\#'} = -k_T\# \frac{\partial T\#}{\partial Y\#} = -\mu_T\# \frac{cp\#}{Pr_T} \frac{\partial T\#}{\partial Y\#} \qquad (2.19)$$

where $k_T\#$ is the turbulent conductivity. Substituting in the closure eqns (2.18) and (2.19), the eqns (2.12), (2.13), (2.14), and (2.15) become:

continuity

$$\frac{\partial \rho\#}{\partial t\#} + \frac{\partial \rho\#u\#}{\partial x\#} + \frac{\partial \rho\#\tilde{v}\#}{\partial Y\#} = 0 \qquad (2.20)$$

x-momentum

$$\frac{\partial \bar{\rho}\# \bar{u}\#}{\partial t\#} + \frac{\partial \bar{\rho}\# \bar{u}\# \bar{u}\#}{\partial x\#} + \frac{\partial \bar{\rho}\# \bar{u}\# \tilde{v}\#}{\partial Y\#} = - \frac{\partial \bar{P}\#}{\partial x\#}$$

$$+ \frac{\partial}{\partial Y\#} \left[\left[\mu\# + \mu_T\# \right] \frac{\partial \bar{u}\#}{\partial Y\#} \right] \qquad (2.21)$$

Y-momentum

$$\frac{\partial \bar{P}\#}{\partial Y\#} = 0 \qquad (2.22)$$

energy

$$\frac{\partial \bar{\rho}\# \bar{H}\#}{\partial t\#} + \frac{\partial \bar{\rho}\# \bar{u}\# \bar{H}\#}{\partial x\#} + \frac{\partial \bar{\rho}\# \tilde{v}\# \bar{H}\#}{\partial Y\#} = \frac{\partial \bar{P}\#}{\partial t\#} + \frac{\partial}{\partial Y\#} \left[\left[\frac{\mu\#}{Pr} + \mu_T\#/Pr_T \right] \frac{\partial \bar{H}\#}{\partial Y\#} \right]$$

$$+ \frac{\partial}{\partial Y\#} \left[\mu\# (1 - 1/Pr) \frac{\partial}{\partial Y\#} (1/2 \, \overline{u\#u\#}) \right]$$

$$+ \frac{\partial}{\partial Y\#} \left[\mu_T\# \left[1 - 1/Pr_T \right] \frac{\partial}{\partial Y\#} (1/2 \, \overline{u\#u\#}) \right] \qquad (2.23)$$

Note that in many references, since the last term in equation (2.23) is very small, it is usually omitted.

The substitution of the Reynolds stress term into the x-momentum equation is mathematically trivial. However, for completeness, the mathematical steps of substituting the closure equations into the energy equation are displayed in detail in Appendix B.

2.2.3 Nondimensionalization

The turbulent boundary layer equations (2.20), (2.21), (2.22), and (2.23), are nondimensionalized using these factors.

$$x = \frac{x\#}{L\#} \qquad Y = \frac{Y\#}{L\#} \qquad t = \frac{t\#U_\infty\#}{L\#} \qquad u = \frac{u\#}{U_\infty\#} \qquad v = \frac{v\#}{U_\infty\#}$$

$$\mu = \frac{\mu\#}{\mu_\infty\#} \qquad \rho = \frac{\rho\#}{\rho_\infty\#} \qquad H = \frac{H\#}{U_\infty\#^2} \qquad P = \frac{P\#}{\rho_\infty\#U_\infty\#^2}$$

$$Pr = \frac{cp\#\mu\#}{k\#} \qquad Re = \frac{u\#L\#\rho\#}{\mu\#} \tag{2.24}$$

The resulting turbulent boundary layer equations are:

continuity

$$\frac{\partial \bar{\rho}}{\partial t} + \frac{\partial \overline{\rho u}}{\partial x} + \frac{\partial \overline{\rho \tilde{v}}}{\partial Y} = 0 \tag{2.25}$$

x-momentum

$$\frac{\partial \overline{\rho u}}{\partial t} + \frac{\partial \overline{\rho uu}}{\partial x} + \frac{\partial \overline{\rho u\tilde{v}}}{\partial Y} = -\frac{\partial \bar{P}}{\partial x} + \frac{\partial}{\partial Y}\left[\left[\mu + \mu_T\right]\frac{1}{Re}\frac{\partial \bar{u}}{\partial Y}\right] \tag{2.26}$$

Y-momentum

$$\frac{\partial \bar{P}}{\partial Y} = 0 \tag{2.27}$$

energy

$$\frac{\partial \overline{\rho H}}{\partial t} + \frac{\partial \overline{\rho uH}}{\partial x} + \frac{\partial \overline{\rho \tilde{v}H}}{\partial Y} = \frac{\partial \bar{P}}{\partial t} + \frac{\partial}{\partial Y}\left[\frac{1}{Re}\left[\frac{\mu}{Pr} + \mu_T/Pr_T\right]\frac{\partial \bar{H}}{\partial Y}\right]$$

$$+ \frac{\partial}{\partial Y}\left[\frac{1}{Re}\left[\mu(1 - 1/Pr) + \mu_T\left[1 - 1/Pr_T\right]\right]\frac{\partial}{\partial Y}(1/2\,\overline{uu})\right] \tag{2.28}$$

2.2.4 Dorodnitsyn Transformation

The Dorodnitsyn transformation (27:2-4) is used to scale these unsteady compressible boundary layer equations into a form similar to the incompressible boundary layer equations. This transformation is

$$X = x \qquad Y = \int_0^Y \rho \, dy \qquad t = t \qquad H = H$$

$$U = u \qquad V = \rho v + \frac{\partial Y}{\partial t} + u \frac{\partial Y}{\partial x} \qquad (2.29)$$

The nondimensional governing equations for turbulent boundary layer flow become

continuity

$$\frac{\partial \bar{U}}{\partial X} + \frac{\partial \tilde{V}}{\partial Y} = 0 \qquad (2.30)$$

x-momentum

$$\frac{\partial \bar{U}}{\partial t} + \bar{U}\frac{\partial \bar{U}}{\partial X} + \tilde{V}\frac{\partial \bar{U}}{\partial Y} = -\frac{1}{\rho}\frac{\partial \bar{P}}{\partial X} + \frac{\partial}{\partial Y}\left[\left[\mu + \mu_T \right] \frac{\rho}{Re} \frac{\partial \bar{U}}{\partial Y} \right] \qquad (2.31)$$

Y-momentum

$$\frac{\partial \bar{P}}{\partial Y} = 0 \qquad (2.32)$$

energy

$$\frac{\overline{\partial H}}{\partial t} + \overline{U}\frac{\overline{\partial H}}{\partial X} + \widetilde{V}\frac{\overline{\partial H}}{\partial Y} = \frac{1}{\overline{\rho}}\frac{\overline{\partial P}}{\partial t} + \frac{\partial}{\partial Y}\left[\left[\frac{\mu}{Pr} + \mu_T/Pr_T\right]\frac{\rho}{Re}\frac{\overline{\partial H}}{\partial Y}\right]$$

$$+ \frac{\partial}{\partial Y}\left[\frac{\rho}{Re}\left[\mu(1 - 1/Pr) + \mu_T\left[1 - 1/Pr_T\right]\right]\frac{\partial \overline{U^2/2}}{\partial Y}\right] \qquad (2.33)$$

Now that the governing equations have been derived, the set of equations can be solved once the turbulent viscosity is known. Several models for the turbulent viscosity will be presented in section 2.4.2.

2.3 *Description of Original Program*

The original computer program solves the unsteady compressible boundary layer equations for laminar flow. The boundary layer equations are first nondimensionalized and then transformed using the Dorodnitsyn transformation. Then these equations are transformed to the computational plane and finite differenced. The momentum and energy equations are solved using optimized successive over-relaxation, while the method of solving the continuity equation has been modified by Coffey (11:34) and solves for the V velocity using trapezoidal integration.

The wall, edge, and initial conditions for the current work are all specified exactly as in the original program (34:34-36). However, the plate was assumed to be stationary

throughout all the investigations, ie., not pitching. Since all the cases performed for this effort were for a flat plate, the edge conditions were the same as the infinity conditions.

2.3.1 Grid

In the program, the flat plate length is 1.25 feet in the $x\#$ direction and approximately two times the fully turbulent boundary layer thickness in the $Y\#$ direction. The program originally had only 61 points in the streamwise direction and 30 points in the normal direction. Although the number of grid points were significantly fewer than other schemes, it produced similar results when compared to other computer codes and theory, but at a faster rate and less cost due to its sparse grid. However, more points in the normal direction were added when the turbulence model was introduced to the program. The program currently has a 61 by 59 point grid.

One of the unique features of the original code is a generalized grid. This adds great capability to the code by enabling it to handle several configurations. For the present analysis, the physical grid varied exponentially in the $x\#$ direction. The $Y\#$ step size varied according to an exponential and power law velocity profile (21). In this study, the grid had a 1/2 power law which is optimum for laminar flow. For fully turbulent flow, a 1/7 power law should be used for the grid. In cases of transition to

turbulence, an optimized grid could be used. This optimized grid could be developed using a grid generation program (22) and then optimized using the adaptive-grid method to minimize truncation error as explained by Coffey (11).

Since the flow is compressible, density variations will essentially cause the physical grid to change. The Dorodnitsyn transformation eliminates the density fluctuations and allows the program to utilize a fixed grid. The Dorodnitsyn fixed grid is shown in Figures 2.1 and 2.3. The physical grid at steady state is shown in Figures 2.2 and 2.4. Both the full grid and an expanded view are shown. Note that the grid is smooth in the computational (Dorodnitsyn grid) plane, but is not in the physical plane at the transition location of x/L = 0.1 .

2.3.2 <u>Computational Grid</u>

A general transformation can be made to a rectangular computational grid. This grid is in the $\xi - \eta$ plane where ξ is in the streamwise direction and η is in the normal direction. The metrics ξ_X , ξ_Y , η_X , and η_Y that appear in the differential equations are solved using

$$\xi_X = Y_\eta / J$$

$$\xi_Y = - X_\eta / J$$

$$\eta_X = - Y_\xi / J$$
(2.34)

$$\eta_Y = X_\xi / J$$
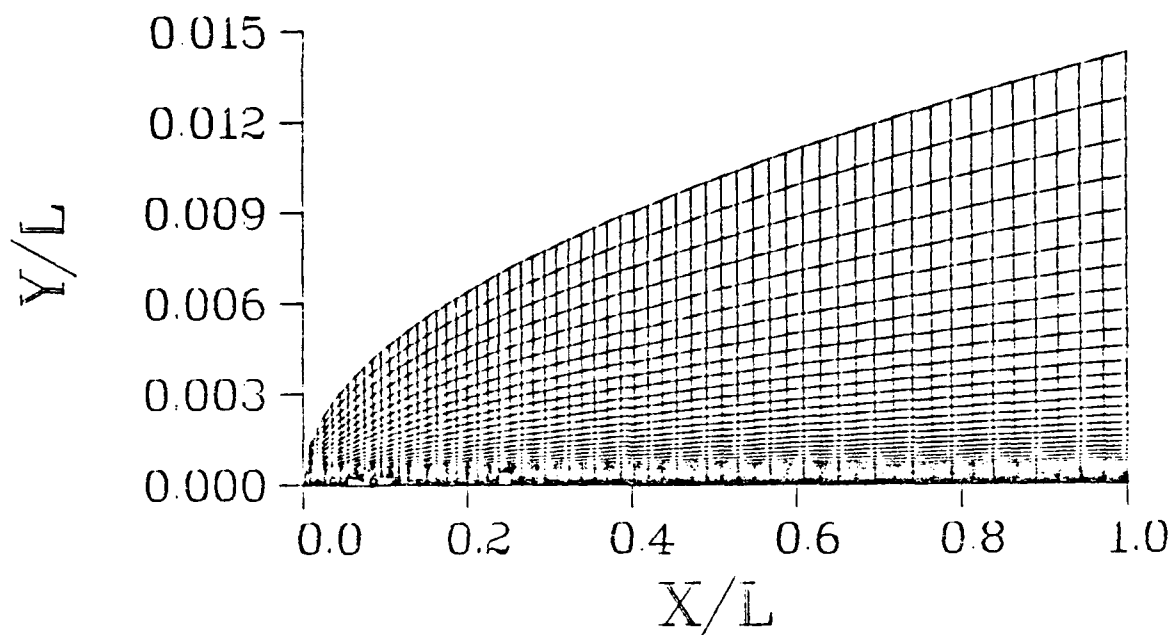
Figure 2.1.   Dorodnitsyn Fixed Grid
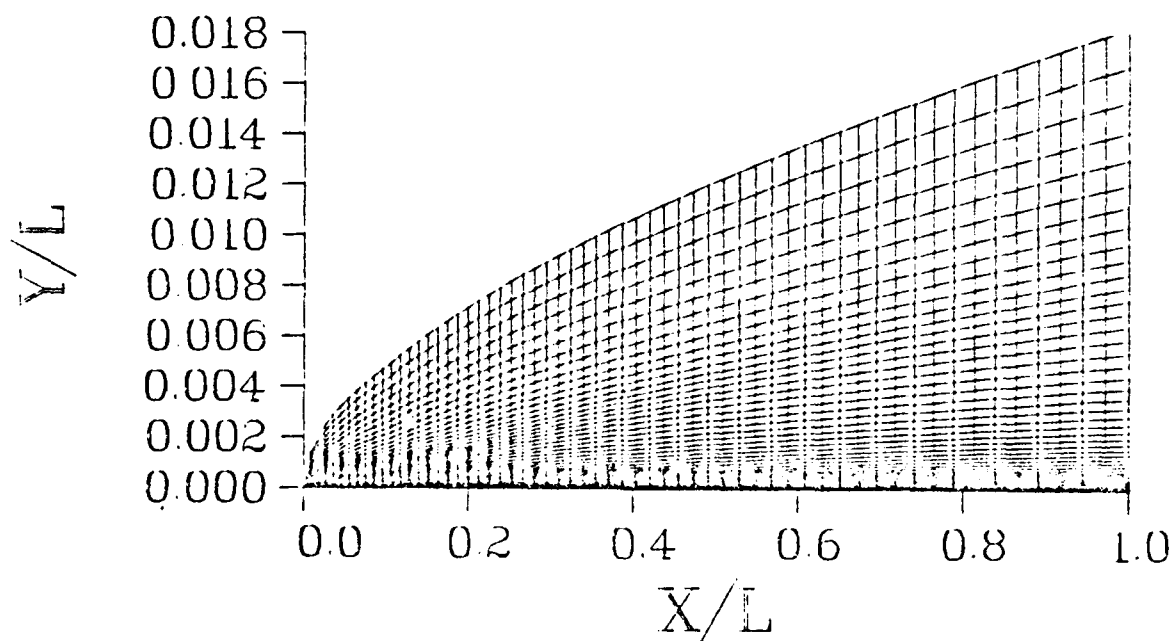
Figure 2.2.   Physical Grid
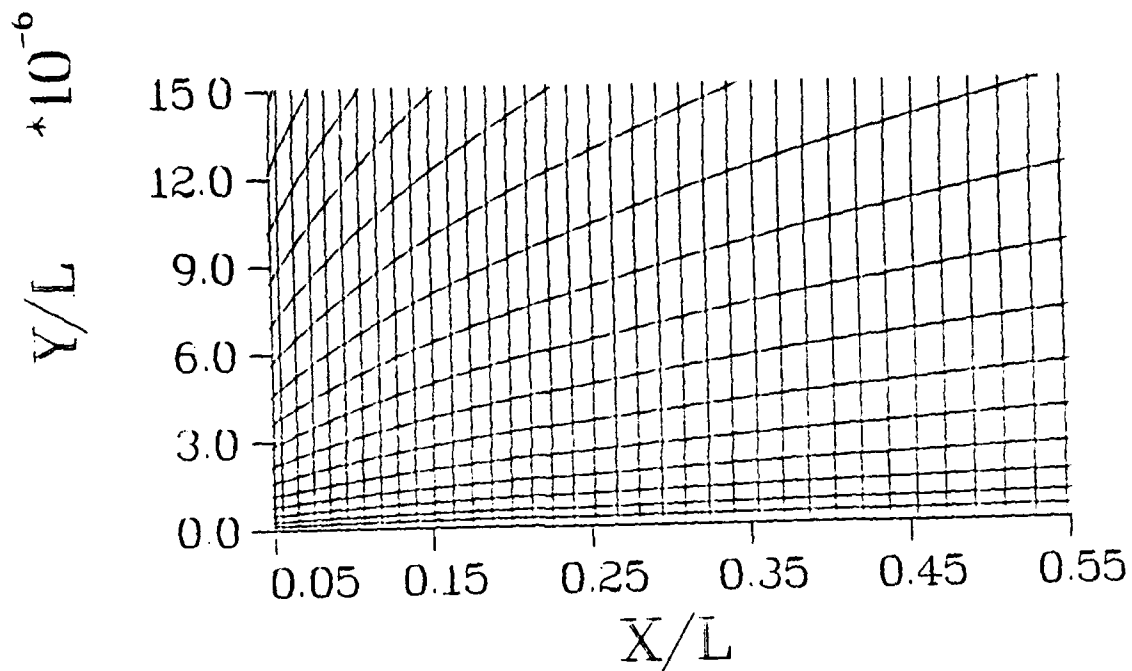
Figure 2.3.   Dorodnitsyn Fixed Grid - Expanded View
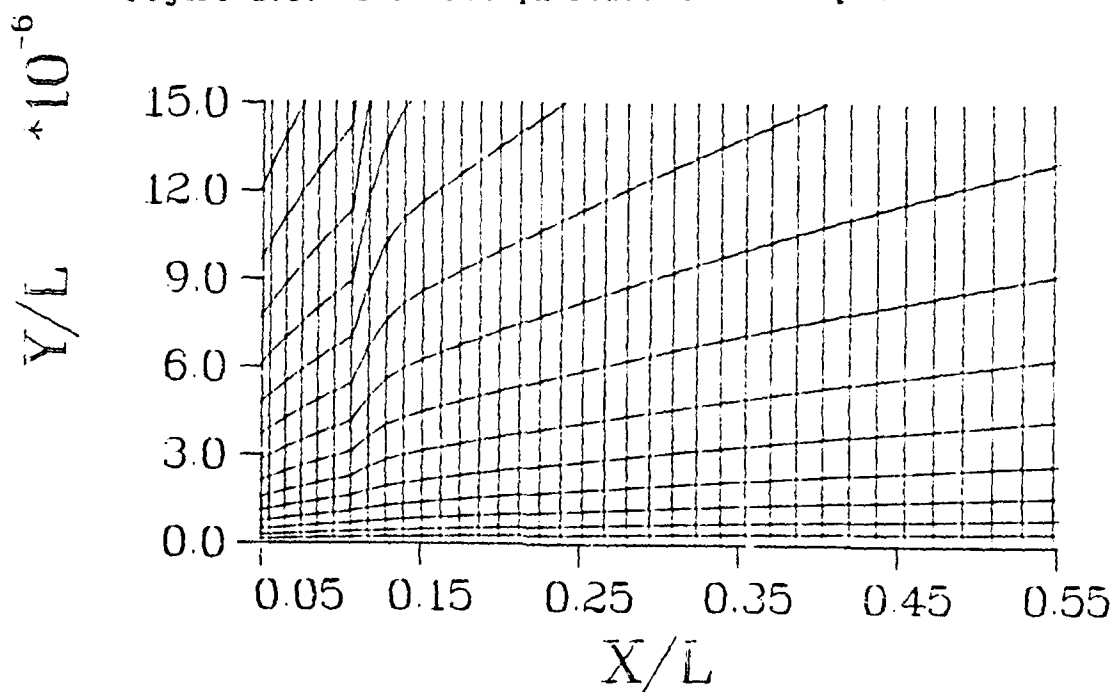
Figure 2.4.   Physical Grid - Expanded View

18

where J is the Jacobian of the transformation,

$$J = X_\xi Y_\eta - Y_\xi X_\eta \qquad (2.35)$$

The terms X_ξ, X_η, and Y_η are determined using finite differences. As in the original program, X does not change in the η direction so $X_\eta = 0$. The Y_ξ metric is determined differently than in Lange's thesis. Hodge (21) developed an analytical metric

$$Y_\xi = \frac{0.5}{X_\xi} \frac{Y}{X} \qquad (2.36)$$

which increases the code's applicability to also include variable X step sizes. Calculating the Y_ξ metric analytically near the leading edge and then using a numerical solution for the remaining points downstream of the leading edge avoids the large leading edge error as found by Lange (34:27). The numerical differencing is the same as described in Lange's thesis. Hodge (21) further modified the program to accept as an input the point from the leading edge at which the program switches from the analytic to the numerical calculation of the Y_ξ metric.

2.3.3 Numerical Method

The unsteady two-dimensional boundary layer equations are solved numerically by using an implicit finite difference scheme because it is unconditionally stable according to linear theory. The governing equations are first nondimensionalized, then transformed by the Dorodnitsyn transformation. Finally, they are then

transformed from the X - Y plane to the ξ - η computational
plane.

Once the equations are transformed to the ξ - η plane,
the first order spatial derivatives in the momentum and
energy equations are differenced using three point upwind
differencing. This differencing scheme guarantees diagonal
dominance and is second order accurate in the computational
plane. The time derivative is differenced using a two point
backward scheme which implies it is only first order
accurate in time. The second derivatives are approximated
with second order accurate central differencing. Similar
terms are then combined.

2.4 Modifications to Original Program

The modifications to the original laminar program that
exist in the turbulent boundary layer code are explained in
this section in detail. A copy of the turbulent boundary
layer code is listed in Appendix C.

The unsteady two-dimensional boundary layer equations
have been time and mass-weighted averaged, non-
dimensionalized, and transformed using the Dorodnitsyn
transformation. The governing equations are then
transformed from the X - Y plane to the ξ - η computational
plane. The continuity, x-momentum, and energy equations
(2.30), (2.31), and (2.33) become

continuity

$$\xi \, \overline{U}_\xi + \eta \, \overline{U}_\eta + \eta \, \tilde{V}_\eta = 0 \qquad\qquad (2.37)$$
$$ X \phantom{\overline{U}_\xi +} X \phantom{\eta \, \overline{U}_\eta +} Y$$

x-momentum

$$\bar{U}_t + \bar{U}\left[\bar{U}_\xi \xi_X + \bar{U}_\eta \eta_X\right] + \tilde{V}\bar{U}_\eta \eta_Y$$

$$= \eta_Y \left[\left[\mu + \mu_T\right]\rho\left[\bar{U}_\eta \eta_Y\right]\right]_\eta \frac{1}{Re} \qquad (2.38)$$

energy

$$\bar{H}_t + \bar{U}\left[\bar{H}_\xi \xi_X + \bar{H}_\eta \eta_X\right] + \tilde{V}\bar{H}_\eta \eta_Y = \frac{1}{\rho}\bar{P}_t$$

$$+ \left[\frac{\rho}{Re}\left[\frac{\mu}{Pr} + \mu_T/Pr_T\right]\bar{H}_\eta \eta_Y\right]_\eta \eta_Y \qquad (2.39)$$

$$+ \left[\frac{\rho}{Re}\left[\mu(1 - 1/Pr) + \mu_T\left[1 - 1/Pr_T\right]\right]\eta_Y\,(1/2\,\bar{U}^2)_\eta\right]_\eta \eta_Y$$

On a stationary flat plate, the pressure gradients in the normal direction are zero from the Y-momentum equation eqn (2.32). The pressure gradient in the streamwise direction has been assumed to be zero since any shock-boundary layer interaction is ignored. Now that the equations have been transformed to the ξ - η plane, the derivatives are finite differenced similar to the original program (cf. section 2.3). The equations for the x-momentum and the energy equation (2.38) and (2.39) become,

Momentum

$$
U^n_{i,j} = \left[U^{n-1}_{i,j} + 2\zeta \, \bar{U}\Delta t U^n_{X \; i-1,j} - .5 \, \zeta \, \bar{U}\Delta t U^n_{X \; i-2,j} \right.
$$

$$
- .5 \left[\eta_X \bar{U}\Delta t + \eta_Y \tilde{V}\Delta t \right] U^n_{i,j-2}
$$

$$
+ \left[2\eta_X \bar{U}\Delta t + 2\eta_Y \tilde{V}\Delta t + \eta_Y \frac{\Delta t}{Re} \left[\rho \left[\mu + \mu_T \right] \right]_{j+1/2} \eta_Y \right] U^n_{i,j-1}
$$

$$
+ \left. \left[\eta_Y \frac{\Delta t}{Re} \left[\rho \left[\mu + \mu_T \right] \right]_{j+1/2} \eta_Y U^n_{i,j+1} \right] \right/ UCOEFF
$$

$$
(2.40)
$$

Energy

$$
H^n_{i,j} = \left[H^{n-1}_{i,j} + 2\zeta \, \bar{U}\Delta t H^n_{X \; i-1,j} - .5\zeta \, \bar{U}\Delta t H^n_{X \; i-2,j} + \frac{1}{\bar{\rho}} d\bar{P} \right.
$$

$$
- .5 \left[\eta_X \bar{U}\Delta t + \eta_Y \tilde{V}\Delta t \right] H^n_{i,j-2}
$$

$$
+ \left[2\eta_X \bar{U}\Delta t + 2\eta_Y \tilde{V}\Delta t + \eta_Y \frac{\Delta t}{Re} \left[\rho \left[\mu/Pr + \mu_T/Pr_T \right] \right]_{j-1/2} \eta Y \right] H^n_{i,j-1}
$$

$$+ \; \P_Y \frac{\Delta t}{Re} \left[\wp \left[\mu/Pr + \mu_T /Pr_T \right] \right]_{j + 1/2} \P_Y \; H^n_{i,j+1}$$

$$+ \; \P_Y \frac{\Delta t}{2Re} \left[\left[\wp \left[\mu(1 - 1/Pr) + \mu_T \left[1 - 1/Pr_T \right] \right] \right]_{j + 1/2} \P_Y \; U^{2\,n}_{i,j+1} \right.$$

$$- \left[\left[\wp \left[\mu(1 - 1/Pr) + \mu_T \left[1 - 1/Pr_T \right] \right] \right]_{j + 1/2} \P_Y \right.$$

$$+ \left[\wp \left[\mu(1 - 1/Pr) + \mu_T \left[1 - 1/Pr_T \right] \right] \right]_{j - 1/2} \P_Y \right] U^{2\,n}_{i,j}$$

$$\left. + \left[\wp \left[\mu(1 - 1/Pr) + \mu_T \left[1 - 1/Pr_T \right] \right] \right]_{j - 1/2} \P_Y \; U^{2\,n}_{i,j-1} \right] \right] /UCOEFF$$

$$(2.41)$$

where

$$UCOEFF = 1 + \frac{3}{2} \xi_X \bar{U} \Delta t + \frac{3}{2} \eta_X \bar{U} \Delta t + \frac{3}{2} \eta_Y \tilde{V} \Delta t$$

$$+ \eta_Y \frac{\Delta t}{Re} \left[\left[\rho \left[\mu/Pr + \mu_T/Pr_T \right] \right]_{j+1/2} \eta_Y \right.$$

$$\left. + \left[\rho \left[\mu/Pr + \mu_T/Pr_T \right] \right]_{j-1/2} \eta_Y \right] \qquad (2.42)$$

Note that i and j are the node points in the $\xi - \eta$ plane, and n is the time level. The momentum and energy equations are nonlinear. To linearize the equations for the first iteration, the coefficients are lagged "in time". The coefficients in this program are based on the solution for U, V, and H at the previous time and same location for the first iteration, and subsequently from each previous iteration.

The linearization is the same as the original program. The calculation of the metrics also remain the same as developed by Hodge and Lange (cf. section 2.3.2). Once the momentum and energy equations are linearized, the equations can be written as:

Momentum

$$
U_{i,j}^{\substack{s+1\\n}} = \Bigg[\; U_{i,j}^{n-1} + \frac{2\Delta t}{X_{\xi}}\, U_{i,j}^{\substack{s\\n}}\, U_{i-1,j}^{\substack{s+1\\n}} \; - \; \frac{\Delta t}{2X_{\xi}}\, U_{i,j}^{\substack{s\\n}}\, U_{i-2,j}^{\substack{s+1\\n}}
$$

$$
- \;.5\Delta t\;\left[\; U_{i,j}^{\substack{s\\n}}\, \eta_{X} \;+\; \frac{1}{Y_{\eta}}\, V_{i,j}^{\substack{s\\n}} \;\right]\; U_{i,j-2}^{\substack{s\\n}}
$$

$$
+\; 2\Delta t\;\left[\; \frac{1}{(Y_{i,j+1} - Y_{i,j-1})\,Re}\; \frac{\left[\phi\left[\mu + \mu_{T}\right]\right]_{j-1/2}}{(Y_{i,j} - Y_{i,j-1})}\right.
$$

$$
\left.+\; U_{i,j}^{\substack{s\\n}}\, \eta_{X} \;+\; \frac{1}{Y_{\eta}}\, V_{i,j}^{\substack{s\\n}} \;\right]\; U_{i,j-1}^{\substack{s\\n}}
$$

$$
+\; 2\,\Delta t\;\; \frac{\left[\phi\left[\mu + \mu_{T}\right]\right]_{j+1/2}}{(Y_{i,j+1} - Y_{i,j-1})\,Re(Y_{i,j+1} - Y_{i,j})}\; U_{i,j+1}^{\substack{s\\n}}\;\Bigg]\; /UCOEFF
$$

$$
(2.43)
$$

Energy

$$
H_{i,j}^{\substack{s+1\\n}} = \Bigg[\; H_{i,j}^{n-1} + 2\Delta t\, U_{i,j}^{\substack{s\\n}}\, H_{i-1,j}^{\substack{s+1\\n}}\frac{}{X_{\xi}} \; - \; .5\Delta t\, U_{i,j}^{\substack{s\\n}}\, H_{i-2,j}^{\substack{s+1\\n}}\frac{}{X_{\xi}}
$$

$$- .5 \, \Delta t \left[U_{i,j}^{\underset{n}{s}} \, q_X + \frac{1}{Y_q} V_{i,j}^{\underset{n}{s}} \right] H_{i,j-2}^{\underset{n}{s}} + \frac{1}{\bar{\rho}} \, d\bar{P}$$

$$+ 2\Delta t \left[\frac{1}{(Y_{i,j+1} - Y_{i,j-1})Re} \frac{\left[\phi \left[\mu/Pr + \mu_T/Pr_T \right] \right]_{j-1/2}}{(Y_{i,j} - Y_{i,j-1})} \right.$$

$$\left. + U_{i,j}^{\underset{n}{s}} \, q_X + \frac{1}{Y_q} V_{i,j}^{\underset{n}{s}} \right] H_{i,j-1}^{\underset{n}{s}}$$

$$+ 2 \, \Delta t \quad \frac{1}{(Y_{i,j+1} - Y_{i,j-1})Re} \frac{\left[\phi \left[\mu/Pr + \mu_T/Pr_T \right] \right]_{j+1/2}}{(Y_{i,j+1} - Y_{i,j})} H_{i,j+1}^{\underset{n}{s}}$$

$$+ 2 \, \Delta t \quad \frac{1}{(Y_{i,j+1} - Y_{i,j-1})Re} \left[\frac{\left[\left[\phi \left[\mu(1-1/Pr) + \mu_T \left[1-1/Pr_T \right] \right] \right] \right]_{j+1/2}}{(Y_{i,j+1} - Y_{i,j})} \frac{U^2 \, {}_{i,j+1}^{\underset{n}{s}}}{2} \right.$$

$$- \left[\dfrac{\left[\phi \left[\mu(1 - 1/Pr) + \mu_T \left[1 - 1/Pr_T \right] \right] \right]_{j + 1/2}}{(Y_{i,j+1} - Y_{i,j})} \right.$$

$$+ \left. \dfrac{\left[\phi \left[\mu(1 - 1/Pr) + \mu_T \left[1 - 1/Pr_T \right] \right] \right]_{j - 1/2}}{(Y_{i,j} - Y_{i,j-1})} \right] U2^{s_n}_{\frac{i,j}{2}}$$

$$+ \dfrac{\left[\phi \left[\mu(1-1/Pr) + \mu_T \left[1-1/Pr_T \right] \right] \right]_{j - 1/2}}{(Y_{i,j} - Y_{i,j-1})} U2^{s_n}_{\frac{i,j-1}{2}} \Big/ UCOEFF \qquad (2.44)$$

where

$$UCOEFF = 1 + \frac{3}{2} \dfrac{U^{s_n}_{i,j}}{X_\xi} \Delta t + \frac{3}{2} U^{s_n}_{i,j} \eta_X \Delta t + \frac{3}{2} \dfrac{V^{s_n}_{i,j}}{Y_\eta} \Delta t$$

$$+ \quad 2\Delta t \left[\frac{\left[\wp\left[\mu/Pr + \mu_T/Pr_T \right] \right]_{j+1/2}}{(Y_{i,j+1} - Y_{i,j})} \right.$$

$$\left. + \frac{\left[\wp\left[\mu/Pr + \mu_T/Pr_T \right] \right]_{j-1/2}}{(Y_{i,j} - Y_{i,j-1})} \right]$$

The overall expression is divided by $(Y_{i,j+1} - Y_{i,j-1})Re$.

$$(2.45)$$

and

$$X_\xi = (X_{i+1,j} - X_{i-1,j})/2$$

$$Y_\eta = (Y_{i,j+1} - Y_{i,j-1})/2$$

$$\eta_X = -\frac{.5 \, Y_\xi}{X_\xi X X_\xi Y_\eta} = -\frac{Y_\xi}{X_\xi Y_\eta}$$

$$[\wp(\mu*)]_{j+1/2} = ([\wp(\mu*)]_{j+1} + [\wp(\mu*)]_j)/2$$

$$[\wp(\mu*)]_{j-1/2} = ([\wp(\mu*)]_j + [\wp(\mu*)]_{j-1})/2$$

$$(2.46)$$

where

$$\mu* = \mu/Pr + \mu_T/Pr_T$$

or

$$\mu* = \mu(1 - 1/Pr) + \mu_T(1 - 1/Pr_T)$$

and s is the iteration level. These equations are then solved in the program using an extension of Thomas' algorithm.

2.4.1 Thomas' Algorithm

Thomas' algorithm (3:99) is a technique for rapidly solving a tridiagonal system of linear algebraic equations. It is important to note that in any tridiagonal elimination scheme, as is Thomas' algorithm, truncation errors can grow quickly if diagonal dominance is not maintained. However, the finite differencing methods used in this program guarantee the existence of diagonal dominance. A diagonally dominant system guarantees errors are not propagated (3:343). The scheme of the Thomas' algorithm is as follows. Given a system of equations, M is the matrix of coefficients, U is the vector of independent variables, and E is the vector of dependent variables.

$$M_{i,j-1} U_{j-1} + M_{i,j} U_{j} + M_{i,j+1} U_{j+1} = E_{i} \qquad (2.47)$$

This system of equations is a tridiagonal system, ie, the matrix M has non-zero values only on the main diagonal and the lower and upper diagonal. The system of equations can be rewritten

$$\begin{bmatrix} d_1 & a_1 & 0 & 0 & 0 \\ b_2 & d_2 & a_2 & 0 & 0 \\ \cdot & \cdot & \cdot & \cdot & \\ & \cdot & \cdot & \cdot & \cdot \\ 0 & b_{JMAX-2} & d_{JMAX-2} & a_{JMAX-2} & 0 \\ 0 & 0 & b_{JMAX-1} & d_{JMAX-1} & a_{JMAX-1} \\ 0 & 0 & 0 & b_{JMAX} & d_{JMAX} \end{bmatrix} \begin{bmatrix} U_1 \\ U_2 \\ \cdot \\ \cdot \\ U_{JMAX-2} \\ U_{JMAX-1} \\ U_{JMAX} \end{bmatrix} = \begin{bmatrix} E_1 \\ E_2 \\ \cdot \\ \cdot \\ E_{JMAX-2} \\ E_{JMAX-1} \\ E_{JMAX} \end{bmatrix}$$

(2.48)

Thomas' algorithm works by eliminating the "b" diagonal and then solving for the U vector beginning at the Jmax location and stepping backwards. After the "b" diagonal is eliminated, the new values of the "d" and "a" diagonal are computed by

$$d_j = d_j - \frac{b_i a_{i-1}}{d_{j-1}} \qquad (2.49)$$

$$a_j = a_j \qquad (2.50)$$

$$e_j = e_j - \frac{b_i e_{i-1}}{d_{j-1}} \qquad (2.51)$$

The values for U may be obtained now by back substitution,

$$U_{Jmax} = \frac{e_{Jmax}}{d_{Jmax}} \qquad (2.52)$$

$$U_j = \frac{e_i - a_i U_{i+1}}{d_j} \qquad \text{for } j = Jmax-1, Jmax-2, \ldots, 1 \qquad (2.53)$$

When examining the governing equations for the momentum and energy equation (2.43) and (2.44), it can be seen that this particular system of equations is not a tridiagonal, but rather a penta-diagonal. An example of this penta-diagonal matrix can be seen in eqn (2.54).

The existence of the fourth or fifth diagonal depends on the sign of the V velocity. If the velocity is positive, the velocity gradients are backward differenced, and an $i,j-2$ term, "f" diagonal in eqn (2.54), will appear. If the velocity is negative the velocity gradients are forward differenced, and an $i,j+2$ term, "c" diagonal in eqn (2.54), will appear.

$$
\begin{bmatrix}
d1 & a1 & c1 & 0 & 0 & 0 \\
b2 & d2 & a2 & c2 & 0 & 0 \\
f3 & b3 & d3 & a3 & c3 & 0 \\
 & & & & & \\
0 & fJMAX-2 & bJMAX-2 & dJMAX-2 & aJMAX-2 & cJMAX-2 \\
0 & 0 & fJMAX-1 & bJMAX-1 & dJMAX-1 & aJMAX-1 \\
0 & 0 & 0 & fJMAX & bJMAX & dJMAX
\end{bmatrix}
$$

(2.54)

This situation is handled in the program differently depending on the sign of the velocity. If the velocity is positive, the $i,j-2$ term is a known value at the previous iteration and included in the e vector and the matrix is solved as a tridiagonal system of equations. If the velocity is negative, the $i,j+2$ term is an unknown and the

matrix is solved as a quad-diagonal. Eqns (2.50) and (2.53) need to be redefined if a quad-diagonal exists. The recursion formulas become:

$$a_j = a_j - \frac{b_i c_{i-1}}{d_{j-1}} \tag{2.55}$$

$$c_j = c_j \tag{2.56}$$

and then for the back substitution,

$$U_{Jmax-1} = \frac{e_{Jmax-1} - a_{Jmax-1} U_{Jmax}}{d_{Jmax-1}} \tag{2.57}$$

$$U_j = \frac{e_i - a_i U_{i+1} - c_i U_{i+2}}{d_j} \tag{2.58}$$

where $j = Jmax-2, Jmax-3,\ldots, 1$. This modification of the use of Thomas' algorithm should improve the efficiency of the program, relative to the efficiency using the optimized successive over-relaxation. A comparison of execution time was completed and the results are shown in a later section.

2.4.2 Turbulence Model

Turbulent boundary layer flow is divided into two regions: an inner region, and an outer region. The inner region is further subdivided into three regions, the viscous sublayer, the transitional region, and the fully turbulent region. The inner region of a turbulent boundary layer is much smaller than the outer region, with a thickness of about 10 to 20 % of the entire boundary layer thickness. An

example of these regions are illustrated in Figure 2.5. To
deal with the different regions, some special parameters
(7:95) have been defined. They are:

$$U_\tau\# = (\tau_W\#/\rho_W\#)^{1/2} \tag{2.59}$$

$$Y^+ = \frac{Y\#U_\tau\#\ \rho\#}{\mu\#} \tag{2.60}$$

$$U^+ = U\#/U_\tau\# \tag{2.61}$$
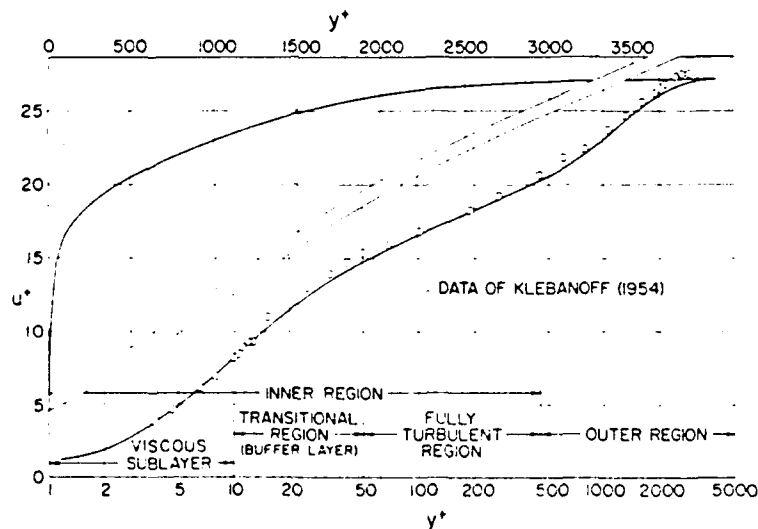
Semilogarithmic and linear plots of mean
velocity distribution across a turbulent
boundary layer with zero pressure gradient.
The linear plot is included to show a true
picture of the thickness of various portions.
(7:94)

Figure 2.5.   Turbulent Boundary Layer Regions

If $Y^+ < 10.0$, the region is typically considered to be the

viscous sublayer. If $10.0 < Y^+ < 500.0$, the region is typically defined as the rest of the inner region. If $Y^+ > 500.0$, the region is typically the outer region. These limits are very dependent upon the specific flow conditions.

In the viscous sublayer, molecular viscosity is assumed to be dominant over the turbulent viscosity, so that the turbulence viscosity approaches zero in this region. For the rest of the inner region, two models will be considered in this study; the Van Driest and Chapman models. In the outer region, the mixing layer model and Clauser's mixing length model have been included. The mixing length model has the turbulent length scale varying proportionately with the boundary layer thickness. Clauser's model has the turbulent viscosity varying proportionately with the kinematic displacement thickness. Clauser's model is recommended for compressible flow cases (7:120; 49:8), since it has been shown in several references to be more accurate.

Turbulence models center around the definition of the turbulent viscosity. Prandtl's Mixing Length Theorem states that the turbulent viscosity is related to two parameters: a turbulent length scale - called a mixing length, l, and the U velocity gradient in the normal direction.

$$\mu_T \# = \rho\# \ 1\#^2 \ \left| \frac{\partial U\#}{\partial Y\#} \right|$$ (2.62)

The two models for the inner region mixing length; the Van Driest model and the Chapman model, will now be examined.

This will be followed by the two models for the outer region, the mixing layer model and Clauser's model.

2.4.2.1 Inner Region Van Driest Model

The Van Driest model for the mixing length for turbulent flow was developed by considering flow over an oscillating plate (Stokes flow). Van Driest modified Prandtl's mixing length equation so that

$$l\# = KY\# \ [\ 1 - \exp \ (-Y\#/A\#) \ ] \tag{2.63}$$

where K is von Karman's constant. K is nominally 0.41, but can be changed in the program for each case since K is an input. If the turbulent viscosity, eqn (2.62) is rewritten,

$$\mu_T\# = \rho\# \ (KY\#)^2 \ Lm \ \left| \frac{\partial U\#}{\partial Y\#} \right| \tag{2.64}$$

where Lm can be called a new mixing length parameter defined by Van Driest (7:213-215) as

$$Lm_{VD} = [\ 1 - \exp \ (-Y\#/A\#) \ ]^2 \tag{2.65}$$

The A# defined originally by Van Driest is limited to incompressible turbulent boundary layers with negligible pressure gradient and zero mass transfer. Cebeci and Smith (7:215-217) include compressibility effects by adding a density ratio to the parameter A# so it becomes,

$$A\# = A^+ \ (\mu\#/\rho\#)_W \ (\tau_W\#/\rho_W\#)^{-1/2} \ (\rho\#/\rho_W\#)^{1/2} \tag{2.66}$$

where $A^+ = 26.0$.

If the definition for Y^+, eqn (2.60), is solved for Y# and substituted in eqn (2.65), Lm_{VD} can be rewritten as

$$Lm_{VD} = \{ 1 - \exp [- (Y^+/A^+)] \}^2 \qquad (2.67)$$

Now that the model has been defined, it is of interest to determine what kind of behavior the Van Driest's mixing length parameter contributes to the Reynold's stress or turbulent viscosity near the wall. If the series expansion for exp(-Y#/A#) near the wall, is

$$\exp (-Y/A) = \sum_{n=0}^{\infty} \frac{(-1)^n}{n!} (Y/A)^n = 1 - Y/A + H.O.T. \qquad (2.68)$$

(where H.O.T. means higher order terms) and is substituted into eqn (2.65), it can be seen that

$$Lm_{VD} = (Y\#/A\#)^2 + H.O.T. \qquad (2.69)$$

where only the first term is retained since it determines the behavior of the function. Substituting this equation for Lm_{VD} back into equation (2.64) one obtains

$$\mu_T\# = \rho\# \ K^2 \ \frac{Y\#^4}{A\#^2} \ \left| \frac{\partial U\#}{\partial Y\#} \right| \qquad (2.70)$$

Therefore, the Van Driest model gives the turbulent viscosity fourth order behavior in Y#.

2.4.2.2 Inner Region Chapman Model

The motivation that Chapman had in deriving a new mixing length model arose from an analysis of oscillating shear flow over an infinite plate; recall Van Driest studied flow over an oscillating plate. Using only the continuity

equation and Taylor series expansions, Chapman, and Reichardt (9:7) earlier, showed that the leading term of the Reynolds stress is proportional to Y^3. Therefore, the turbulent viscosity should also be proportional to Y^3.

Prandtl's Mixing Length equation with Van Driest's initial modification, eqn (2.63), is used in the Chapman model. However, the mixing length for turbulent flow needed in eqn (2.64) as given by Chapman (9:8) is

$$Lm_C = [1 - 2 \cos \beta \exp (-\beta) + \exp (-2\beta)]^{1/2} \qquad (2.71)$$

where $\beta = Y^+ / AOS^+$, and AOS is usually 111.0 for incompressible flow. [Reference (9) has a typographical error, eqn (2.71) is correct (8)]. For this analysis it was assumed that the same density ratio compressibility factor, as developed by Cebeci and Smith for the Van Driest model, could also be included in AOS to account for compressibility effects.

$$AOS^{\#} = AOS^+ (\rho/\rho_W)^{1/2} \qquad (2.72)$$

where $AOS^+ = 111.0$ and β becomes

$$\beta = \frac{Y^+}{AOS^+} \qquad (2.73)$$

To determine the type of behavior the Chapman model contributes to the turbulent viscosity, the series representation of the cosine function and the exponential function,

$$\cos(\beta) = \sum_{n=0}^{\infty} \frac{(-1)^n}{(2n)!} (\beta)^{2n} = 1 - .5\beta^2 + \text{H.O.T.} \qquad (2.74)$$

$$\exp(-\beta) = \sum_{n=0}^{\infty} \frac{(-1)^n}{n!} \beta^n = 1 - \beta + \text{H.O.T.} \qquad (2.75)$$

$$\exp(-2\beta) = \sum_{n=0}^{\infty} \frac{(-1)^n}{n!} (2\beta)^n = 1 - 2\beta + \text{H.O.T.} \qquad (2.76)$$

are substituted into equation (2.71) so that Lm_C can be rewritten in the form

$$Lm_C = [\ 1 - 2(1-.5\beta^2+...)(1-\beta+...) + (1-2\beta+...)]^{1/2} \qquad (2.77)$$

$$Lm_C = [\ \beta^2 + \text{H.O.T.}\ ]^{1/2} \approx \beta + \text{H.O.T} \qquad (2.78)$$

Substituting the leading term of eqn (2.78) into the equation for the turbulent viscosity, eqn (2.64), one obtains

$$\mu_T{}^\# = \frac{\varrho^\#}{\frac{+}{AOS}} K^2 Y\#^3 \left| \frac{\partial U\#}{\partial Y\#} \right| \qquad (2.79)$$

Therefore, it can be seen that Chapman developed his model to achieve third order behavior in $Y\#$ for the turbulent viscosity.

The Van Driest and Chapman mixing length theories will both be used in the program and the differences between their results examined in a later section.

2.4.2.3 Outer Region Mixing Length Model

In the outer region, the flow is very different than the inner region, so a new scaling for the mixing length is

needed. Again, using Prandtl's mixing length theorem, the applicable equation for turbulent viscosity is equation (2.62). During the calculations of the mixing length 1#, when the parameter 1# becomes equal to .089δ#, the equation for 1# is changed to

$$lo\# = 0.089 \ \delta\# \qquad\qquad (2.80)$$

This new equation for 1#, eqn (2.80) (3:223), insures that the inner and the outer regions will be piecewise continuous in the turbulent length scale and the turbulent viscosity.

2.4.2.4 Outer Region Clauser Model

The Clauser model (3:225) assumes the turbulent viscosity is proportional to the kinematic viscosity, δ*#. The equation for the turbulent viscosity for the Clauser model is:

$$\mu_T\# = \alpha* \ \rho\# \ U_e\# \ |\delta*\#| \qquad\qquad (2.81)$$

where α* accounts for low Reynolds number effects. For Reynold's numbers greater than 5000,

$$\alpha* \approx 0.0168 \qquad\qquad (2.82)$$

and the kinematic displacement thickness is defined by

$$\delta*\# = \int_0^\infty \left[1 - \frac{U\#}{U_e\#} \right] \ dY\# \qquad\qquad (2.83)$$

For the cases run in this study, the edge velocity is equivalent to the freestream velocity, so U∞# is used in eqn (2.83). The integral is evaluated using a trapezoidal rule

with U averaged about the j-1/2 point prior to the integration. When the Clauser's model is used in the program, the switch between the inner region and the outer region occurs when μ_T (outer) = μ_T (inner) so that the turbulent viscosity is piecewise continuous between the two regions.

2.4.2.5 Intermittency

As the edge of the boundary layer is approached in the outer region, the turbulence becomes intermittent; that is, only a fraction, σ, of the time the flow is turbulent. Without a factor to account for this intermittency, the amount of turbulence calculated to be present in the outer region would be overpredicted. The intermittency factor is defined by an error function (7:110) but is approximated by (50:4)

$$\sigma = [\ 1 + 5.5 \ (Y\#/\delta\#)^6 \ ]^{-1} \qquad (2.84)$$

The intermittency parameter is introduced into the model by multiplying μ_T by σ.

2.4.3 Transition Model

The transition model bridges the gap between laminar flow and fully turbulent flow. One such model (18:29) considers the transition region, and introduces a transition parameter that varies from 0, the edge of the laminar region, to 1, the beginning of the fully turbulent region. This transition parameter multiplies the turbulent

viscosity. Therefore, only a fraction of the turbulent viscosity is added to the governing equations, depending on the position of the flow in the transition region.

The transition parameter, Γ, is defined as (18:29)

$$\Gamma = 1 - \exp(-.412\ \Theta^2) \tag{2.85}$$

where Θ is the normalized streamwise coordinate in the transition region. Θ is defined by

$$\Theta = \frac{x - x_{T,I}}{\Xi} \qquad \text{where} \qquad x_{T,I} \le x \le x_{T,F} \tag{2.86}$$

with $x_{T,I}$ being the location of the beginning of transition and $x_{T,F}$ is the final location of transition, or the beginning of the fully turbulent region. The x is the location that is being analyzed. The measure of the extent of the transition region is Ξ where it is defined by

$$\Xi = x\big|_{\Gamma = 3/4} - x\big|_{\Gamma = 1/4} \tag{2.87}$$

Usually Ξ is allowed to vary until agreement with experimental data is reached. The use of this model insures a smooth transition from laminar to fully turbulent flow.

2.4.4 Heat Transfer and Viscosity

The original program references the heat transfer calculations to reference conditions. These references are not useful for turbulent flow data. To examine the turbulent heat transfer data on a flat plate, it is customary to compare the Stanton number with the local Reynold's number, Rex, as shown in Figure 2.6. The Stanton number is defined as

41

$$St = \frac{HC}{c_p \rho_\infty U_\infty} \qquad (2.88)$$

with the heat transfer coefficient being defined as

$$HC = \frac{q}{T_{AW} - T_W} \qquad (2.89)$$

The local Reynold's number is defined as

$$Re_x = \frac{\rho U_\infty x}{\mu} \qquad (2.90)$$
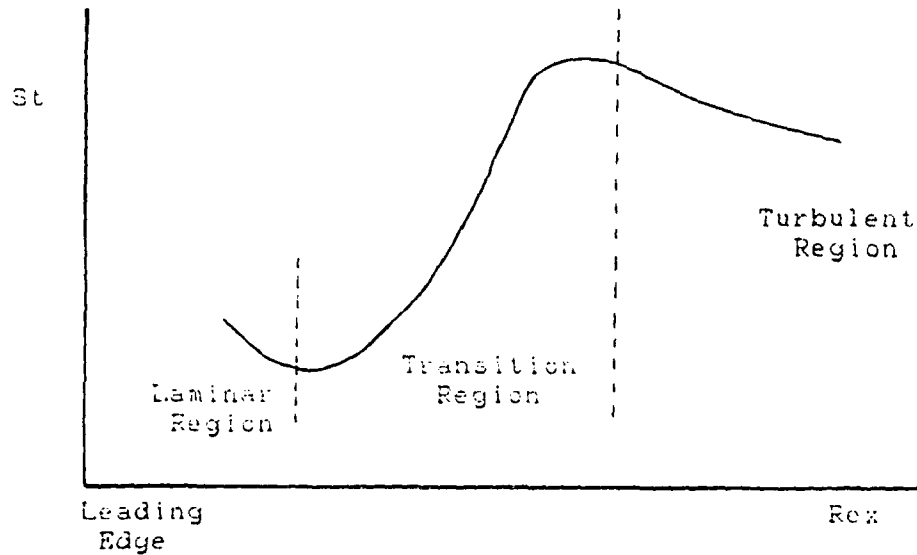
Figure 2.6. Heat Transfer on a Flat Plate

where x is the position on the plate where the Stanton number was obtained. If r is the recovery factor, the adiabatic wall temperature is defined as

$$T_{AW} = T_o [\ 1 + .5\ r\ (\gamma-1)\ M_\infty^2\ ] \qquad (2.91)$$

The recovery factor in this study is defined as

42

$$r = Pr^{1/2} \qquad \text{for laminar flow} \qquad (2.92)$$

$$r = Pr^{1/3} \qquad \text{for turbulent flow} \qquad (2.93)$$

The transition model is used to vary the value of the recovery factor in the transition region. The value of the Prandtl number is 0.72.

In turbulence models, a turbulent Prandtl number is defined as

$$Pr_T = \mu_T \, cp \, / \, k_T \qquad (2.94)$$

and its nominal value is 0.90. The turbulent Prandtl number is a counterpart of the molecular Prandtl number to take into account the turbulent energy transport. However, the turbulent Prandtl number is used as a tool to obtain the turbulent conductivity, k_T. Since the turbulent Prandtl number and the heat capacity for constant pressure are both constants, it is interesting to note that

$$k_T \approx \mu_T \qquad (2.95)$$

This says that the diffusion of the turbulent energy is directly related to the turbulent viscosity.

The local skin friction coefficient, c_f, is calculated by the program using (7:28)

$$c_f = \frac{2 \, \tau_W}{\rho_\infty \, U_\infty^2} \qquad (2.96)$$

The theoretical skin friction coefficient for incompressible flow on a smooth flat plate is given by (7:187)

43

$$c_f = 0.664 \, (Re_x)^{1/2} \tag{2.97}$$

The viscosity is calculated throughout the program using Keyes viscosity equation, which is

$$\mu = \frac{2.32 \times 10^{-8} \, T^{1/2}}{1 + \frac{220}{T \times 10^{9/T}}} \quad \frac{lb \, sec}{ft^2} \tag{2.98}$$

where T is in degrees Rankine. Keyes viscosity law is more accurate (34:5) in the temperature range encountered in hypersonic wind tunnels than the popular Sutherland's viscosity law. In hypersonic tunnels, the static freestream temperature is generally between 30°R and 200°R, which is below 300°R, the demonstrated range of applicability of Sutherland's law.

2.5 Program Verification

The thesis computer code is verified by comparison of its results to experimental data and another computer code. The experimental data was obtained from several sources, and will be described later in each of the pertinent sections. The other computer code, hereafter called the ITRACT computer code, was developed by the Hypersonic Research Laboratory at Wright-Patterson Air Force Base. The code is a steady state compressible boundary layer code using the Van Driest eddy viscosity turbulence model (49).

2.5.1 Incompressible Laminar

The program inputs used for comparison against incompressible laminar flow over a flat plate (Blausius' solution) are $M_\infty=.05$ and $T_w = 530^\circ$ R. The Y_t metric was calculated analytically over the entire plate. In Figure 2.7, the Blausius solution (46:42) for the velocity is plotted against the numerical solution for the program in laminar flow. The computer results fall almost directly on top of the theoretical results. In Figure 2.8, the ratio of the numerical skin friction coefficient to the theoretical skin friction coefficient is plotted against x#/L#. Since the results are very nearly a constant 1.0, the computer results almost exactly match the theoretical results.

At this Mach condition, the flow is incompressible and laminar so the Dorodnitsyn transformation and turbulence model are still unverified. However, the Thomas algorithm has been verified to be correct.

2.5.2 Incompressible Turbulent Isothermal

It is necessary to verify the validity of the turbulence model. This is done by comparing its results with that of experimental data. The data are taken from a NASA memorandum (44:24). The probable errors in the local Stanton numbers is $\pm3\%$, and the probable errors in the local Reynolds number is $\pm1\%$ (44:17). The NASA reference calculated the heat transfer coefficient using

$$HC = \frac{q}{T_W - T_\infty} \qquad (2.99)$$

The ITRACT computer code calculated HC using

$$HC = \frac{q}{T_o - T_W} \qquad (2.100)$$

The thesis computer code calculates HC using

$$HC = \frac{q}{T_{AW} - T_W} \qquad (2.101)$$

The two computer codes were first modified so that the heat transfer coefficient was calculated by the eqn (2.99) which was used by the NASA reference. The data from the three different sources could now be compared. The Y_t metric in the thesis computer program was calculated analytically over the entire plate. Note that the computer code actually calculates compressible flow conditions, but the density variations are on the order of 1% .

Figure 2.9 shows the results of the comparison when the Van Driest model is used for the inner region, and Clauser's model is used for the outer region. The ITRACT computer solution is approximately 20% lower than the experimental data, while the thesis computer solution is approximately 10% lower than the experimental data. This difference could be due to the value of the empirical constants used in the turbulence models, and also truncation errors. However, the thesis code does an adequate job in predicting heat transfer for incompressible turbulent flows.

2.5.3 Incompressible Turbulent Nonisothermal

The thesis code can now be verified using experimental data for incompressible turbulent flow with a nonisothermal wall, or thermal mismatch of approximately 20°F. The data are obtained from a NASA memorandum (45:27). The NASA reference calculates the heat transfer coefficient as shown in eqn (2.99). Again the thesis computer code was modified so that the calculation of the heat transfer coefficient was consistent with the experimental data. The Y_k metric in the thesis computer program was calculated analytically over the entire plate.

When the Van Driest model is used in the inner region and Clauser's model is used in the outer region, Figure 2.10 shows the results of the the comparison. The thesis solution is very close to the experimental data.

2.5.4 Compressible Turbulent Isothermal

The turbulence model and the Dorodnitsyn transformation need to be validated for compressible flow. This will be done by comparing the code to experimental shock tube data of compressible turbulent flow. The data are obtained from a NASA Contractor Report (4:131). The report verifies that the shock tube data agree with perfect gas results to within 3 %.

The experimental data shows a spike in the heating at the beginning of transition. This spike is characteristic of shock tube data. Transition in a shock tube is first

indicated by a series of spikes in the heat transfer data. These spikes are associated with "turbulent bursts" created at the edge of the viscous sublayer (23:6,12). The experimental data also calculates the heat transfer coefficient differently than the thesis computer program. The reference calculates the heat transfer coefficient using

$$HC = \frac{q\ cp}{H_o - H_W} \qquad (2.102)$$

Assuming constant heat capacity, the ITRACT and thesis codes were modified to be consistent with the experimental data.

When the Van Driest model is used for the inner region and Clauser's model is used for the outer region, Figure 2.11 shows the results of the comparison. The ITRACT code for the fully turbulent case is approximately 20% higher than the experimental data. The thesis code is 10% higher than the experimental data, but does model the peak heating at the end of transition very well. Both codes do an excellent job in predicting the laminar portion of the curve.

Figure 2.12 shows a comparison between all the models used in this study. Four cases were examined: Van Driest / Clauser, Van Driest / Mixing Length, Chapman / Clauser, and Chapman / Mixing Length. The inner region models, Van Driest and Chapman, produce results to within 1% of each other, with Chapman giving slightly lower results. This indicates that the argument between the models, the Y^4

versus Y^3 dependence on the turbulent viscosity is mainly an academic discussion for this case. The outer region models, mixing length and Clauser, also produce similar results, with the mixing length model giving 1.5% higher results than Clauser's model.

2.6 Results of Computational Effort

2.6.1 Decrease in Computer Time

A comparison between the original program with the optimized successive over-relaxation method and the modified program with the Thomas algorithm was completed for laminar flow. Table (2.1) gives the results of the comparison. NT is the number of time steps, DT was the temporal increment in artificial units, and the maximum error allowed was EPS. For these runs, NT = 10, and DT = 1000. As the maximum error allowed increases, the difference between the two algorithms decreases, so there would be no advantage to using the Thomas algorithm versus optimized successive over-relaxation when high accuracy is not important. However, it is evident for the error criteria specified in these cases, the Thomas algorithm is more efficient for solving this particular differencing scheme, especially for grids with a larger number of points.

Table 2.1.   Comparison of SOR and Thomas Algorithm

	SOR (CPU Seconds)	Thomas (CPU Seconds)
EPS = 10^{-5} 61x30 Grid	20	16
EPS = 10^{-6} 61x30 Grid	32	21
EPS = 10^{-5} 61x59 Grid	297	35

2.6.2 Laminar

The thesis program is excellent in predicting the flow properties of incompressible laminar flows.   The program verification of the U velocity and skin friction coefficient showed the results were nearly identical to the theoretical results.

2.6.3 Turbulence

The thesis program predicts the heat transfer of incompressible and compressible turbulent flows very well. The thesis program results were approximately 10% different than the experimental data.   This 10% error could perhaps be due to truncation error.   The use of an optimized grid could probably improve the results.   However, the program accurately predicted the heat transfer results of the incompressible turbulent flow when a thermal mismatch of 20° was present.   Comparisons of the inner region and outer region models showed very little difference between the results, with the Chapman model giving 1% lower results

compared to Van Driest, and the mixing length model giving 1.5% higher results compared to Clauser.
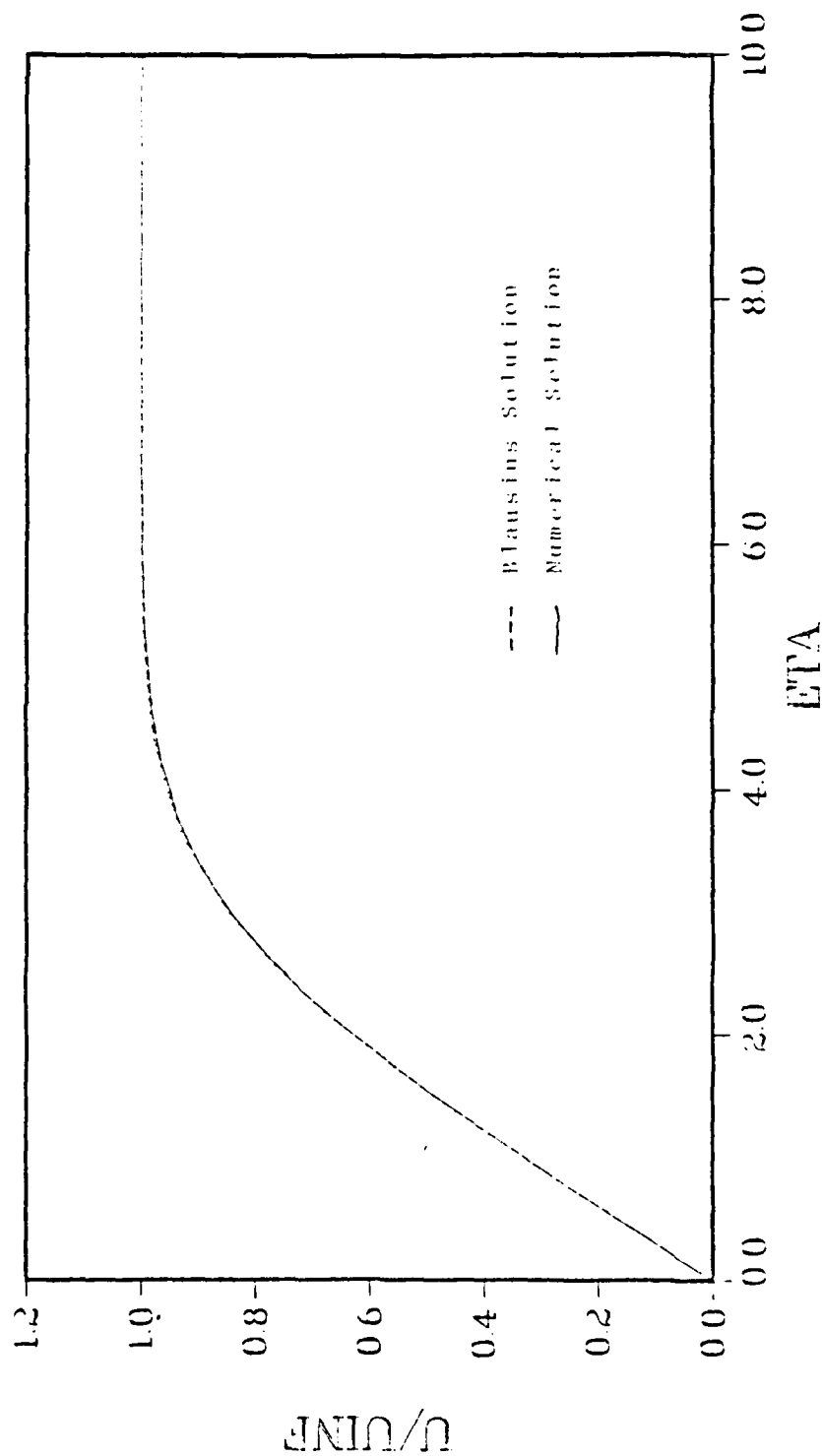
Figure 2.7. Incompressible Flow Verification

52
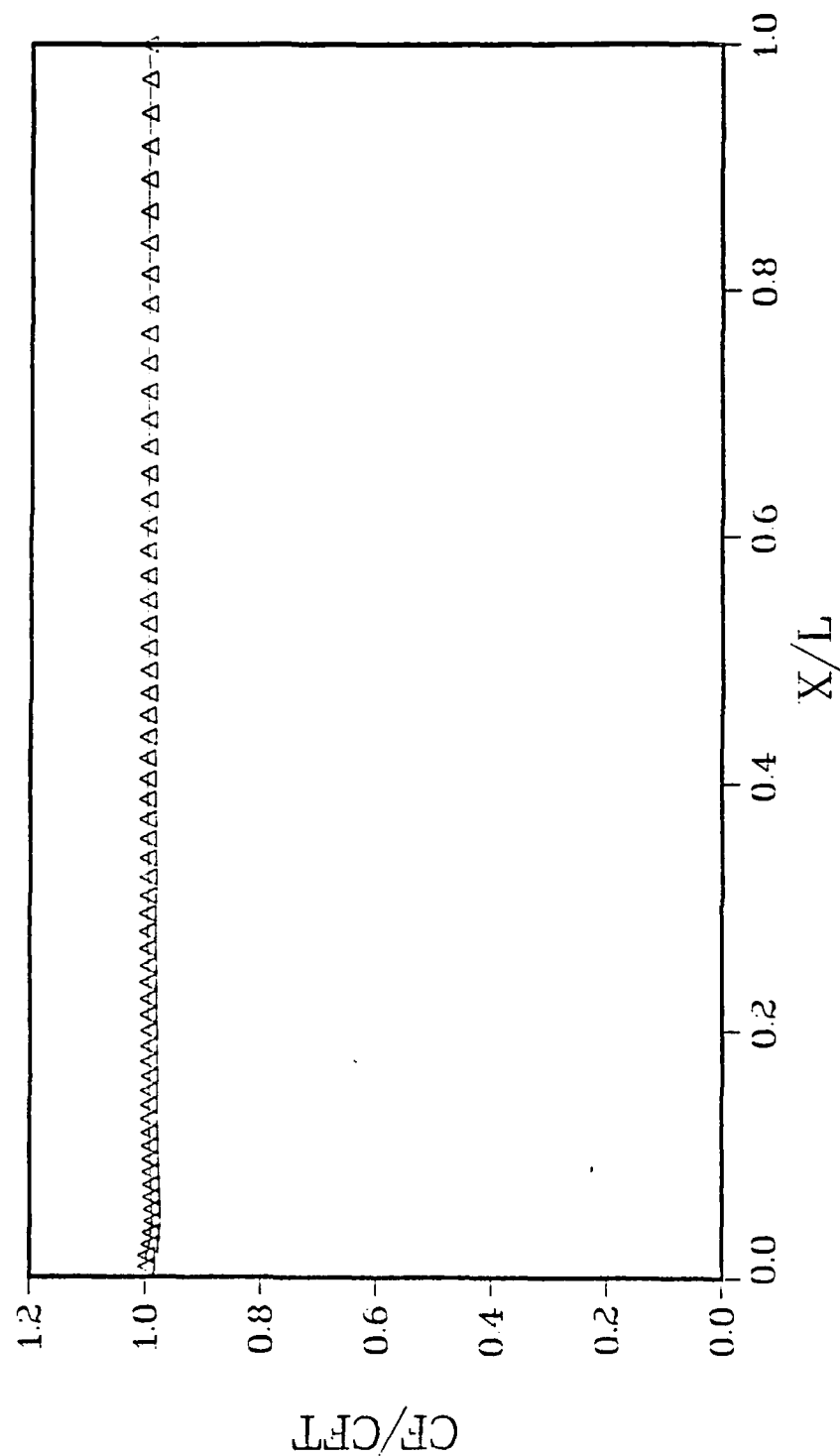
Figure 2.3.   Incompressible Skin Friction Verification

53
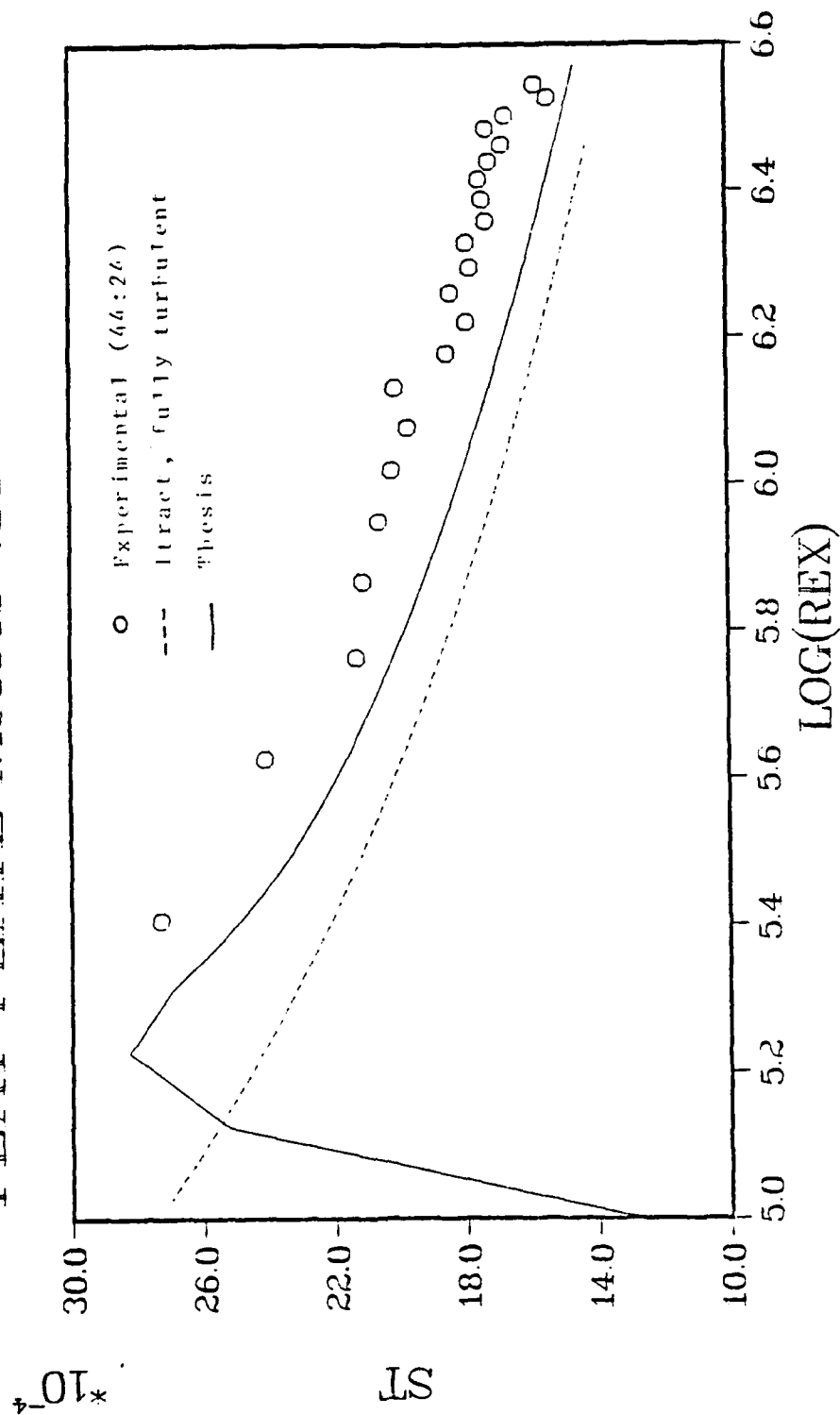
Figure 2.9. Incompressible Turbulent Flow Verification -
Van Driest/Clauser Models
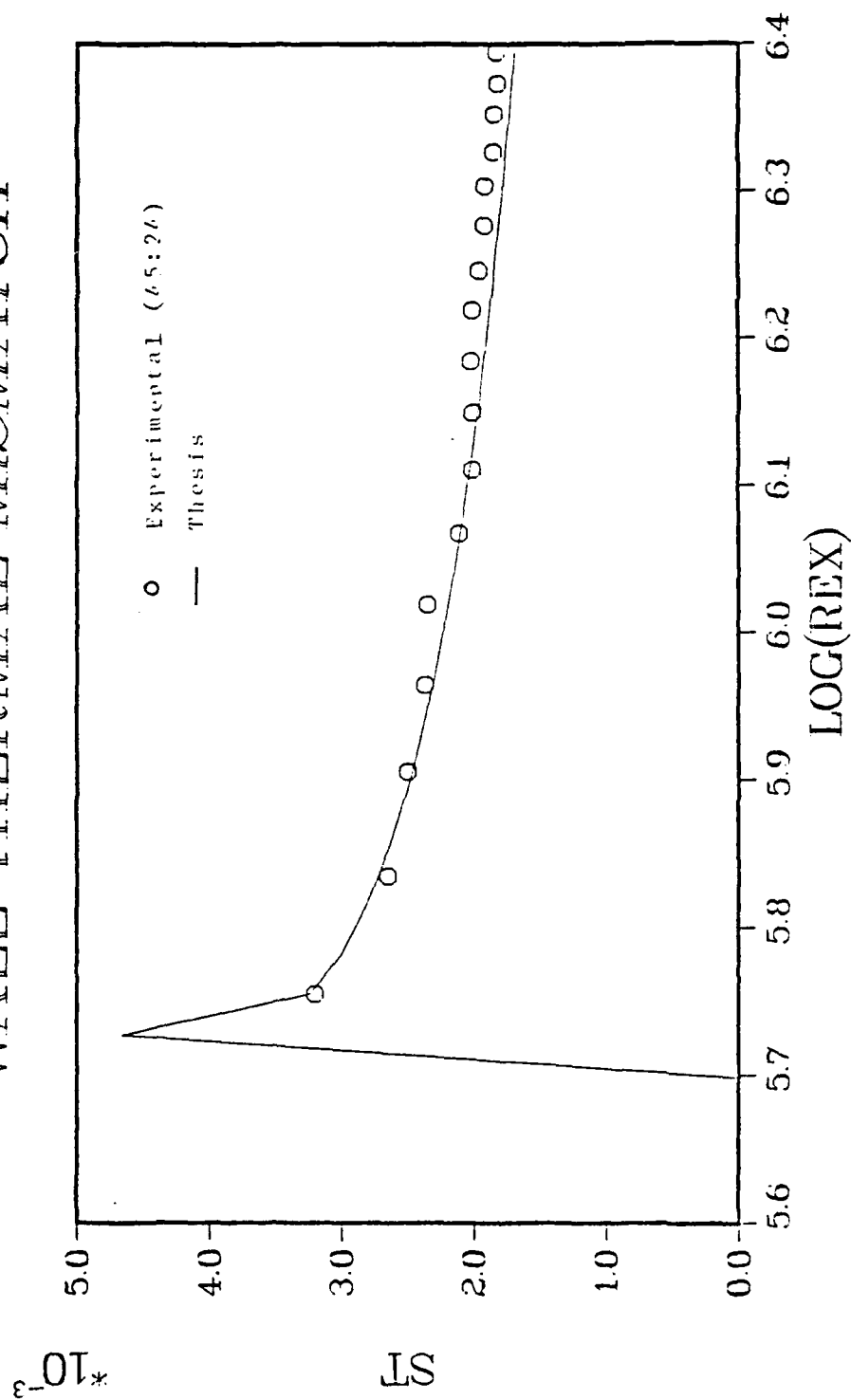
Figure 2.10.   Incompressible Turbulent Flow with Thermal
Mismatch - Van Driest/Clauser Models

FLAT PLATE MACH=7 COMPARISON
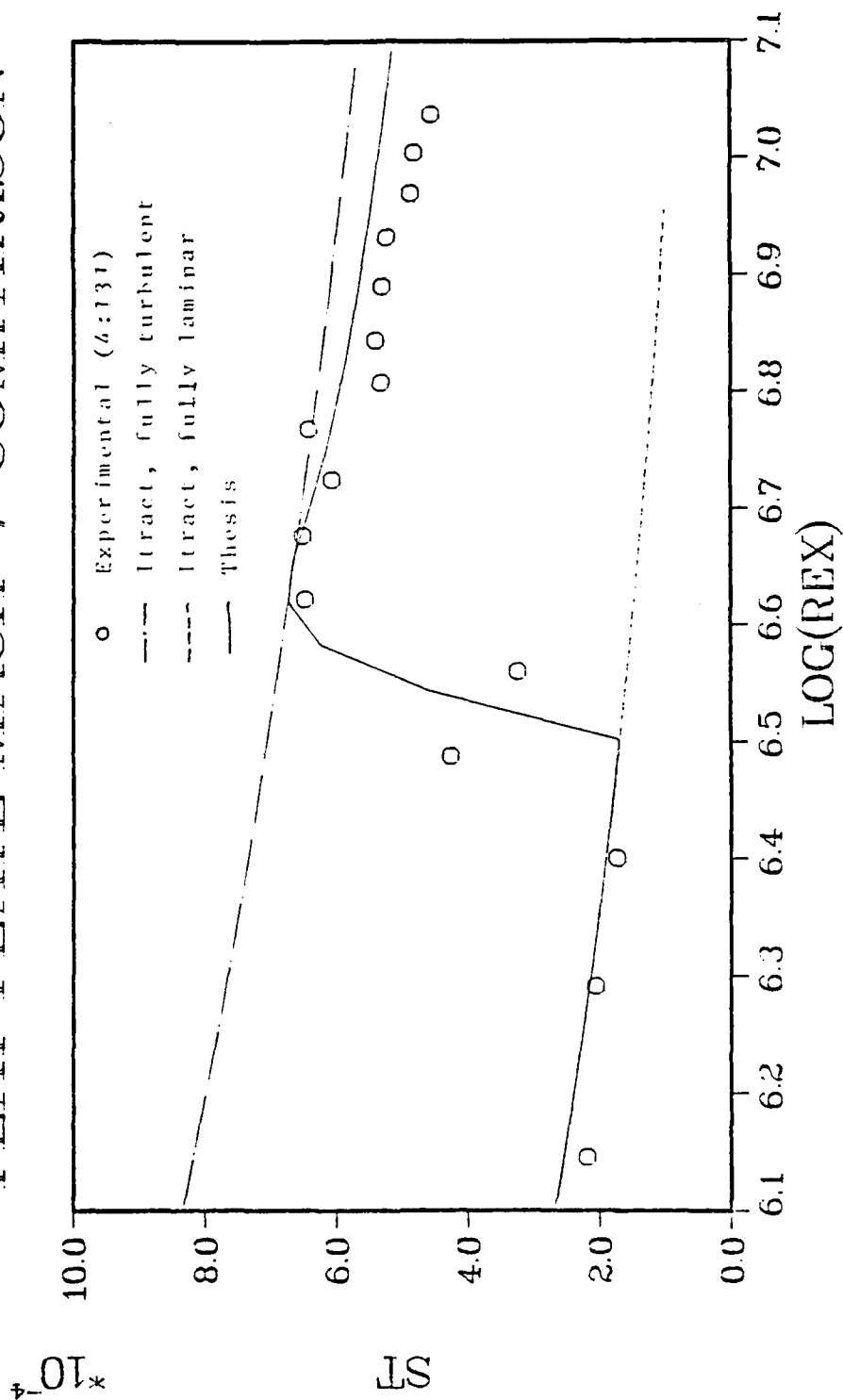
Figure 2.11.   Compressible Turbulent Flow Verification -
Van Driest/Clauser Models
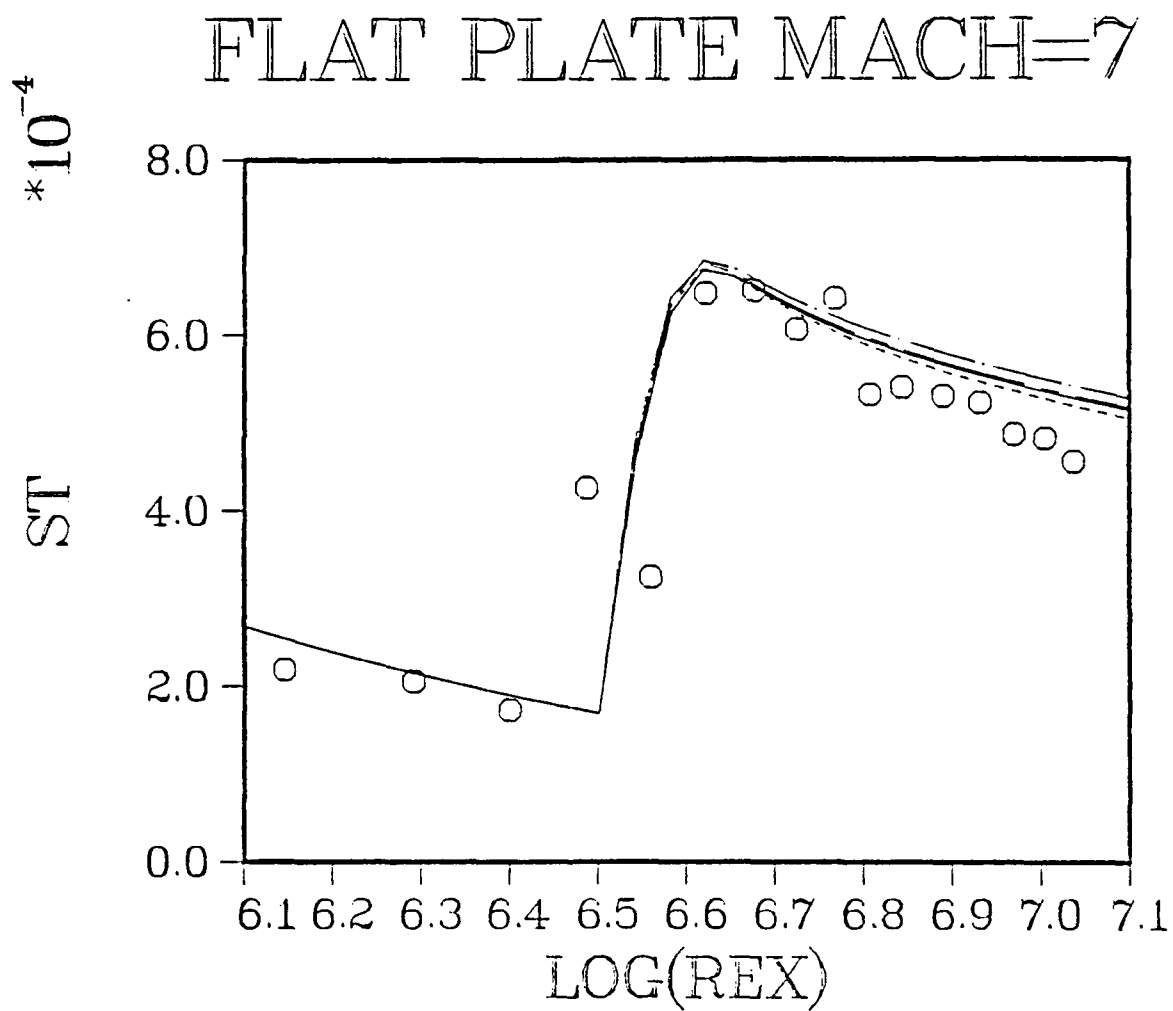
FLAT PLATE MACH=7

Figure 2.12. Compressible Turbulent Comparison - All Models

III. Experimental Effort

3.1 Introduction

The experimental effort consisted of the study of a blunt fin at incidence on a sharp nosed flat plate. The phenomena of interest was the areas of high heating on the expansion side of the blunt fin. The research consisted of three main phases:

Phase I: Calibration of the von Karman Institute H-3 wind tunnel to determine the extent of the uniform velocity jet.

Phase II: Study of the flow on a flat plate to determine the location of transition and turbulence.

Phase III: Study of the interaction flow on a flat plate on the expansion side of a blunt fin in laminar flow.

The flow studies include flow visualization techniques, such as oil flow, sublimation, shadowgraph, and liquid crystals, and then also quantitative thin film and coax gage heat transfer tests. Tests were completed at a Mach number of 6.0 at two Reynolds numbers, 0.844×10^7/m and 1.69×10^7/m which correspond to two reservoir pressures, 10 and 20 bars, respectively. DeGraef (14) had completed liquid crystal tests on this particular interaction flow at Mach 5.26, but only in turbulent flow.

3.2 H-3 Blowdown Wind Tunnel

This research was conducted in the VKI H-3 blowdown intermittent tunnel illustrated in Figure 3.1. The test gas is air and is supplied from a 40 bars compressor. The air is heated by a pebble bed, to avoid condensation of air components (principally nitrogen) occurring during the test (35:137). When condensation occurs, isentropicity is lost, and the test data can no longer be interpreted correctly. Daum and Gyarmathy (13:464) have developed a method to determine the minimum stagnation temperature which may be used to avoid condensation. For the test conditions in this study, their method gives a minimum stagnation temperature of 406 °K. All the tests in this study were completed at a stagnation temperature of approximately 473 °K. The tunnel uses an air ejector to evacuate the test chamber to ease startup conditions. The high pressure air in the reservoir is expanded in the axisymmetric nozzle giving a uniform free jet of Mach 6. The nozzle exit diameter is approximately 154 mm. The size of the uniform Mach 6 jet will be determined from the tunnel calibration.

There is a model injection system which is driven by a pneumatic mechanism. The test section contains a three degree of freedom (incidence angle, yaw angle, and axial position) traversing mechanism for the model and probe support.

HYPERSONIC TUNNEL H 3
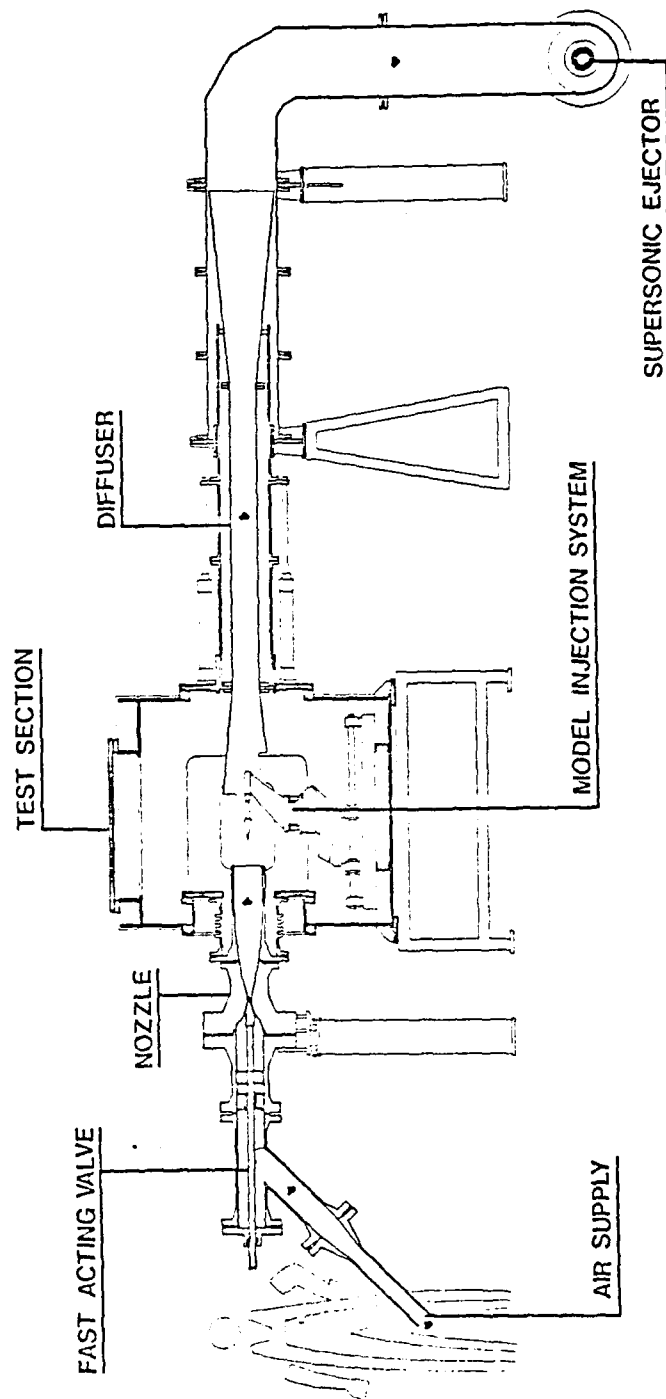
Figure 3.1.   VKI H-3 Wind Tunnel

The reservoir chamber pressure can vary from 7 to 35 bars corresponding to a unit Reynold's number from 10^7 to 4×10^7 / meter. Running times up to five minutes are available. However, in order to reduce energy consumption, experiments usually have a short duration.

3.3 Calibration of the H-3 Wind Tunnel

3.3.1 Purpose

To determine the size of the flat plate model to construct, the scope of the Mach 6 uniform free jet must be determined. The first time the tunnel was calibrated was after its installation in 1970 (29). That previous calibration showed the existence of a small centerline disturbance and the slow streamwise growth of the outer shear layer. Details of the calibration procedure used and results obtained in this study are included in Appendix E.

3.3.2 Conclusions of Calibration

The results from this study also shows the presence of a slow growing shear layer and centerline disturbance. The experimental errors in the Mach number are less than .5%. The extent of the uniform flow has been obtained and the centerline Mach number variations have been shown to be within 2.2% of the mean flow in this uniform flow region. The streamwise flow at a radial distance of 39 mm from the centerline shows a slow rise in Mach number as the distance from the nozzle increases, from a mean Mach number of approximately 5.97 to 6.00. The streamwise flow at the

center of the tunnel also shows a rise in Mach number, but the rise is more dramatic. The rise is sudden between x = 3.5 mm and 53.5 mm, the mean centerline flow increases from an approximate Mach number of 5.89 to 6.04. Then, the rise is much slower, perhaps even becoming constant after x = 143.5 mm at a Mach number of 6.05.

From the calibration, the flow can be considered to be a uniform axisymmetric jet of Mach 6. The uniform flow has been determined to within ± 2 mm to be approximately 117 mm in diameter at the nozzle exit and it remains relatively constant until a distance of 103.5 mm downstream of the nozzle exit. The uniform flow then decreases to approximately 98 ± 2 mm in diameter at 143.5 mm downstream of the nozzle exit. Using the data from Table E.2, the region of uniform flow is sketched in Figure 3.2. The boundary of the uniform flow region beginning at the nozzle exit is interpolated to 143.5 mm behind the nozzle exit. After x = 143.5 mm, the region of uniform flow could be extrapolated to x = 300 mm. However, the region of uniform flow resulting from the extrapolation appears unrealistic. It is difficult to believe that the shear layer would grow as fast as the extrapolation indicated. This seems to indicate that there is not enough information available to draw a conclusion about the extent of the growth of the shear layer farther than the 143 mm after the nozzle exit. More calibration tests are required if tunnel models exceed
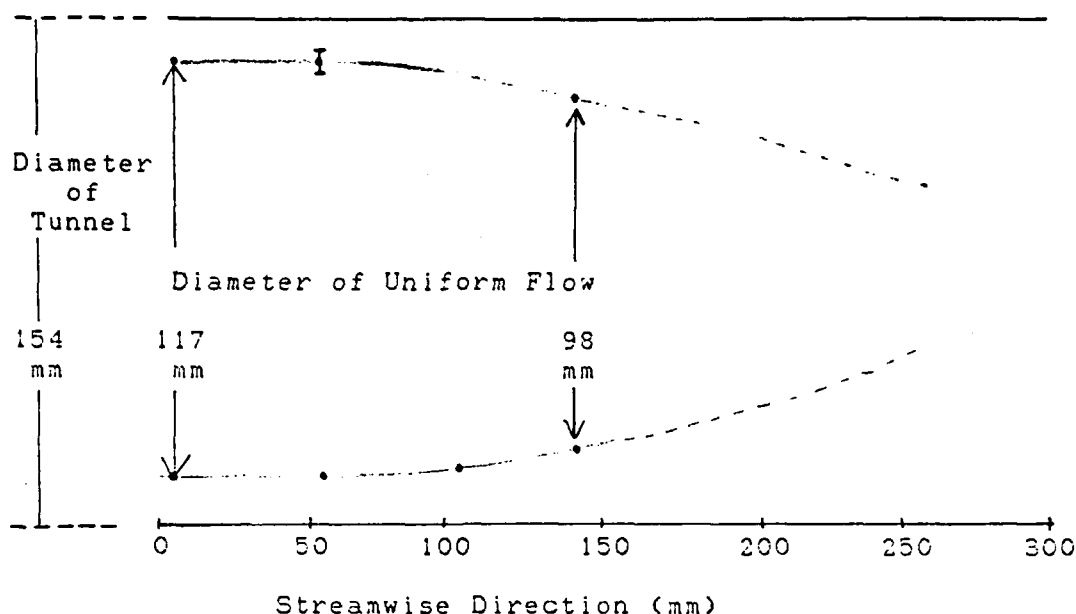
Figure 3.2. Sketched Regions of Uniform Flow

150 mm in length, but this would entail, not only conducting more tests, but designing a new pressure rake to avoid the occurrence of tunnel blockage.

3.4 Theory

3.4.1 Isentropic Flow Calculations

The static properties of the flow are calculated using isentropic flow relations.   Since   the   reservoir   total pressure and temperature are known, the static pressure and temperature can be obtained using these equations (35:53)

$$T = T_o (1 + .5(\gamma-1)M^2)^{-1} \qquad (3.1)$$

$$P = P_o (1 + .5(\gamma-1)M^2)^{-[\gamma/(\gamma-1)]} \qquad (3.2)$$

The static density can be computed using the perfect gas law

$$\rho = P/(RT) \tag{3.3}$$

where $R = 287.0$ Nm/kg°K and is the gas constant for air. The local speed of sound can be calculated using

$$a = (\gamma RT)^{1/2} \tag{3.4}$$

and the local velocity is $U = aM$. For viscosity, Keyes law is used, which is in foot-pound-second units

$$\mu_{FPS} = \frac{2.32 \times 10^{-8} \, T^{1/2}}{1 + \frac{220.0}{T \times 10^{9/T}}} \tag{3.5}$$

μ_{FPS} has units of lb sec/ft² or slug/ ft-sec with T in °R. The static temperature is converted initially from °K to °R using

$$°R = (9/5) \, T°K \tag{3.6}$$

The viscosity is then computed in units of lb sec/ft² using eqn (3.5) and converted to metric units of kg/m-sec when multiplied by a conversion factor

$$\mu = \mu_{FPS} \, (3.281 \text{ ft/m})(14.59 \text{ kg/slug}) \tag{3.7}$$

The Reynolds number is calculated using

$$Re = U\rho/\mu \qquad\qquad \text{per meter} \tag{3.8}$$

The local Reynolds number, Rex, is found by multiplying Re by the x location from the leading edge of the plate.

$$Rex = U\rho x/\mu \tag{3.9}$$

3.4.2 Oblique Shock Theory

From the calibration tests, it is assumed throughout the study that the uniform free jet has a Mach number of 6.0. When the model is at 0° incidence, the flat plate will theoretically see a flow of Mach 6.0. Almost all of the tests completed in this study were with the plate at zero degree incidence. Some preliminary tests were completed at a different Mach number. Since the H-3 tunnel has a fixed geometry nozzle, the only way to change the Mach number of the flow over the plate is to put the plate at a negative angle of attack (leading edge down). Theoretically, when the plate is at a negative angle of attack, a weak oblique shock is formed and *the Mach number downstream of the shock* will need to be calculated using oblique shock theory. In reality, due to the presence of the boundary layer, an extremely weak oblique shock is formed when the plate is also at zero degree incidence.

Figure 3.3 gives the orientation of the plate and defines the incidence angle of the plate, α, and the shock angle, Θ. The Mach number behind the shock can be calculated using the following equation (17:492).

$$M_2^2 = \frac{1 + .5(\gamma-1)M_1^2}{\gamma M_1^2 \sin^2\Theta - .5(\gamma-1)} + \frac{M_1^2 \cos^2\Theta}{1 + .5(\gamma-1)M_1^2\sin^2\Theta} \qquad (3.10)$$

3.4.3 Heat Transfer

The heat transfer distribution on a flat plate, Figure 2.6, distinguishes three regions; laminar, transition, and turbulent. For the case of an isothermal flat plate in the absence of leading edge and viscous interactions, ie., conditions at the edge of the boundary layer are those of the free stream, Korkegi (31:124) gives approximate expressions for laminar and turbulent Stanton numbers for compressible flows. These equations are obtained from approximate expressions for laminar and turbulent skin friction based on a "reference" temperature TF.

For laminar flow:

$$St = \frac{0.41}{Re_x^{1/2} (TF/T_\infty)^{.12}} \qquad (3.12)$$

$$TF/T_\infty = 1 + .032 M_\infty^2 + .58 [(T_W/T_\infty) - 1] \qquad (3.13)$$

For turbulent flow:

$$St = \frac{0.037}{Re_x^{1/5} (TF/T_\infty)^{.648}} \qquad (3.14)$$

$$TF/T_\infty = 1 + .035 M_\infty^2 + .45 [(T_W/T_\infty) - 1] \qquad (3.15)$$

where T_∞ is the freestream static temperature and Re_x is defined by eqn (3.9). The experimental data will be plotted with these approximate expressions for comparison purposes.

3.5 Description of Test Models

The dimensions of the flat plate were chosen to be 150 mm in length and 100 mm in width. The rear edges of the
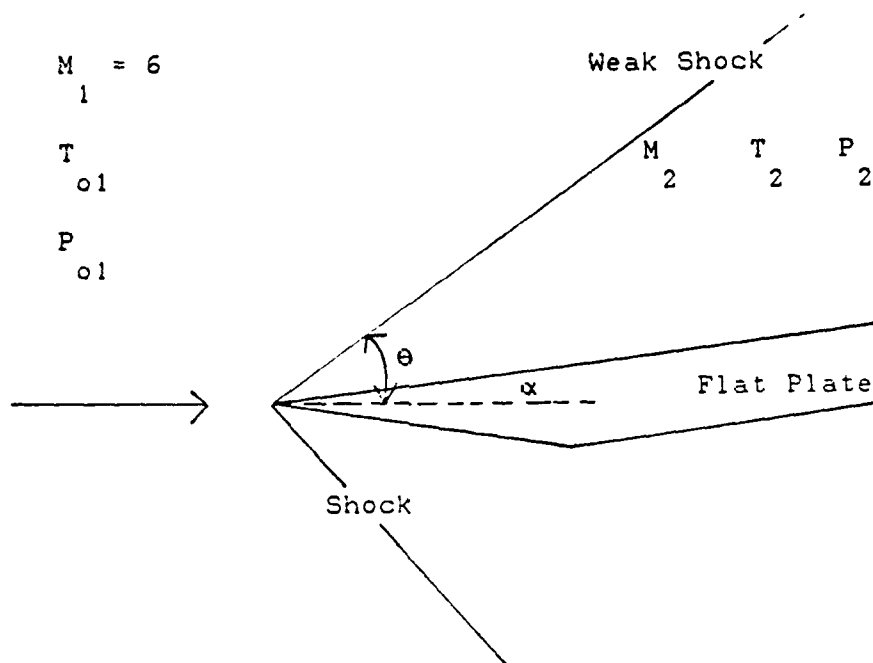
Figure 3.3. Oblique Shock Configuration

The NACA tables (2:22,42,43) have oblique shock data, so if α and M_1 are known, Θ can be obtained. Then, the normal component of the Mach number, $M_1 \sin\Theta$, can be calculated and the ratios P_2/P_1, and T_2/T_1 can be obtained from normal shock tables. For this study,

$$\alpha = -5.5° \qquad\qquad \Theta = 13.5°$$
$$\tag{3.11}$$
$$P_2/P_1 = 2.12 \qquad\qquad T_2/T_1 = 1.255$$

Therefore, $M_2 = 5.26$.

plate will therefore be slightly in the shear layer, but no data will be taken near those regions.

The oil flow and sublimation visualization tests for the flat plate were completed on a plexiglas model and repeated with an aluminum model. The dimensions of the model are shown in Figure 3.4. The top surface of the model for the oil and sublimation experiment was sprayed with a dark blue color. The tests done with the plexiglas model were repeated since the leading edge was easily damaged during the tests by particles in the flow. Small nicks in the leading edge caused large disturbances in the oil flow tests. The plexiglas model was chosen initially for the test since it was already machined and had the correct dimensions.

The liquid crystal test was completed on a stainless steel model with a plexiglas insert. The dimensions of the model are shown in Figure 3.5. A single coax gage was installed in the stainless steel portion of the model for calibration purposes. The model was painted black and then the liquid crystals were sprayed on the entire model.

The heat transfer test for a flat plate was completed on a stainless steel model. The dimensions of the model are shown in Figure 3.6. The model had two coax gages installed in it and also had a ceramic insert for the thin film gages.

The aluminum flat plate, with its previously described dimensions shown in Figure 3.4, was used in the three

dimensional flow visualization tests. Five fins of varying sweep angle and height, were constructed out of bronze and sequentially placed on the model for the sublimation and oil flow tests. The dimensions of the fins are shown in Figure 3.7.

It was desired to determine the location of transition on the undisturbed flat plate so that a laminar interaction with the fin could be studied. Experimental data from previous VXI studies completed in the H-3 wind tunnel were examined. Table 3.1 shows the results that were found.

Table 3.1. Location of Transition

Mach Number	Re (/m)* $\times 10^{-7}$	x transition (mm)	Reference
5.2	3.2	110	(14)
5.2	1.6	120	(14)
6.0	2.3	95	(15)
6.0	1.7	test conditions of this study	
6.0	0.84		

* based on Keyes viscosity law

Table 3.1 shows that as the Reynolds number is decreased, the transition location moves downstream. Therefore, transition is expected to occur at least 95 mm downstream of the plate leading edge for the test conditions in this study. A more accurate determination of the transition

location was determined in later tests. The results are discussed in section 3.7.4. Therefore, to obtain a laminar interaction, the fins were installed so that the leading edge of the fin was approximately 60 mm downstream of the leading edge and 40 mm from the right side of the plate when looking forward from the rear of the plate.

The heights of the fins were chosen so there would be no interference with the oblique shock originating at the plate leading edge when the plate was at -5.5° angle of attack (Mach 5.26). This height was calculated using the theoretical shock angle and then verified for "no interference" using the shadowgraph technique. However, once the sublimation tests began and the phenomena of interest was detected for the Mach 6 test case, the Mach 5.26 test case was dropped from the remainder of the test plan. Since the fins were already machined at the shortened height and had already been used for the oil flow tests they were retained for the remainder of the test plan. Future tests at Mach 6 should be completed with taller fins to determine if fin height produces any difference in the flow field for varying values of fin sweep and incidence angle.
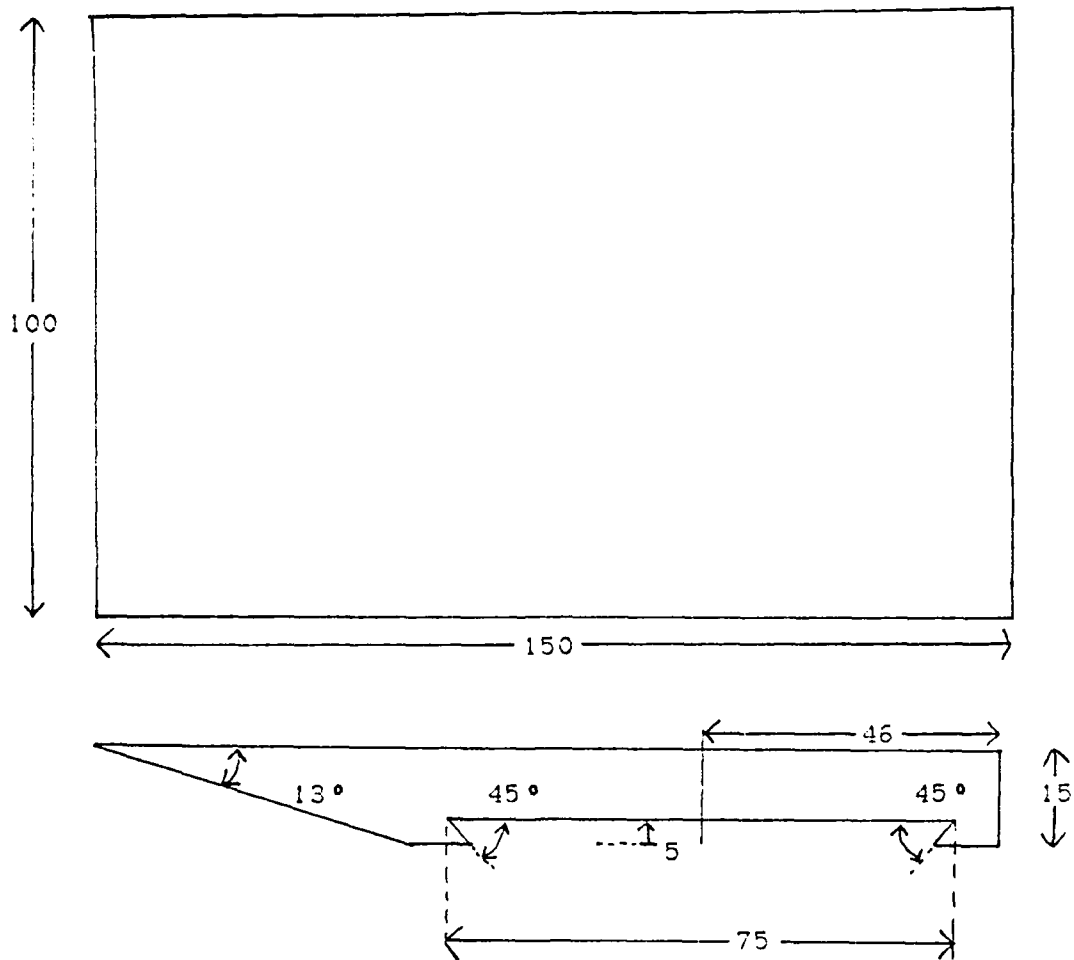
Dimensions are in millimeters

Figure 3.4.   Flow Visualization Flat Plate Model

Cut AA - Stainless Steel

Cut BB - Stainless Steel

Cut AA - Plexiglas

Cut BB - Plexiglas

Dimensions are in millimeters
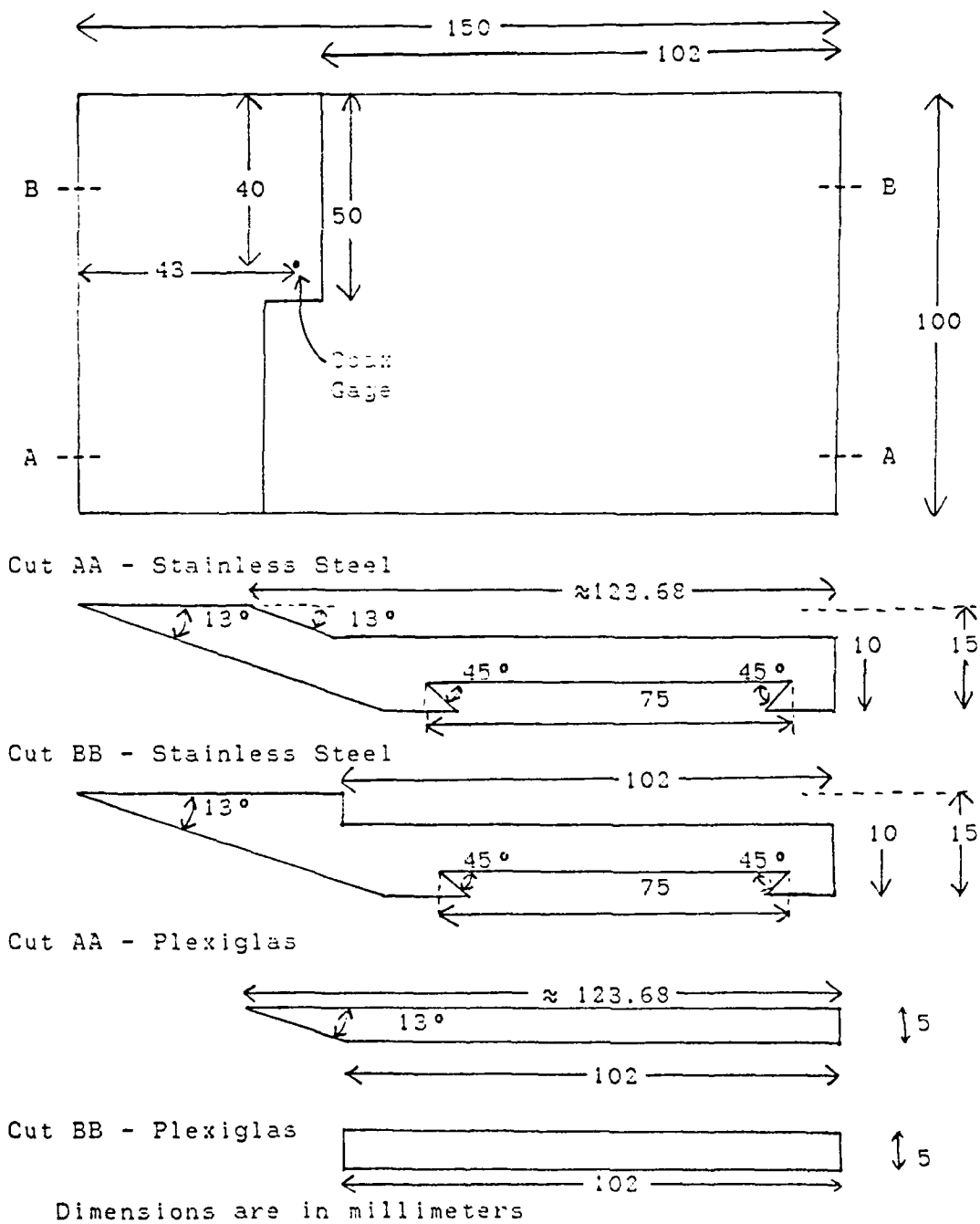
Figure 3.5. Liquid Crystal Flow Visualization Plate Model

Top View of the Model

150

40

Coax
Gage

Coax
Gage

A ---   --- A

50   36

B ---   --- B   10 15

40

40

Cut AA - Stainless Steel

150

50   36

15

Cut BB - Stainless Steel

150

40

6   7

Top View - Ceramic

120

10   15

End View - Ceramic   Side View - Ceramic

15   120

7

2.5
7
4.5

Dimensions are in millimeters
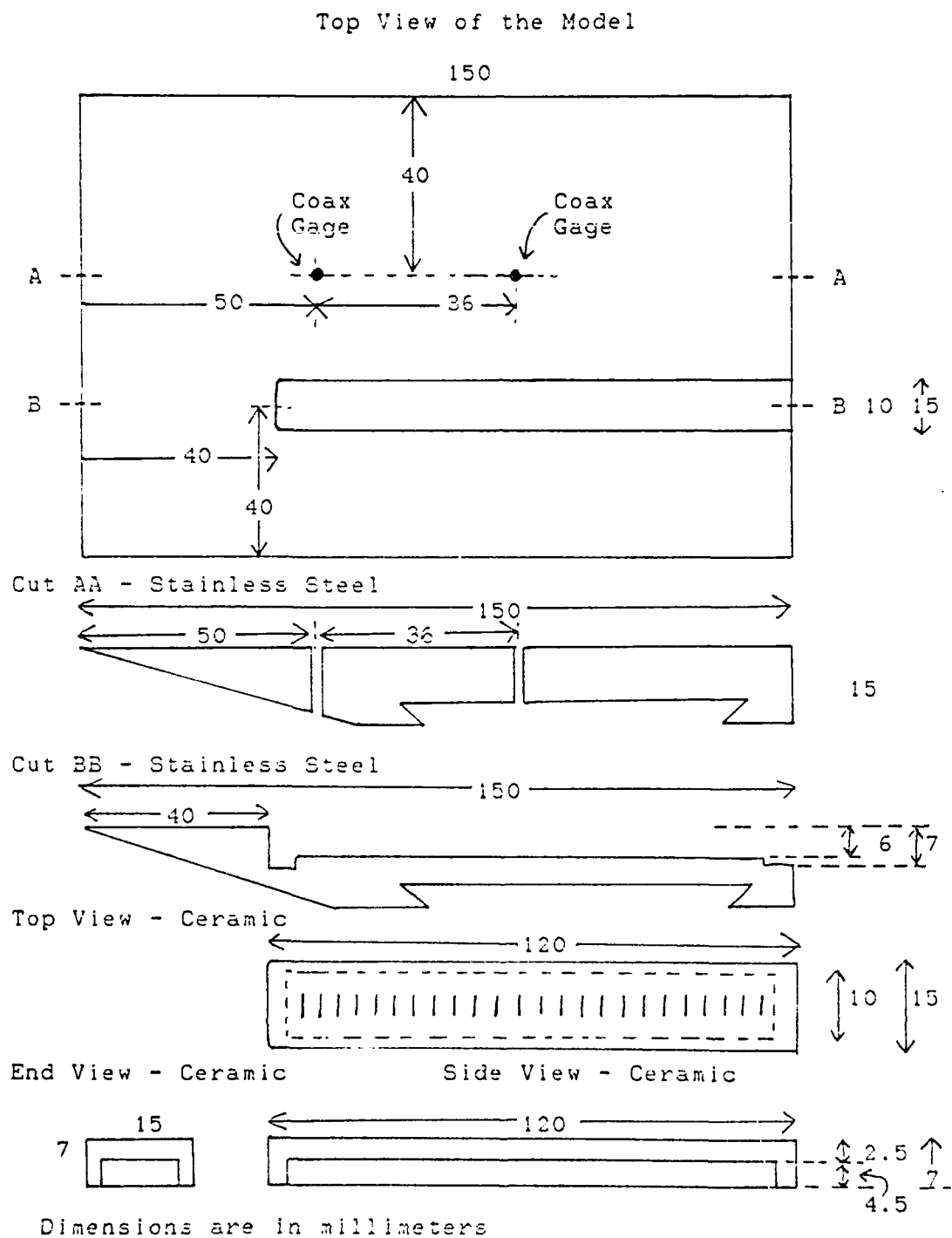
Figure 3.6.   Flat Plate Heat Transfer Model

Side View

Ω=75°

8

Top View

4

60

Side View

Ω=60°

8

Top View

4

60

Side View

Ω=30°

6

Top View

4

60

Side View

Ω=0°

6

Top View

4

60

Side View

Ω=0°

15

Top View

4

60
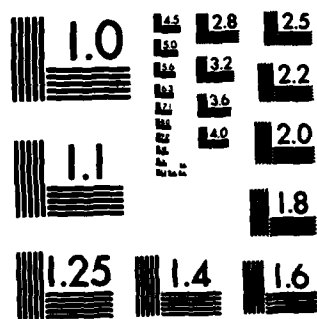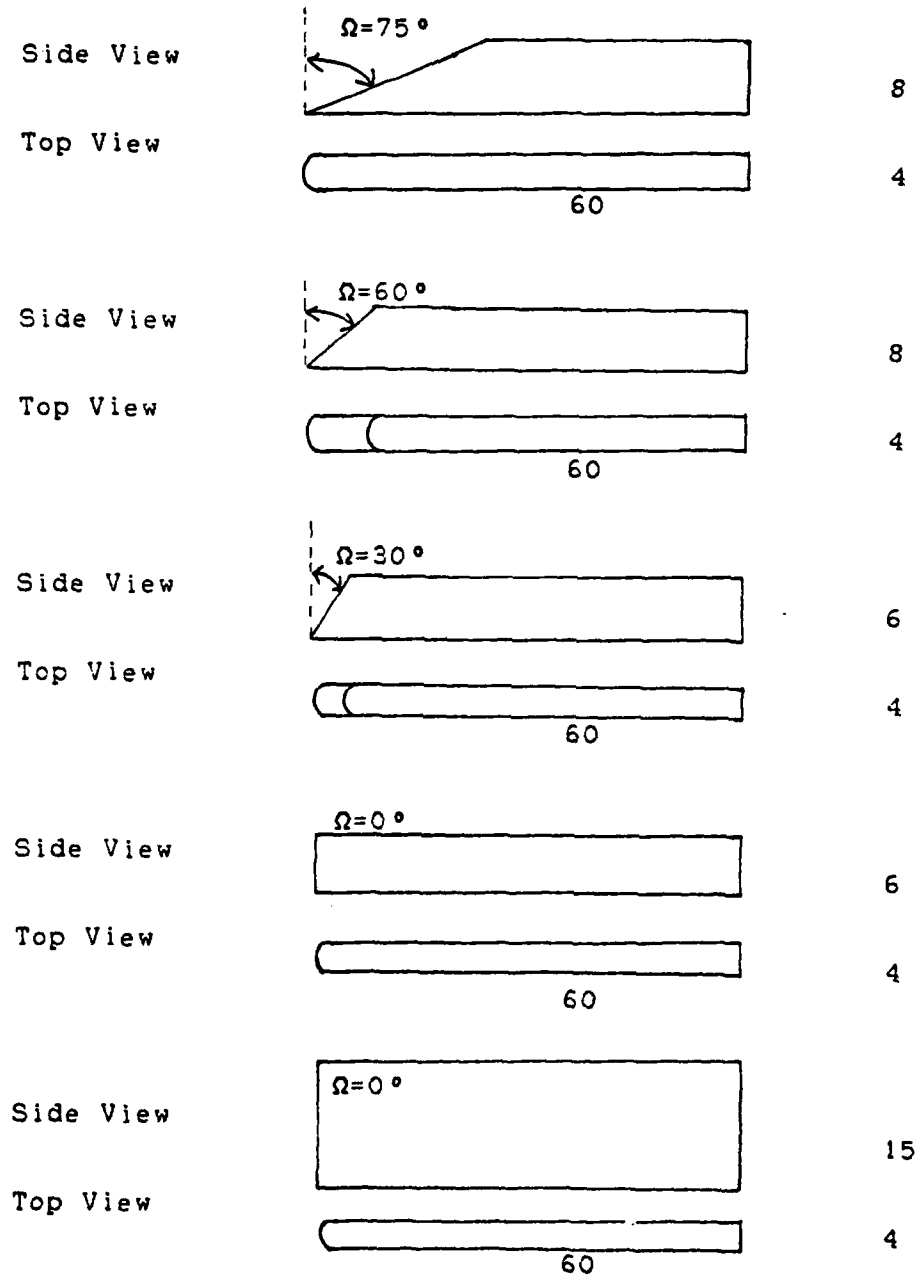
Dimensions are in millimeters

Figure 3.7. Blunt Fin Models

74

3.6 Experimental Techniques

3.6.1 Oil Flow Visualization Technique

The surface oil flow technique is intended to quickly and easily investigate the nature of the flow over the surface of a wind tunnel model. A mixture of gasoline, titanium (IV) oxide (talcum powder), and oleic acid was used for the flat plate tests, but was found to be inadequate for the three dimensional flow visualization. A new mixture of motor oil and titanium oxide was used with excellent results. The surface of the model was lightly painted with the oil mixture. The air flowing over the surface carries the oil with it and leaves a streaky deposit of the powder remaining to mark the direction of flow. The patterns made by the streaks indicate the surface streamlines and the local direction of flow on the surface.

In interpreting oil flow patterns, Maskell's definition of a three dimensional separation line is used (40:161). This says that

> "the three dimensional separation line is an envelope of converging limiting surface streamlines."

In many three dimensional situations, oil may accumulate along a line because the surface shear becomes too low to overcome the friction and surface tension of the oil. Care must be taken not to interpret this accumulation line as a separation line. The true separation line, in the Maskell sense, has streamlines converging on it from either side.

Another complication in interpreting oil flow patterns in three dimensional flow interactions is the separation line in the absence of an oil film and the line of oil accumulation will differ due to two reasons (51:29):

1. The effective body shape of the model will be altered by the change of the oil film height, thus altering the inviscid flow properties.

2. The separation of the air flow will be delayed in the presence of an oil film, due to the finite velocity of the air at the oil surface. This will increase the momentum of the air boundary layer leading to flow separation at a place of higher pressure gradient.

This difference is illustrated in Figure 3.8. However, since these influences are small, the oil flow technique is still a very valuable visualization tool.

Oil Film

S - Separation Point
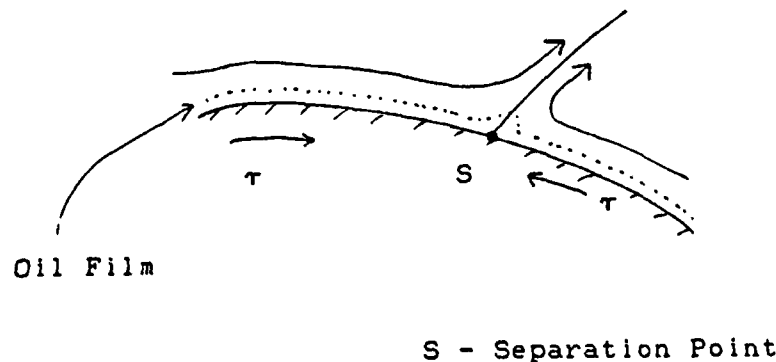
Figure 3.8. Separation in Oil Flow Experiments

The ratio of ingredients, oil : powder, to achieve good
test results is a matter of trial and error. For these
tests, a thin consistency mixture produced the best results.
However, if the mixture was too thin, the oil tended to drip
too fast over the plate after the plate is taken out of the
injected position, therefore ruining the important patterns.
Painting the model with a minimum quantity of the mixture,
also seemed to work best.

3.6.2 Sublimation Visualization Technique

The sublimation method is a visualization technique to
detect the location of the transition and turbulent regions
(51:19-21). The technique consists of coating the model
surface with a dark colored paint, and then coating the
model with a thin, constant thickness layer of a subliming
material, in this case, acenaphthene. The acenaphthene is
dissolved in ether and sprayed on the model. The ether
evaporates quickly and leaves the white acenaphthene on the
model. During exposure to an airstream, sublimation occurs
along the surface at varying rates, depending on the
diffusion mass transfer of the substance in gaseous form
into the air boundary layer. The diffusion mass transfer
rates depend on the character of the boundary layer; whether
it is laminar, transitional, or turbulent. The mass
transfer of an attached turbulent boundary layer is
approximately one order of magnitude larger than for an
attached laminar boundary layer (51:19).

For zero pressure gradient boundary layers, Reynold's analogy states that the amount of heat transfer (characterized by the Stanton number), can be directly related to the momentum transfer (skin friction coefficient). The heat transfer can also be related to the mass transfer. This relation is explained in detail by Stock (51:22-23). The skin friction coefficient, c_f, distribution in a flat plate boundary layer is shown in Figure 3.9. From Figure 3.9, it can be seen that the regions of highest skin friction coefficient will sublime first - exposing the dark model underneath. Therefore, an indication of the location of transition will be determined using the sublimation technique.
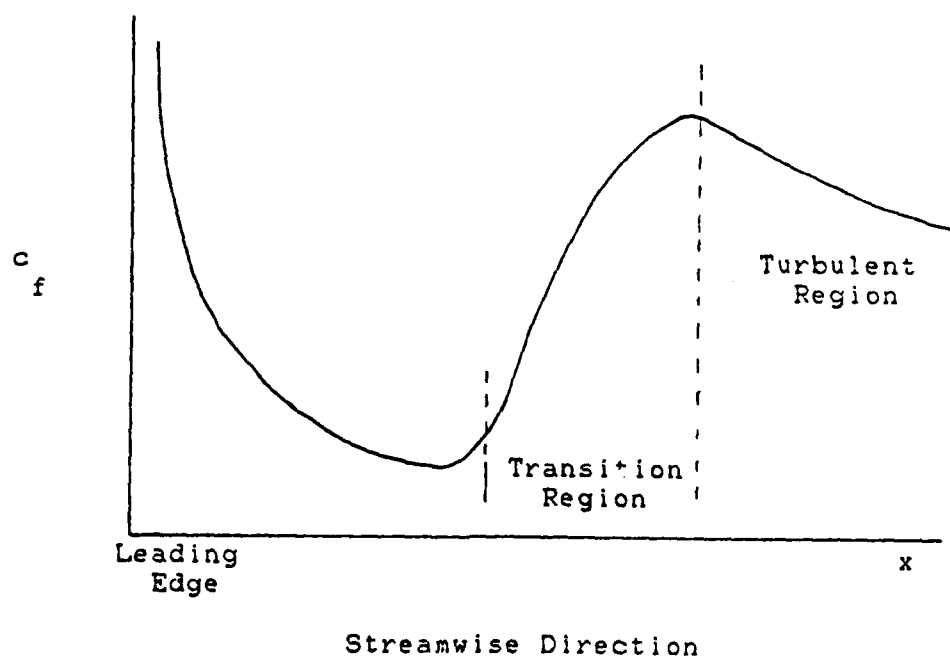
Figure 3.9. Skin Friction versus Streamwise Direction

73

For three dimensional flows, regions near the fin on the flat plate will also have different skin friction coefficients so the sublimation technique will also be used to examine this flow interaction region.

3.6.3 Shadowgraph Optical Technique

A popular optical system used in wind tunnels is the shadowgraph system. The principal behind the shadowgraph technique is very similar to the schlieren technique, except that there is no knife edge. The shadowgraph system gives an image representative of the variation of density gradients throughout the complete flow field. The VKI H-3 wind tunnel has a "double-pass" shadowgraph/schlieren system, that is, the light rays are passed through the test section twice. When axisymmetric models are being tested, the double-pass system is used rather than a single-pass system because in hypersonic tunnels the test section density is very low. Therefore it is usually difficult to obtain high quality shadowgraph or schlieren pictures with a single-pass system (42:233).

The shadowgraph photographs were used to examine the height of the laminar boundary layer, the shock formed from the leading edge of the flat plate at incidence, and the flow interaction with the fin.

3.6.4 Liquid Crystal Technique

The liquid crystal technique is a qualitative and semi-quantitative technique to visualize the global heating of an

area of interest. An advantage of using liquid crystals over phase change paints is that a coat of liquid crystals can be used for several tests. Phase change materials must be reapplied for every test, which is very inconvenient. Liquid crystals also have a response time on the order of milliseconds (47:15) making it more effective for transient heat transfer tests.

The liquid crystals that will be used in this test are cholesterics. Cholesteric molecules have a helical structure. One of the most interesting properties of the cholesterics is the influence of the temperature on their structure. When a light beam is sent parallel to the helical axis, the reflected wave length depends on the characteristics of the lattice and also on the angle of observation. Therefore, when the helical structure changes with temperature, the reflected wavelength will also be modified, and if the wavelength is in the visible spectrum, the temperature will be associated with a change of colors. The typical colors that will be encountered in this test are red (24.5°C), yellow, green, and blue (28.5°C).

The helical structure of normal liquid crystals are sensitive to shear stress. The shear stresses produced by hypersonic flows produce shifting of the helical structure, thus changing the reflected wavelength. It is impossible to determine in a wind tunnel whether a change of color is due to temperature or shear stress. To overcome this problem,

encapsulated liquid crystals are used. Small droplets of the cholesteric material are embedded in gelatin bubbles with a diameter of three to five micron. This gelatin bubble shields the liquid crystals from shear. Disadvantage of the encapsulation will be loss in the brilliancy of the colors.

To determine the temperature changes of a surface due to a flow, the surface material should have a low thermal conductivity. Since it is desired to record the changes seen by the liquid crystals, it is important that the heat does not conduct through the material. If this should occur, then the heat transfer effects seen will be much lower than in reality due to the conduction effects. The tests will therefore be completed on a plexiglas insert rather than directly on the metal model.

The surface color changes for the flat plate tests will be recorded by color photographs during each test. With an accurate correlation between color and temperature, the temperature time history can be determined. For complicated flows, the color changes could be recorded by a color video camera and the determination of the temperature could be enhanced with the use of a digital image processing (DIP) technique which can distinguish between shades of red, green, or blue from the intensity. For completeness, the DIP is explained in a little more detail in Appendix G.

3.6.4.1 Theory

Once the surface temperatures are determined from the liquid crystals, the heat transfer rate can be determined. To obtain the relation to solve for the heat transfer rate from surface temperature, the one dimensional heat equation must be solved for an initially isothermal semi-infinite slab. The heat equation is

$$\frac{\partial T}{\partial t} = \alpha \frac{\partial^2 T}{\partial y^2} \qquad (3.16)$$

The solution of the heat equation is shown in great detail by Degrez (15:57-60). If $Ts(0)=0$, and if the heat flux is a constant in time,

$$q = \frac{(\rho c_p k \pi / t)^{1/2}}{2} \; Ts(t) \qquad (3.17)$$

The Stanton number can then be calculated using

$$St = \frac{HC}{c_p \rho_\infty U_\infty} \qquad (3.18)$$

where HC is the heat transfer coefficient and is defined by

$$HC = \frac{q}{T_{AW} - T_W} \qquad (3.19)$$

T_{AW} is the adiabatic wall temperature and is defined by

$$T_{AW} = T_\infty \; [1 + .5r(\gamma-1)M_l^2] \qquad (3.20)$$

where r is the recovery factor, and for laminar flow is

$$r = Pr^{1/2} \qquad (3.21)$$

3.6.4.2 Validity of Assumptions

The assumptions used in the theoretical analysis of the
liquid crystal technique are

1) one dimensional heat transfer

2) semi-infinite slab

3) constant heat flux

4) liquid crystals do not disturb the surface heat flux
to the model

Each assumption will be examined to determine if it is valid
for the conditions of the test.

The heat transfer into the model must be one
dimensional. This will be assumed to be true for the model,
except near the edges of the model or at any discontinuity
of the material.

The plexiglas on which the liquid crystals are mounted
must be thick enough so that the heat transfer into the
substrate is similar to that of a semi-infinite solid.
Therefore, the base of the plexiglas should remain at a
constant temperature. The thickness at which T_x/T_s and
q_x/q_s remain smaller than 1% for a given time is
approximately (48:8)

$$x = 4 (\alpha t)^{1/2} \qquad (3.22)$$

This equation can then be solved for t. Since the thickness
of the plexiglas is five mm, the time at which the semi-
infinite slab assumption is valid is shown in Table 3.2 for
plexiglas, and also stainless steel and aluminum for

comparison. Table 3.2 clearly shows why the plexiglas insert was chosen for the test.

The third assumption used in the analysis was constant heat flux. The validity of this assumption can be examined at the conclusion of the test. When the heat transfer rate is constant, the surface temperature increases as the square root of t. This can be seen from equation (3.17). If $(T_s)^2$ versus t is plotted, the resulting curve should be a straight line. If the line is not straight, the constant heat flux assumption is not valid.

Table 3.2. Semi-Infinite Slab Criteria

	Plexiglas	Stainless Steel	Aluminum
$\rho(kg/m^3)$	1.19×10^3	7.9×10^3	2.7×10^3
$k(Watts/m\,^\circ K)$	0.188	15.0	
$c_p(J/kg\,^\circ K)$	1463	440	
$\alpha(cm^2/sec)$	0.0011	0.043	0.85
$t(sec)(x=5mm)$	14.5	0.36	0.018

The fourth assumption used in this technique is that the liquid crystals do not disturb the surface heat flux to the model. This will be assumed to be true since the layer of liquid crystals is very thin, on the order of 10^{-6} meter.

3.6.4.3 Calibration of the Liquid Crystals

The calibration of the liquid crystals is critical in that it is the basis of the correlation between the colors on the photograph and temperature on the surface of the model. The calibration is performed on the metal portion of the model. A coax gage is installed in the stainless steel and the entire model is sprayed with the liquid crystal solution. The details of the model preparation are described in Appendix F. Details concerning the coax gage will be considered in section 3.6.6. Since metals are good heat conductors, the temperature found by the coax gage can be assumed to be uniform. This will also be shown during the calibration if the liquid crystals on the metal portion are a uniform color.

To obtain calibration data that will be applicable to the subsequent tests, the same conditions must be present for the calibration as the actual tests. This requires that the position of the model, camera, and light remain constant. The position of the model for filming will always be in the injected "test" position. The camera and light should not be moved after the calibration until all the tests are completed.

After the model is installed in the tunnel, a vacuum pump is installed to produce a vacuum in the test chamber. The purpose of the vacuum is to prevent any convective heating. Since it is impossible to seal the H-3 chamber,

85

the vacuum pump evacuates the test chamber to approximately 0.4 bar, this taking about two hours. The amount of convective heating should be very small at this low pressure. The model is placed in the injected position where it is heated by two 1000 watt lamps until the model has reached at least the temperature that corresponds the : e color of the liquid crystals. The highest temperature visualized by the liquid crystal corresponds to the blue color. The plate required over 60 seconds of heating before the first color appeared. Then the lights are turned off and the model is allowed to cool. When the liquid crystals on the metal portion of the model reaches a uniform color, or steady state temperature, the model is photographed and the voltage from the coax gage is recorded. The model is then allowed to cool some more and this process is repeated until all the colors have been photographed.

3.6.5 Thin Film Heat Transfer Gages

The thin film technique is well suited for measurements in transient conditions due to the fast response time. However, thin film gages have a disadvantage that large errors can occur if used for long duration tests, due to nonisothermal wall effects. The thin film gage is actually a thin-film surface resistance thermometer. The gages consist of thin metallic films applied to the surface of substrates of low heat conductivity. If the thin film gages are properly made, the heat flow into the substrate is one

dimensional and similar to that of heat flow into a semi-infinite solid. The variation of temperature with time is obtained from the thin film gages. The gages become one leg of a wheatstone bridge. Before a test, at ambient conditions, the bridge is balanced. During a test, as the plate is heated the resistances of each gage change and the unbalance of the bridge can then be related to the variation of temperature. The heat flux may then be deduced using a numerical procedure or an electrical analog circuit.

The construction of a thin film gage requires a lot of time, patience, and very precise workmanship. The instructions will not be elaborated upon in this report but the details of the construction of a thin film gage are explained very well by Ligrani, et al (37:3-10). Since ceramic is easier than quartz to machine to precise dimensions, ceramic was chosen as the substrate for the thin film gages in this study. The dimensions of the ceramic must be chosen carefully because the depth of the substrate is dependent on the tunnel running time. Since the semi-infinite slab assumption is used in the data reduction technique, this aspect must be considered.

3.6.5.1 Theory

The one-dimensional heat equation, equation (3.16) is used in the analysis of thin film gage data. Recall that the detailed solution of the one-dimensional heat equation is given in (15:57-60). However, at this point in the

87

analysis, the heat flux is not yet assumed to be constant. The equation for the heat flux is given by:

$$q_s(t) = \frac{(\rho cpk/\pi)^{1/2}}{2} \left[\frac{2Ts(t)}{t^{1/2}} + \int_0^t \frac{Ts(t) - Ts(\tau)}{(t-\tau)^{3/2}} d\tau \right] \qquad (3.23)$$

The evaluation of the heat transfer rate from the observed surface temperature record may be obtained by integrating eqn (3.23) numerically or by the use of electrical analogs.

Arts (5) mentions that the method using the electrical analog circuit to integrate the temperatures is more accurate than the numerical integration methods due to the uncertainty of the exact time of the beginning of the heat flux. If the exact time of the beginning of the heat trace is not known, an approximate time is used for the numerical integration methods. This error is then propagated in the numerical integration. The electrical analog circuit method, is not as sensitive to this problem.

For either method, the surface temperature rise, Ts(t), in equation (3.23) is found from the resistance change of the thin film. For the film,

$$R = RREF [1 + \alpha_R (T - TREF)] \qquad (3.24)$$

where R is the film resistance at surface temperature T, RREF is the film resistance at temperature TREF, and α_R is the film temperature coefficient of resistance. By Ohm's law, when the film is supplied with a constant current

$$V = VREF_R [1 + \alpha (T - TREF)] \qquad (3.25)$$

If the reference voltage VREF is measured at the ambient

temperature, Ta, before a test then Ta = TREF, and

$$Ts = \frac{\Delta V}{\alpha \, VREF_R} \qquad (3.26)$$

where ΔV is the film output voltage, V - VREF, and VREF is

the initial film voltage.

The numerical computation of heat transfer rate from

the temperature measurements can be made on the basis of

equation (3.23). This method may be called a direct method

in that q(t) is obtained directly. Note that there is a

singularity at $t = \tau$. If $\Delta V(t)$ is assumed to be piecewise

linear the final equation is

$$q_s(t_n) = \frac{2(\rho c_p k / \pi)^{1/2}}{\alpha \, VREF_R} \sum_{i=1}^{n} \frac{\Delta V(t_i) - \Delta V(t_{i-1})}{(t_n - t_i)^{1/2} + (t_n - t_{i-1})^{1/2}} \qquad (3.27)$$

where $\Delta V(t)/(\alpha \, VREF_R)$ is the rise in surface temperature

Ts(t) as shown in equation (3.26). To use eqn (3.27), it is

generally necessary to eliminate any noise from the data

before integration. Details of the derivation of equation

(3.27) can be found in Schultz and Jones (48:35-37).

Another method to numerically compute the heat transfer

rate from temperature measurements is an indirect method, in

that Q(t), the cumulative heating, is obtained first and

then differentiated with respect to time to obtain q(t).

$$Q_n(t_n) = \frac{(\rho cpk/\pi)^{1/2}}{\alpha \frac{VREF}{R}} \sum_{i=0}^{n} \frac{[\,\Delta V(t_i) + \Delta V(t_{i+1})\,]\,\Delta t}{(t_n - t_i)^{1/2} + (t_n - t_{i-1})^{1/2}} \qquad (3.28)$$

$$q(t) = \frac{dQ(t)}{dt} \qquad (3.29)$$

This differentiation is performed using a 4 point central finite differencing scheme

$$q(t) = \frac{-2Q(i-8) - Q(i-4) + Q(i+4) + 2Q(i+8)}{40\,\Delta t} \qquad (3.30)$$

In the indirect method, the integration tends to smooth the data and no preliminary noise reduction is necessary. The only approximation used in equations (3.27) and (3.28) was the local linearization of $\Delta V(t)$.

If the electrical analog circuit is used to do the integration in equation (3.23), an examination of the analog circuit is warranted. The electrical analog circuits are explained in detail in Appendix H. From the solution of the one dimensional heat equation, assuming that the heat flux is constant, equation (3.31) gives the heat flux in terms of surface temperature.

$$q_s(t) = \frac{1}{2}(\rho cpk\pi/t)^{1/2}\, Ts(t) \qquad (3.31)$$

If equation (3.26) for Ts is substituted into equation (3.31), then

$$q_s(t) = \frac{1}{2}(\rho cpk\pi/t)^{1/2}\, \frac{\Delta V}{\alpha \frac{VREF}{R}} \qquad (3.32)$$

where α_R is determined for each gage before testing using the equation

$$\alpha_R = \frac{1}{RREF}\frac{(R - RREF)}{(T - TREF)} \qquad (3.33)$$

If this calibration is done on a different day than the test itself, the ambient temperature may be different. Therefore, the measurement of RREF may be made at a temperature TREF different than the gage temperatures initially before a test, Ta. In order to correct for this difference, the value of α_R in eqn (3.33) must be corrected before data reduction. Correcting for this effect, equation (3.32) becomes

$$q_s = \frac{(\rho c_p k \pi / t)^{1/2}}{2}\frac{\Delta V}{\alpha_R VREF}[1 + \alpha_R (Ta - TREF)] \qquad (3.34)$$

which is then the same as equation (3.32) when Ta = TREF. Typically, this correction term may account for 1% of q_s if the difference of the temperatures is between 5 to 10°C.

From the electrical analog circuit analysis in Appendix H, where VOUT is the voltage output from the analog circuit,

$$\frac{A*}{\beta} = \frac{\Delta V}{2\,VOUT}(\pi / t)^{1/2} \qquad (3.35)$$

solving for ΔV and substituting into equation (3.34) the new equation for the heat flux is

$$q_s = \frac{VOUT}{VREF}\frac{(\rho c_p k)^{1/2}}{\alpha_R}\frac{A*}{\beta}[1 + \alpha_R (Ta - TREF)] \qquad (3.36)$$

The calibration of the thin film gages and determination of all the terms in equation (3.36), VREF, α_R, $(\rho cpk)^{1/2}$, and $A*/\beta$, are described in detail in Appendix I.

3.6.5.2 Validity of Assumptions

The assumptions used in the theoretical analysis of the thin film gage technique are

1) one dimensional heat transfer

2) semi-infinite slab

3) thin film gages do not disturb the surface heat flux to the model

and for the electrical analog integration, an additional assumption is

4) constant heat flux

Each assumption will be examined individually to determine its validity.

The heat transfer into the model has been assumed to be one dimensional. This will be valid provided the gages are not placed near the edges of the substrate or near the holes in the substrate which may be used for wire connections. A rule of thumb is to place gages away from substrate discontinuities at distances equivalent to or greater than those required for a semi-infinite substrate behavior.

The ceramic on which the gages are mounted must be thick enough so that the heat transfer into the ceramic is similar to that of a semi-infinite solid. It is desired

that the base of the ceramic should remain at a constant temperature. The thickness at which T_x/T_s and q_x/q_s remain smaller than 1% for a given time has been previously given in equation (3.22). For a substrate thickness of 2.5 mm, the test time for a valid test has been determined to be approximately 0.65 seconds.

The third assumption used in this technique is that the thin film gage does not disturb the surface heat flux to the model. This will be assumed to be true since the layer of metal film is very thin, on the order of 10^{-6} to 10^{-7} m (37:23) and it has a high thermal conductivity.

For the electrical analog circuit, the theoretical analysis had an additional assumption: constant heat flux. Again, the validity of the assumption will be considered later by plotting T_s^2 versus t and examining its deviation from a straight line.

3.6.5.3 Data Acquisition - Numerical

Data acquisition for the numerical technique will consist of determining $\Delta V/(\alpha_R \text{VREF})$. α_R will have been determined previously as explained in Appendix I. However, before a test can even be started, the data channels of the acquisition system must be calibrated. Using the variable resistors in the current generator box, the Wheatstone bridge must be balanced before any calibration or test. The output from the bridge should pass through the amplifier and be recorded by the data acquisition system. These data

93

units should be close to zero for a balanced bridge. A resistor, Ra, is then added in series to the thin film gage. The output of the data acquisition system can then be amplified to cause the output to be near the full scale of the data acquisition system. The calibration coefficient may then be expressed in terms of ohms/digital units. Once the calibration coefficient is established, the amplifier setting for each data channel must not be changed. The resistance, Ra, is chosen using the resistance versus temperature calibration plots for α_R for each gage depending on the expected maximum temperature rise during an actual test.

During a test, the thin film gages are supplied with a constant current by a differential amplifier circuit. The voltage output of the gage may be read from the readout window on the current generator. At ambient conditions before a test, the voltage read from this window is VREF, the initial film voltage. The resistance of the thin film gage, RFILM, should also be recorded by an ohm meter at ambient conditions before test, to determine the initial temperature of the gage.

The voltages are then numerically integrated using equation (3.27) or (3.28). The program used to perform this integration is shown in Appendix L. Once the heat transfer rate is determined, the Stanton number can be calculated using equations (3.18) through (3.21).

3.6.5.4 Data Acquisition - Electrical Analog

The voltage output of the gage is determined exactly as previously described in the data acquisition for the numerical technique. However, the calibration of the data channel as described using a resistor in series with the gages is not necessary since the electrical analog circuit will be used to reduce the data from the thin film gages. The data channels will be calibrated in conjunction with the analog circuit, as described in Appendix I when determining the $A*/\beta$ term.

The output from the thin film gage after amplification is connected to the analog circuit which allows the conversion of a parabolic wave into a step wave. The output from the analog circuit is then amplified again, and the output is called VOUT. Using equation (3.36), the heat transfer trace can be obtained. This trace should be examined, and a time interval, from $\tau1$ to $\tau2$, over which steady flow conditions are present should be chosen. The time interval is important for signal processing. It should be long enough to obtain enough data points for a least squares data fit, but also should not include intervals when flow conditions are not well established, ie., during model injection. This time interval chosen will correspond to temperatures T1 and T2.

The next step in the signal processing is to reconstruct the surface temperature versus time trace from a

given heat transfer rate versus time trace. This is done using an equation given by Oldfield, Jones, and Schultz (37:34)

$$\Delta T_s(t) = \frac{4}{3}(\rho c_p k \pi)^{-1/2} \sum_{n=0}^{m} \left[q_{n+1} + q_{n-1} - 2q_n \right] (t-t_n)^{3/2} H(t-t_n)$$

(3.37)

In equation (3.37), q_n is the measured heat transfer rate at time $t_n = n\Delta t$. $H(t - t_n)$ equals 1 for $t \geq t_n$, and zero for $t < t_n$. If the time t may be expressed as $m\Delta\tau$, where $\Delta\tau$ is the time interval between data samples, then equation (3.37) may be rewritten as:

$$\Delta T_s(m\Delta\tau) = \frac{4}{3}[\Delta\tau/(\pi\rho c_p k)]^{1/2} \sum_{n=0}^{m} \left[q_{n+1} + q_{n-1} - 2q_n \right] (m-n)^{3/2}$$

(3.38)

Alternatively, if q_{n+1}, q_{n-1} and q_n are expressed in terms of data units instead of dimensionally in watts/m²,

$$\Delta T_s(m\Delta\tau) = D \sum_{n=0}^{m} \left[Nq_{n+1} + Nq_{n-1} - 2\, Nq_n \right] (m - n)^{3/2}$$

(3.39)

where

$$D = \frac{4}{3}[\Delta\tau/(\pi\alpha\, VREF)]^{1/2} \frac{A*}{R\, \beta}$$

(3.40)

Equations (3.37) through (3.40) are based on a fit of the heat transfer versus time trace using a series of ramps. The derivation of equation (3.37) is given in (37:44). The

computer program used for the reconstruction of the temperature versus time trace is shown in Appendix M.

After obtaining the heat flux versus time and the temperature versus time plots, the heat transfer versus temperature curve may be constructed. A least squares data fit to a straight line is made between the two temperatures, T1 and T2. This line is then extrapolated back to the value of q_s at the initial test surface temperature which is usually the same as ambient. This value of q_s is then equivalent to that obtained for isothermal test conditions. The program used to find the isothermal heat flux is listed in Appendix N. Once the heat transfer rate is determined, the Stanton number can be calculated using equations (3.18) through (3.21).

3.6.6 Co-axial Thermocouple Gages

The coax heat transfer gage is a coaxial surface thermocouple. The temperature time history is obtained from this gage and used to determine the surface heat flux. The coax gage assembly is illustrated in Figure 3.10. An electrically insulated center conductor, chromel, is enclosed within a cylindrical jacket of constantan. The surface thermocouple junction is formed by the vacuum deposition of a metal about one micron thick. An advantage to the use of the coax gage is that it is thermally matched
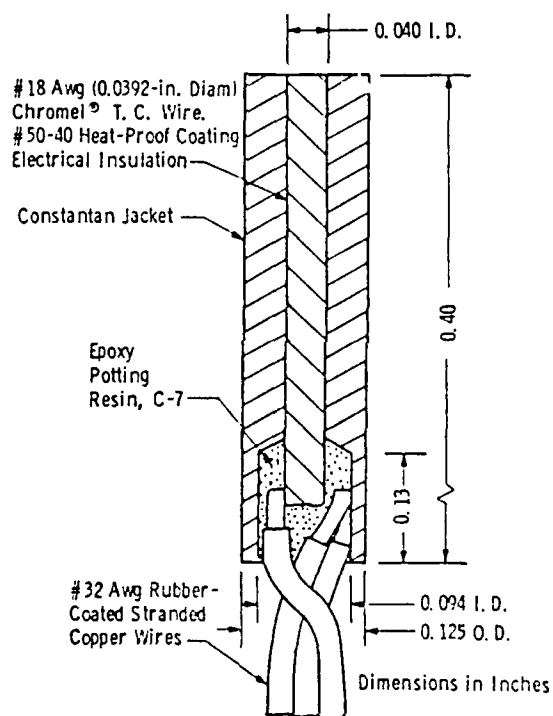
Figure 3.10. Coax Gage Assembly

to the model, therefore allowing it to be used for long duration tests. A disadvantage with the coax gages is that it has a low output.

The choice of material for the center conductor and outer cylindrical jacket is dependent upon the test model material, or vice versa. In this test, the material is stainless steel, so the thermal properties of the gage must be similar to that of stainless steel. Chromel and constantan fulfill this requirement, as shown in Table 3.3 (10:7). The stainless steel used for the model was AISI 304 stainless steel.

Table 3.3. Thermal Properties of Materials

	$(\rho c_p k)^{1/2}$	α	c_p	k
	$\dfrac{BTU/sec}{ft^2 \; ^\circ F}^{1/2}$	$\dfrac{ft^2}{hr}$	$\dfrac{BTU}{lb \; ^\circ F}$	$\dfrac{BTU}{ft \; hr \; ^\circ F}$
Chromel	0.410	0.19	0.107	11.0
Constantan	0.408	0.23	0.098	13.0
304 Stainless Steel	0.353	0.17	0.105	8.7
17-4 PH Stainless Steel	0.409			
302 Stainless Steel		0.16	0.110	9.4
410 Stainless Steel		0.27	0.110	14.0
Aluminum		3.30	0.214	119.0
Copper		4.30	0.092	219.0

The coax gage is installed through the model wall so that the outer model suface temperature may be measured using wires emerging from the back surface. The gages used in this study have an additional wire that enables the measurement of the temperature of the back side of the gage. This is significant in that these coax gages are not restricted by the semi-infinite slab assumption used by many other heat transfer gages. During long tests, the back side temperature rise can be monitored and accounted for in the data reduction technique.

The popularity of the coax gage has arisen due to several reasons (10:6). The coax gage measures surface temperatures more accurately than other gages because the conduction losses are minimized since the thermocouple materials are actually part of the wall, ie, have the same thermal properties as the wall material. The gage is durable in that it is able to withstand high levels of erosion during testing. The gage may be contoured exactly to the model surface by sanding, so convective or other material flow over the surface in undisturbed. Also the small mass of the thermal junction allows a nominal response time of approximately one microsecond for the vacuum deposited junction or ten microseconds for junctions created by sanding. The coax gage can also be manufactured very small, which allows a very close spacing of thermocouples. The gages are available in probe diameters starting from

0.015 inches (0.381 mm).   Also, the voltage versus temperature correlation is a property of the gage materials and is already determined by the manufacturer so no gage calibration is necessary.

3.6.6.1 Theory

The heat equation for one dimensional flow is:

$$\frac{\partial T}{\partial t} = \alpha \frac{\partial^2 T}{\partial y^2} \tag{3.41}$$

To account for gage back side heat loss, a finite difference solution of the heat equation was developed (25:3).   A simple forward time and central spaced explicit method was applied to the heat equation.

$$\frac{T(N+1,I) - T(N,I)}{\Delta t} = \alpha \frac{T(N,I+1) - 2T(N,I) + T(N,I-1)}{(\Delta y)^2} \tag{3.42}$$

Solving for T(N+1,I) results in the following equation.

$$T(N+1,I) = \Theta s[T(N,I-1) + T(N,I+1) + (1/\Theta s - 2) T(N,I)] \tag{3.43}$$

The heat transfer rate is solved using a three point forward differencing scheme.

$$q(N) = -\frac{k}{2\Delta y} [-3T(N,wall) + 4T(N,wall+1) - T(N,wall+2)] \tag{3.44}$$

$$\text{where} \quad \Theta s = \frac{\alpha \Delta t}{\Delta y^2} \tag{3.45}$$

For this scheme, boundary conditions are imposed to force the temperature at the inner wall surface (I=1) to match the coax gage surface temperature while the gage back side temperature (I=Imax) is forced to match the back side

temperature measurement. An important restriction for the
NSWC method is that the stability constant, Θs, must be less
than 0.5 for the solution procedure to be numerically
stable.

3.6.6.2 Validity of Assumptions

For the coax gage, there are only two assumptions used
in the analysis and technique,

1) one dimensional heat transfer

2) coax gage does not disturb the surface heat flux to
   the model

Each assumption will be considered individually for its
validity.

One dimensional heat transfer is assumed to be true
since the thermal properties of the gage are similar to
those of the stainless steel model. In complicated flows
with high heating in localized areas, insulation of the gage
may be required so that the peak heating from one point does
not conduct laterally to a neighboring gage. For short coax
gages, a portion of the heat transfer in the lateral
direction can be taken into account by the use of the back
face gage. However, for this study, the test duration is
very short - approximately 500 milliseconds, so one
dimensional heat transfer is assumed to be correct.

It is also assumed that the gage does not disturb the
surface heat flux to the model since the gage is installed

in the body of the model. The surface of the gage is installed flush with the model surface.

3.6.6.3 Data Acquisition

The data acquisition involves recording the voltage from the coax gage. However, before the data channel of the acquisition system is used to process the signal from the coax gage, calibration of the amplifier and data channel is required. The calibration is completed by placing a known dc voltage into the amplifier and recording the data units from the data acquisition system to determine a volts/unit calibration constant.

Once the voltage from the coax gage is known, the temperature of the surface and back side can be determined using the calibration tables supplied by the manufacturer. These tables, referenced at 0°C, are included in Appendix Q. Once the surface and back side temperatures are known, the heat transfer rate can be determined using equations (3.43) through (3.45). Appendix R lists the computer program used for this computation. Once the heat transfer rate is known, the Stanton number can also be determined using equations (3.18) through (3.21).

3.7 Results of the Flat Plate Study

Table 3.4 shows the test conditions for all the photographs included in this report for tests on the flat plate. Appendix S shows the test conditions and VKI photograph catalog numbers for every test completed in this study. The shadowgraph photographs showed the undisturbed boundary layer height at approximately 60 mm from the plate leading edge to be less than 1 mm. According to Schlicting (46:140), the boundary layer thickness for incompressible flow, if defined when $U=.99U_\infty$, can be calculated using equation (3.46) at $x = .06$ meters

$$\delta = 5.0 \left[\frac{\mu x}{\rho U_\infty} \right]^{1/2} \qquad (3.46)$$

Table 3.4. Flat Plate Test Conditions

Test	P_o (Bars)	α (degrees)	M	Re $(\times 10^{-7})$ $(/m)$
O-1	20	0.0	6.0	1.69
O-2	20	5.5	5.26	2.23
L-1	20	0.0	6.0	1.69
L-2	10	0.0	6.0	0.844
H-1	20	0.0	6.0	1.69
H-2	10	0.0	6.0	0.844

where O - Oil flow test
       L - Liquid crystal test
       H - Heat transfer test

Table 3.5 shows the resulting calculated boundary layer thickness using eqn (3.46). The boundary layer thickness

was calculated at the appropriate test conditions using the numerical code explained in the computational effort, and the results are very similar to those from eqn (3.46).

Table 3.5. Boundary Layer Thickness

	δ (mm)
Po = 20 bar, Re = 1.69×10^7 /m	.3
Po = 10 bar, Re = $.844 \times 10^7$ /m	.5

3.7.1 Oil Flow Results

Figure 3.11 shows the results of the oil flow study on the flat plate at Mach = 6, Re = 1.69×10^7 /m and Po = 20 bar. The oil flow photograph shows the entire flat plate model with the direction of the flow being from left to right. At Mach = 6, most of the limiting surface streamlines are straight and parallel. The Mach 6 case was repeated many times because the results were not reproducible. Some photographs showed the flow as totally straight and parallel while some photographs showed some bending of the streamlines at the rear edges of the plate. However, the bent streamlines sometimes appeared on the right rear edge of the plate, and then the next test they appeared on the left rear edge of the plate. In conclusion, the flow near the edges of the plate at Mach 6 seems to be highly unsteady, but for most of the plate, there is parallel flow at Mach = 6.

Figure 3.12 shows the results of the oil flow study at
Mach 5.26, Re = .844x10^7/m and Po = 20 bar. In the center
of the plate, the streamlines are straight and parallel.
However, toward the edges, the streamlines bend toward the
edges of the plate. This occurs since the plate is at an
incidence and the flow spills over the sides of the plate.

3.7.2 Sublimation Results

The sublimation test did not produce much information.
For all the test cases, sublimation only occurred at the
leading edge of the flat plate. This indicates that the end
of transition for each of the flow cases, occurs farther
downstream than 150 mm, the edge of the plate. The results
obtained are consistent with the findings of previous
studies (15:F10-F12; 14:F20-F21; 31:110).

3.7.3 Liquid Crystal Results

The liquid crystal technique worked well, but some
difficulties arose in trying to record the data. The
photographs that recorded the color changes were very dark.
There was very little contrast between the colors. The use
of the digital image processing would probably make the
reading of the colors easier. A strobe light was initially
used to illuminate the model for photographic purposes. The
strobe light proved to be inadequate as it did not uniformly
illuminate the model and caused a large glare spot in the
center of the model. One 1000 watt lamp was used next, but
it did not produce enough light to obtain a good picture.

Finally, two 1000 watt lamps were used to illuminate the model. The lamps were turned on after the model was injected to keep the time that the model is illuminated down to a minimum. The ejector was run for approximately 15 seconds to verify that the two lamps did not heat the model enough to cause color changes during test conditions. The time of a actual test is less than 13 seconds. Although no color changes were detected during this preliminary time, the lamps were probably adding a small unknown amount of heat to the model. Future tests with liquid crystals need to use a different light source; one that has more illumination power, yet produces less heat.

The coax gage was referenced to the ambient temperature during the calibration. The calibration and test photographs were taken on the same roll of color film and developed at the same time so that the correlation between temperature to color would still be valid.

The surface of the liquid crystal is visually marred at the junction of the plexiglas and stainless steel. Apparently the epoxy glue used to fill the crack did not cure properly after application and the glue spreads into the liquid crystal layer. This did not disturb the flow, but just disturbed the visualization of the colors near the material boundaries.

One difficultly arose in the data reduction method used for the liquid crystal technique. This difficulty was in

determining the temperature of the surface of the model at time t = 0, just before injection of the model. The coax gage was not connected during the tests, but its voltage output was recorded before the tunnel was started to obtain the surface temperature of the model at ambient conditions. Later, from the thin film gage heat transfer tests, it was found that the model surface is cooled several degrees when the tunnel ejector is started - so the actual surface temperature of the model at the start of the test is quite lower than that at ambient conditions. The temperature of the model at time = 0 could not be ascertained from the liquid crystals for the temperature was too low for the appearance of any color. Therefore, the initial temperature was obtained from the coax gages in the quantitative heat transfer test. Although the zero data from one test (H-1) is used in another test (L-1), this will introduce only a very small error to the liquid crystal results since the startup and initial conditions of the tunnel were the same for both tests.

The results of the liquid crystal test at Po = 20 and 10 bars is shown in Figures 3.13 and 3.14. Theoretical results obtained from eqns (3.12) and (3.14) are also plotted with the experimental data. The experimental errors associated with the liquid crystal tests are 8% for the log(Rex) and 5% for the Stanton number calculations. The results of the liquid crystal tests match very well with the

theoretical results. A check on the validity of the constant heat flux assumption could not be made using liquid crystal data since it was impossible to obtain temperature versus time data at a constant location. This is due to the limited calibration information. The validity of this assumption will be examined in the next section using the thin film gage data since the heating characteristics of the model are the same, just the method of obtaining the data are different.

3.7.4 Heat Transfer Results

Two thin film gage ceramic pieces were constructed as specified in Figure 3.6. Although only one piece was needed, the second was made in case the first piece was broken during testing. The first piece had thin film gages of 4 mm in length. The second piece had thin film gages of 2 mm in length. The 4 mm gage length piece was used in this test. The second piece, because of the shorter gage length, would be better suited for heat transfer measurements in three dimensional flows.

The film coefficient of resistance calibration data for the 4 mm thin film gages are shown in Table 3.6 and plotted in Figures 3.15 through 3.20. In Table 3.7 are the values of the film coefficient of resistance and other values obtained from the film coefficient of resistance data using a least squares algorithm for the 4mm long gages. The least

squares algorithm solves for the coefficients of eqn (3.47) which corresponds to eqn (3.33).

$$\Delta R = A0 + A1 \Delta T \qquad\qquad (3.47)$$

where A0 is the intercept of the line and should be approximately zero.

$$\Delta R = R - RREF$$

$$\Delta T = T - TREF \qquad\qquad (3.48)$$

$$A1 = \frac{\alpha\ RREF}{R} = \text{slope of the line}$$

and F is a correlation coefficient that indicates how well the data matches the resulting equation of a straight line. Table 3.8 lists the film coefficient of resistance calibration data for the 2 mm thin film gages, and the same data is plotted in Figures 3.21 through 3.26. The second set of data in Table 3.6 and Table 3.8; gages 25, 26, and 27, correspond to the small gages made for the determination of the ceramic thermal product in the CT-2 tunnel. The value of the thermal product for the 4 mm gage ceramic piece was determined in CT-2 and is 1950.0 $J/m**2$ °K $sec^{1/2}$. For the 2 mm gage ceramic piece, the thermal product is equal to 2100.0 $J/m**2$ °K $sec^{1/2}$. The value of the film coefficient of resistance and other output from the least squares algorithm are listed in Table 3.9. The computer program with the least squares algorithm is listed in Appendix J.

The equipment setup is shown in Figure 3.27. The large box on the right contains the constant current generator,

110

100 gain amplifier, wheatstone bridge, electrical analog circuits, and the parabolic voltage generator. The next set of boxes, stacked four high, are an additional 16 adjustable gain amplifiers. The next piece of equipment is the medium speed data acquisition system with a maximum of 16 data channels, and then the computer console was used to start the acquisition program on the PDP computer. The heat transfer flat plate model installed in the tunnel is shown in Figure 2.28. The coax gages are referenced to an ice bath for the heat transfer tests.

Several complications arose during the initial portion of this testing period. There was initially a tremendous amount of noise in the data. This noise was decreased by grounding all the equipment in the data acquisition chain together and grounding the cables from the gages to the tunnel floor. The noise that remains is nearly the same order of magnitude as the data. The noise varies for each gage, but at worst has an unamplified magnitude of 0.2 millivolts, and has a frequency of 50 hertz. The magnitude and frequency of the noise did not change after all the lights and unnecessary equipment were shut off.

The second complication was due to the fact that a negative heat flux occurred on the surface of the plate prior to injection of the model. This negative heat flux occurs when the tunnel ejector is started and the test section is evacuated. This negative heat flux is several

111

times the magnitude of the data to be recorded. Because of this problem and the relatively large amount of noise present, the integration of the temperature trace using the analog circuit would be too inaccurate so could not be used. The numerical integration method was the only possible way to interpret the data under these conditions. This method is complicated by the reference shift during the test.

Before any good tests could be performed the air compressor for the tunnel broke. It was initially thought that the compressor would not be fixed in a short amount of time so testing was stopped and the medium speed data acquisition system was given to another student. However, the compressor started working after a couple days, so oscilloscopes were used to photograph the temperature trace so some data could be obtained. However, an accurate recording of the reference shift could not be obtained when using the oscilloscope. As a last resort, the high speed data acquisition system was obtained and two tests were performed and the data successfully recorded. Due to time limitations, only the two coax gages and ten thin film gages were recorded during each test. The final equipment setup was similar to that shown in Figure 3.27, except that the high speed data acquisition system was used, and only 12 additional amplifiers were available for the tests.

An example of the temperature trace obtained from a thin film gage is shown in Figure 3.29. The 50 hertz noise

was "smoothed" using an averaging technique. (A least squares algorithm was used initially, but gave incorrect results.) The data was averaged over one period of the noise. An example of the data after smoothing is shown in Figure 3.30. The averaging algorithm is shown in Appendix K. A comparison between raw versus smoothed data shows the smoothed data accurately represents the real data. The raw and smooth data for each channel was plotted and it was verified that the "real" data was kept intact before the numerical integration was performed.

A sample heat transfer rate versus temperature curve is shown in Figure 3.31. The curve shows a rise in heat flux to some maximum and then a decrease in the heat flux corresponding to the fact that the plate is heating up. The isothermal heat flux is obtained from the second portion of the curve and extrapolated back to the temperature of the plate at time = 0. An example of the heat flux versus temperature curve for the two data reduction methods are shown in Figures 3.22 and 3.33. These plots show the rise in heat flux, but the test time was apparently too short to obtain the second portion of the curve. For this reason, the value of the heat flux used to calculate the Stanton number is obtained near the end of the trace. Due to this reasoning, the Stanton number is expected to be lower than expected.

To verify the accuracy of the assumption of constant heat flux, the square of the surface temperature is plotted versus time in Figure 3.34 for one of the gages. If the initial portion of the curve is omitted because of the model injection, the trace is indeed a straight line for the period of the test, approximately .6 seconds.

Unfortunately, most of the data from the coax gages were unusable. An example of a trace is shown in Figure 3.35. Since a very small temperature increase was expected during the test, approximately 1 °C, the amplifiers were set for a gain of 1000, but this was not enough amplification to distinguish the real signal from the noise. A comparison between the thin film gage and the coax gage should be done at test conditions that will produce higher heating rates, ie. higher chamber pressure and lower Mach number.

The computer programs used to convert the data from the VKI PDP computer acquisition file is listed in Appendix K. Appendix L contains the input data files needed to convert the data from digital units to physical units. Appendix M lists the data conversion program, Appendix N is the numerical integration program for the thin film gages. Appendix P lists the program used to calculate the heat flux for an isothermal flat plate. Although not used in this study, Appendix O contains the temperature reconstruction program and Appendix R the coax gage reduction program.

The results of the heat transfer test at Po = 20 and 10 bars are shown in Figures 3.36 and 3.37. These results show the beginning of transition. There is very little difference in the results from the direct method when compared to the results of the indirect method. The experimental errors in the heat transfer test are large, approximately 12%, due to the low amount of heat flux measured. The results of the heat transfer test are quite lower than the results from the theoretical equations (3.12) and (3.14).

Figure 3.36 shows the onset of transition for Re = 1.69 $x10^7$ /m could be at log (Rex) = 6.26 (x = 107 mm). However, what is missing from the figure is the fourth data point corresponding to log (Rex) = 6.19 (x = 91 mm). The gain on the amplifier was too high for the heat flux trace that was present so no quantitative data could be taken. It is possible that it is just a stray point due to a bad gage, but it could also be an indication of transition.

Figure 3.37 shows the results for Re = .844 x 10^7 /m. Again the fourth data point corresponding to log(Rex) = 5.89 and x=91 mm is missing due to a high signal. Because of the lower Stanton numbers after transition, it appears that the position of fully turbulent flow is further downstream than for the higher Reynolds number case. Since no other data is available to determine if the fourth data point is bad, the beginning of transition for both Reynolds number cases

occurs between x = 83 mm and 91 mm. More data points need
to be taken to better define the location of transition.
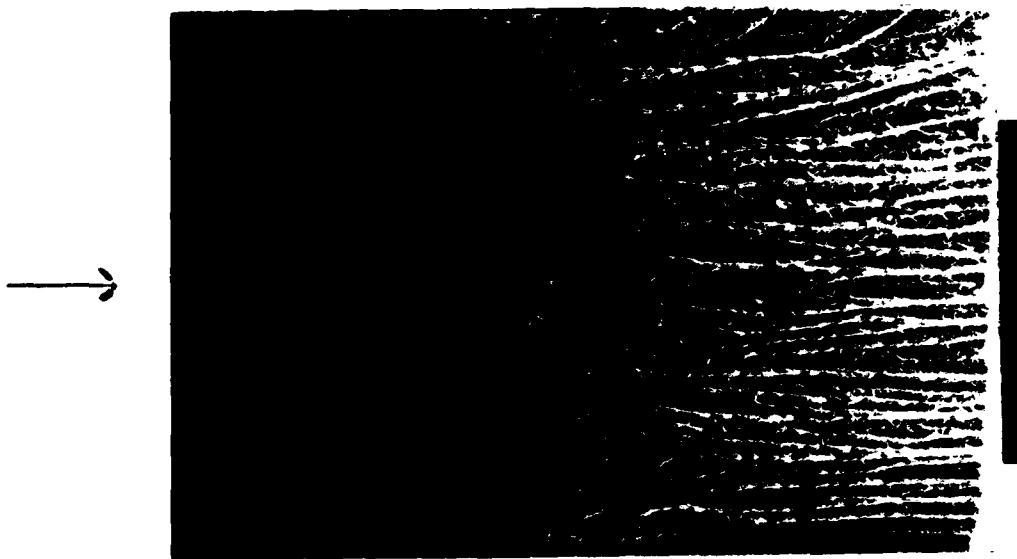
Figure 3.11.   Plate, Oil Test O-1, M = 6, Re = 1.69×10^7 /m
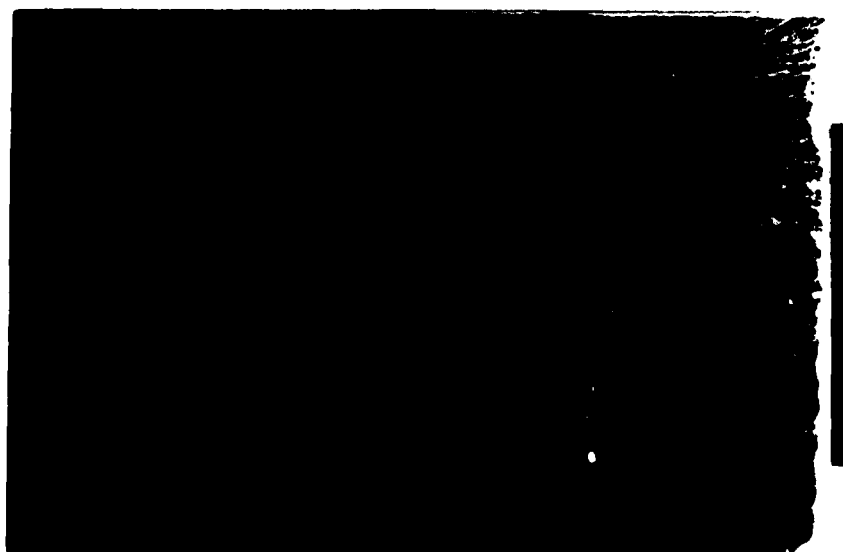
Figure 3.12.   Plate, Oil Test O-2, M = 5.26, Re = 2.23×10^7 /m
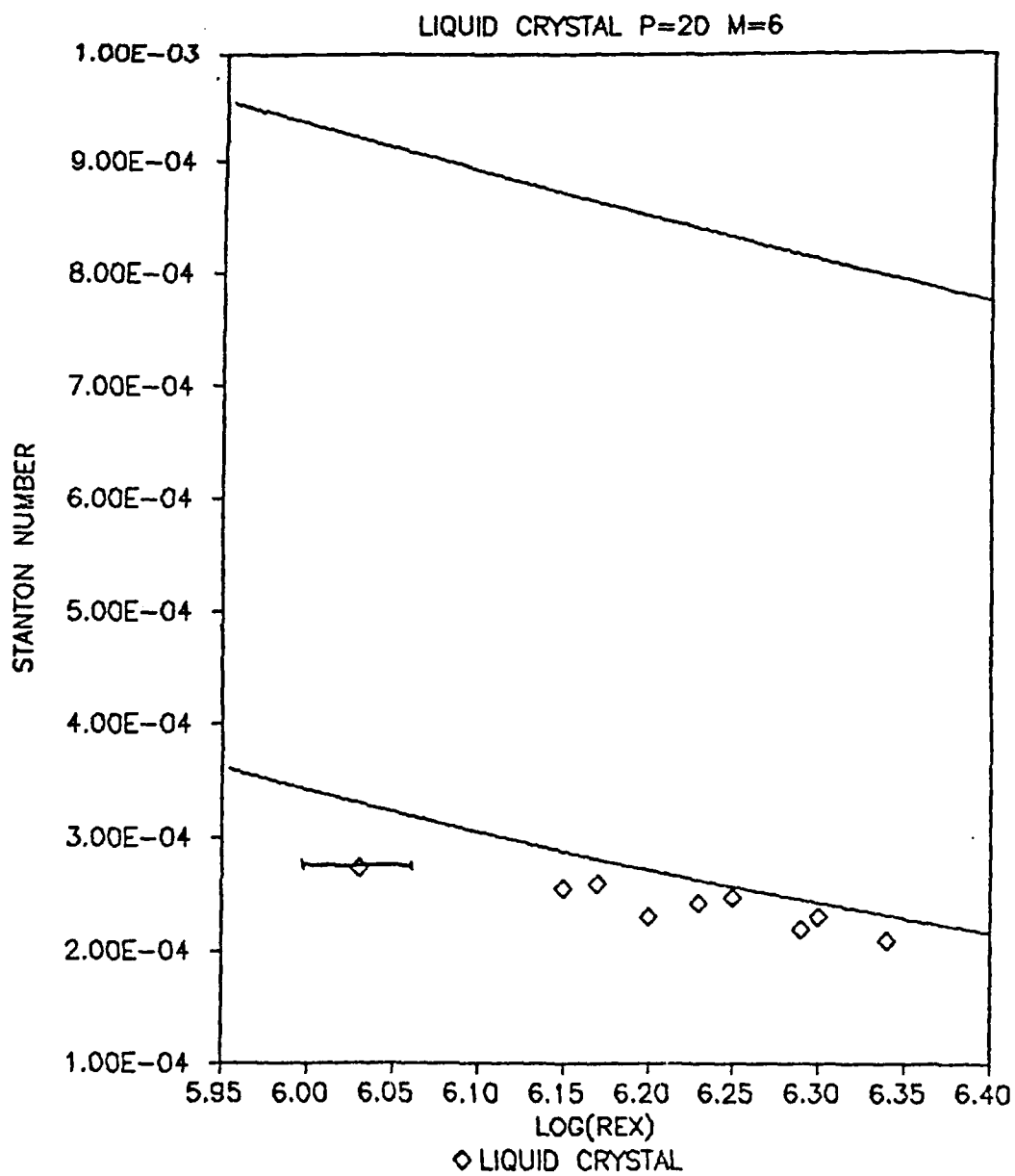
Figure 3.13.   Plate, Liquid Crystal L-1, Re=1.69x10⁷ /m
M = 6, Po = 20 bar
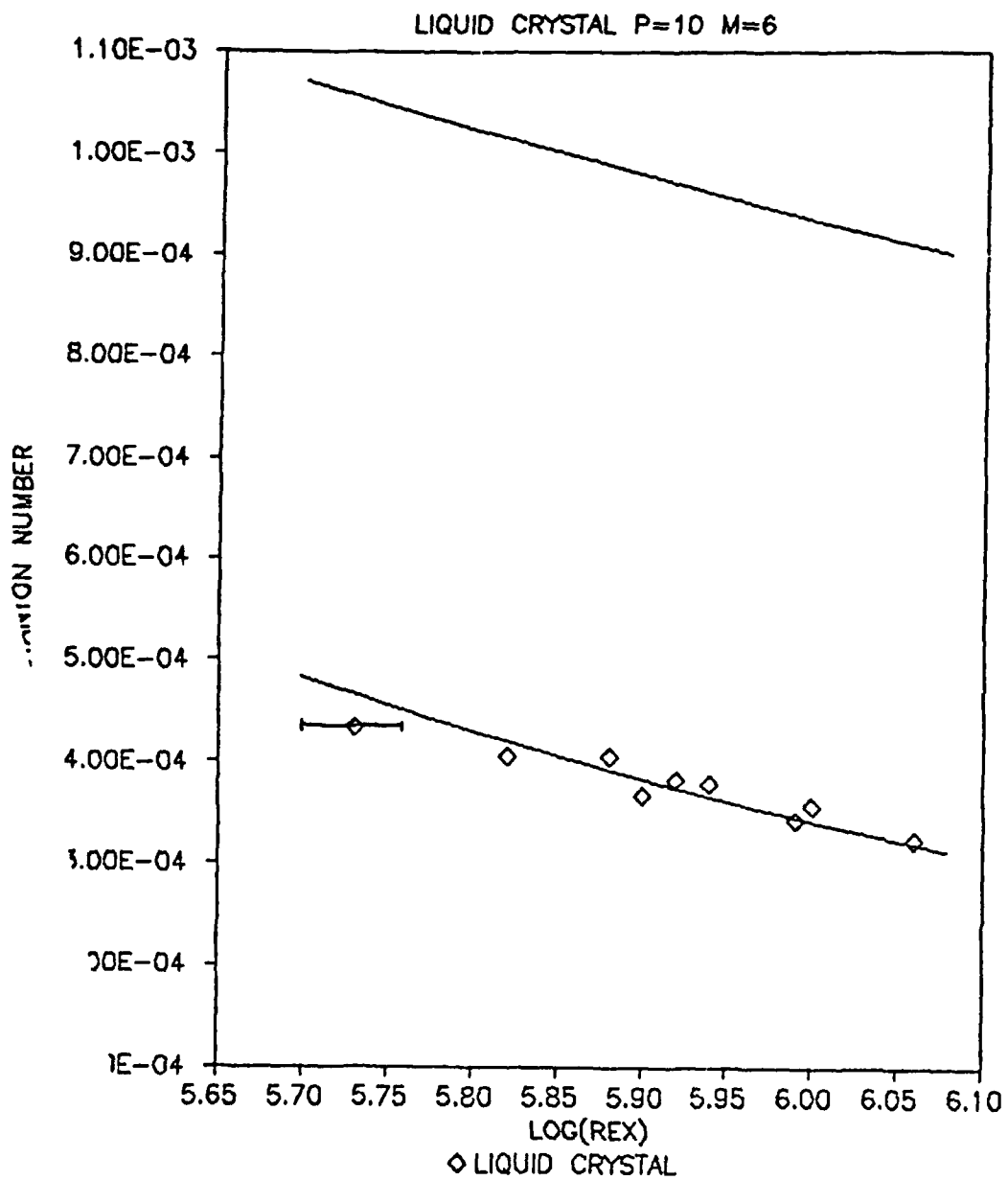
Figure 3.14.   Plate, Liquid Crystal L-2, Re=.844x10^7/m
M = 6, Po = 10 bar

Table 3.6. Coefficient of Resistance Calibration Data
For 4 mm Thin Film Gage

Gage Resistances (ohms)

T °C	20.5	30.0	41.2	49.0	62.65	69.65	
Gage No.							
1	46.26	47.37	48.43	49.28	50.75	51.45	
2	50.84	52.04	53.27	54.20	55.85	56.66	
3	51.59	52.80	53.27	54.91	56.90	57.33	
4	46.06	47.20	48.24	49.15	50.58	51.39	
5	47.52	48.62	49.80	50.67	52.20	53.01	
6	51.83	53.26	54.29	55.37	56.94	57.90	
7	54.41	55.63	56.89	59.84	59.48	60.36	
8	47.34	48.39	49.46	50.30	51.72	52.47	
9	59.24	60.60	62.05	63.11	64.98	65.96	
10	51.72	52.97	54.30	55.27	56.99	57.88	
11	57.30	58.58	59.90	60.88	62.62	63.50	
12	51.18	52.36	53.52	54.41	55.96	56.77	
13	49.09	50.17	51.28	52.12	53.58	54.33	
14	45.29	46.27	47.27	48.01	49.34	50.00	
15	46.39	47.36	48.37	49.12	50.46	51.11	
16	47.60	48.77	49.67	50.52	51.86	52.60	
17	54.73	55.87	57.04	57.90	59.44	60.21	
18	50.31	51.38	52.53	53.24	54.64	55.37	
19	57.41	59.27	59.81	61.05	62.36	63.40	*
20							@
21	55.41	57.42	57.61	58.82	59.98	61.00	**
22	57.19	58.35	59.37	60.24	61.66	62.43	
23	40.05	43.38	41.87	45.01	46.27	46.90	***
24	51.95	53.06	54.13	54.92	56.36	57.08	
4-25	56.81	58.22	59.11	60.18	61.00	62.38	
4-26							@
4-27	44.12	44.99	45.89	46.46	47.62	48.17	

@ Infinite resistance, gage unusable

* From Figure 3.18, the second data point looks
incorrect, so was omitted from the α_R calculation

** From Figure 3.19, the second data point looks
incorrect, so was omitted from the α_R calculation

*** From Figure 3.19, the first and third data points look
incorrect, so were omitted from the α_R calculation

Table 3.7. Coefficient of Resistance
For 4mm Thin Film Gage

Gage No.	α_R +3 x 10 (/°K)	A0 (ohms)	A1 (ohms/°K)	F	
1	2.27	.0359	.1051	.9995	
2	2.32	.0210	.1180	.9998	
3	2.32	.0001	.1197	.9955	
4	2.33	.0313	.1071	.9992	
5	2.34	.0058	.1111	.9998	
6	2.33	.0865	.1206	.9973	
7	2.21	.0211	.1202	.9998	
8	2.19	.0130	.1037	.9997	
9	2.30	.0175	.1360	.9999	
10	2.41	.0180	.1247	.9999	
11	2.19	.0269	.1255	.9998	
12	2.20	.0348	.1127	.9996	
13	2.16	.0213	.1060	.9998	
14	2.10	.0239	.0953	.9998	
15	2.06	.0179	.0957	.9998	
16	2.10	.0748	.0998	.9981	
17	2.03	.0299	.1109	.9998	
18	2.02	.0559	.1018	.9995	
19	2.10	.0026	.1208	.9967	
20					
21	2.03	-.0053	.1124	.9952	
22	1.84	.0537	.1052	.9991	
23	2.05	-.0196	.0889	.9997	
24	1.99	.0487	.1034	.9995	
4-25	1.85	.1785	.1051	.9823	*
4-26					
4-27	1.85	.0338	.0818	.9995	

* Electrical connection is bad, gage cannot be used

Table 3.8.   Coefficient of Resistance Calibration Data For 2 mm Thin Film Gage

Gage Resistances (ohms)

T °C	20.5	30.0	41.2	49.0	62.65	69.65	
Gage No.							
1	51.35	53.00	53.73	54.70	56.27	56.85	*
2	45.72	46.79	47.87	48.66	50.09	50.87	
3	47.53	48.59	49.79	50.62	52.15	52.94	
4	50.35	51.94	52.82	54.01	55.34	56.44	*
5	62.76	64.25	65.59	66.73	68.64	69.66	
6	55.90	57.60	58.52	59.72	61.35	62.43	
7	45.71	47.12	47.90	49.94	50.31	51.17	**
8	49.57	50.75	51.88	52.77	54.35	55.14	
9	51.01	52.20	53.40	54.32	55.96	56.78	
10	57.51	58.99	60.21	61.36	63.09	64.13	
11	61.34	62.84	64.27	65.40	67.40	68.39	
12	55.65	57.13	58.29	59.36	61.08	62.01	
13	50.91	52.14	53.38	54.30	55.97	56.79	
14	48.72	49.89	51.04	51.93	53.46	54.27	
15	50.18	51.46	52.49	53.41	54.87	55.69	
16	50.12	51.30	52.50	53.37	54.97	55.78	
17	47.54	48.59	49.75	50.50	51.99	52.73	
18	45.85	46.93	48.00	48.80	50.24	50.97	
19	47.88	49.02	50.20	52.04	52.59	53.37	***
20	49.01	50.14	51.24	52.08	53.56	54.33	
21	40.35	41.34	42.29	43.03	44.31	44.97	
22	41.80	42.78	43.78	44.52	45.83	46.49	
23	50.49	51.77	52.85	53.80	55.31	56.13	
24	52.43	53.63	54.76	55.62	57.15	57.96	
2-25	44.88	45.82	46.71	47.47	48.71	49.36	
2-26	41.88	42.78	43.70	44.42	45.66	46.30	
2-27	48.70	49.61	50.57	51.23	52.51	53.13	

* From Figure 3.21, the second data point looks
incorrect, so was omitted from the α_R calculation

** From Figure 3.22, the fourth data point looks
incorrect, so was omitted from the α_R calculation

*** From Figure 3.24, the fourth data point looks
incorrect, so was omitted from the α_R calculation

Table 3.9. Coefficient of Resistance
For 2 mm Thin Film Gage

Gage No.	$\alpha_R \times 10^{+3}$ (/°K)	AO (ohms)	A1 (ohms/°K)	F
1	2.21	.0392	.1136	.9984
2	2.27	.0225	.1036	.9996
3	2.31	-.0027	.1097	.9999
4	2.43	.0078	.1222	.9970
5	2.21	.0421	.1388	.9992
6	2.29	.1543	.1280	.9937
7	2.35	.1199	.1075	.9943
8	2.27	.0279	.1125	.9995
9	2.29	.0153	.1168	.9997
10	2.30	.0658	.1322	.9985
11	2.32	.0397	.1424	.9995
12	2.28	.0922	.1271	.9983
13	2.34	.0309	.1190	.9997
14	2.30	.0340	.1119	.9996
15	2.19	.0872	.1100	.9984
16	2.28	.0288	.1143	.9997
17	2.21	.0178	.1050	.9998
18	2.25	.0312	.1034	.9996
19	2.32	.0034	.1110	.9998
20	2.19	.0360	.1072	.9996
21	2.31	.0363	.0931	.9996
22	2.27	.0288	.0948	.9998
23	2.24	.0755	.1130	.9988
24	2.12	.0505	.1111	.9994
2-25	2.02	.0156	.0905	.9994
2-26	2.14	.0062	.0895	.9997
2-27	1.84	.0163	.0897	.9997
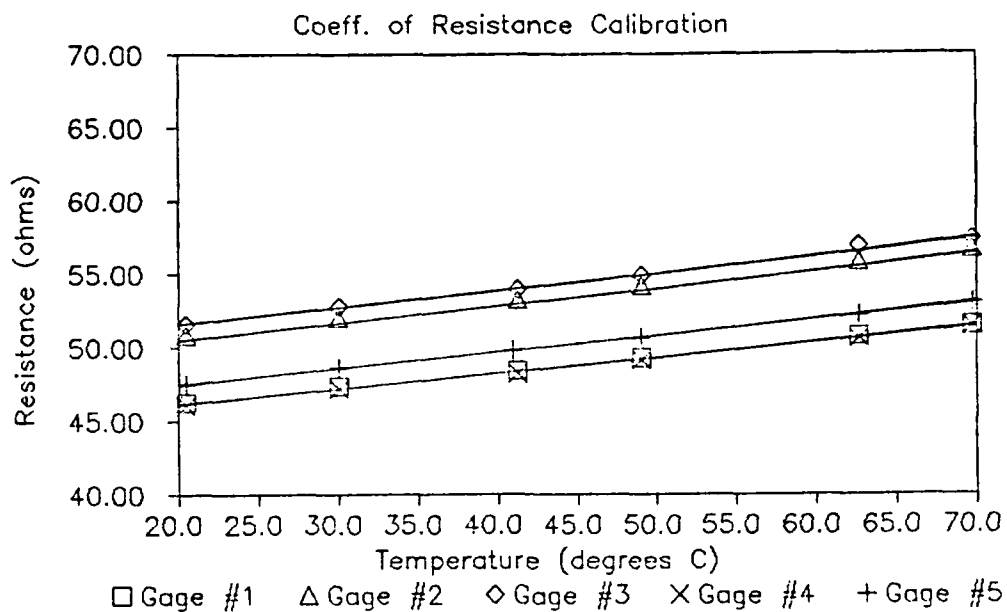
**Figure 3.15. Film Coefficient of Resistance Calibration
For 4mm Gage: Gages 1 through 5**
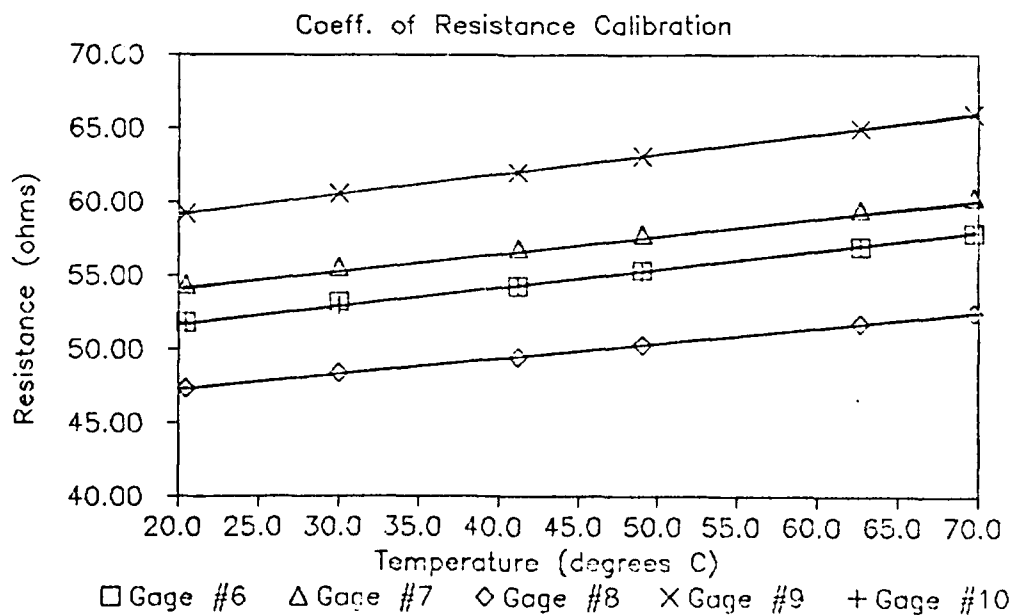
**Figure 3.16. Film Coefficient of Resistance Calibration
For 4mm Gage: Gages 6 through 10**
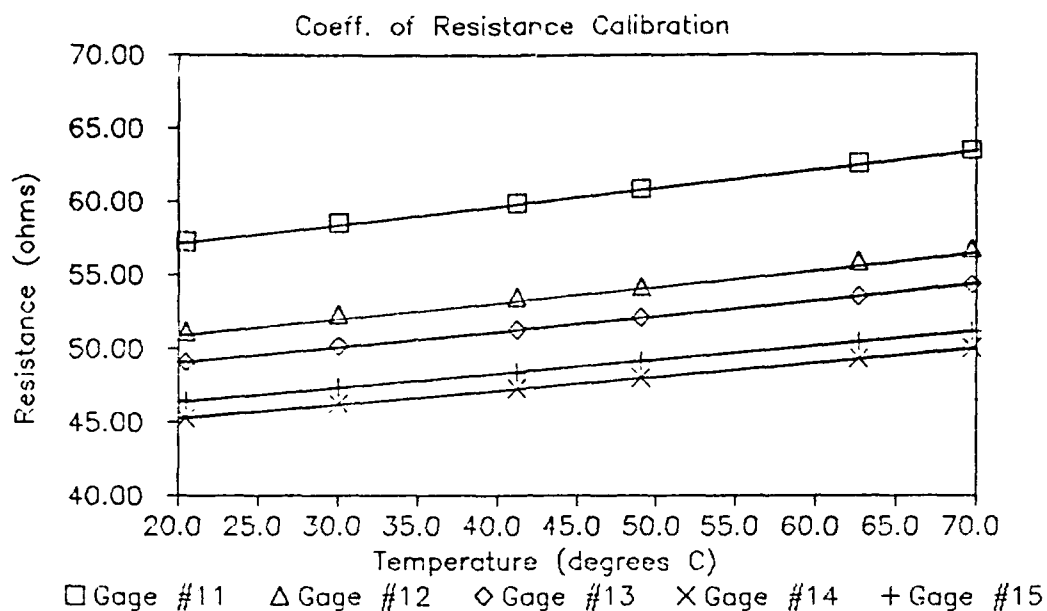
Figure 3.17. Film Coefficient of Resistance Calibration
For 4mm Gage: Gages 11 through 15
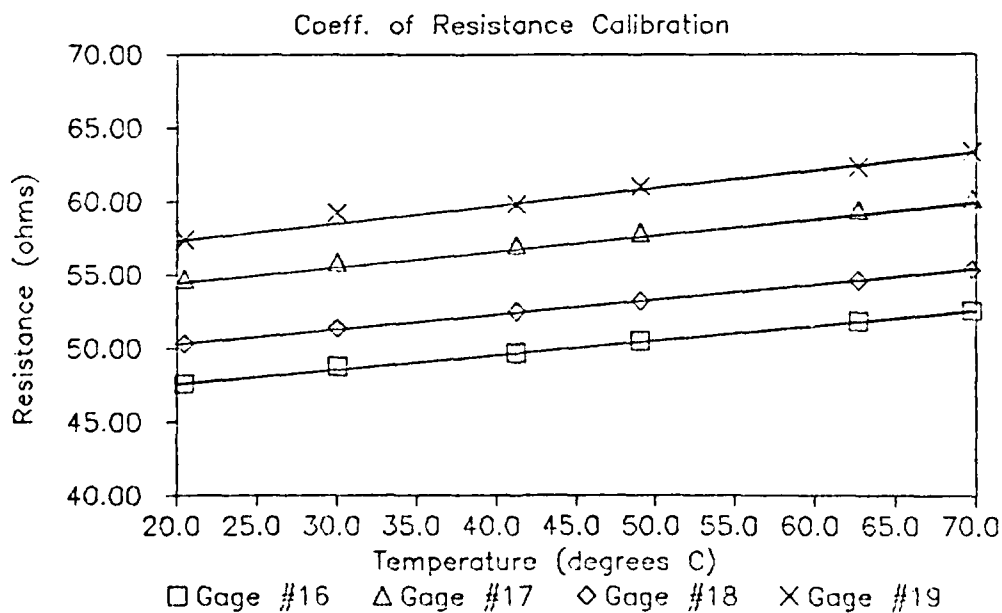
Figure 3.18. Film Coefficient of Resistance Calibration
For 4mm Gage: Gages 16 through 19
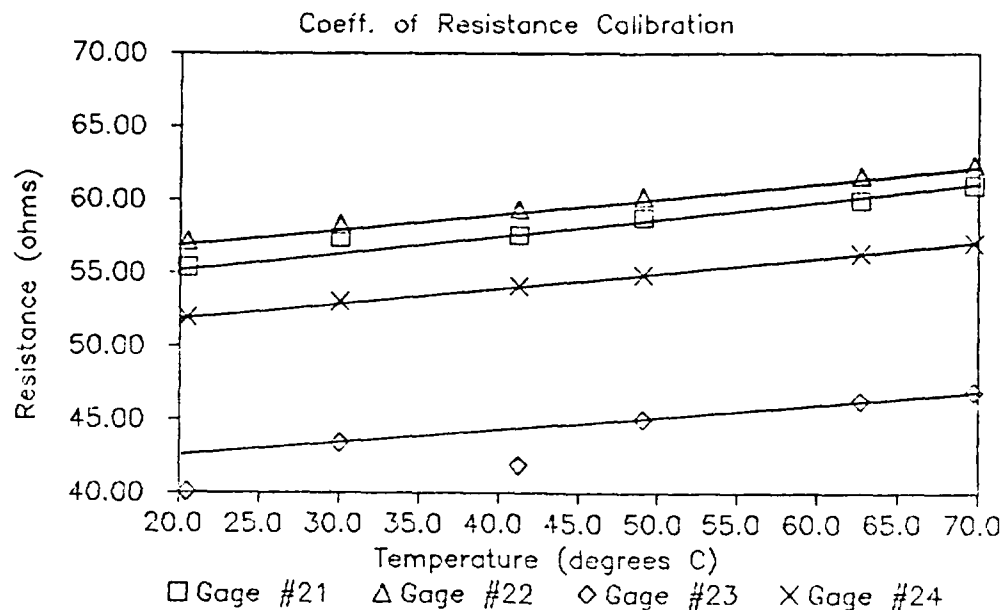
Figure 3.19. Film Coefficient of Resistance Calibration For 4mm Gage: Gages 21 through 24
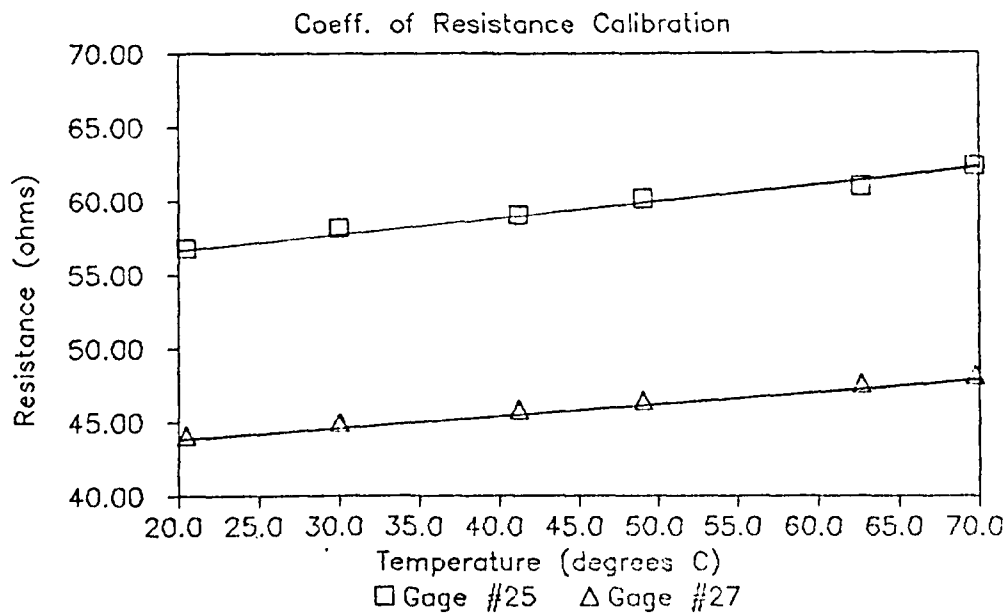
Figure 3.20. Film Coefficient of Resistance Calibration For 4mm Gage: Gages 25 through 27
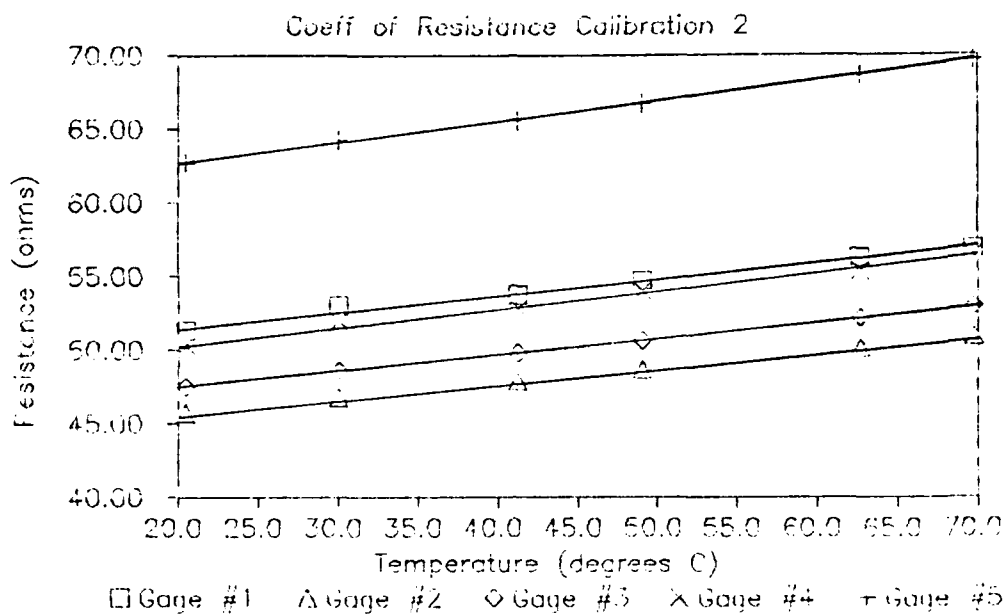
Figure 3.21. Film Coefficient of Resistance Calibration For 2mm Gage: Gages 1 through 5
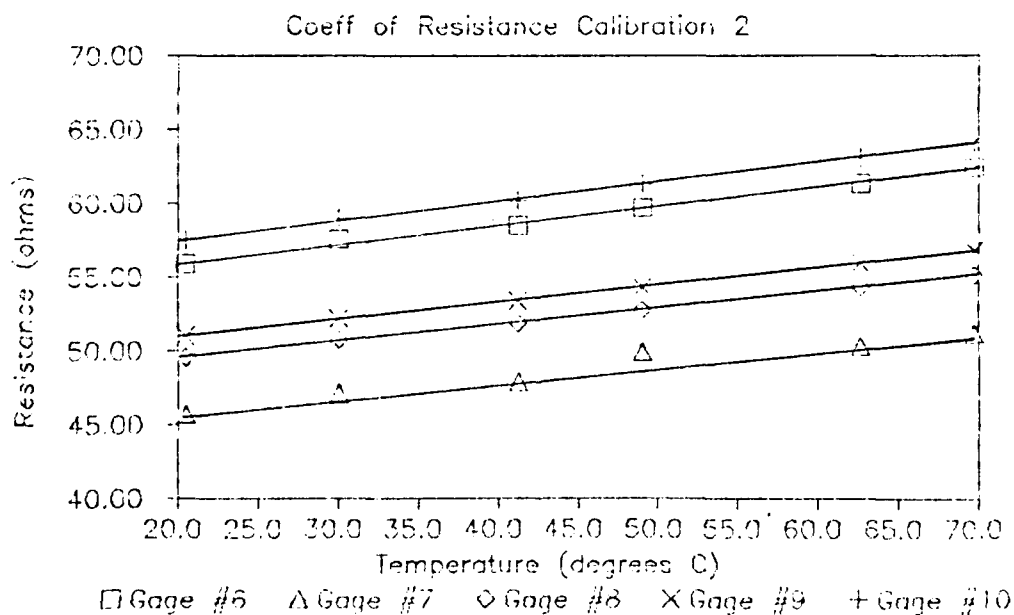
Figure 3.22. Film Coefficient of Resistance Calibration For 2mm Gage: Gages 6 through 10
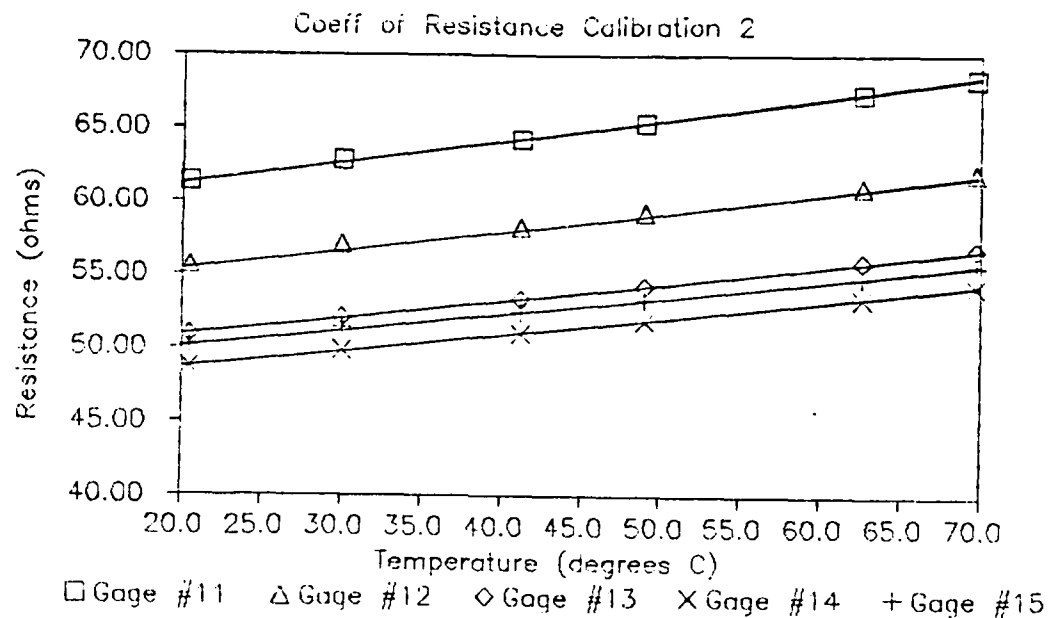
Figure 3.23. Film Coefficient of Resistance Calibration For 2mm Gage: Gages 11 through 15
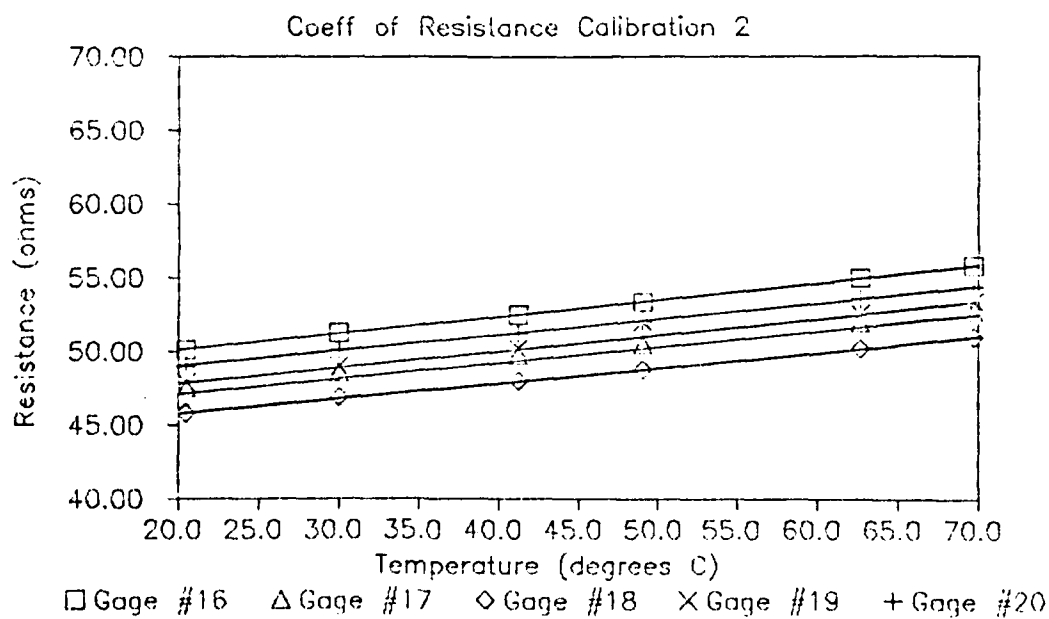
Figure 3.24. Film Coefficient of Resistance Calibration For 2mm Gage: Gages 16 through 20
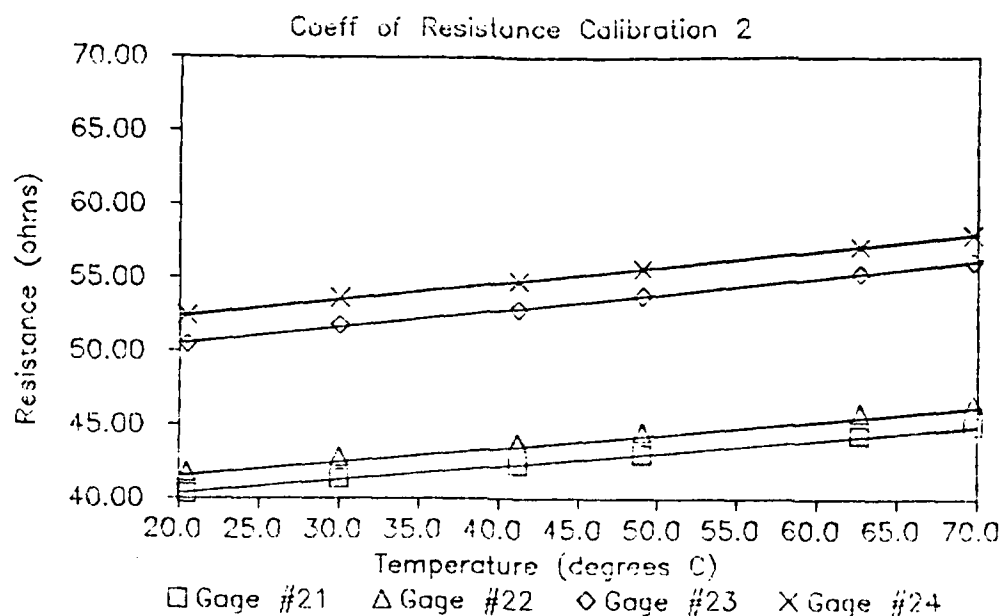
Figure 3.25. Film Coefficient of Resistance Calibration
For 2mm Gage: Gages 21 through 24
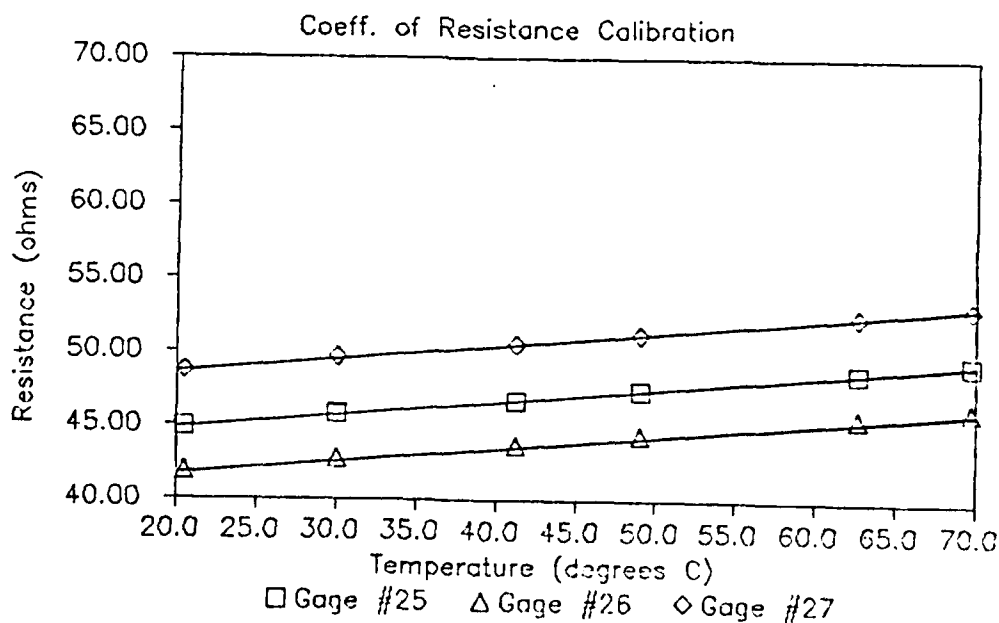
Figure 3.26. Film Coefficient of Resistance Calibration
For 2mm Gage: Gages 25 through 27

Figure 3.27.   Data Acquisition System for Heat Transfer Test
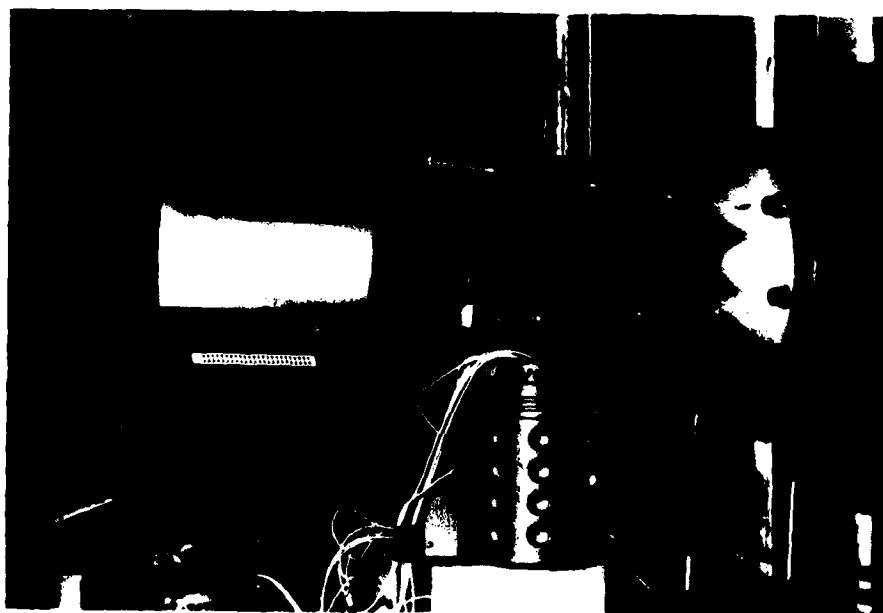
Figure 3.28.   Heat Transfer Model Installed in Tunnel
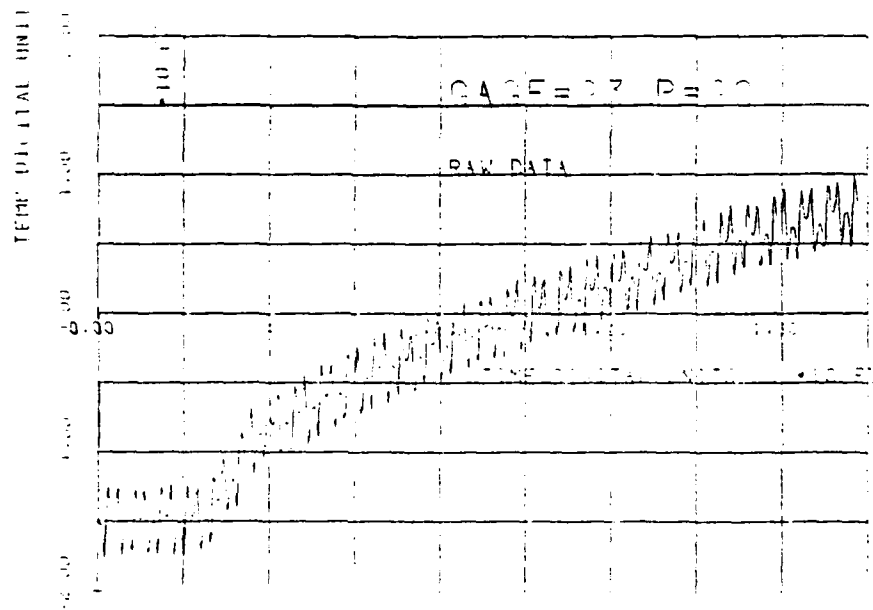
Figure 3.29.   Temperature versus Time, Re = 1.69×10^7 /m
Raw Data, Gage No 23
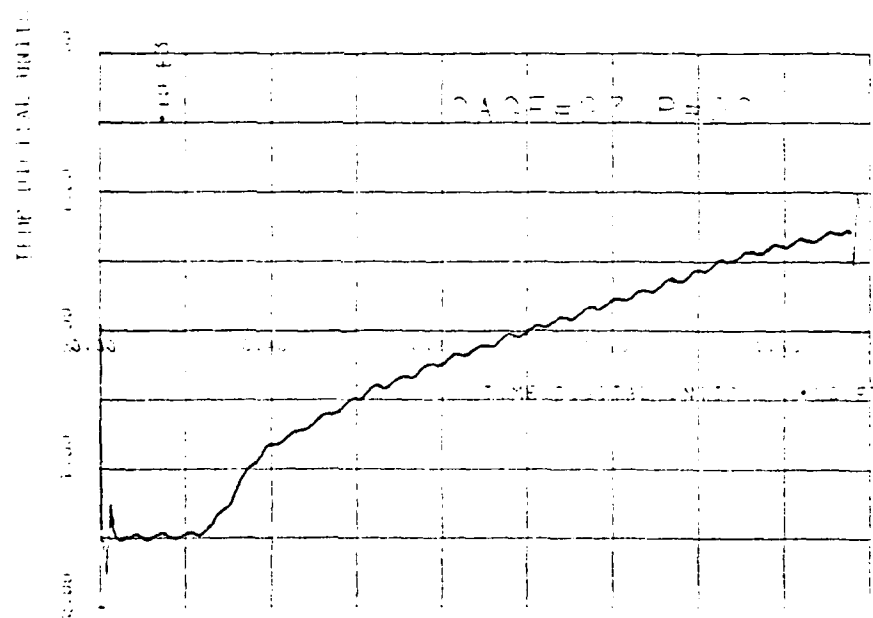
Figure 3.30.   Temperature versus Time, Re=1.69×10^7 /m
Averaged Data, Gage No 23
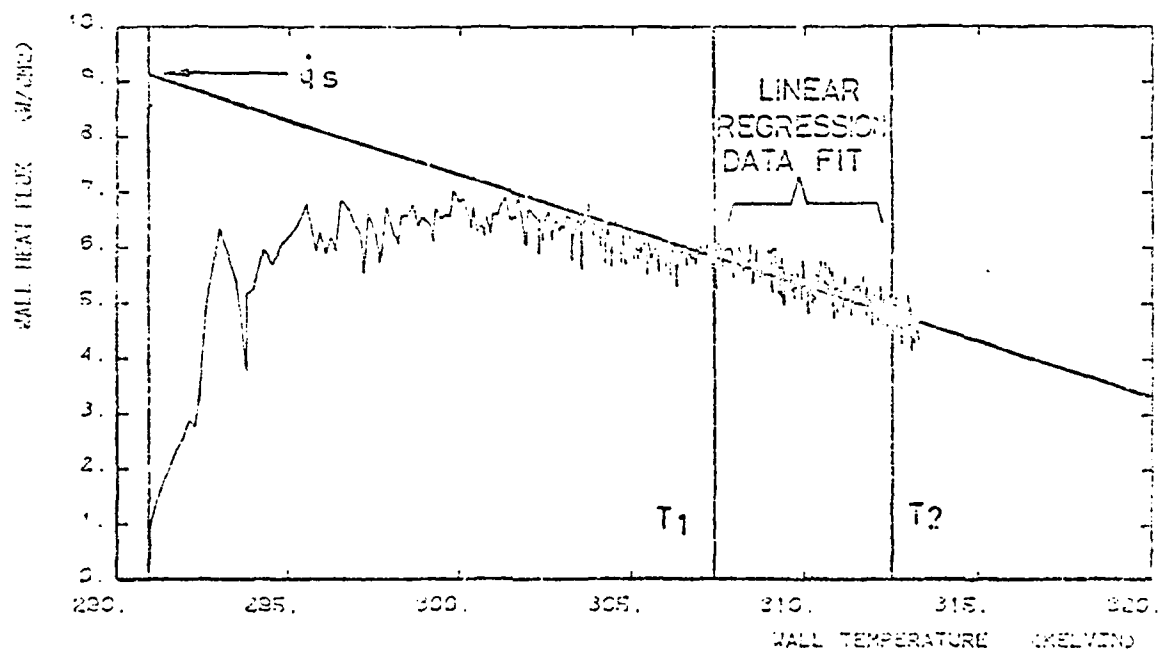
Figure 3.31. Sample of Heat Flux versus Temperature Trace
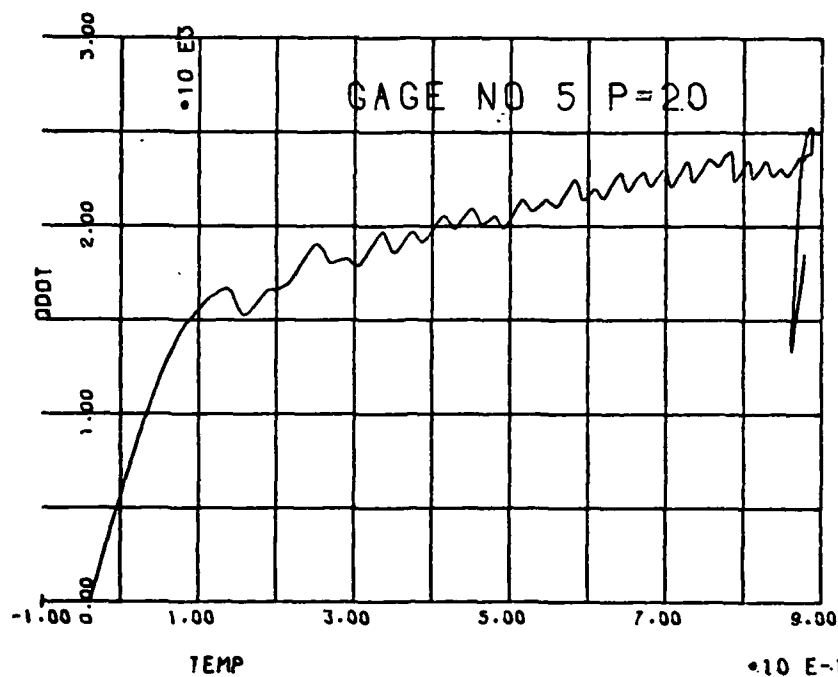
Figure 3.32. Heat Flux versus Temperature, Re=1.69x10^7/m
Gage No 5, Direct Method
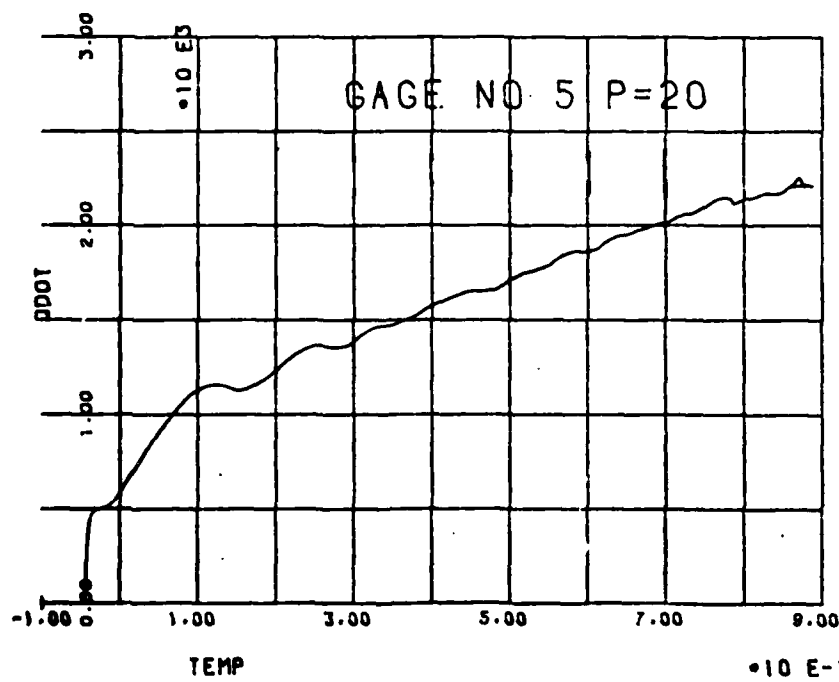
Figure 3.33. Heat Flux versus Temperature, Re=1.69x10^7/m
Gage No 5, Indirect Method

133
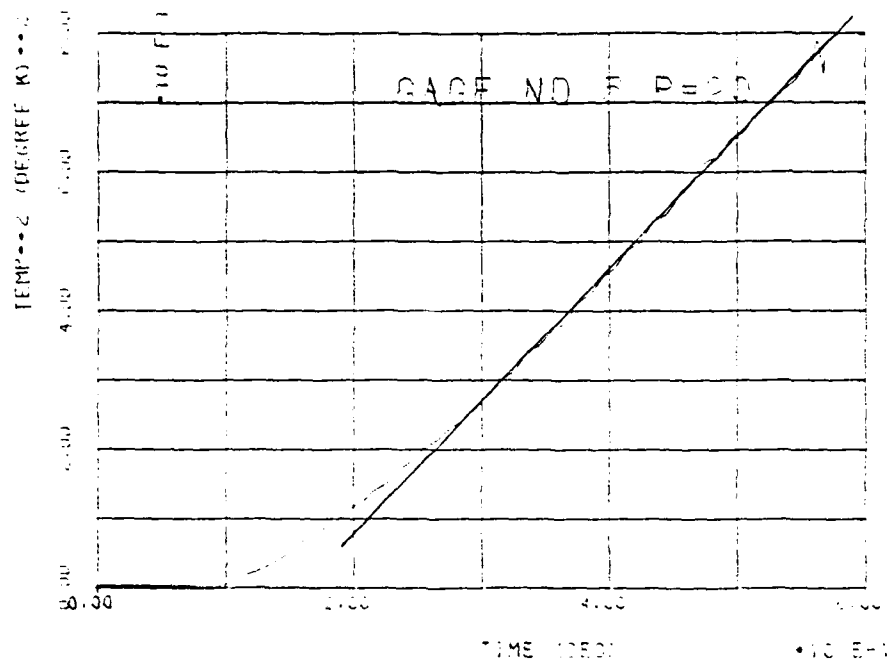
Figure 3.34.   Constant Heat Flux Assumption Verification
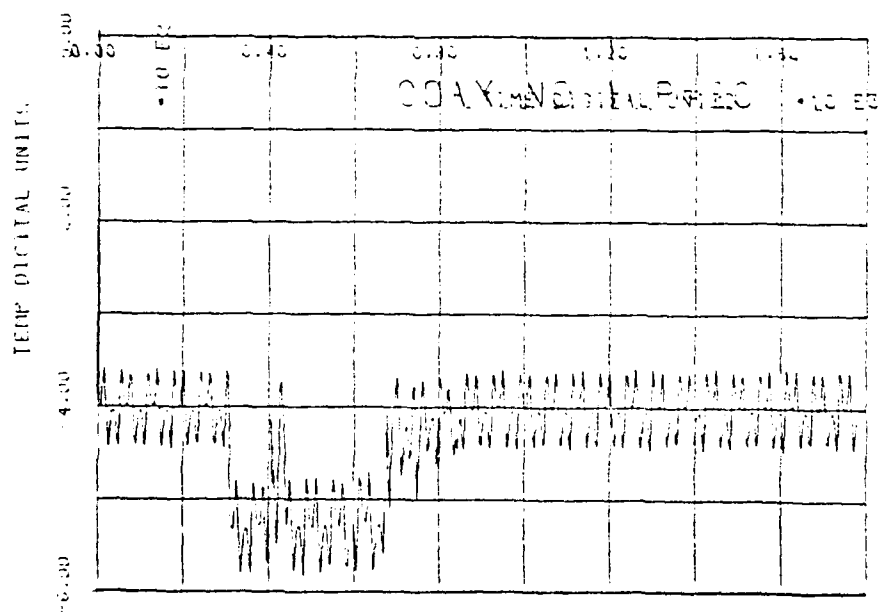
Figure 3.35.   Coax Gage #1, Re=1.69x10^7 /m, Po = 20 bar
Temperature versus Time
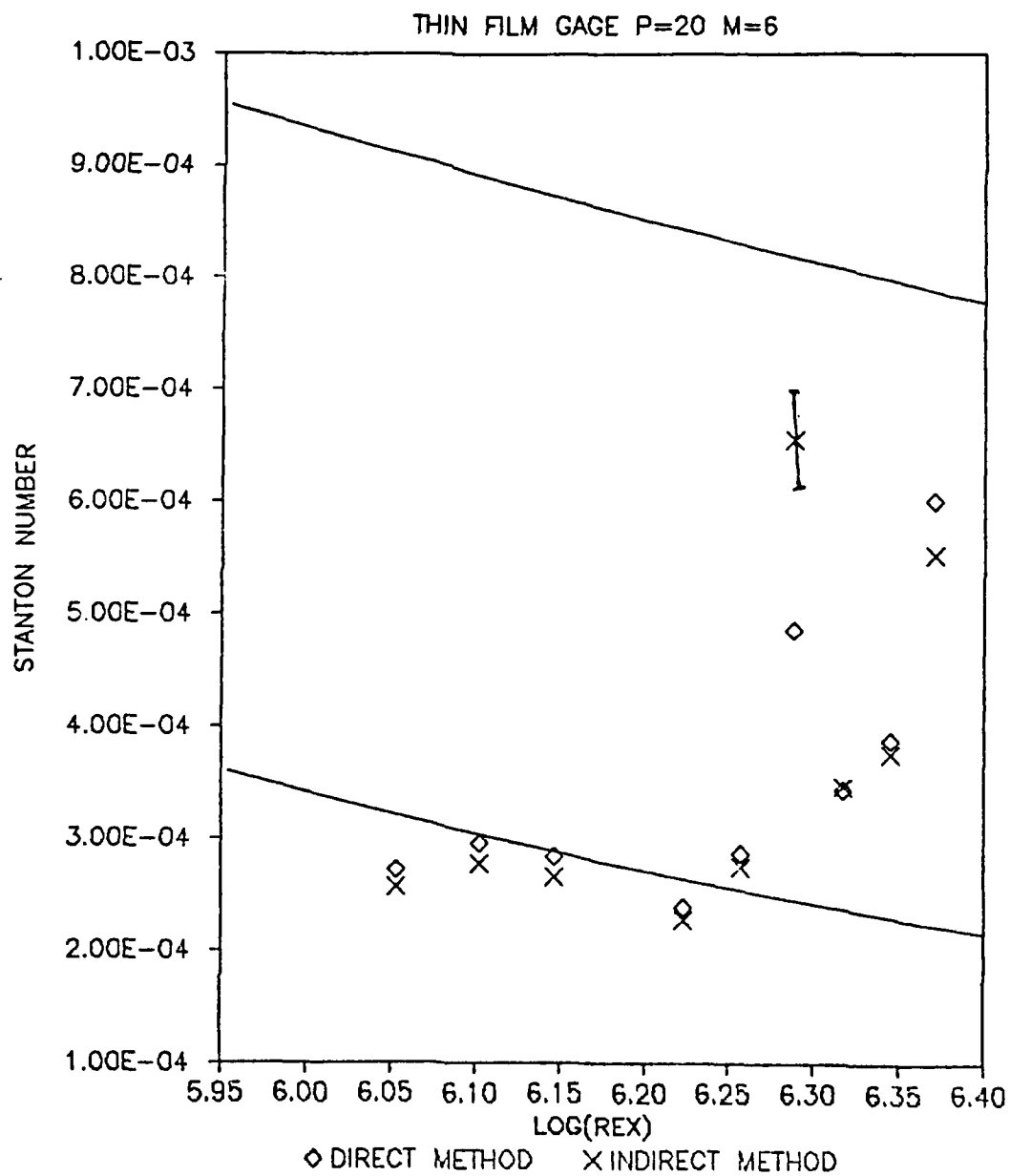
Figure 3.36.   Plate, Heat Transfer H-1, M=6, Re=1.69x10^{7} /m
               Stanton Number versus Log(Rex)

THIN FILM GAGE P=10 M=6
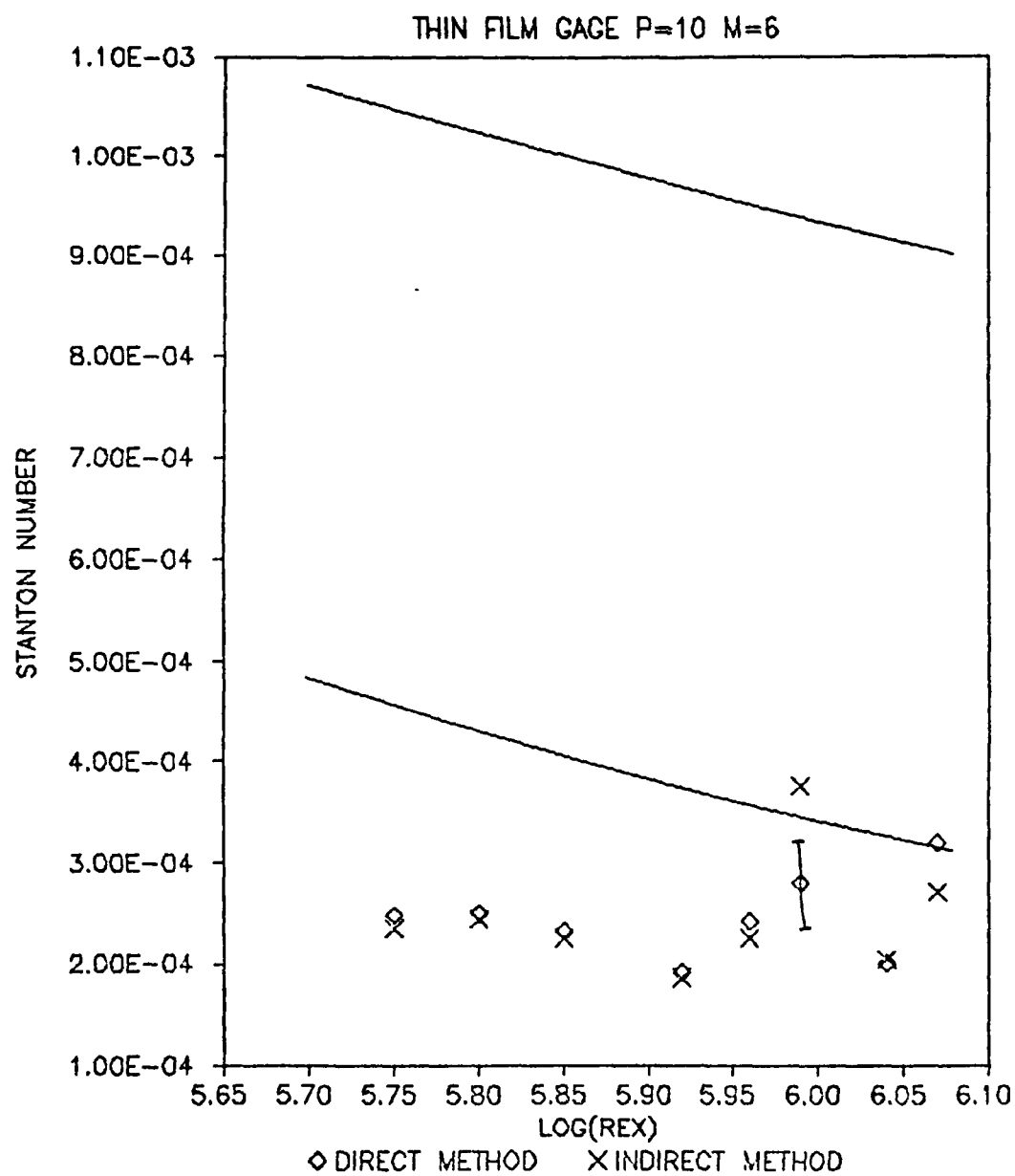
Figure 3.37.   Plate, Heat Transfer H-2, M=6, Re=.844x10^{7}/m
            Stanton Number versus Log(Rex)

3.8 Flow Interaction

At Mach numbers above 4, the most severe problems of atmospheric flight are associated with viscous-inviscid interactions (33:177). Cruise vehicles and lifting re-entry vehicles have highly complex, three-dimensional configurations in which exist many regions of high compression that can cause boundary layers to separate. The flow reattachment that follows this separation, causes a rise in heat rates that can far exceed those for an attached boundary layer. A possibly more serious viscous interaction problem is the impingement of shock waves generated by the forebody resulting in local heat rates that may be many times larger than stagnation point values. However, unlike stagnation point heating where the location is obvious, the problem with complex configurations is to determine where the high heat rates are likely to occur, as well as their magnitude.

This study will examine one viscous interaction problem area, that of flow interaction past a blunt fin. The interaction of the bow shock of a fin with the boundary layer on a plate can cause widespread separation and vorticity of a three-dimensional nature. Adjacent to the fin, parallel, finely spaced embedded vortices may form and cause striation heating. The embedded vortices produce highly localized heating rates that are significantly greater than heating in adjacent undisturbed areas. Oil

flow visualization tests were conducted to examine the
general structure of the flow interaction region.
Sublimation tests were conducted to determine the global
heating of the interaction area. The information obtained
by first employing sublimation, rather than heat transfer
gages, can be used to better determine where to locate those
thin film or coax gages in future tests.

3.8.1 Topological Rules

It has been postulated by Peake and Tobak (41) that all
cases of three dimensional flow separation and reattachment
can be described mathematically. Using

> "the assumption of continuous vector fields of skin
> friction lines and external flow streamlines, when
> coupled with simple laws of topology, provides a flow
> grammar"

which enables one to create plausible flow structures. The
elementary singular points of the flow field: nodes, spiral
nodes (foci), and saddlepoints, can be categorized
mathematically. Therefore,

> "the types of singular point, their number, and the
> rules governing the relations between them, can be said
> to characterize the pattern."

Figure 3.38 shows the structure of these elementary singular
points; the solid lines represent the skin friction lines
while the dashed lines represent the surface vortex lines
which are orthogonal at every point to the system of skin
friction lines.   By utilizing these ideas, mean flow
characteristics and flow mechanisms can be deduced when wind
tunnel results give insufficient information.

(a) Node.

(b) Spiral node

(c) Saddle.
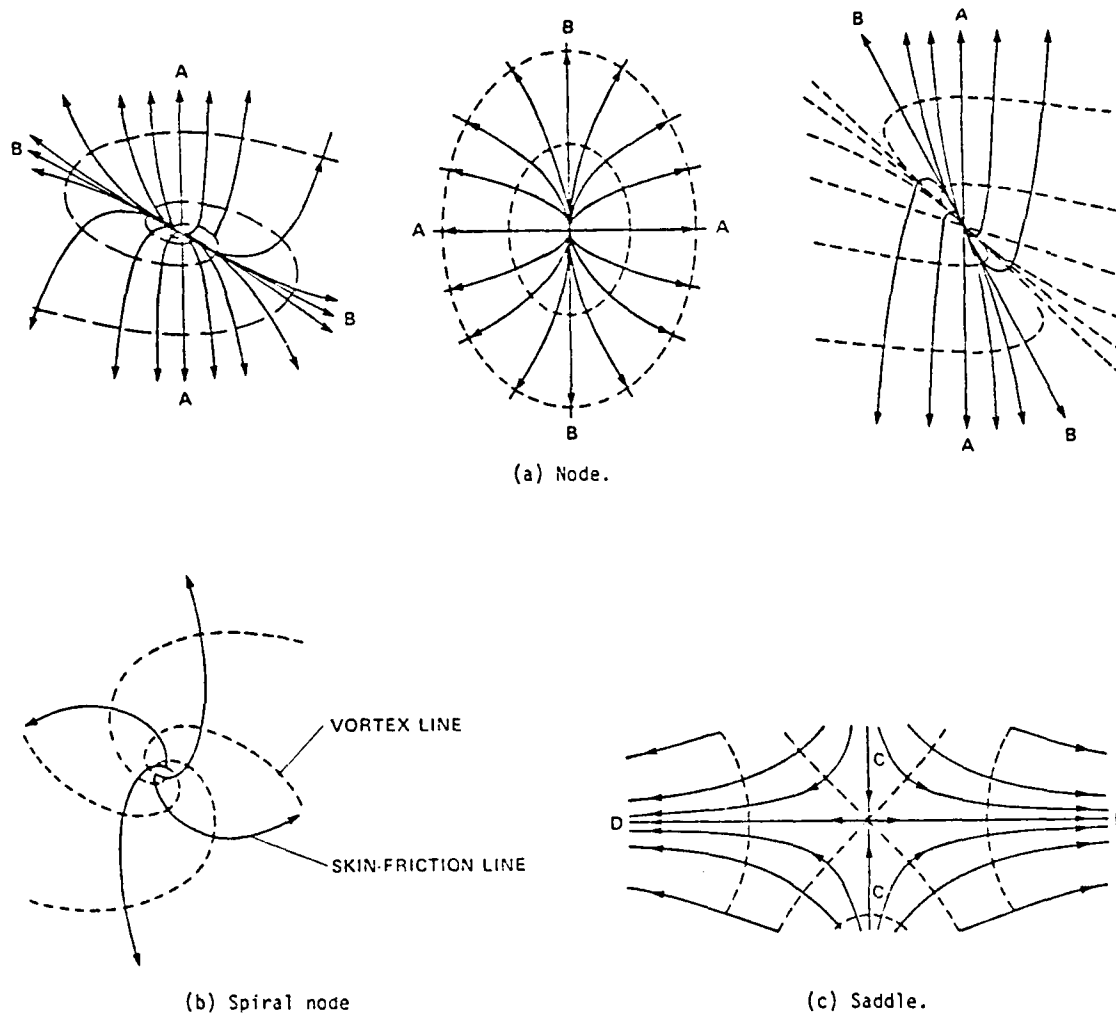
Figure 3.38. Singular Points

Peake and Tobak (41:1-5) list five special topological rules that apply to flow past wings and bodies at angle of attack. Of these five rules, only three could apply to the flow field in this study and are listed here:

1. Skin friction lines on a three dimensional body:

$$\Sigma_N - \Sigma_S = 2 \qquad (3.49)$$

2. Skin friction lines on a three-dimensional body B connected simply without gaps to a plane wall P that either extends to infinity both upstream and downstream or is the surface of a torus:

$$\left[\Sigma_N - \Sigma_S \right]_{P+B} = 0 \qquad (3.50)$$

3. Streamlines on a two dimensional plane cutting a three dimensional body:

$$\left[\Sigma_N + 1/2 \, \Sigma_{N'} \right] - \left[\Sigma_S + 1/2 \, \Sigma_{S'} \right] = -1 \qquad (3.51)$$

However, in terms of this study, more information is required before the method of topology can be really useful. Namely, the flow on the fin and the flow on the plate near the trailing edge of the fin needs to be studied to get an approximate picture of the entire three dimensional flow pattern before this method of using topological rules can be utilized.

3.8.2 Flow Ahead of the Fin

3.8.2.1 Flow Structure

High speed flow over a blunt fin on a surface results in a very complex, inviscid-viscid interaction flow field. The bow shock from the fin causes the boundary layer to separate from the surface ahead of the fin, resulting in a separated flow region composed of horseshoe vortices near the surface and a lambda-type shock pattern in the plane of symmetry ahead of the fin. Experiments completed by Kaufmann, Korkegi, and Morton (26:5) reveal that the separated flow is very unsteady. Shadowgraph photographs were blurry until the exposure time was decreased to times on the order of microseconds. This is attributed to a "pulsating, scavenging action of the horseshoe vortices" which results in large oscillations of the impinging shock wave.

Korkegi states that the characteristics of skewed shock induced separated regions (32:599) do not exhibit any basic differences between laminar and turbulent flow for comparable extents of separation. (However, the adverse pressure gradients needed for extensive separation, are much larger for turbulent than for laminar flow, and the detail of the flow structure differs because of turbulent mixing in one case and molecular mixing in the other.) Therefore, it is possible to define the structure of the separated flow region, resulting from the interaction of a skewed shock

wave with either a laminar or turbulent boundary layer. This reasoning, which is developed from separated regions induced by skewed shocks, is extended to separated regions induced by bow shocks.

One possible interaction flow field of a separated region induced by a fin bow shock is shown in Figure 3.39 (54:47). This flow field is proposed by Winkelman for turbulent flows and is similar to two dimensional separated flows ahead of steps or ramps. The pressure rise across the fin bow shock presents a strong adverse pressure gradient to the boundary layer flow on the flat plate surface, causing the boundary layer to separate from the surface and form a region of reverse flow adjacent to the plate surface. The effects of the pressure rise are propagated upstream through the reverse flow region. The reverse flow forms several horseshoe vortices in which the flow quickly curves downstream, away from the plane of symmetry (26:4). A nodal point of attachment is postulated to exist between the primary and secondary separation lines, or separated regions. The nodal point is indicated to be produced by adjacent regions of recirculating vortex flow. The reverse flow in the vortices is fed by the separated stream flow and spirals downstream very rapidly. Severe heating rates are
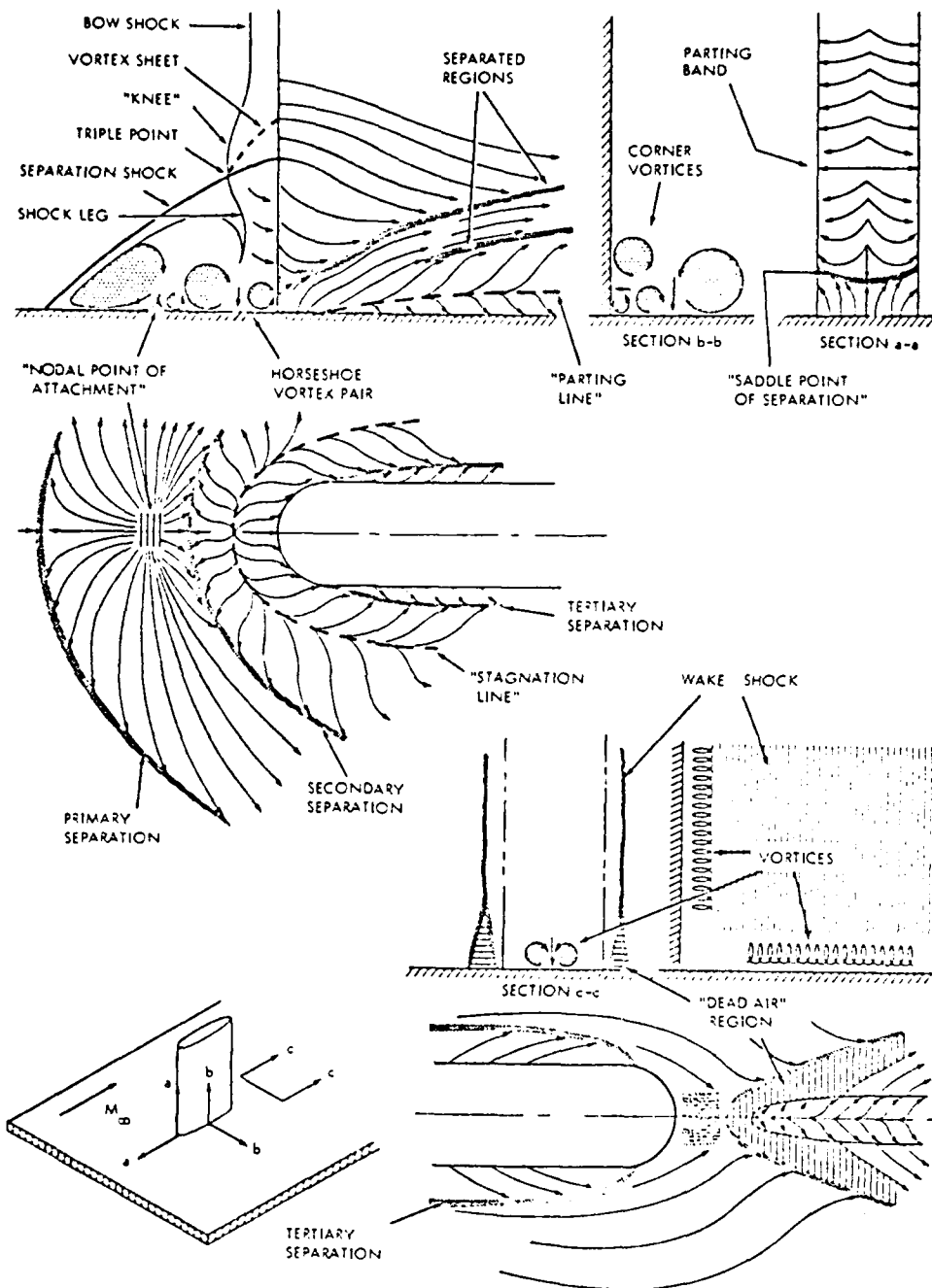
Figure 3.39. Flow Interaction Model

caused by these vortices bringing high energy air flow into close proximity with the surface. This has been shown experimentally in that the heat transfer rates are shown to peak at reattachment regions following a region of separation. In a skewed shock interaction (32:599) in laminar flow, Figure 3.40, Korkegi shows that the two peaks in the heat transfer rate are associated with the two reattachment lines, denoted by R, in the flow interaction region.
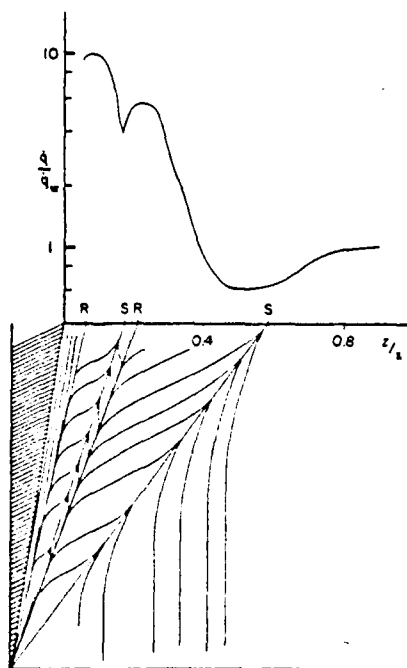
Figure 3.40. Spanwise Heat Transfer for Laminar Flow
M = 20, Wedge Angle = 10°

3.8.2.2 Separation Distance

The separation distance upstream of a fin leading edge is found to scale with fin diameter for conditions when the

fin is slender, is at zero degree incidence, and its diameter is larger than the boundary layer thickness (55:31). As in two dimensional flow, this distance is considerably greater for laminar than for turbulent flow (30:361). For laminar flow, this separation distance is Mach number and Reynold's number dependent. Limited data indicate that the extent of entirely laminar separation ahead of a fin increases with increasing Reynold's number. Laminar separation lengths exceeding six diameters have been observed (55:24) for both Mach 3 and Mach 5 flows.

However, separation is a strong disturbance to a laminar boundary layer and causes earlier transition than for attached undisturbed boundary layers. In this case, transition can occur either ahead of the separated location (turbulent separation) or in the free shear layer bounding the reverse flow region ahead of the fin (transitional separation). The extent of transitional separation diminishes toward the turbulent value as the separation location approaches the undisturbed boundary layer transition location, as can be seen in Figure 3.41 (26:25).

For turbulent flow, the separation distance appears to be insensitive to Reynold's number. The magnitude of the separation distance is usually twice the diameter of the fin, for cases when the fin diameter is larger than the boundary layer thickness.
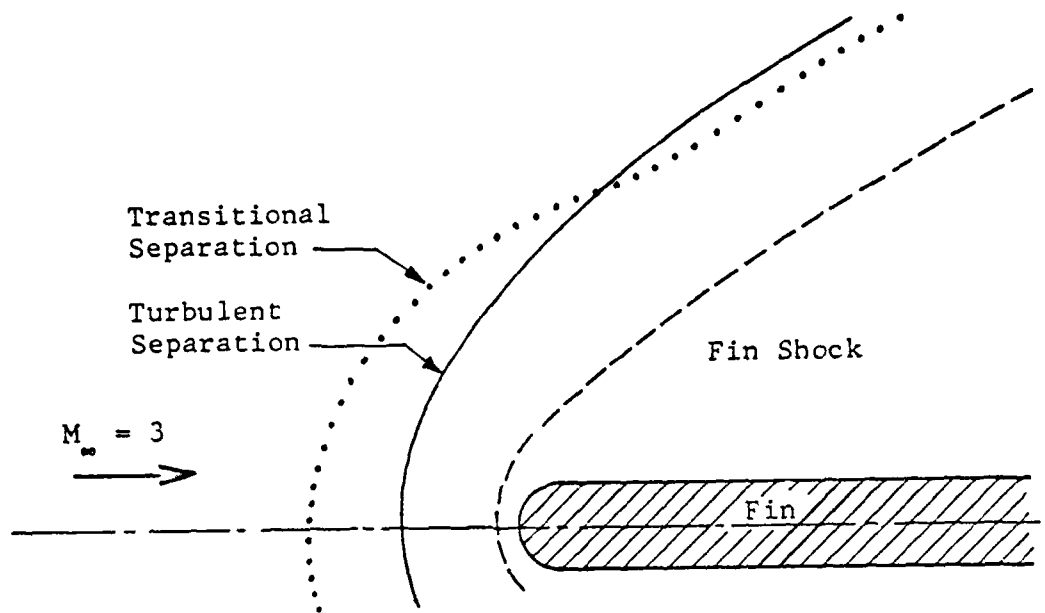
Figure 3.41. Transitional and Turbulent Separation
Line Shapes

The effect of leading edge sweep on the extent of the
interaction has been investigated by Price and Stalling (43)
for supersonic turbulent flow. They find that for sweep
angles from 0° to 30° there is a sharp decrease in extent of
separation, but no change in the first peak pressure. For
larger sweep angles, both decrease until they are barely
perceptible at 75°.

For a fin incidence angle of 10° (6:698), Reynold's
number affects both the scale of the separation and the
surface streamline patterns aft of the separation. Placing

the fin at an incidence of 10° also resulted in a region of increased heat transfer which originated near the leading edge and extended the length of the fin.

Price and Stalling (43) have studied the effect of fin height on turbulent flows past protuberances. Their results were a little surprising in that they found no difference in leading edge separation distances when the fin height varied for lengths smaller than the boundary layer height to many times the extent of the boundary layer.

3.8.3 Embedded Vortices

Striation heating is attributed to streamwise vortex formations embedded in the boundary layer which produce locally enhanced heating levels. Persen (28:1) has suggested that the formation of the embedded vortex system

> "is connected with the stability of curved flow, ie.,
> flows where the streamlines are non-parallel, exhibit a
> curvature, a pressure gradient and a velocity
> gradient."

No agreement exists on a universal explanation of regularly spaced streamwise embedded vortices, but several mechanisms have been identified by researchers. One of these mechanisms produce what is known as Goertler vortices. Schlicting (46:526,532-535) describes these streamwise vortices which can occur in boundary layer flow over concave walls. In such boundary layers, the fluid particles near the wall experience a lower centrifugal force than those nearer the boundary layer edge. Such flows are inherently unstable and provide a mechanism for transition from laminar

to turbulent boundary layer flow. When a critical Reynold's number is exceeded, small disturbances will amplify and form a system of streamwise vortices within the boundary layer, as shown in Figure 3.42.
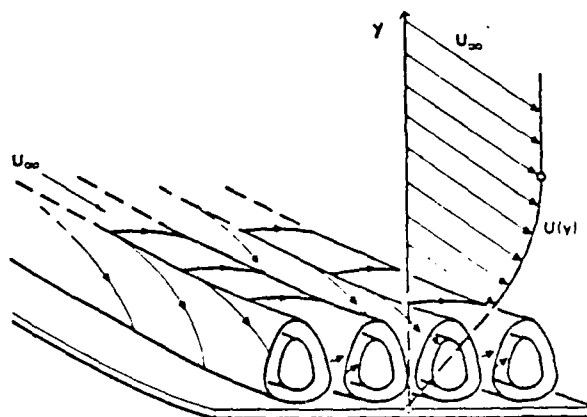
Figure 3.42. Goertler Vortices

It has been suggested by Kipp and Helms (28:3) that a separation bubble resulting from a shock - boundary layer interaction can cause a concave turning of the boundary layer flow, thereby initiating Goertler vortices.

3.9 Results of the Flat Plate with Blunt Fin Study

Table 3.10 shows the test conditions for all the photographs included in this report for tests completed on the flat plate with the blunt fin. Appendix S shows the test conditions and VKI photograph catalog number for every test completed.

Table 3.10. Flat Plate with Fin Test Conditions

Test	P_o (Bars)	Re -7 (x10) (/m)	Fin Incidence $\emptyset$ (degrees)	Fin Sweep Ω (degrees)	Fin Height h (mm)
WO-1, WS-1	10	0.844	15	0	6
WO-2, WS-2	10	0.844	15	30	6
WO-3, WS-3	20	1.69	15	30	6
WO-4, WS-4	10	0.844	15	60	8
WO-5, WS-5	10	0.844	-15	75	8
WO-6, WS-6	10	0.844	40	0	6
WO-7, WS-7	10	0.844	40	30	6
WO-8, WS-8	10	0.844	40	60	8
WO-9, WS-9	10	0.844	40	75	8
WO-10, WS-10	10	0.844	40	0	15
WO-11	20	1.69	0	0	6
WO-12	20	1.69	0	0	15
WO-13	20	1.69	15	0	6
WO-14	10	0.844	15	0	15

where   WO - Oil flow test
        WS - Sublimation flow test

Table 3.11 shows the fin heights nondimensionalized with the undisturbed boundary layer height which was shown in Table 3.5.

Table 3.11. Nondimensional Fin Height

	h=6mm	h=8mm	h=15mm
Re=1.69×10^7 /m, Po=20 bar	12	16	30
Re=$.844 \times 10^7$ /m, Po=10 bar	20	26	50

3.9.1 Shadowgraph Results

The shadowgraph results were very blurry and did not give very much detailed information. For future studies on a flat plate model, it may be better to use single-pass shadowgraph/schlieren. Since the model is essentially two dimensional, the photographs are too blurry due to the "double" exposure of the double-pass system. Another factor contributing to the blurriness of the photographs was the time of exposure. Previous studies have shown that the three dimensional flow interaction is so unsteady that it requires exposure times on the order of microseconds. The photographs in this study had an exposure time of 10 milliseconds.

However, the photographs did show that the shock originating from the separation region did not impinge on the fins of 0° sweep and 6 mm in height. It is possible that the flow structure on the plate could change if the fin was made taller and a shock impingement on the fin occurred.

3.9.2 Oil Flow and Sublimation Results

Several photographs of the results from oil flow and sublimation tests are shown in Figures 3.43 through 3.66. The oil flow photographs were taken after the tunnel was stopped and accurately represent the oil flow pattern in the tunnel during the tests except for some oil splattering and spreading of accumulation lines.

In the interaction oil flow photographs of the fins with zero sweep, there appears to be a "bump" present in the secondary separation line, as shown for example in Figure 3.48. This bump is a real phenomena, as its appearance is repeatable. This bump is not really evident in the sublimation photographs. No similar bump was found in a review of the limited references of blunt fin interaction in laminar flow. This bump does not appear to be caused by fin height, as can be seen in a comparison of Figures 3.43 and 3.44. Since a sign of early transition caused by the separated flow occurs on the primary separation line, (refer to Figure 3.41 and section 3.8.2.2), this bump does not indicate early transition since it occurs on the secondary separation line. The bump moves downstream (becomes less noticeable) as the Reynolds number increases, as can be seen in Figures 3.44 and 3.48. It is evident only on the expansion side of the fin when the fin is at incidence. The cause of the bump could be an interaction between the vortices on either side of the secondary separation line, the bump being produced when the vortex closer to the fin is stronger than the other vortex and dominates over the weaker vortex's flow area.

The separation distance ahead of the fin, l, non-dimensionalized with the fin diameter, d, is plotted against the Reynold's number based on the distance from the plate leading edge to the separation line, in Figures 3.67 through

3.69. The figures show the l/d distance for a fin incidence of 0, 15, and 40°. The separation distance is measured from the fin leading edge to the middle of the primary separation line or region. The errors in these measurements vary according to the amount of oil spreading that occurred on the primary separation line. For the short fin height at 0 and 15° incidence, the error corresponds to ±.2 l/d or 4%. At 40° incidence and for all the h=15 mm tests, the error corresponds to ±.3 l/d or 5%. A trend that is apparent is that the separation distance increases as the sweep angle is decreased. This is in agreement with the results found by Price and Stallings (43). A Reynolds number dependence on separation distance could not be determined from the oil flow photographs.

There appears to be no effect of fin height on the separation distance for zero sweep as shown in Figures 3.67 and 3.68, for incidence angles of 0 and 15°. This is also shown in the oil flow photographs, Figures 3.42 and 3.44, for 0° incidence. Another effect of fin height can also be seen in these figures. The secondary separation line is much blunter ahead of the fin leading edge for the taller fin. This bluntness can a'   be seen in Figure 3.48. For a fin incidence angle of 40°, there is a strong effect of fin height for the heights studied in this test, the separation distance increased dramatically when the fin height was increased from 6 to 15 mm, as can be seen in Figure 3.69.

The oil flow/sublimation photographs, Figures 3.45/3.46 and 3.59/3.60, compare the effect of fin height for a fin of 40° incidence and zero sweep. The flow patterns are also very different. In the h = 6 mm case, four reattachment regions are apparent. However, if the height of the fin is increased, there are only three reattachment regions. It is hypothesized that the flow passing over the fin combines with the vortices forming the second reattachment region causing an instability, thereby causing an additional vortex pair to form another reattachment region.

Changing the Reynolds number appears to have some effect on the flow patterns, other than increasing the separation distance. The main difference is the change of the "bump" and this can be seen by comparing the oil flow photographs, Figures 3.44 and 3.48, and 3.47 and 3.50. Slight differences in the flow structure can be seen in the oil flow photographs but the corresponding sublimation photographs do not show the same detail.

Kipp and Helms (28:8) show an example of striation heating caused by embedded vortices on the side fuselage of a Space Shuttle orbiter model during a thermal mapping wind tunnel test. (Kipp and Helms reference their Reynolds number to a characteristic length.) The striations were not present at Mach 10, $Re_{\infty} = 2.4 \times 10^6$ and $\alpha = 20°$, but the streaks appeared when the angle of attack was increased to 40°. Striations also appeared at Mach 6, $Re_{\infty} = 2.7 \times 10^6$ and

$\alpha = 40°$ and increasing the Reynold's number at Mach 6 to $Re_\infty = 7.3x10^6$ resulted in a larger number of striations. These streaks from Kipp and Helms (28) look very similar to the streaks shown in Figure 3.66 which were produced in a similar test regime of Mach 6, $Re_\infty = 8.66x10^6$, fin sweep angle of 75° and a fin incidence angle of 40°. Figure 3.64 also shows that the streaks begin to appear when the fin sweep is 60°. However, when the fin is at an incidence angle of 15°, there is no indication of striation heating at sweep angles of 60 or 75°, as can be seen in Figures 3.56 and 3.58.

3.9.3 Proposed Flow Interaction Models

Possible models for the flow interaction region have been developed from the oil flow and sublimation photographs. The details of the models are dependent upon the fin incidence and fin sweep. The models are sketched in Figures 3.70 through 3.74. The models are characterized by a nodal point of attachment and counter-rotating vortex pairs that create the alternating regions of separation and reattachment.
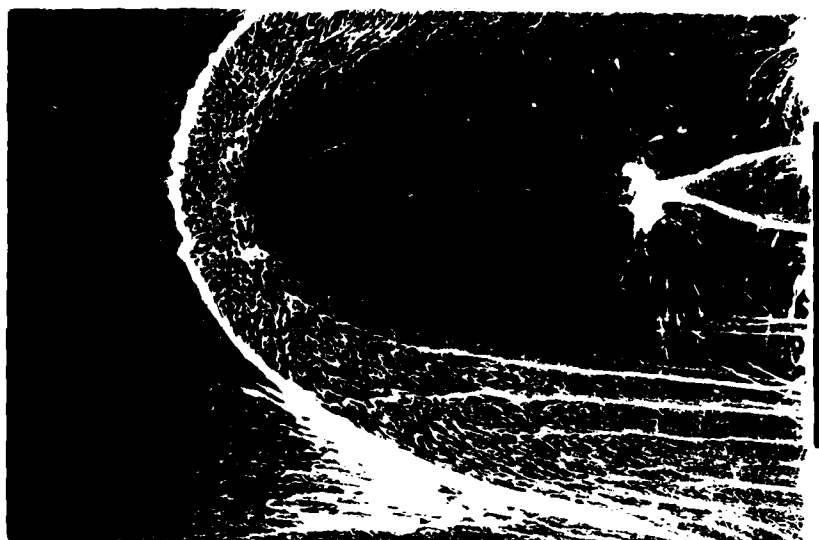
Figure 3.43. Fin, Oil Flow Test WO-11, M=6, Re=1.69x10^7 /m, $\emptyset$ = 0°, Ω = 0°, h/δ = 20, h = 6 mm

Figure 3.44. Fin, Oil Flow Test WO-12, M=6, Re=1.69x10^7 /m $\emptyset$ = 0°, Ω = 0°, h/δ = 50, h = 15 mm

Figure 3.45. Fin, Oil Flow Test WO-10, M=6, Re=.844x10^7/m
$\emptyset = 40°$, $\Omega = 0°$, $h/\delta = 30$, $h = 15$ mm

Figure 3.46. Fin, Sublimation Test WS-10, M=6, Re=.844x10^7/m
$\emptyset = 40°$, $\Omega = 0°$, $h/\delta = 30$, $h = 15$ mm
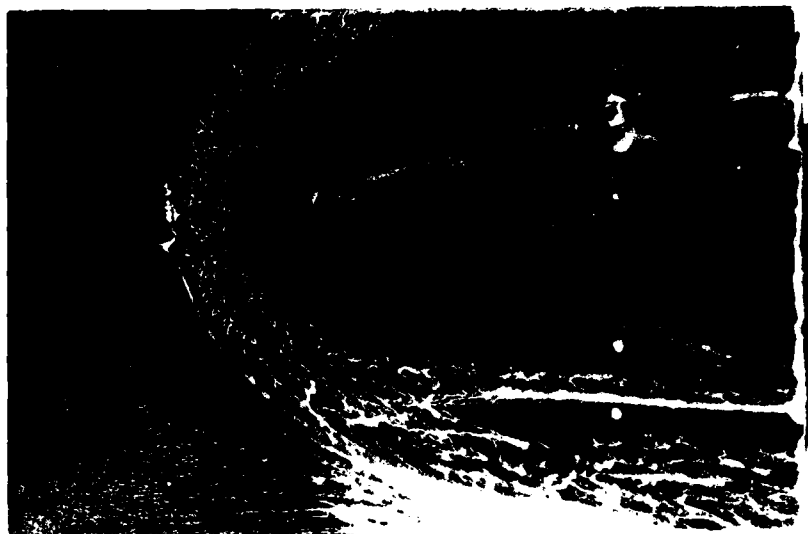
Figure 3.47. Fin, Oil Flow Test WO-13, M=6, Re=1.69x10^7/m
Ø = 15°, Ω = 0°, h/δ = 20, h = 6 mm
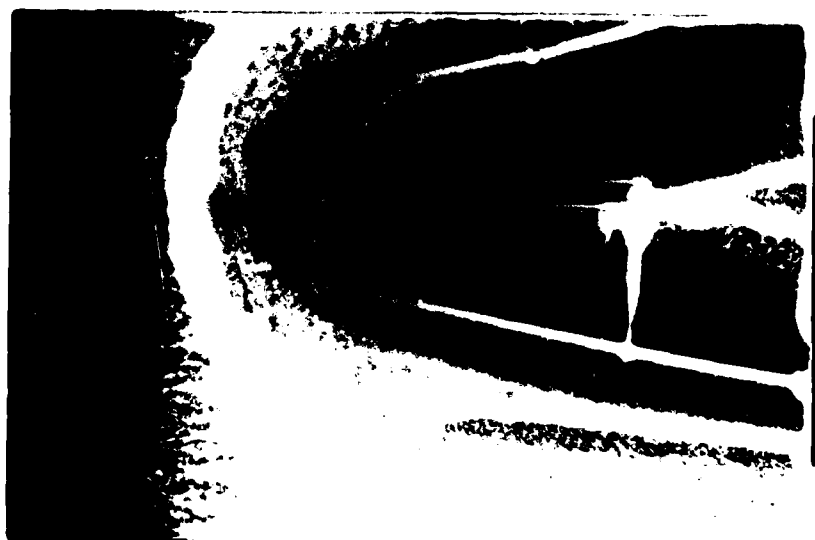
Figure 3.48. Fin, Oil Flow Test WO-14, M=6, Re=.844x10^7/m
Ø = 0°, Ω = 0°, h/δ = 30, h = 15 mm
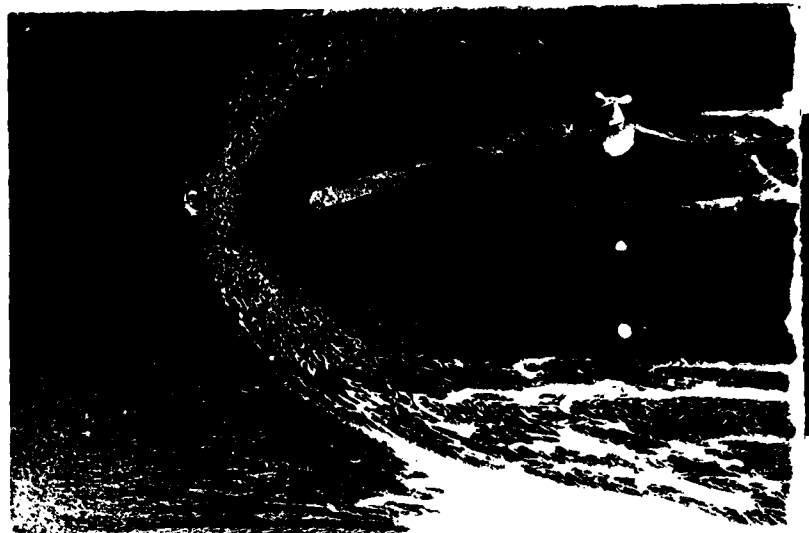
Figure 3.49.   Fin, Oil Flow Test WO-1, M=6, Re=.844x10^7 /m
Ø = 15°, Ω = 0°, h/δ = 12, h = 6 mm

Figure 3.50.   Fin, Sublimation Test WS-1, M=6, Re=.844x10^7 /m
Ø = 15°, Ω = 0°, h/δ = 12, h = 6 mm
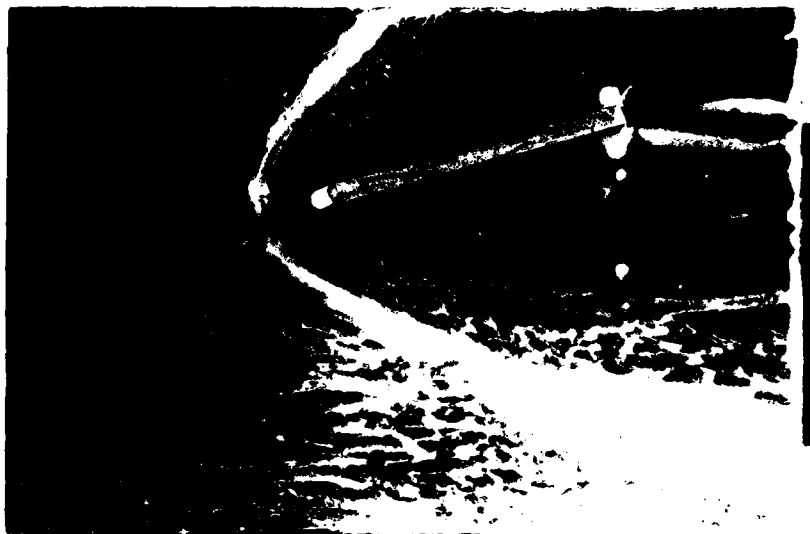
Figure 3.51. Fin, Oil Flow Test WO-2, M=6, Re=.844x10^7 /m
Ø = 15°, Ω = 30°, h/δ = 12, h = 6 mm

Figure 3.52. Fin, Sublimation Test WS-2, M=6, Re=.844x10^7 /m
Ø = 15°, Ω = 30°, h/δ = 12, h = 6 mm
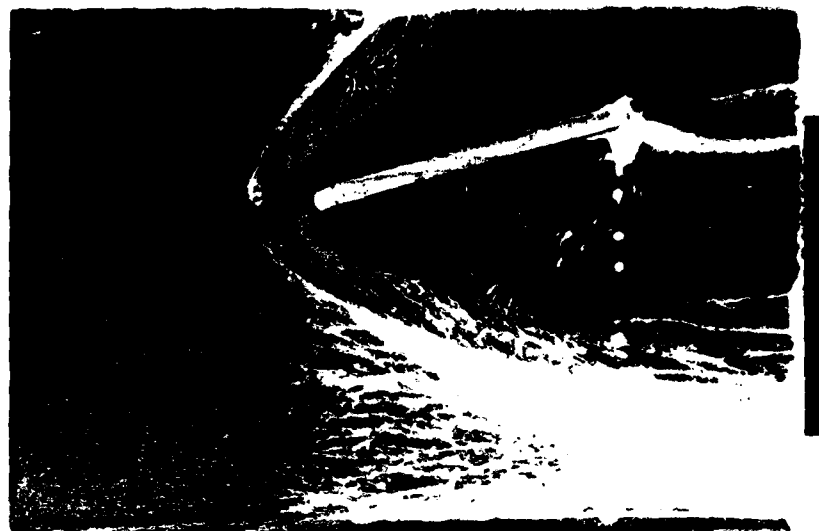
Figure 3.53. Fin, Oil Flow Test WO-3, M=6, Re=1.69x10^7/m
$\emptyset = 15°$, $\Omega = 30°$, $h/\delta = 20$, $h = 6$ mm

Figure 3.54. Fin, Sublimation Test WS-3, M=6, Re=1.69x10^7/m
$\emptyset = 15°$, $\Omega = 30°$, $h/\delta = 20$, $h = 6$ mm

Figure 3.55.   Fin, Oil Flow Test WO-4, M=6, Re=.844x10^7/m
$\emptyset$ = 15°, Ω = 60°, h/δ = 16, h = 8 mm

Figure 3.56.   Fin, Sublimation Test WS=4, M=6, Re=.844x10^7/m
$\emptyset$ = 15°, Ω = 60°, h/δ = 16, h = 8 mm

Figure 3.57.   Fin, Oil Flow Test WO-5, M=6, Re=.844x10^{7} /m
Ø = 15°, Ω = 75°, h/δ = 16, h = 8 mm

Figure 3.58. Fin, Sublimation Test WS-5, M=6, Re=.844x10^{7} /m
Ø = 15°, Ω = 75°, h/δ = 16, h = 8 mm

Figure 3.59.   Fin, Oil Flow Test WO-6, M=6, Re=.844x10^7/m
Ø = 40°, Ω = 0°, h/δ = 12, h = 6 mm

Figure 3.60. Fin, Sublimation Test WS-6, M=6, Re=.844x10^7/m
Ø = 40°, Ω = 0°, h/δ - 12, h = 6 mm

Figure 3.61.   Fin, Oil Flow Test WO-7, M=6, Re=.844x10^7/m
Ø = 40°, Ω = 30°, h/δ = 12, h = 6 mm

Figure 3.62.   Fin, Sublimation Test WS-7, M=6, Re=.844x10^7/m
Ø = 40°, Ω = 30°, h/δ = 12, h = 6 mm

Figure 3.63. Fin, Oil Flow Test WO-8, M=6, Re=.844x10^7/m
$\emptyset = 40°$, $\Omega = 60°$, $h/\delta = 16$, $h = 8$ mm

Figure 3.64. Fin, Sublimation Test WS-8, M=6, Re=.844x10^7/m
$\emptyset = 40°$, $\Omega = 60°$, $h/\delta = 16$, $h = 8$ mm

Figure 3.65. Fin, Oil Flow Test WO-9, M=6, Re=.844x10^7/m
Ø = 40°, Ω = 75°, h/δ = 16, h = 8 mm
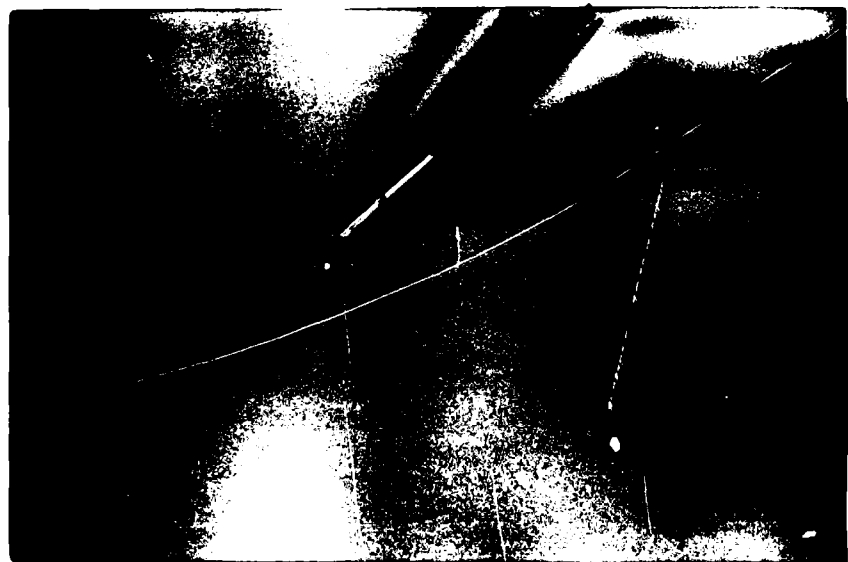
Figure 3.66. Fin, Sublimation Test WS-9, M=6, Re=.844x10^7/m
Ø = 40°, Ω = 75°, h/δ = 16, h = 8 mm

Separation Distance

□ 0 Sweep, h = 6 mm   + 0 Sweep, h = 15 mm
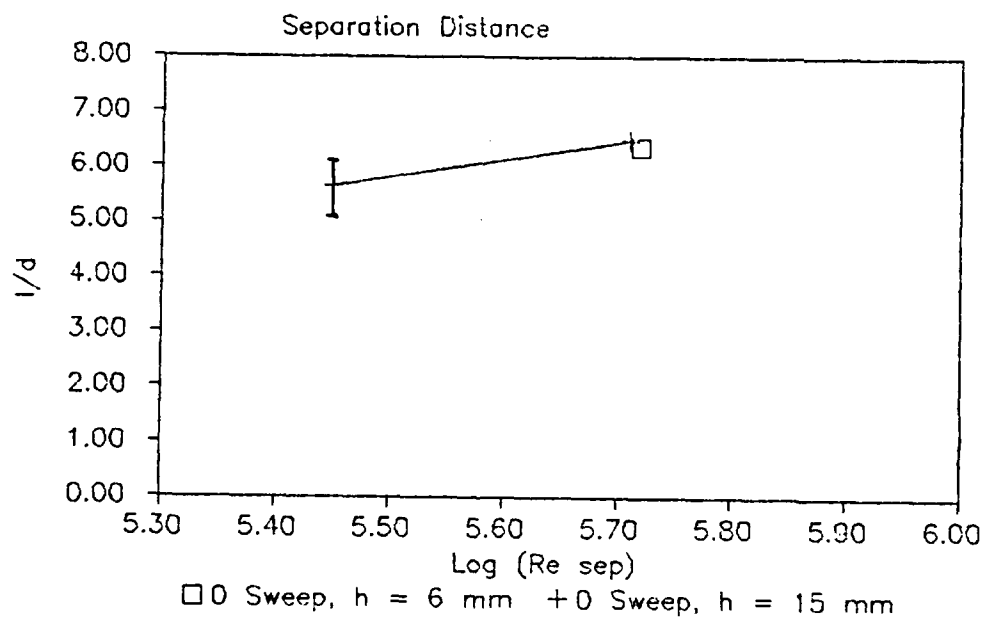
Sweep Angles

Figure 3.67.   Separation Distance, Ø = 0°
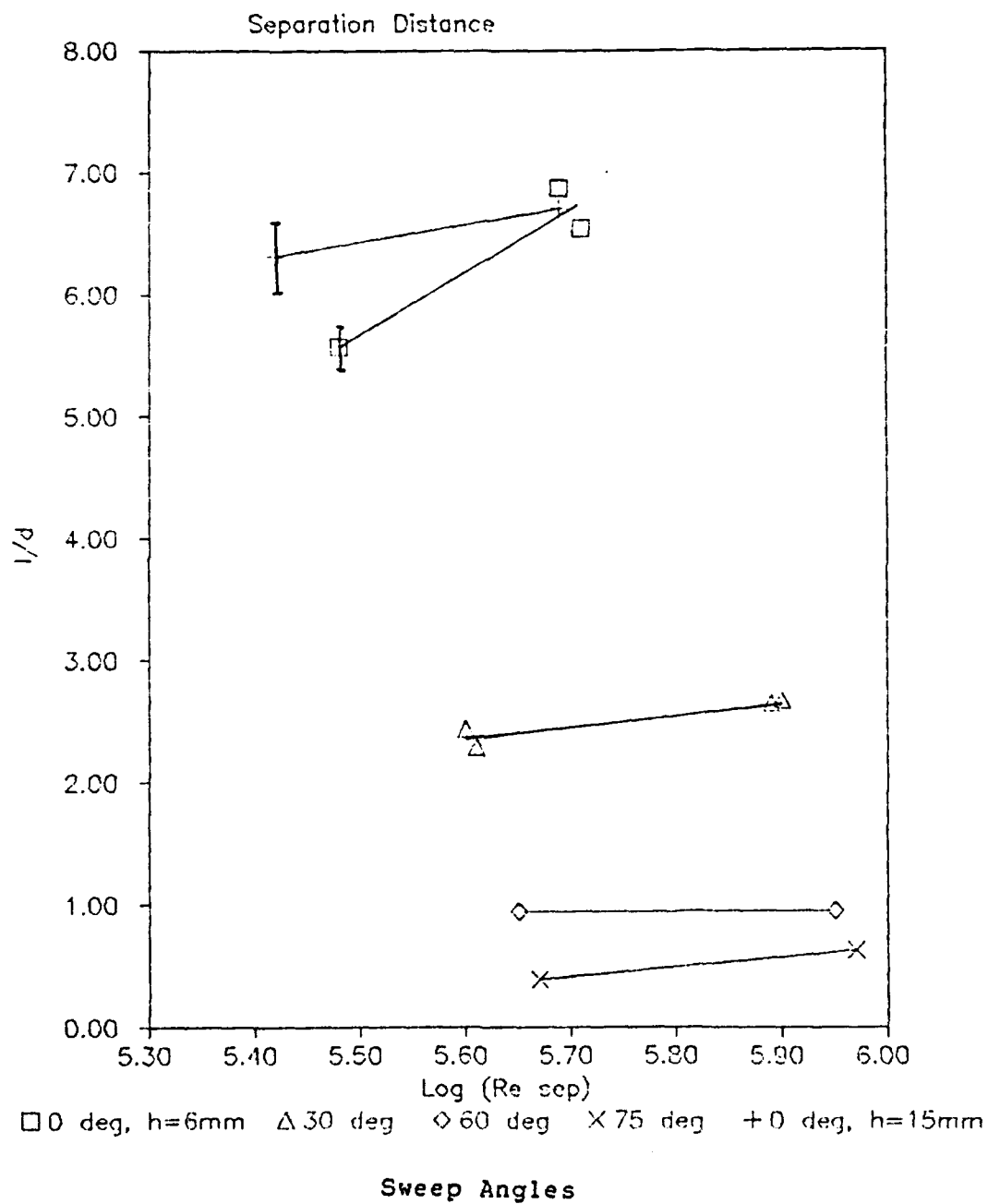
Figure 3.68. Separation Distance, $\emptyset = 15°$
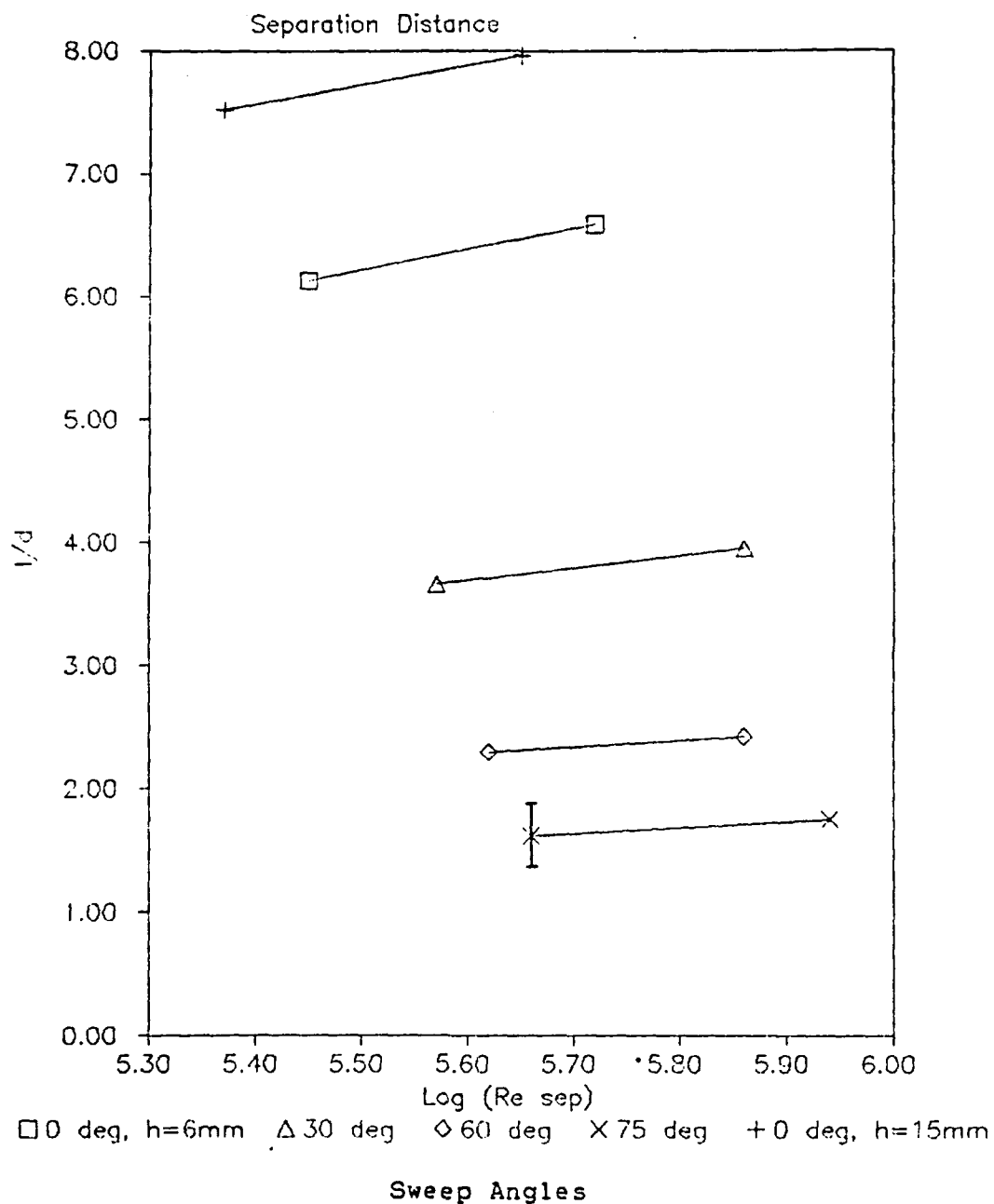
Figure 3.69. Separation Distance, $\emptyset$ = 40°
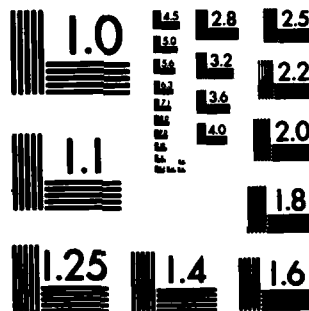
MICROCOPY RESOLUTION TEST CHART
NATIONAL BUREAU OF STANDARDS-1963-A
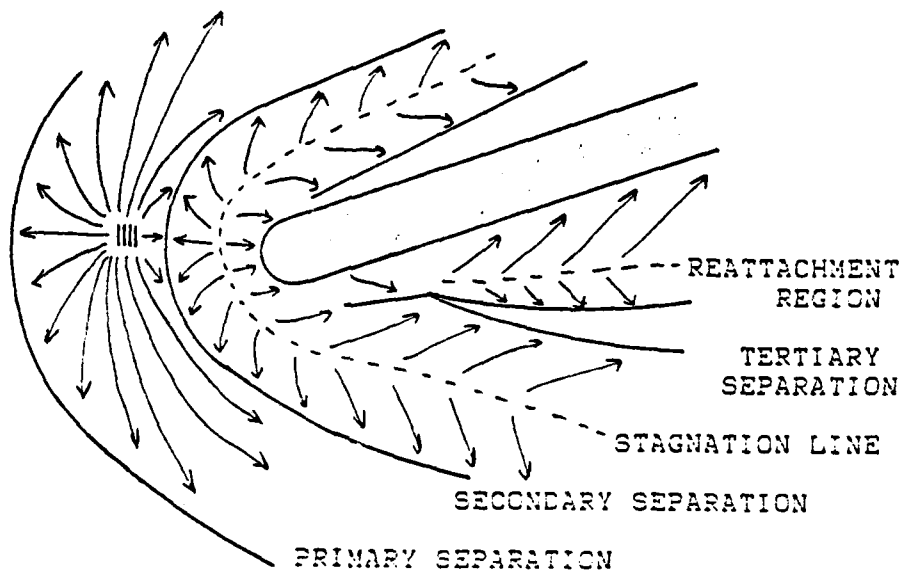
Figure 3.70.   Flow Interaction Model, Ø = 15°,
Ω = 0, 30, 60°
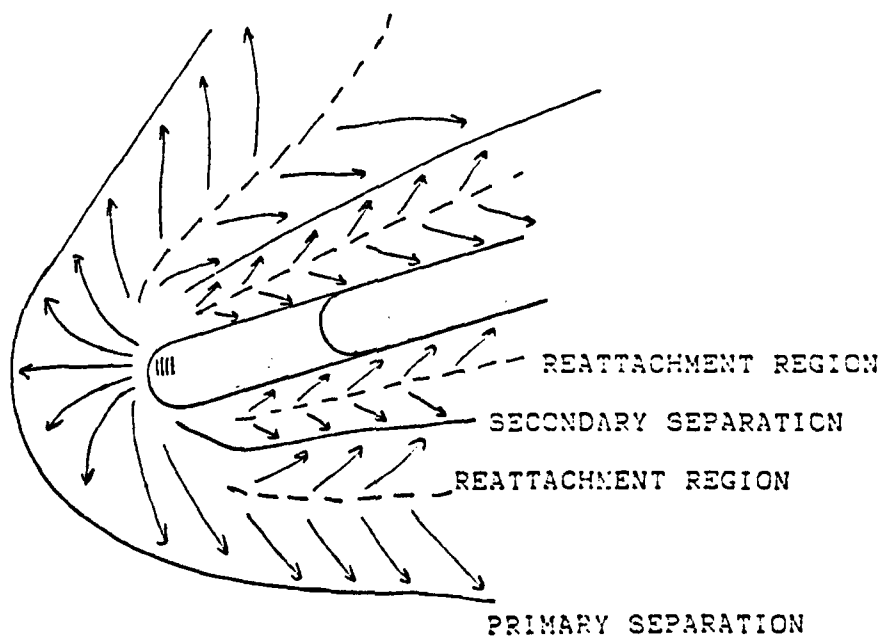
Figure 3.71.   Flow Interaction Model, Ø = 15°, Ω = 75°

REATTACHMENT
REGION

4th SEPARATION

REATTACHMENT
REGION

TERTIARY
SEPARATION

REATTACHMENT REGION

SECONDARY SEPARATION

PRIMARY SEPARATION
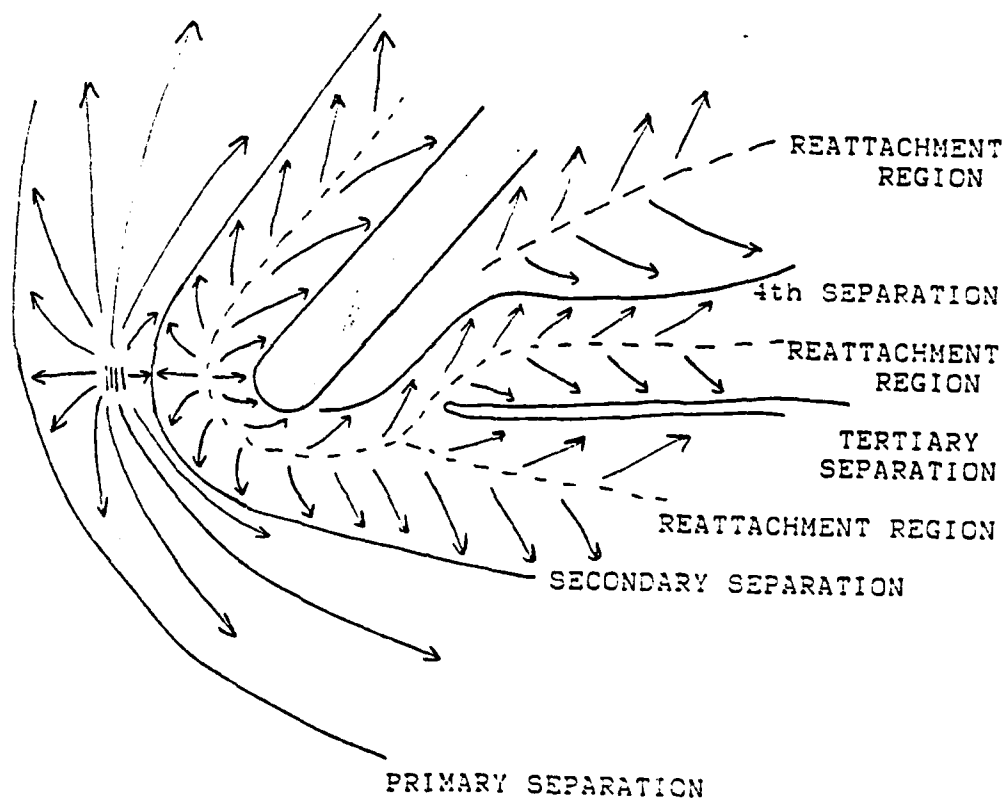
Figure 3.72. Flow Interaction Model, $\emptyset = 40°$, $\Omega = 0$, $30°$
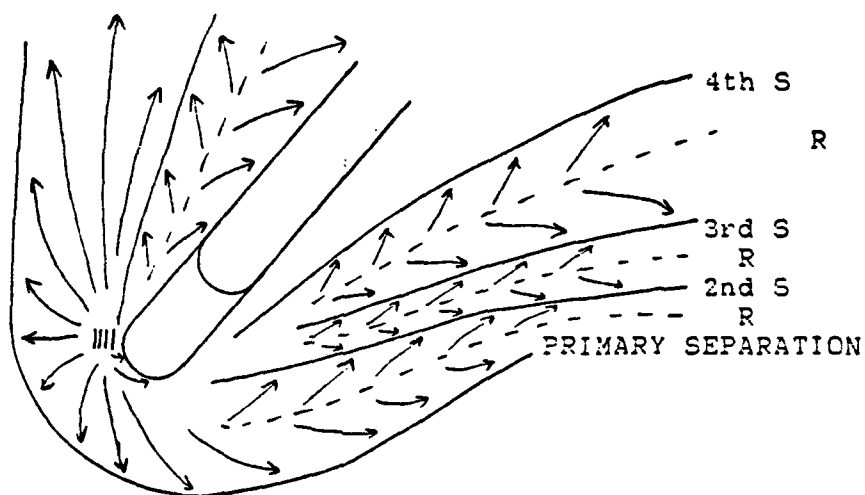
Figure 3.73. Flow Interaction Model, Ø = 40°, Ω = 60°
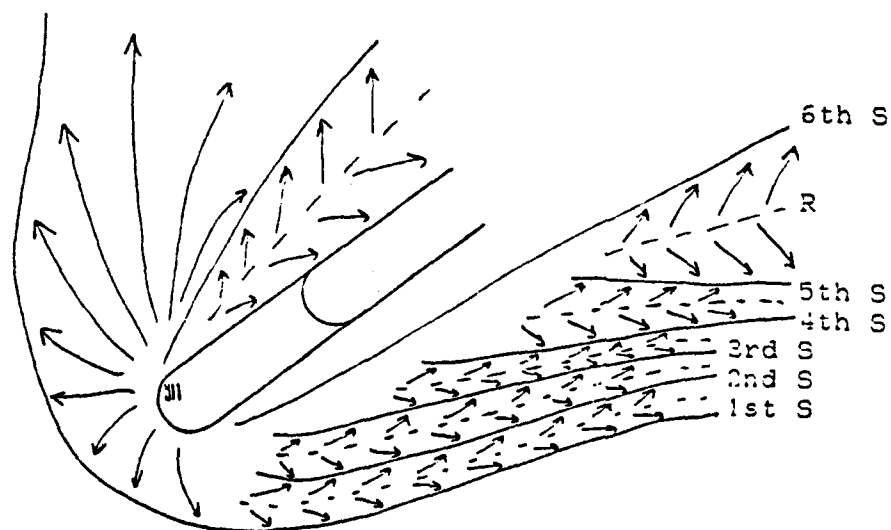
Figure 3.74. Flow Interaction Model, Ø = 40°, Ω = 75°

IV. Overall Results

The experimental flat plate data obtained from this study are compared to the results of the thesis computer program. The results from the numerical code are for the fully laminar case. The comparisons are completed for two Reynolds numbers, $.844 \times 10^7$/m and 1.69×10^7/m, and are shown in Figures 3.75 and 3.76, respectively.

The lower Reynolds number comparison, Figure 3.75, shows the experimental data differing 20% with the numerical results. The liquid crystals being 20% high and the thin film gage being 20% low. The results from the higher Reynolds number case, Figure 3.76, agrees much better with the numerical code. This is in part due to the higher signal that is recorded at the higher Reynolds number.

Figure 3.75. Experimental and Numerical Comparison
Mach = 6, P = 10 bar, Re = .844x10^{7}/m
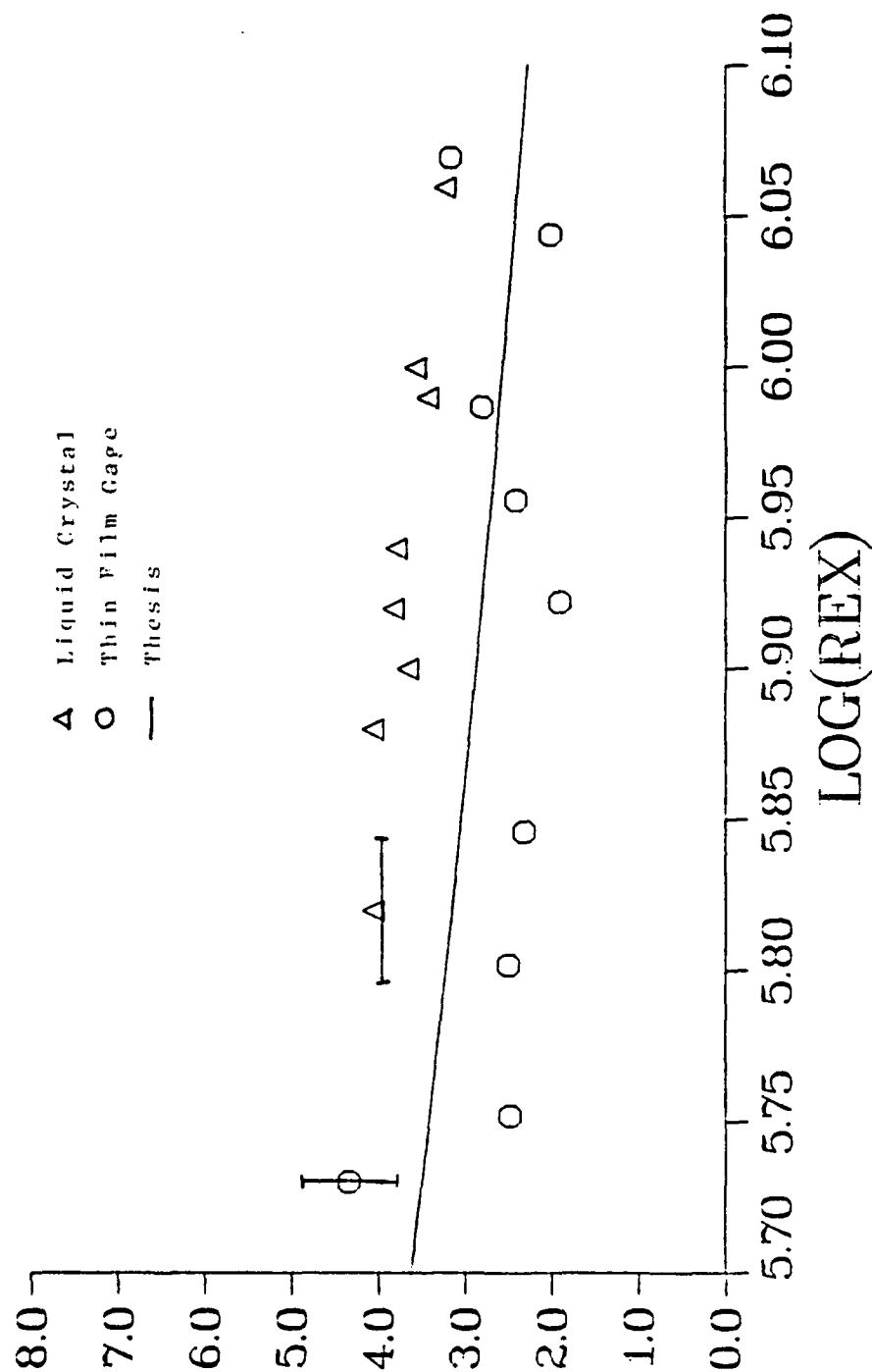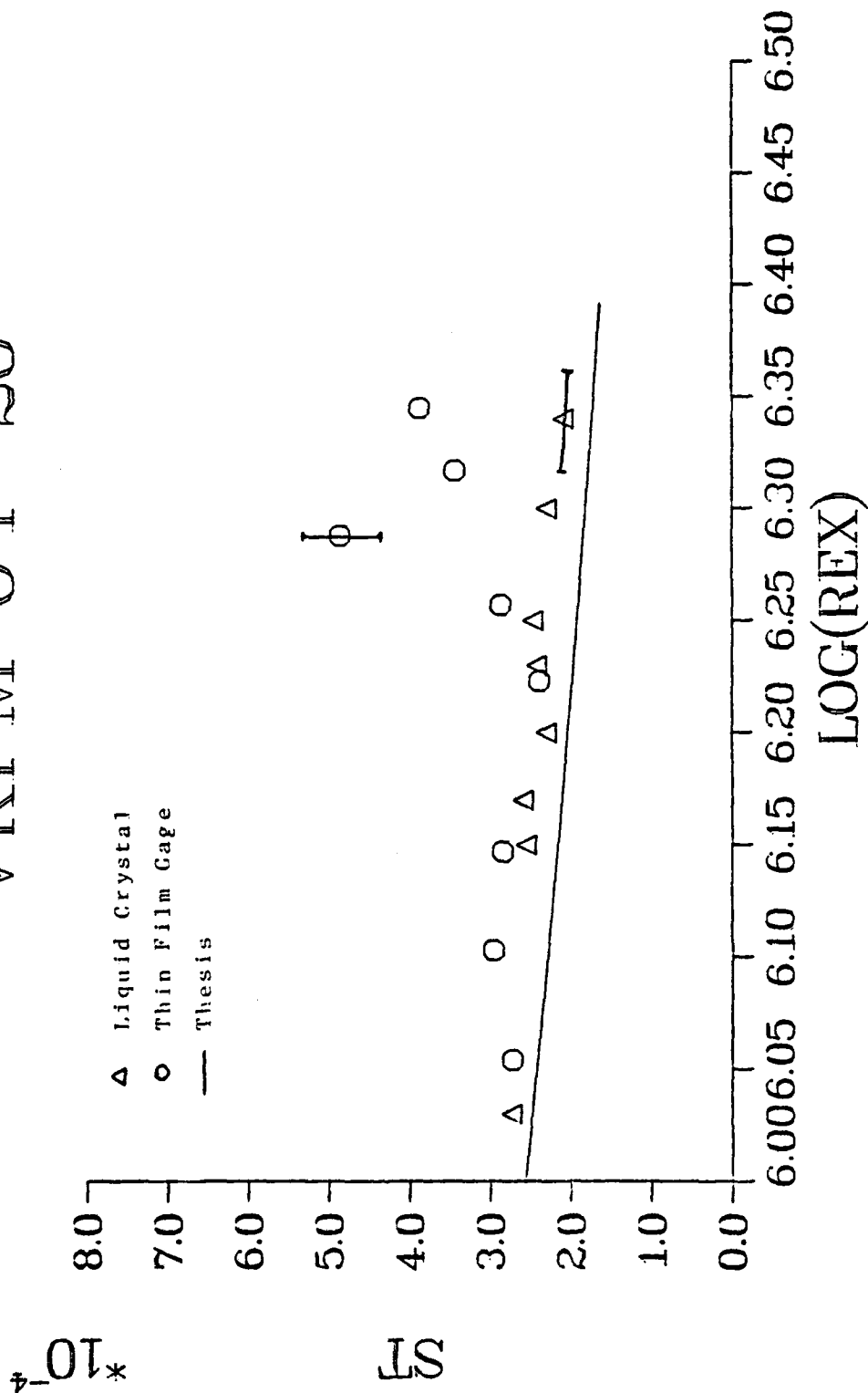
Figure 3.76. Experimental and Numerical Comparison
Mach = 6, P = 20 bar, Re = 1.69×10^7 /m

V. Overall Conclusions

The modification of using the Thomas algorithm in solving the momentum and energy equations instead of using the optimized successive over-relaxation method improved the efficiency of the program for large grids or when high accuracy is required. The steady eddy viscosity turbulence models; Van Driest and Chapman for the inner region, and mixing length and Clauser for the outer region, when compared in a compressible case, showed very little difference in the heat transfer rates (Stanton number).

The liquid crystal results agreed with theory very well, but the method did not show any indication of transition. This is probably due to the poor quality of the color photographs that were used to record the information. The thin film gage data were quite low with respect to theoretical results, and this is due in part to the short testing time.

A large amount of useful information was obtained with the oil flow and sublimation photographs of the flow interaction region of the fin on the flat plate. It was found that the separation distance upstream of the fin increased as the sweep angle is decreased. Striation heating appeared in two cases that were examined. The flow regime tht produced the striation heating was Mach 6 flow, $Re = .844 \times 10^7 / m$, fin with 60° or 75° sweep and 40°

incidence. Several flow interaction models were suggested for the different test cases.

The heat transfer results obtained from the numerical technique and experimental technique were compared. Agreement to within 20% exists for the lower Reynolds number comparison. At the higher Reynolds number cases, the agreement between numerical data and experimental data are very good.

VI. Recommendations

Several recommendations for future study have been realized during the course of this project. They are:

1. Modify the steady turbulence model to an unsteady model using the method of Lorber (38).

2. Generate a grid to account for the increase in the boundary layer due to turbulence.

3. Add to the program an adaptive grid method optimized for minimizing truncation error.

4. Extend the code to axisymmetric problems, ultimately to three dimensional cases.

5. Modify the code to solve the momentum and continuity equations in a coupled manner, such as the Davis-Coupled Scheme, to accelerate convergence of the lagged coefficients (3:339).

6. Place the fin closer to the leading edge of the plate (to obtain fully laminar flow) to determine if the "bump" seen in the oil flow photographs is caused by transition or another phenomena.

7. Continue the study of the three dimensional flow interaction region with different shaped fins, ie., taller, wider, sharp edged, using flow visualization and schlieren with shorter exposure times.

8. Expand the flow visualization area of study to include

the fin and the plate area near the trailing edge of the fin to develop a flow interaction model using topological rules (41).

9. Continue the study of the three dimensional flow interaction region using liquid crystals and digital image processing.

10. Obtain quantitative data on the three dimensional flow interaction region using coax gages or thin film gages.

11. Study the heat transfer rates on the fin.

12. Design a new pressure rake to permit calibration of the wind tunnel farther than 143 mm from the nozzle exit.

Appendix A

Time and Mass-Weighted Averaging

A combination of conventional time averaging and mass-weighted averaging (7:49-55) has been used in the development of the governing equations for turbulent boundary layers. The time averaged variables are defined as follows:

$$\rho = \bar{\rho} + \rho"$$
(A.1)

$$P = \bar{P} + P"$$
(A.2)

where $\bar{\rho}$ and $\bar{P}$ are the time averages of the bulk density and pressure, respectively, and $\rho"$ and $P"$ are the superimposed density and pressure fluctuations, respectively. The time average or "mean" of any quantity $q(t)$ is defined by

$$\bar{q(t)} = \lim_{\Delta t \to \infty} \frac{1}{\Delta t} \int_{t_0}^{t_0 + \Delta t} q(t)\, dt$$
(A.3)

For a fluctuating quantity $q"(t)$, the mean is zero by definition, ie.,

$$\overline{q"(t)} = 0$$
(A.4)

therefore,

$$\overline{\rho"} = 0$$
(A.5)

$$\overline{P"} = 0$$
(A.6)

The mass-weighted variables are defined as follows:

$$u = \tilde{u} + u' \tag{A.7}$$

$$v = \tilde{v} + v' \tag{A.8}$$

$$H = \tilde{H} + H' \tag{A.9}$$

$$T = \tilde{T} + T' \tag{A.10}$$

A mass-weighted mean quantity is defined as:

$$\tilde{q} = \frac{\overline{\rho q}}{\bar{\rho}} \tag{A.11}$$

where the bar denotes conventional time averaging and the tilde denotes mass-weighted averaging. A consequence of combining the time and mass-weighted averaging definitions for the product ρq:

$$\rho q = (\bar{\rho} + \rho'')(\tilde{q} + q') = \bar{\rho}\tilde{q} + \rho''\tilde{q} + \bar{\rho}q' + \rho''q' \tag{A.12}$$

is when the time average is taken, eqn (A.12) becomes

$$\overline{\rho q} = \overline{\bar{\rho}\tilde{q}} + \overline{\bar{\rho}q'} + \overline{\rho''q'} \quad \text{since } \overline{\rho''} = 0 \tag{A.13}$$

$$\overline{\rho q} = \bar{\rho}\tilde{q} + \overline{\bar{\rho}q'} \quad \text{since } \bar{\rho} = \rho + \rho'' \tag{A.14}$$

By definition, from equation (A.11), $\bar{\rho}\tilde{q} = \overline{\bar{\rho}q}$, therefore

$$\overline{\rho q'} = 0 \tag{A.15}$$

Therefore, by analogy let

$$\overline{\rho u'} = 0 \tag{A.16}$$

$$\overline{\rho v'} = 0 \tag{A.17}$$

$$\overline{\rho H'} = 0 \tag{A.18}$$

$$\overline{\rho T'} = 0 \tag{A.19}$$

Total enthalpy can also be expressed in another form including the static enthalpy.

$$\varrho H = h + 1/2\ \varrho u^2 \qquad\qquad (A.20)$$

If the total enthalpy, eqn (A.20), is mass averaged,

$$\varrho \tilde{H} + \varrho H' = \varrho \tilde{h} + \varrho h' + 1/2\ \varrho\ (\ \tilde{u}\tilde{u} + 2\tilde{u}u' + u'u'\ ) \qquad (A.21)$$

Taking the mean of equation (A.21) gives

$$\varrho \overline{\tilde{H}} = \varrho \overline{\tilde{h}} + 1/2\ \varrho \overline{\tilde{u}\tilde{u}} + 1/2\ \overline{\varrho u'u'} \qquad\qquad (A.22)$$

$$\tilde{H} = \tilde{h} + 1/2\ \tilde{u}\tilde{u} + 1/2\ \frac{\overline{\varrho u'u'}}{\overline{\varrho}} \qquad\qquad (A.23)$$

Since $H = \tilde{H} + H'$, using the definition: $H = h + 1/2\ u^2$

$$H = \tilde{h} + h' + 1/2\ (\ \tilde{u} + u'\ )^2 \qquad\qquad (A.24)$$

$$\tilde{H} + H' = \tilde{h} + h' + 1/2\ \tilde{u}\tilde{u} + \tilde{u}u' + 1/2\ u'u' \qquad (A.25)$$

Solving for H' and substituting eqn (A.23) into eqn (A.25):

$$H' = h' + \tilde{u}u' + 1/2\ u'u' - 1/2\ \frac{\overline{\varrho u'u'}}{\overline{\varrho}} \qquad (A.26)$$

This result will be used later in Appendix B.

Averaging of the Boundary Layer Equations

The boundary layer equations are given as follows. The equation numbers correspond to the number given originally to the same equation in the main body of the report.

continuity

$$\frac{\partial \varrho}{\partial t} + \frac{\partial \varrho u}{\partial x} + \frac{\partial \varrho v}{\partial Y} = 0 \qquad\qquad (2.1)$$

x-momentum

$$\frac{\partial \rho\# u\#}{\partial t\#} + \frac{\partial \rho\# u\# u\#}{\partial x\#} + \frac{\partial \rho\# u\# v\#}{\partial Y\#} = - \frac{\partial P\#}{\partial x\#} + \frac{\partial}{\partial Y\#} \left[\mu\# \frac{\partial u\#}{\partial Y\#} \right] \qquad (2.2)$$

Y-momentum

$$\frac{\partial P\#}{\partial Y\#} = 0 \qquad (2.3)$$

energy

$$\frac{\partial \rho\# H\#}{\partial t\#} + \frac{\partial \rho\# u\# H\#}{\partial x\#} + \frac{\partial \rho\# v\# H\#}{\partial Y\#} = \frac{\partial P\#}{\partial t\#} + \frac{\partial}{\partial Y\#} \left[k\# \frac{\partial T\#}{\partial Y\#} \right]$$

$$+ \frac{\partial}{\partial Y\#} \left[\mu\# u\# \frac{\partial u\#}{\partial Y\#} \right] \qquad (2.4)$$

Apply mass-weighted averaging on the boundary layer eqns (2.1), (2.2), (2.3), and (2.4).

Continuity

The continuity equation (2.1) after mass-weighted averaging becomes

$$\frac{\partial \rho\#}{\partial t\#} + \frac{\partial \rho\#(u\# + \overset{\sim}{u\#'})}{\partial x\#} + \frac{\partial \rho\#(v\# + \overset{\sim}{v\#'})}{\partial Y\#} = 0 \qquad (A.27)$$

Taking the mean of the equation,

$$\frac{\partial \overline{\rho\#}}{\partial t\#} + \frac{\partial \overline{\rho\# \overset{\sim}{u\#}}}{\partial x\#} + \frac{\partial \overline{\rho\# u\#'}}{\partial x\#} + \frac{\partial \overline{\rho\# \overset{\sim}{v\#}}}{\partial Y\#} + \frac{\partial \overline{\rho\# v\#'}}{\partial Y\#} = 0 \qquad (A.28)$$

But, noting that

$$\overline{\rho\# u\#'} = 0 \qquad \text{and} \qquad \overline{\rho\# v\#'} = 0 \qquad (A.29)$$

Which results finally in the time and mass-weighted averaged continuity equation:

$$\frac{\partial \overline{\rho\#}}{\partial t\#} + \frac{\partial \overline{\rho\# \overset{\sim}{u\#}}}{\partial x\#} + \frac{\partial \overline{\rho\# \overset{\sim}{v\#}}}{\partial Y\#} = 0 \qquad (A.30)$$

x-momentum

The x-momentum equation (2.2) after mass-weighted averaging becomes

$$\frac{\partial \rho\#(\tilde{u}\#+u\#')}{\partial t\#} + \frac{\partial \rho\#(\tilde{u}\#\tilde{u}\#+2\tilde{u}\#u\#'+u\#'u\#')}{\partial x\#} + \frac{\partial \rho\#(\tilde{u}\#+u\#')(\tilde{v}\#+v\#')}{\partial Y\#}$$

$$= -\frac{\partial \bar{P}\#}{\partial x\#} + \frac{\partial}{\partial Y\#}\left[\mu\# \frac{\partial(\tilde{u}\# + u\#')}{\partial Y\#}\right] \qquad (A.31)$$

Taking the mean of the equation,

$$\frac{\partial \overline{\rho\#\tilde{u}\#}}{\partial t\#} + \frac{\partial \overline{\rho\#u\#'}}{\partial t\#} + \frac{\partial \overline{\rho\#\tilde{u}\#\tilde{u}\#}}{\partial x\#} + 2\frac{\partial \overline{\rho\#\tilde{u}\#u\#'}}{\partial x\#} + \frac{\partial \overline{\rho\#u\#'u\#'}}{\partial x\#} + \frac{\partial \overline{\rho\#\tilde{u}\#\tilde{v}\#}}{\partial Y\#}$$

$$+ \frac{\partial \overline{\rho\#u\#'\tilde{v}\#}}{\partial Y\#} + \frac{\partial \overline{\rho\#\tilde{u}\#v\#'}}{\partial Y\#} + \frac{\partial \overline{\rho\#u\#'v\#'}}{\partial Y\#} = -\frac{\partial \bar{P}\#}{\partial x\#}$$

$$+ \frac{\partial}{\partial Y\#}\left[\mu\# \frac{\partial}{\partial Y\#} \overline{\tilde{u}\#(1 + u\#'/\tilde{u}\#)}\right] \qquad (A.32)$$

From eqns (A.29) and (A.32) this results finally in the time and mass-weighted averaged x-momentum equation:

$$\frac{\partial \bar{\rho}\#\tilde{u}\#}{\partial t\#} + \frac{\partial \bar{\rho}\#\tilde{u}\#\tilde{u}\#}{\partial x\#} + \frac{\partial \overline{\rho\#u\#'u\#'}}{\partial x\#} \frac{\partial \bar{\rho}\#\tilde{u}\#\tilde{v}\#}{\partial Y\#} + \frac{\partial \overline{\rho\#u\#'v\#'}}{\partial Y\#} = -\frac{\partial \tilde{P}\#}{\partial x\#}$$

$$+ \frac{\partial}{\partial Y\#}\left[\mu\# \frac{\partial \tilde{u}\#}{\partial Y\#} \overline{(1 + u\#'/\tilde{u}\#)}\right] \qquad (A.33)$$

Y-momentum

Taking the mass-weighted average of the Y-momentum eqn (2.3) has no meaning since the pressure is only averaged in time. Therefore taking the time average of the pressure,

$$\frac{\partial \overline{(P\# + P\#')}}{\partial Y\#} = 0 \tag{A.34}$$

and realizing that, $\overline{P\#'} = 0$, results in the time averaged Y-momentum equation:

$$\frac{\partial \overline{P\#}}{\partial Y\#} = 0 \tag{2.14}$$

Energy

$$\frac{\partial \rho\# H\#}{\partial t\#} + \frac{\partial \rho\# u\# H\#}{\partial x\#} + \frac{\partial \rho\# v\# H\#}{\partial Y\#} = \frac{\partial P\#}{\partial t\#} + \frac{\partial}{\partial Y\#}\left[k\# \frac{\partial T\#}{\partial Y\#} \right]$$

$$+ \frac{\partial}{\partial Y\#}\left[\mu\# u\# \frac{\partial u\#}{\partial Y\#} \right] \tag{2.4}$$

Before the energy equation (2.4) is mass-averaged, the right hand side of the equality sign can be rewritten in a more convenient form using $h\# = cp\# T\#$,

$$\text{LHS of } (2.4) = \frac{\partial P\#}{\partial t\#} + \frac{\partial}{\partial Y\#}\left[\frac{k\#}{cp\#} \frac{\partial h\#}{\partial Y\#} \right] + \frac{\partial}{\partial Y\#}\left[\frac{\mu\# \partial(1/2\ u\# u\#)}{\partial Y\#} \right] \tag{A.35}$$

Since $h\# = H\# - 1/2\ u\# u\#$:

$$\text{LHS of } (2.4) = \frac{\partial P\#}{\partial t\#} + \frac{\partial}{\partial Y\#}\left[\frac{k\#}{cp\#} \frac{\partial H\#}{\partial Y\#} \right] + \frac{\partial}{\partial Y\#}\left[\frac{\mu\# \partial(1/2\ u\# u\#)}{\partial Y\#} \right]$$

$$- \frac{\partial}{\partial Y\#}\left[\frac{k\#}{cp\#} \frac{\partial(1/2\ u\# u\#)}{\partial Y\#} \right] \tag{A.36}$$

Rearranging of eqn (A.36) results in a more convenient form of the energy equation:

$$\frac{\partial \rho_\# H_\#}{\partial t_\#} + \frac{\partial \rho_\# u_\# H_\#}{\partial x_\#} + \frac{\partial \rho_\# v_\# H_\#}{\partial Y_\#} = \frac{\partial P_\#}{\partial t_\#} + \frac{\partial}{\partial Y_\#}\left[\frac{k_\#}{cp_\#}\frac{\partial H_\#}{\partial Y_\#}\right]$$

$$+ \frac{\partial}{\partial Y_\#}\left[(\mu_\# - k_\#/cp_\#)\frac{\partial\,(1/2\ u_\# u_\#)}{\partial Y_\#}\right] \quad (A.37)$$

Taking the mass-weighted average of equation (A.37) gives,

$$\frac{\partial \rho_\# \tilde{H}_\#}{\partial t_\#} + \frac{\partial \rho_\# H_\#{}'}{\partial t_\#} + \frac{\partial \rho_\# \tilde{u}_\# \tilde{H}_\#}{\partial x_\#} + \frac{\partial \rho_\# u_\#{}' \tilde{H}_\#}{\partial x_\#} + \frac{\partial \rho_\# \tilde{u}_\# H_\#{}'}{\partial x_\#} + \frac{\partial \rho_\# u_\#{}' H_\#{}'}{\partial x_\#}$$

$$+ \frac{\partial \rho_\# \tilde{v}_\# \tilde{H}_\#}{\partial Y_\#} + \frac{\partial \rho_\# v_\#{}' \tilde{H}_\#}{\partial Y_\#} + \frac{\partial \rho_\# \tilde{v}_\# H_\#{}'}{\partial Y_\#} + \frac{\partial \rho_\# v_\#{}' H_\#{}'}{\partial Y_\#} = \frac{\partial P_\#}{\partial t_\#}$$

$$+ \frac{\partial}{\partial Y_\#}\left[\frac{k_\#}{cp_\#}\frac{\partial}{\partial Y_\#}\ \tilde{H}_\#\ (1 + H_\#{}'/\tilde{H}_\#)\right]$$

$$+ \frac{\partial}{\partial Y_\#}\left[(\mu_\# - k_\#/cp_\#)\frac{\partial}{\partial Y_\#}\ (1/2\ \tilde{u}_\# \tilde{u}_\# + \tilde{u}_\# u_\#{}' + 1/2\ u_\#{}' u_\#{}')\right]$$

$$(A.38)$$

The mean is then taken of equation (A.38) to obtain

$$\overline{\frac{\partial \rho_\# \tilde{H}_\#}{\partial t_\#}} + \overline{\frac{\partial \rho_\# H_\#{}'}{\partial t_\#}} + \overline{\frac{\partial \rho_\# \tilde{u}_\# \tilde{H}_\#}{\partial x_\#}} + \overline{\frac{\partial \rho_\# u_\#{}' \tilde{H}_\#}{\partial x_\#}} + \overline{\frac{\partial \rho_\# \tilde{u}_\# H_\#{}'}{\partial x_\#}} + \overline{\frac{\partial \rho_\# u_\#{}' H_\#{}'}{\partial x_\#}}$$

$$+ \overline{\frac{\partial \rho_\# \tilde{v}_\# \tilde{H}_\#}{\partial Y_\#}} + \overline{\frac{\partial \rho_\# v_\#{}' \tilde{H}_\#}{\partial Y_\#}} + \overline{\frac{\partial \rho_\# \tilde{v}_\# H_\#{}'}{\partial Y_\#}} + \overline{\frac{\partial \rho_\# v_\#{}' H_\#{}'}{\partial Y_\#}} = \overline{\frac{\partial P_\#}{\partial t_\#}}$$

$$+ \frac{\partial}{\partial Y_\#}\left[\frac{k_\#}{cp_\#}\frac{\partial}{\partial Y_\#}\ \overline{H_\#\ (1 + H_\#{}'/H_\#)}\right]$$

$$+ \frac{\partial}{\partial Y\#}\left[(\mu\# - k\#/cp\#)\frac{\partial}{\partial Y\#} \overline{(1/2\ u\#u\# + u\#u\#' + 1/2\ u\#'u\#')} \right]$$

(A.39)

Combining eqn (A.39) with eqns (A.16), (A.17) and (A.18) results in the time and mass-weighted averaged energy equation:

$$\frac{\partial \bar{\rho}\# \tilde{H}\#}{\partial t\#} + \frac{\partial \bar{\rho}\# \tilde{u}\# \tilde{H}\#}{\partial x\#} + \frac{\partial \overline{\rho\# u\#' H\#'}}{\partial x\#} + \frac{\partial \bar{\rho}\# \tilde{v}\# \tilde{H}\#}{\partial Y\#} + \frac{\partial \overline{\rho\# v\#' H\#'}}{\partial Y\#} = \frac{\partial \bar{P}\#}{\partial t\#}$$

$$+ \frac{\partial}{\partial Y\#}\left[\frac{k\#}{cp\#} \frac{\partial}{\partial Y\#} \overline{H\#(1+H\#'/H\#)} \right] + \frac{\partial}{\partial Y\#}\left[(\mu\# - k\#/cp\#) \frac{\partial}{\partial Y\#} \overline{(1/2\ u\#u\#)} \right]$$

$$+ \frac{\partial}{\partial Y\#}\left[(\mu\# - k\#/cp\#) \frac{\partial}{\partial Y\#} \overline{(\ u\#u\#' + 1/2\ u\#'u\#')} \right] \quad \text{(A.40)}$$

Comparison with Original Equations

The resulting x-momentum equation (A.33) has three terms that make it different than eqn (2.2). These terms are:

$$\frac{\partial \overline{\rho\# u\#' u\#'}}{\partial x\#} \ , \quad \frac{\partial \overline{\rho\# u\#' v\#'}}{\partial Y\#} \ , \text{ and } \frac{\partial}{\partial Y\#}\left[\mu\# \frac{\partial}{\partial Y\#} \overline{u\#(\ u\#'/u\#)} \right] \quad \text{(A.41)}$$

The energy equation (A.40) has four terms that make it different than equation (A.37). These terms are:

$$\frac{\partial \overline{\rho\# u\#' H\#'}}{\partial x\#} \ , \quad \frac{\partial \overline{\rho\# v\#' H\#'}}{\partial Y\#} \ , \quad \frac{\partial}{\partial Y\#}\left[\frac{k\#}{cp\#} \frac{\partial}{\partial Y\#} \overline{H\# (\ H\#'/H\#)} \right]$$

$$\frac{\partial}{\partial Y\#}\left[(\mu\# - k\#/cp\#)\frac{\partial}{\partial Y\#}(\ \overline{u\#u\#'}\ +\ 1/2\ \overline{u\#'u\#'})\right] \qquad (A.42)$$

An order of magnitude analysis needs to be completed to determine which of these extra seven terms could be neglected.

Appendix B

Substitution of the Closure Equations

After an order of magnitude analysis is completed on the time and mass-weighted averaged energy equation, an extra term exists which is different than the original form of the energy equation. That term is

$$\frac{\partial \overline{\rho\#v\#'H\#'}}{\partial Y\#} \tag{B.1}$$

However, a closure equation is given in Anderson (3:225) which says

$$\overline{\rho\#cp\#v\#'T\#'} = - \frac{\mu\#}{T}\frac{cp\#}{Pr_T}\frac{\partial \overline{T\#}}{\partial Y\#} \tag{B.2}$$

From a previous analysis completed in Appendix A, it is known that

$$H' = h' + \tilde{u}u' + 1/2\ u'u' - 1/2\ \frac{\rho u'u'}{\overline{\rho}} \tag{A.26}$$

Substituting eqn (A.26) into the term $\rho\#v\#'H\#'$, one obtains

$$\overline{\rho\#v\#'H\#'} = \overline{\rho\#v\#'h\#'} + \overline{\rho\#v\#'u\#u\#'} \tag{B.3}$$

$$\overline{\rho\#v\#'H\#'} = \overline{\rho\#cp\#v\#'T\#'} + \overline{u\#\rho\#u\#'v\#'} \tag{B.4}$$

Substituting the closure equations for the two terms gives

$$\overline{\rho\#v\#'H\#'} = - \frac{\mu\#}{T}\frac{cp\#}{Pr_T}\frac{\partial \overline{T\#}}{\partial Y\#} - \overline{u\#}\left[\frac{\mu\#}{T}\frac{\partial \overline{u\#}}{\partial Y\#}\right] \tag{B.5}$$

Putting eqn (B.5) into a form with the total enthalpy,

$$\overline{\rho\#v\#'H\#'} = -\underset{\dfrac{T}{Pr_T}}{\mu\#} \frac{\partial \overline{H\#}}{\partial Y\#} + \underset{\dfrac{T}{Pr_T}}{\mu\#} \, 1/2 \, \frac{\partial \overline{u\#^2}}{\partial Y\#} - \overline{u\#} \, \underset{T}{\mu\#} \, \frac{\partial \overline{u\#}}{\partial Y\#} \qquad (B.6)$$

$$\overline{\rho\#v\#'H\#'} = -\underset{\dfrac{T}{Pr_T}}{\mu\#} \frac{\partial \overline{H\#}}{\partial Y\#} - \underset{T}{\mu\#} \, (1 - 1/Pr_T) \, 1/2 \, \frac{\partial \overline{u\#u\#}}{\partial Y\#} \qquad (B.7)$$

The energy equation, as previously developed, has the form:

$$\frac{\partial \overline{\rho\#}\overline{H\#}}{\partial t\#} + \frac{\partial \overline{\rho\#}\overline{u\#}\overline{H\#}}{\partial x\#} + \frac{\partial \overline{\rho\#}\overline{v\#}\tilde{H\#}}{\partial Y\#} + \frac{\partial \overline{\rho\#v\#'H\#'}}{\partial Y\#} = \frac{\partial \overline{P\#}}{\partial t\#}$$

$$+ \frac{\partial}{\partial Y\#}\left[\frac{k\#}{\overline{cp\#}} \frac{\partial \overline{H\#}}{\partial Y\#}\right] + \frac{\partial}{\partial Y\#}\left[\left[\mu\# - \frac{k\#}{\overline{cp\#}}\right] \frac{\partial}{\partial Y\#} \, (1/2 \, \overline{u\#}\overline{u\#})\right] \qquad (2.15)$$

Rewriting the energy eqn (2.15) using the definition that

$$\frac{k\#}{cp\#} = \frac{\mu\#}{Pr} \qquad (B.8)$$

The energy equation (2.15) becomes

$$\frac{\partial \overline{\rho\#}\overline{H\#}}{\partial t\#} + \frac{\partial \overline{\rho\#}\overline{u\#}\overline{H\#}}{\partial x\#} + \frac{\partial \overline{\rho\#}\overline{v\#}\tilde{H\#}}{\partial Y\#} + \frac{\partial \overline{\rho\#v\#'H\#'}}{\partial Y\#} = \frac{\partial \overline{P\#}}{\partial t\#}$$

$$+ \frac{\partial}{\partial Y\#}\left[\frac{\mu\#}{Pr\#} \frac{\partial \overline{H\#}}{\partial Y\#}\right] + \frac{\partial}{\partial Y\#}\left[\mu\# \, (1 - 1/Pr) \, \frac{\partial}{\partial Y\#} \, (1/2 \, \overline{u\#}\overline{u\#})\right] \qquad (B.9)$$

Substituting eqn (B.7) into the energy equation (B.9) gives

$$\frac{\partial \overline{\rho\#}\overline{H\#}}{\partial t\#} + \frac{\partial \overline{\rho\#}\overline{u\#}\overline{H\#}}{\partial x\#} + \frac{\partial \overline{\rho\#}\overline{v\#}\tilde{H\#}}{\partial Y\#} = \frac{\partial \overline{P\#}}{\partial t\#} + \frac{\partial}{\partial Y\#}\left[\left[\frac{\mu\#}{Pr} + \underset{T}{\mu\#}/Pr_T\right] \frac{\partial \overline{H\#}}{\partial Y\#}\right]$$

$$+ \frac{\partial}{\partial Y\#}\left[\left[\mu\#(1 - 1/Pr) + \underset{T}{\mu\#}(1 - 1/Pr_T)\right] \frac{\partial}{\partial Y\#} \, (1/2 \, \overline{u\#}\overline{u\#})\right] \qquad (2.23)$$

190

Appendix C

Turbulent Boundary Layer Code

```
      PROGRAM UNCOMBL(INPUT,OUTPUT,TAPE5,TAPE6=OUTPUT,TAPE7)
      COMMON/RESTRT/TIME,X(61),Y(61,59),U(61,0:60),V(61,59),
     &            H(61,0:60),TW(61),W(61,59)
      DIMENSION A(18362)
      EQUIVALENCE (A,TIME)
      DIMENSION DX(61),DY(61,59),DYXI(61,59),DYB(61,59),DYF(61,59),
     &          ETAX(61,59),RHO(59),T(59),DYRE(61,59),
     &          UNM1(61,59),HNM1(61,59),VNM1(61,59),UIM1(59),
     &          HIM1(59),UIM2(59),HIM2(59),Q(61),HHREF(61),
     &          YP(61,59),AA(60),D(60),E(60),BB(60),CC(60)
      DIMENSION AAH(60),DH(60),EH(60),BBH(60),CCH(60)
      DIMENSION TAU(61),CF(61),HC(61)
      DIMENSION MUT(59),MUHT(59),MUKT(59)
      REAL MUT,MUHT,MUKT,MUCLS
      REAL LAM,MU,MUINF,L,MINF,MUW,MUEDG,ME,LL,MUTURB,MUSTAR
      REAL LLI,LLO
      REAL MITT,CHAP,VO,YPLUS
      INTEGER RST,CNT,MODEL
      LOGICAL IFSOR
      DATA IDIM,JDIM/61,59/
      DATA IMAX,JMAX,NT,CNT,KT,NTW,RST/61,30,020,010,10,005,0/
C     DATA MINF,PINF,TINF/.01,2116.2,530./
      DATA MINF,PINF,TINF/14.24,.50343,48.6/
C     DATA DT,CP,RG,L,PRL,GAM,EPS/200.,6006.,1715.,28.95,1.,1.4,.00001/
      DATA DT,CP,RG,L,PRL,GAM,EPS/200.,6006.,1715.,1.25,.72,1.4,.00001/
C     DATA ME,PE,TE,DPDT,TW1,TW2/.01,2116.2,530.,0.0,530.,530./
      DATA ME,PE,TE,DPDT,TW1,TW2/6.271,11.06,228.,0.0,530.,530./
      OPEN(UNIT=8,FILE='RESTART',FORM='UNFORMATTED')
      OPEN(UNIT=9,FILE='WALLQ')
      OPEN(UNIT=10,FILE='FIELD')
      OPEN(UNIT=11,FILE='GRID')
      REWIND 11
      REWIND 9
      REWIND 10
      OPEN(UNIT=13,FILE='ANSWER')
      OPEN(UNIT=12,FILE='STANREX')
      REWIND 12
      REWIND 13
      REWIND 7
C
C
CCCCCCCCCCCCCCCCCCCCCCCCCCCCCCCCCCCCCCCCCCCCCCCCCCCCCCCCCCCCCCCCCCCCCCCCC
C     THIS PROGRAM SOLVES THE UNSTEADY BOUNDARY LAYER EQUATIONS
C     ALSO IT SOLVES FOR THE HEAT RATE AT THE WALL AND DETERMINES
C     A HEAT TRANSFER COEFFICIENT
C
C     SYMBOLS:
C
C     APLUS           VAN DRIEST DAMPING LENGTH CONSTANT
C     CF              SKIN FRICTION COEFFICIENT
C     CNT             THE NUMBER OF TIME STEPS BETWEEN PRINTOUT
C     CP              COEFFICIENT OF HEAT(FT-LB/SLUG/R)
C     DDX             X DISTANCE BETWEEN I AND I+1 NODES
C     DEL             BOUNDARY LAYER THICKNESS
C     DDEL            NONDIM TURB BOUNDARY LAYER THICKNESS IN TRANSFORMED
C     DDELP            NONDIM TURB BOUNDARYLAYER IN PHYSICAL THICKNESS
C     DSTAR            NONDIM TURB DISPLACEMENT THICKNESS
C     DX              DERIVATIVE OF X WRT XI
C     DY              DERIVATIVE OF Y WRT ETA
C     DYXI            DERIVATIVE OF Y WRT XI
C     DYB             Y DIFFERENCE BETWEEN J AND J-1
C     DYC             CENTRAL Y DIFFERENCE
C     DYF             Y DIFFERENCE BETWEEN J+1 AND J
C     DT              DELTA TIME
C     EPS             CONVERGENCE EPSILON
```

```
C     EMAX                MAX ERROR
C     EXTENT              PARAMETER THAT MEASURES THE EXTENT OF TRANSITION
C          FSOR               SAFETY FACTOR ON OPTIMUM SOR ACCELERATION PARAMETER
C     FUDGE               PARAMETER THAT MODIFIES THE AMOUNT OF
C                         TURBULENCE IN THE MODEL DURING TRANSITION
C     GAM                 RATIO OF SPECIFIC HEATS (GAMMA)
C     GRDFC               SCALE FACTOR ON Y FOR GRID
C     H                   TOTAL ENTHALPY
C     HNM1                TOTAL ENTHALPY AT OLD TIME LEVEL
C     HIM1                ENTHALPY AT I-1 LOCATION
C     HIM2                ENTHALPY AT I-2 LOCATION
C     HC(I)               HEAT COEFFICIENT(BTU/FT2/S/R)
C     HREF                REFERENCE HEAT COEFFICIENT(BTU/FT2/S/R)
C     I                   COUNTER IN XI DIRECTION
C     IMAX                MAX NUMBER OF STEPS IN XI DIRECTION
C     IFSOR               LOGICAL FLAG FOR SOR(T) OR QUADDIAGONAL
C     ITRANS              TRANSITION TO TURBULENCE OCCURS AT I=ITRANS
C     ITURB               TRANSITION TO TURBULENCE ENDS AT I=ITURB
C                         FLOW IS FULLY TURBULENT
C     J                   COUNTER IN ETA DIRECTION
C     JMAX                MAX NUMBER OF STEPS IN ETA DIRECTION
C     K                   COUNTER IN ITERATIONS
C     KT                  MAX NUMBER OF ITERATIONS
C     L                   LENGTH OF PLATE (FEET)
C     LL                  PARAMETER OF LENGTH
C     MINF                MACH AT INFINITY
C     MODEL=1     VAN DRIEST INNER MODEL
C     MODEL=2     CHAPMAN INNER MODEL
C     KMODL<= 0 CLAUSER'S OUTER MODEL
C     KMODL>0     MIXING LENGTH OUTER MODEL BASED ON BL THICKNESS
C     MU                  VISCOSITY, NONDIMENSIONAL
C     MUINF               VISCOSITY AT INFINITY(SLUGS/FT/S)
C     MUTURB              TURBULENT VISCOSITY, NONDIMENSIONAL AT
C     MUCLS       CLAUSERS OUTER TURB VISCOSITY,NODIMENSIONAL
C     MUT(J)      LAMINAR+TURB VISCOSITY, NONDIMENSIONAL
C     MUHT(J)     LAMINAR VISC/PRL+TURB VISC/PRT , NONDIMENSIONAL
C     MUKT(J)     LAMINAR VISC(PRL-1)/PRL + TURB VISC(PRT-1)/PRT NONDIM
C     N                   COUNTER IN TIME
C     NT                  MAX NUMBER OF TIME STEPS
C     NTW                 NUMBER OF TIME STEPS TO CALCULATE OMEGA
C     PRESS               NONDIMENSIONALIZED EDGE PRESSURE
C     PRL                 PRANDTL NUMBER
C     PRT                 TURBULENT PRANDTL NUMBER
C     PE                  PRESSURE AT THE EDGE OF B.L.(LB/FT2)
C     Q                   HEAT RATE AT THE WALL(BTU/FT2/S)
C     RHO                 DENSITY
C     RM                  DENSITY TIMES VISCOSITY
C     RE                  REYNOLD'S NUMBER
C     RST                 RESTART INDICATOR
C     RINF                DENSITY AT INFINITY CONDITIONS (SLUG/FT**3)
C     T                   TEMPERATURE
C     TAU                 SKIN FRICTION(LB/FT2)
C     TTAU                SHEAR STRESS
C     TIME                TOTAL TIME ACCUMULATED
C     TW                  TEMPERATURE AT THE WALL(R)
C     TE                  TEMPERATURE AT THE EDGE OF B.L.(R)
C     TINF                TEMPERATURE AT INFINITY (DEG RANKINE)
C     TOINF               TOTAL TEMPERATURE AT INFINITY (DEG RANKINE)
C     U                   VELOCITY IN X DIRECTION
C     UCLAUS              TURB CHARACTERISTIC VELOCITY OUTER LAYER BY CLAUSER
C     UNM1                VELOCITY IN X DIRECTION AT OLD TIME LEVEL
C     UE                  VELOCITY AT THE EDGE OF B.L.(FT/S)
C     UFE                 INFINITY TO EDGE VELOCITY RATIO
C     UIM1                VELOCITY VECTOR AT I-1 LOCATION
C     UIM2                VELOCITY VECTOR AT I-2 LOCATION
```

```
C      UINF               VELOCITY AT INFINITY CONDITION (FT/SEC)
C      V                  VELOCITY IN Y DIRECTION
C      VK                 VON KARMEN UNIVERSAL CONSTANT
C      VNM1               VELOCITY IN Y DIRECTION AT OLD TIME LEVEL
C      W                  OPTIMIZATION OMEGA
C      XBAR               PARAMETER
C      XTRANS             INITIAL POSITION OF TRANSITION TO TURBULENCE
C      XTURB              FINAL POSITION OF TRANSITION TO TURBULENCE
C                            FLOW IS FULLY TURBULENT
C      Y                  TRANSFORMED NONDIM NORMAL COORDINATE
C      YP                 NONDIM NORMAL PHYSICAL COORDINATE
C      YPLUS              PARAMETER
C
CCCCCCCCCCCCCCCCCCCCCCCCCCCCCCCCCCCCCCCCCCCCCCCCCCCCCCCCCCCCCCCCCCCC
C
       DATA MODEL,XTRANS,XTURB,EXTENT/1,.25,.5,.05/
       DATA PRT,VK,YPLSMX/.9,.4,500000./
       COSJ=COS(3.14159/FLOAT(JMAX))
       WRITE(6,*)'IDIM,JDIM=',IDIM,JDIM
       WRITE(6,*)'IMAX,JMAX='
       READ(5,*)IMAX,JMAX,GRDFC
       WRITE(6,*)'NUMERICAL YXI METRIC AFTER IMET='
       READ(5,*)IMET
       WRITE(6,*)'L(FT)='
       READ(5,*)L
       WRITE(6,*)'MINF,PINF,TINF='
       READ(5,*)MINF,PINF,TINF
       WRITE(6,*)'ME,PE,TE='
       READ(5,*)ME,PE,TE
       WRITE(6,*)'TW1,TW2,XTW2='
       READ(5,*)TW1,TW2,XTW2
       WRITE(6,*)'ITEQ=0 NO RADIATION EQUILIBRIUM WALL'
       WRITE(6,*)'ITEQ='
       READ(5,*)ITEQ
       WRITE(6,*)'IPRINT=0 NO LISTING ON FILE FIELD'
       WRITE(6,*)'IPRT='
       READ(5,*)IPRT
       WRITE(6,*)'NT,CNT,KT,RST='
       READ(5,*)NT,CNT,KT,RST
       WRITE(6,*)'DT,EPS='
       READ(5,*)DT,EPS
       WRITE(10,*) 'THE INPUT FOR THIS RUN :'
       WRITE(10,*)'NT,CNT,KT,RST = ',NT,CNT,KT,RST
        WRITE(10,*) 'DT,EPS = ',DT,EPS
       JMM1=JMAX-1
       GGM1=GAM/(G.'4-1.)
C      MUINF=(TINF**1.5*2.27E-8)/(TINF+198.6)
         MUINF=TINF**.5*2.32E-8/(1.+220./(TINF*10.**(9./TINF)))
       AINF=SQRT(GAM*RG*TINF)
       UINF=MINF*AINF
       RINF=PINF/(RG*TINF)
       TOINF=TINF*(1+(GAM-1.)*.5*MINF**2)
       RE=RINF*UINF*L/MUINF
       AE=SQRT(GAM*RG*TE)
       UE=ME*AE
       DO 11 J=1,JMAX
       MUTURB=0.
 11    CONTINUE
C      MUEDG=(TE**1.5*2.27E-8)/(TE+198.6)
         MUEDG=TE**.5*2.32E-8/(1.+220./(TE*10.**(9./TE)))
       REE=(PE/(RG*TE))*UE*L/MUEDG
       WRITE(9,*)'RE=',RE
       WRITE(9,*)'RINF,UINF,MUINF=',RINF,UINF,MUINF
       WRITE(9,*)'MINF,AINF,TINF,PINF=',MINF,AINF,TINF,PINF
       PRESS=PE/(RINF*UINF**2)
```

```fortran
      PRESSO=PRESS
      WRITE(9,*)'ME,PE,TE,AE,UE=',ME,PE,TE,AE,UE
      HREF=.332*CP*SQRT(MUINF*RINF*UINF)/PRL**(2./3.)/778.3
      WRITE(9,*)'HREF=',HREF
      WRITE(13,*)'I,J,Y+,U+,MU,MUTURB,FUDGE,MITT,LLI,LLO,DDELP,YP(I,J)'
      DATA ALPHA,TIME/14,0./
C REFERENCE CAN BE BASED ON FREESTREAM OR EDGE CONDITIONS!!!!
C
C     DA IS THE 2 DEG/SEC PITCH RATE NONDIMESIONALIZED TIME
      DA=2*L/UINF
C
C     TS IS THE NONDIMESIONAL TIME TO PITCH 11 DEG(14DEG-3DEG)
      TS=11/DA
      NTS=TS + 5*UINF/L
      NNTS=NTS + TS
C
C     GENERATE A GRID AND INITIAL CONDITIONS
C
      CALL FIRST(IMAX,JMAX,REE,CP,TW,TE,UE,UINF,PRESS,GGM1,X,Y,U,V,H,
     &PRL,XTW2,TW1,TW2,IMET,GRDFC)
      DO 10 I=1,IMAX
        U(I,0)=0.
        H(I,0)=0.0
        U(I,JMAX+1)=0.0
        H(I,JMAX+1)=0.0
10    CONTINUE
C
C     IF RESTARTING THE PROBLEM, READ THE INITIAL GUESS FROM TAPE 8
C
      REWIND 8
      IF(RST.EQ.1)READ(8)A
      WRITE(6,*)'ALPHA,TIME='
      READ(5,*)ALPHA,TIME
      WRITE(6,*)'RC,DA='
      READ(5,*)RC,DA
      WRITE(6,*)'ITERPO=0 DO NOT INTERPOLATE FOR EDGE CONDITIONS'
      WRITE(6,*)'ITERPO='
      READ(5,*)ITERPO
        IF(ITERPO.NE.0)CALL TERPO(ALPHA,UINF,RINF,CP,UE,PE,HE)
      PRESS=PE/(RINF*UINF**2)
        DO 1888 I=1,IMAX
          U(I,JMAX)=UE/UINF
          H(I,JMAX)=CP*TE/UINF**2+U(I,JMAX)**2*.5
1888  CONTINUE
      PRINT*,'MODEL,XTRANS,XTURB,EXTENT='
      READ(5,*)KMODL,XTRANS,XTURB,EXTENT
      MODEL=ABS(KMODL)
       IF (MODEL .EQ. 1) THEN
         WRITE(10,*) 'TURBULENCE MODEL CONTAINS THE VAN DRIEST MODEL'
         WRITE(9,*) 'TURBULENCE MODEL CONTAINS THE VAN DRIEST MODEL'
         WRITE(13,*)'TURBULENCE MODEL CONTAINS THE VAN DRIEST MODEL'
       ENDIF
       IF (MODEL .EQ. 2) THEN
         WRITE(10,*) 'TURBULENCE MODEL CONTAINS THE CHAPMAN MODEL'
         WRITE(9,*) 'TURBULENCE MODEL CONTAINS THE CHAPMAN MODEL'
         WRITE(13,*) 'TURBULENCE MODEL CONTAINS THE CHAPMAN MODEL'
       ENDIF
      PRINT*,'PRL,PRT,VON KARMEN CONSTANT,YPLUS MAX FOR SWITCH='
      READ(5,*)PRL,PRT,VK,YPLSMX
      PRL1=(PRL-1.)/PRL
      PRT1=(PRT-1.)/PRT
      PRINT*,'IFSOR FLAG(F OR T),NO TIME STEPS OPT W=,FSOR?'
      READ(5,*)IFSOR,NTW,FSOR
      COSJ=COSJ*FSOR
      WRITE(12,*)'X,REX,REXL,ST,STREXA,STREXB,CF,CFREXA,CFREXB'
```

```
      DA=DA*L/UINF
      RC=RC*UINF/L
      IF(ABS(DA).GT.1.E-16)THEN
          TS=11./DA
          NTS=TS+5.*UINF/L
          NNTS=NTS+TS
      END IF
C
C     CALCULATE DERIVATIVES XI WRT X, ETA WRT Y, AND ETA WRT X
C     XI WRT X EQUALS 1/DX, ETA WRT Y EQUALS 1/DY, AND
C     ETA WRT X EQUALS -DYXI/(DX*DY)
C
      ILOOK=1
      ILOOK2=1
      ITRANS=IMAX+1
      ITURB=IMAX+2
      DO 30 I=2,IMAX
         IM1=I-1
         IM2=I-2
         IP=I+1
         IF(I.EQ.IMAX)THEN
           DX(I)=X(I)-X(IM1)
         ELSE
           DX(I)=(X(IP)-X(IM1))/2.
         ENDIF
         IF ((X(I) .GE. XTRANS) .AND. (ILOOK .EQ. 1)) THEN
           ITRANS=I
           ILOOK=2
         ENDIF
         IF ((X(I) .GE. XTURB) .AND. (ILOOK2 .EQ. 1)) THEN
           ITURB=I
           ILOOK2=2
         ENDIF
         DYXI(I,1)=0.0
         DO 32 J=2,JMM1
            JP=J+1
            JM1=J-1
            JM2=J-2
            DY(I,J)=(Y(I,JP)-Y(I,JM1))/2
            IF(I.GT.IMET)THEN
              IF (I .EQ. IMAX) THEN
                DYXI(I,J)=Y(I,J)-Y(IM1,J)
              ELSE
                DYXI(I,J)=(Y(IP,J)-Y(IM1,J))*.5
                DYXI(I,J)=1.5*Y(I,J)-2.*Y(IM1,J)+.5*Y(IM2,J)
              ENDIF
            ELSE
              DYXI(I,J)=Y(I,J)*.5*DX(I)/X(I)
            ENDIF
            DYB(I,J)=Y(I,J)-Y(I,JM1)
            DYC=(Y(I,JP)-Y(I,JM1))/2.
            DYF(I,J)=Y(I,JP)-Y(I,J)
            ETAX(I,J)=-DYXI(I,J)/(DX(I)*DY(I,J))
            DYRE(I,J)=1./(DYC*RE)
   32    CONTINUE
         DYF(I,1)=Y(I,2)-Y(I,1)
         DY(I,1)=DYF(I,1)
         DYF(I,JMAX)=DYF(I,JMAX-1)
   30 CONTINUE
C
C     PUT INFORMATION INTO THE OLD TIME LEVEL INITIALLY
C
      DO 40 I=1,IMAX
        DO 40 J=1,JMAX
          UNM1(I,J)=U(I,J)
```

```
           VNM1(I,J)=V(I,J)
           HNM1(I,J)=H(I,J)
          IF(RST.EQ.O) W(I,J)=1.0
40     CONTINUE
C
       IF(RST.EQ.O)THEN
       DO 43 I=2,IMAX
       DO 43 J=1,11
          W(I,J)=1.6-(J-1)*.06
43     CONTINUE
       END IF
C
C      START THE TIME LOOP
C
       DO 500 N=1,NT
         TIME=TIME+DT
C
       IF(TIME.LE.O.)GO TO 2001
       IF(TIME.GT.(NNTS+DT))GO TO 2001
C      THIS SECTION PITCHES THE PLATE FROM 14 DEG TO 3 DEG AND BACK TO 14
C
         IF (TIME.LE.TS)ALPHA=ALPHA - DA*DT
C
         IF(ALPHA.LE.3.O)ALPHA=3.0
         IF(TIME.GT.TS.AND.TIME.LE.NTS)ALPHA=3.0
         IF(TIME.GT.NTS.AND.TIME.LE.NNTS)ALPHA=ALPHA + DA*DT
         IF(ALPHA.GE.14.)ALPHA=14.0
         IF(TIME.GT.NNTS)ALPHA=14.
         IF(ITERPO.NE.O)CALL TERPO(ALPHA,UINF,RINF,CP,UE,PE,HE)
       PRESS=PE/(RINF*UINF**2)
         DO 2000 I=1,IMAX
           U(I,JMAX)=UE/UINF
           H(I,JMAX)=CP*TE/UINF**2+U(I,JMAX)**2*.5
2000   CONTINUE
       DPDT=(PRESS - PRESSO)
       PRESSO=PRESS
2001   CONTINUE
       IF(N.EQ.1)GO TO 2003
       IF(ITEQ.EQ.O)GO TO 2003
       DO 2002 I=2,IMAX
       IF(X(I).GT.XTW2)THEN
       IF(Q(I).GT.O.)THEN
       TEQ=(Q(I)/(778.3*.85*4.761E-13))**.25
       ELSE
       TEQ=0.
       END IF
       DTRC=DT/RC
       IF(DTRC.GT.34.)DTRC=34.
       EXPRC=EXP(-DTRC)
       TW(I)=TW(I)*EXPRC+(1.-EXPRC)*TEQ
       HW=CP*TW(I)/UINF**2+U(I,1)**2/2.
       H(I,1)=HW
       END IF
2002   CONTINUE
2003   CONTINUE
C      START BACK AT BEGINNING OF GRID--REINITIALIZE VECTORS
C
         DO 510 J=1,JMAX
           UIM1(J)=0.0
           HIM1(J)=0.0
510    CONTINUE
C
C      START I LOOP--MARCH IN XI DIRECTION
C
       FUDGE=0.
```

```
      DO 400 I=2,IMAX
C TURB MODEL THAT DOES NOT CHANGE WITH N OR I
        IF (I .GE. ITRANS) THEN
          IF ( I .GE. ITURB) THEN
            FUDGE=1.0
          ELSE
          XBAR=(X(I)-XTRANS)/EXTENT
            FUDGE=1.0 - 1.0/(EXP(.412*XBAR**2))
          ENDIF
        ENDIF
C
        DELM=0.0
C     PUT NEW INFORMATION INTO THE VELOCITY AND ENTHALPY VECTORS AT THE
C     I-1 AND I-2 LOCATIONS
C
        DO 410 J=1,JMAX
          UIM2(J)=UIM1(J)
          UIM1(J)=U(I-1,J)
          HIM2(J)=HIM1(J)
          HIM1(J)=H(I-1,J)
410     CONTINUE
C
C     DEFINE CONSTANTS TO DETERMINE THE COEFFICIENTS FOR THE U AND V
C     VELOCITY EQUATIONS AND THE ENTHALPY EQUATION
C
        IF(I.EQ.2)THEN
          CIJ1=1.
          CIM1=1.
          CIM2=0.
          CVIJ=-.5
          CVIM1=.5
          CVIM2=0.
        ELSE
          CIJ1=1.5
          CIM1=2.0
          CIM2=-.5
          CVIJ=-.75
          CVIM1=1.
          CVIM2=-.25
        ENDIF
C
C     START THE ITERATION LOOP
C
        DO 300 K=1,KT
          EMAX=0.0
        EUMAX=0.
        EVMAX=0.
        EHMAX=0.
C
C     CALCULATE NEW VALUES FOR TEMPERATURE,DENSITY, AND VISCOSITY USING
C     THE NEW VALUES OF U, V, AND H (CALCULATED AT THE OLD ITERATION LEVEL)
C
C CALCULATE TURB MODEL PARAM THAT DO NOT CHANGE WITH J
        IF(I.GT.ITRANS)THEN
        UFE=UINF/UE
        YP(I,1)=0.
        DSTAR=0.
        DO 309 J=2,JMAX
        YP(I,J)=YP(I,J-1)+(1./RHO(J)+1./RHO(J-1))*.5*(Y(I,J)-Y(I,J-1))
        DSTAR=DSTAR+((1.-U(I,J)*UFE)/RHO(J)+(1.-U(I,J-1)*UFE)/RHO(J-1))*
     &.5*(Y(I,J)-Y(I,J-1))
 309    CONTINUE
C FIND B.L. THICKNESS
        DO 306 J=2,JMAX
        IF(U(I,J).GE.(0.99*U(I,JMAX)))THEN
```

```
      JM1=J-1
      DUMX=(.99*U(I,JMAX)-U(I,JM1))/(U(I,J)-U(I,JM1))
      DDEL=Y(I,JM1)+(Y(I,J)-Y(I,JM1))*DUMX
      DDELP=YP(I,JM1)+(YP(I,J)-YP(I,JM1))*DUMX
      GO TO 307
      END IF
306   CONTINUE
307   CONTINUE
      LLO=.089*DDELP
      UCLAUS=.0168/UFE*DSTAR
      IOUT=0
      END IF
         DO 310 J=1,JMAX
            T(J)=H(I,J)-U(I,J)**2/2.
            TEMP=T(J)*UINF**2/CP
            RHO(J)=GGM1*PRESS/T(J)
            MU=TEMP**.5*2.32E-8/(1.+220./(TEMP*10.**(9./TEMP)))/MUINF
            IF (I .GT. ITRANS) THEN
            IF (J .EQ. 1) THEN
              MUW=MU
               MUTURB=0.
              GOTO 312
            ENDIF
            IF(J.EQ.JMAX)GOTO 312
C    CEBECI AND SMITH
            USTAR=SQRT(MUW*RHO(1)*U(I,2)/(Y(I,2)*RE*RHO(J)))
            YPLUS=USTAR*RHO(J)*YP(I,J)*RE/MU
       IF (YPLUS .GE. 15000.) THEN
        DD=1.0
        GOTO 311
        ENDIF
            IF (MODEL .EQ. 1) THEN
              VD=YPLUS/26.0
              DD=(1.0-1.0/(EXP(VD)))**2
            ENDIF
            IF (MODEL .EQ. 2) THEN
              CHAP=YPLUS/111.0
              DD=1.0-2.*COS(CHAP)*1.0/EXP(CHAP)+1.0/EXP(2.0*CHAP)
      DD=SQRT(DD)
            ENDIF
311   CONTINUE
            LLI=VK*YP(I,J)*SQRT(DD)
         IF(IOUT.EQ.1)GO TO 312
      JP=J+1
      IF(KMODL.GT.0)THEN
      IF(LLO.LT.LLI)THEN
         LL=LLO
      ELSE
      IF(YPLUS.GT.YPLSMX)THEN
      IOUT=1
      END IF
         LL=LLI
      END IF
         MUTURB=RE*RHO(J)**2*LL**2*
     &        ABS(U(I,JP)-U(I,J-1))/(2.0*DY(I,J))
      ELSE
         LL=LLI
      MUTURB=RE*RHO(J)**2*LL**2*
     &        ABS(U(I,JP)-U(I,J-1))/(2.0*DY(I,J))
      MUCLS=RE*RHO(J)*UCLAUS
         IF(MUTURB.LT.MUCLS.AND.YPLUS.GT.YPLSMX)THEN
            IOUT=1
         END IF
         IF(IOUT.EQ.0.AND.(MUTURB.GT.MUCLS))THEN
            IOUT=1
```

```
                MUTURB=MUCLS
          ' END IF
       END IF
 312   CONTINUE
                MITT=1.0/(1.+5.5*(YP(I,J)/DDELP)**6)
       TURB=MITT*FUDGE*MUTURB
       MUT(J)=MU+TURB
       MUHT(J)=MU/PRL+TURB/PRT
       MUKT(J)=MU*PRL1+TURB*PRT1
        IF (N .EQ. NT)THEN
       UPLUS=U(I,J)/USTAR
       WRITE(13,*)I,J,YPLUS,UPLUS.MU,MUTURB,FUDGE,MITT,LLI,LLO,
      $DDELP,YP(I,J)
         ENDIF
        ELSE
       MUT(J)=MU
       MUHT(J)=MU/PRL
       MUKT(J)=MU*PRL1
       END IF
 310   CONTINUE
C
C      START J LOOP--MARCHING IN ETA DIRECTION, SOLVING FOR U
C
       DO 200 J=JMM1,2,-1
         JM1=J-1
         JM2=J-2
         JP=J+1
       IF(IFSOR)THEN
         UOLD=U(I,J)
         HOLD=H(I,J)
         IF(K.EQ.1)THEN
           WOPT=1.0
         ELSE
           WOPT=W(I,J)
         ENDIF
       END IF
C
C      SETUP CONSTANTS TO DETERMINE COEFFICIENTS IN U, V, AND H EQUATIONS
C
C
C
         DRMF=(RHO(JP)*MUT(JP)+RHO(J)*MUT(J))/DYF(I,J)*.5
         DRMB=(RHO(JM1)*MUT(JM1)+RHO(J)*MUT(J))/DYB(I,J)*.5
         CON=ETAX(I,J)*U(I,J) + V(I,J)/DY(I,J)
         IF(CON.LT.0.0)THEN
           IF(J.EQ.JMM1) THEN
           CIJ2=-1.0
           CJM1=-1.0
           CJM2=0.0
           ELSE
           CIJ2=-1.5
           CJM1=-2.0
           CJM2=.5
           ENDIF
           DRM1=DRMF
           DRM2=DRMB
           J1=JP
           J2=J+2
           J3=JM1
         ELSE
         IF(J.EQ.2)THEN
           CIJ2=1.
           CJM1=1.
           CJM2=0.
         ELSE
```

199

```fortran
          CIJ2=1.5
          CJM1=2.0
          CJM2=-.5
        ENDIF
        DRM1=DRMB
        DRM2=DRMF
        J1=JM1
        J2=JM2
        J3=JP
        ENDIF
C    SOLVE FOR U VELOCITY
        CIJ=1. + CIJ1*DT/DX(I)*U(I,J) + CIJ2*DT*CON
     &        + DT*DYRE(I,J)*(DRMF+DRMB)
        CONJ1=CJM1*DT*CON + DT*DYRE(I,J)*DRM1
        CONJ2=CJM2*DT*CON
        CONIM=DT/DX(I)*U(I,J)
        CONVS=DT*DYRE(I,J)*DRM2
      IF(IFSOR)THEN
        US=(UNM1(I,J) + CIM1*CONIM*UIM1(J) + CIM2*CONIM*UIM2(J) +
     &     CONJ1*U(I,J1) + CONJ2*U(I,J2) + CONVS*U(I,J3))/CIJ
        U(I,J)=WOPT*US + (1.-WOPT)*U(I,J)
      ELSE
      E(J)=(UNM1(I,J)+CIM1*CONIM*UIM1(J)+CIM2*CONIM*UIM2(J))
      D(J)=CIJ
      CC(J)=-CONJ2
      IF (CON .GE. 0.0) THEN
        AA(J)=-CONVS
        BB(J)=-CONJ1
        E(J)=E(J)-CC(J)*U(I,J2)
        CC(J)=0.0
      ELSE
        AA(J)=-CONJ1
        BB(J)=-CONVS
      ENDIF
      ENDIF
C
C    SOLVE FOR ENTHALPY
C
        CON=ETAX(I,J)*U(I,J) + V(I,J)/DY(I,J)
        DRHF=(RHO(JP)*MUHT(JP)+RHO(J)*MUHT(J))/DYF(I,J)*.5
        DRHB=(RHO(JM1)*MUHT(JM1)+RHO(J)*MUHT(J))/DYB(I,J)*.5
        DRKF=(RHO(JP)*MUKT(JP)+RHO(J)*MUKT(J))/DYF(I,J)*.5
        DRKB=(RHO(JM1)*MUKT(JM1)+RHO(J)*MUKT(J))/DYB(I,J)*.5
        IF(CON.LT.0.0)THEN
          IF(J.EQ.JMM1) THEN
          CIJ2=-1.0
          CJM1=-1.0
          CJM2=0.0
          ELSE
          CIJ2=-1.5
          CJM1=-2.0
          CJM2=.5
          ENDIF
          DRH1=DRHF
          DRH2=DRHB
          J1=JP
          J2=J+2
          J3=JM1
        ELSE
        IF(J.EQ.2)THEN
          CIJ2=1.
          CJM1=1.
          CJM2=0.
        ELSE
          CIJ2=1.5
```

200

```fortran
              CJM1=2.0
              CJM2=-.5
          ENDIF
          DRH1=DRHB
          DRH2=DRHF
          J1=JM1
          J2=JM2
          J3=JP
          ENDIF
          CIJ=1. + CIJ1*DT/DX(I)*U(I,J) + CIJ2*DT*CON
     &        + DT*DYRE(I,J)*(DRHF+DRHB)
          CONJ1=CJM1*DT*CON + DT*DYRE(I,J)*DRH1
          CONJ2=CJM2*DT*CON
          CONIM=DT/DX(I)*U(I,J)
          CONVS=DT*DYRE(I,J)*DRH2
          TCON=DYRE(I,J)*DT*.5
       IF(IFSOR)THEN
          HS=(HNM1(I,J) + CIM1*CONIM*HIM1(J) + CIM2*CONIM*HIM2(J) +
     &        CONJ1*H(I,J1) + CONJ2*H(I,J2) + CONVS*H(I,J3) +
     &        DPDT/RHO(J)+TCON*(DRKF*U(I,JP)**2-(DRKF+DRKB)*U(I,J)**2+
     &        DRKB*U(I,JM1)**2))/CIJ
          H(I,J)=WOPT*HS + (1.-WOPT)*H(I,J)
C
C         COMPUTE THE ERROR
C
          EU=ABS(U(I,J)-UOLD)
          ERH=ABS(H(I,J)-HOLD)
          IF(EU.GE.EUMAX)EUMAX=EU
          IF(ERH.GE.EHMAX)EHMAX=ERH
        ELSE
         CCH(J)=-CONJ2
         DH(J)=CIJ
         EH(J)=(HNM1(I,J)+CIM1*CONIM*HIM1(J)+CIM2*CONIM*HIM2(J))
     &    +(DPDT/RHO(J)+TCON*(DRKF*U(I,JP)**2.-(DRKF+DRKB)*U(I,J)**2.
     &    +DRKB*U(I,JM1)**2.))
         IF (CON .GE. 0.0) THEN
          AAH(J)=-CONVS
          BBH(J)=-CONJ1
          EH(J)=EH(J)-CCH(J)*H(I,J2)
          CCH(J)=0.0
         ELSE
          AAH(J)=-CONJ1
          BBH(J)=-CONVS
         ENDIF
        ENDIF
       ENDIF
 200   CONTINUE
C END J LOOP
C
       IF(.NOT.IFSOR)THEN
       AA(1)=0.0
       CC(1)=0.0
       E(1)=0.0
       BB(1)=0.0
       D(1)=1.0
C
C NOW WORK ON THE MATRIX
C
       CALL THOMAS(U,I,JMAX,E,AA,D,CC,BB,EUMAX)
       BBH(1)=0.0
       DH(1)=1.0
       AAH(1)=0.0
       CCH(1)=0.0
       EH(1)=CP*TW(I)/UINF**2.
C
C NOW WORK ON THE ENTHALPY MATRIX
```

```fortran
C
      CALL THOMAS(H,I,JMAX,EH,AAH,DH,CCH,BBH,EHMAX)
C
      END IF
C
C
C COMPUTE THE ERROR FOR ENTHALPY AND U VELOCITY
C
      IF(EUMAX.GE.EMAX)EMAX=EUMAX
      IF(EHMAX.GE.EMAX)EMAX=EHMAX
C
C     CALCULATE V VELOCITY
      DO 250 J=2,JMM1
        JM1=J-1
        VOLD=V(I,J)
        D1=DY(I,J)/DX(I)
        D2=DYXI(I,J)/DX(I)
        VCNIJ=CVIJ*D1 + D2
        VCNJ1=CVIJ*D1 - D2
C     V(I,J)=V(I,JM1) + VCNIJ*U(I,J) + CVIM1*D1*UIM1(J) +
C    &         CVIM2*D1*UIM2(J) + VCNJ1*U(I,JM1) + CVIM1*D1*UIM1(JM1)
C    &         + CVIM2*D1*UIM2(JM1)
      V(I,J)=V(I,JM1)+((DYXI(I,J)+DYXI(I,JM1))*.5*(U(I,J)-U(I,JM1))+
     & (Y(I,J)-Y(I,JM1))*(CVIJ*(U(I,J)+U(I,JM1))+
     &                    CVIM1*(UIM1(J)+UIM1(JM1))+
     &                    CVIM2*(UIM2(J)+UIM2(JM1))))/DX(I)
        EV=ABS(V(I,J)-VOLD)
        IF(EV.GE.EVMAX)EVMAX=EV
      IF(EVMAX.GE.EMAX)EMAX=EVMAX
250   CONTINUE
C
C     CHECK CONVERGENCE
C
      IF(EMAX.LE.EPS) GO TO 420
C     IF(K.EQ.KT)THEN
C        WRITE(10,6)
C      ENDIF
C
C     END ITERATION LOOP
300   CONTINUE
420   CONTINUE
      DO 275 J=1,JMAX
        U(1,J)=U(2,J)
        H(1,J)=H(2,J)
        V(1,J)=V(2,J)
  275 CONTINUE
      DO 435 J=2,JMM1
      DEL=ABS(U(I,J) - UNM1(I,J))
      IF(DEL.GT.DELM)DELM=DEL
      DEL=ABS(H(I,J) - HNM1(I,J))
      IF(DEL.GT.DELM)DELM=DEL
435   CONTINUE
C     MOVE THE RESULTS INTO THE OLD TIME LEVEL
C
      DO 430 J=1,JMAX
        UNM1(I,J)=U(I,J)
        HNM1(I,J)=H(I,J)
        VNM1(I,J)=V(I,J)
430   CONTINUE
C
C     CALCULATE THE HEAT RATE AT THE WALL
C
      FDELY=(-3.*Y(I,1) + 4.*Y(I,2) - Y(I,3))/2.
C     CONDUCTIVITY IS EQUAL TO MUW*CP/PR=K
      MUW=TW(I)**.5*2.32E-8/(1.+220./(TW(I)*10**(9./TW(I))))
```

```
            Q(I)=MUW/PRL*RHO(1)/FDELY*(-3.*T(1) + 4.*T(2) - T(3))/2.*
     &              UINF**2/L /778.3
C TAW SHOULD USUALLY BE BASED ON EDGE CONDITIONS FORMALLY
C BUT CAN BE BASED ON FREESTREAM IF YOU ARE CONSISTENT!!!!
      IF(I.GT.ITRANS)THEN
      REC=FUDGE*(PRL)**(1./3.)+(1.-FUDGE)*SQRT(PRL)
      ELSE
      REC=SQRT(PRL)
      END IF
      REC=1.
      TAW=TE*(1.+REC*(GAM-1.)*.5*ME**2)
      HC(I)=Q(I)/(TAW- TW(I))
      HHREF(I)=HC(I)/HREF*SQRT(X(I)*L)
      TAU(I)=MUW*RHO(1)*UINF/L/FDELY*(-3*U(I,1)+4*U(I,2)-U(1,3))*.5
      CF(I)=2.*TAU(I)/(RINF*UINF**2)
C
C
C     CALCULATE THE OPTIMIZATION FACTOR OMEGA EVERY NTW TIME STEPS
C
      IF(N.EQ.(N/NTW)*NTW)THEN
      DO 519 J=2,JMM1
      W(I,J)=1.85
 519  CONTINUE
C
C
C     COMPUTE OMEGA
C
      DO 530 J=2,JMM1
      DRM=RHO(J)*MUT(J)/DY(I,J)
      DIV=1./DT + 1.5*(U(I,J)/DX(I) + ABS(U(I,J)*ETAX(I,J) +
     &    V(I,J)/DY(I,J))) + DYRE(I,J)* DRM*2.
      LAM=(-2.*SQRT(ABS(ABS((ETAX(I,J)*U(I,J) + V(I,J)/DY(I,J)) +
     &    DYRE(I,J)*DRM) *
     &    (DYRE(I,J)*DRM))))/DIV*COSJ
      IF(LAM.GT.0.97)LAM=0.97
      WN=2./(1.+SQRT(1.-LAM**2))
      IF(WN.LT.W(I,J))W(I,J)=WN
 530  CONTINUE
      ENDIF
C     END I LOOP
 400  CONTINUE
C
C     WRITE OUT SOLUTION AT A TIME STEP
C
      IF(N.EQ.(N/CNT)*CNT)THEN
      REWIND 8
      WRITE(8)A
      WRITE(10,1)N,TIME
      WRITE(6,*)'DELT=',DELM,'K=',K,'U,V,H ERR=',EUMAX,EVMAX,EHMAX
      WRITE(10,*)'DELT=',DELM,'K=',K,'U,V,H ERR=',EUMAX,EVMAX,EHMAX
      DO 440 I=1,IMAX
      WRITE(10,2)I,X(I)
      IF(IPRT.EQ.0)GO TO 451
      WRITE(10,3)
      DO 450 J=1,JMAX
      T(J)=H(I,J)-U(I,J)**2/2.
      TEMP=T(J)*UINF**2/CP
      RHO(J)=GGM1*PRESS/T(J)
      WRITE(10,4)J,Y(I,J),U(I,J),H(I,J),T(J),TEMP,V(I,J),RHO(J)
 450  CONTINUE
 451  CONTINUE
      IF(I.EQ.1) GO TO 440
      WRITE(10,5)Q(I),HHREF(I)
      TIMEP=TIME*L/UINF
C CF RATIO TO BLASIUS CAN BE BASED ON EDGE OR FREESTREAM RE
```

```fortran
           CFCF=CF(I)/.664*SQRT(REE*X(I))
       REX=RE*X(I)
       REXLOG=ALOG10(REX)
       CFREXA=CF(I)*SQRT(REX)
       CFREXB=CF(I)*REX**.8
       ST=HC(I)*778.3/(RINF*UINF*CP)
       STREXA=ST*SQRT(REX)
       STREXB=ST*REX**.8
           WRITE(9,7)TIMEP,ALPHA,X(I),HHREF(I),TW(I),CFCF
       WRITE(12,77)X(I),REX,REXLOG,ST,STREXA,STREXB,CF(I),CFREXA,CFREXB
440        CONTINUE
       ENDIF
C      END TIME LOOP
500    CONTINUE
C
C      COMPUTE PHYSICAL Y VALUES
       DO 1001 J=1,JMAX
         YP(1,J)=0.0
       WRITE(11,8)X(1),Y(1,J),YP(1,J)
1001   CONTINUE
       DO 650 I=2,IMAX
         DO 460 J=1,JMAX
           T(J)=H(I,J) - U(I,J)**2/2
           RHO(J)=GGM1*PRESS/T(J)
460      CONTINUE
C
         YP(I,1)=0.0
         WRITE(11,8)X(I),Y(I,1),YP(I,1)
         DO 470 J=2,JMAX
       YP(I,J)=YP(I,J-1) + (1/RHO(J) + 1/RHO(J-1))/2*(Y(I,J)-Y(I,J-1))
           WRITE(11,8)X(I),Y(I,J),YP(I,J)
470      CONTINUE
650    CONTINUE
8      FORMAT(3(2X,E13.5))
C
C      THIS SECTION FIGURES OUT THE THEORETICAL NONISOTHERMAL VALUES
C      FOR H/HREF
C
C CAUTION! TSTAR BASED ON TW1! DO YOU WANT CONSTANT REFERENCE OR ACTUAL TW?
       TAW=TE*(1.+SQRT(PRL)*(GAM-1.)*.5*ME**2)
       TSTAR=TE+.5*(TW1-TE)+.22*(TAW-TE)
       RSTAR=PE/(RG*TSTAR)
       MUSTAR=(2.32E-8*TSTAR**.5/(1.+220./(TSTAR*10.**(9./TSTAR))))
       HISO=.332*CP*SQRT(MUSTAR*RSTAR*UE)/PRL**(2./3.)*SQRT(X(I)*L)/HREF
       WRITE(6,*)'HISO=',HISO
       WRITE(9,*)'HISO=',HISO
       DO 1000 I=1,IMAX
         IF (I .GE. ITRANS) THEN
           XBAR=(X(I)-XTRANS)/EXTENT
           IF (I .GE. ITURB) THEN
             FUDGE=1.0
           ELSE
             FUDGE=1.0-1.0/(EXP(.412*XBAR**2))
           ENDIF
         ENDIF
         HT=HISO
         IF(X(I).GE.XTW2)THEN
           IF(ABS(XTW2-X(I)).LT.1E-3)THEN
             DO 1002 J=1,4
               XX=X(I)+ DX(I)/FLOAT(5)*FLOAT(J)
       TAW=TE*(1.+SQRT(PPL)*(GAM-1)*.5*ME**2)
       TSTAR=TE+.5*(TW1-TE)+.22*(TAW-TE)
       RSTAR=PE/(RG*TSTAR)
       MUSTAR=(2.32E-8*TSTAR**.5/(1.+220./(TSTAR*10.**(9./TSTAR))))
       HISO=.332*CP*SQRT(MUSTAR*RSTAR*UE)/PRL**(2./3.)*SQRT(X(I)*L)/HREF
```

```fortran
          PHI=((TAW-TW1)-(1.-(XTW2/XX)**.75)**(-1./3.)*
     &          (TW2-TW1))/(.9*TOINF-TW2)
          HT=HISO*PHI
          WRITE(9,9)XX,HT
1002          CONTINUE
          ELSE
            XX=X(I)
      TAW=TE*(1.+SQRT(PRL)*(GAM-1.)*.5*ME**2)
      TSTAR=TE+.5*(TW1-TE)+.22*(TAW-TE)
      TAW=TE*(1.+SQRT(PRL)*(GAM-1.)*.5*ME**2)
      RSTAR=PE/(RG*TSTAR)
      MUSTAR=(2.32E-8*TSTAR**.5/(1.+220./(TSTAR*10.**(9./TSTAR))))
      HISO=.332*CP*SQRT(MUSTAR*RSTAR*UE)/PRL**(2./3.)*SQRT(X(I)*L)/HREF
          PHI=((TAW-TW1)-(1.-(XTW2/XX)**.75)**(-1./3.)*
     &          (TW2-TW1))/(.9*TOINF-TW2)
          HT=HISO*PHI
          WRITE(9,9)X(I),HT
          ENDIF
          ELSE
          WRITE(9,9)X(I),HT
          ENDIF
1000  CONTINUE
      REWIND 8
      WRITE(8)A
1     FORMAT(///,2X,'N=',I6,5X,'TIME=',F15.6,1X,'SEC')
2     FORMAT(//,2X,'I=',I6,5X,'X-LOCATION=',F13.5)
3     FORMAT(/,4X,'J',5X,'Y-LOC',5X,'U',5X,'H',5X,'T',5X,'TEMP(R)',
     &5X,'V',5X,'RHO',/)
4     FORMAT(1X,I3,7F13.5)
5     FORMAT(/,2X,'HEAT RATE (Q)=',F13.6,5X,'H/HREF=',F13.6)
6     FORMAT(/,'THIS SOLUTION HAS NOT CONVERGED WITH KT ITERATIONS',/)
7     FORMAT(7(2X,F13.5))
9     FORMAT(34X,2(2X,F13.5))
77    FORMAT(9(1X,E13.5))
600   CONTINUE
      CLOSE(8)
      CLOSE(10)
      CLOSE(12)
      STOP
      END
      SUBROUTINE FIRST(IMAX,JMAX,RE,CP,TW,TE,UE,UINF,PRESS,GGM1,
     &                 X,Y,U,V,H,PR,XTW2,TW1,TW2,IMET,GRDFC)
C     THIS SUBROUTINE TAKES THE BLASIUS SOLUTION, MODIFIES IT BY
C     THE DENSITY, AND FORMS A GRID.  IT ALSO DETERMINES INITIAL
C     CONDITIONS
      DIMENSION X(61),Y(61,59),DY(61),U(61,0:60),H(61,0:60),RHO(59)
      DIMENSION V(61,59),YN(59),YOLD(59),TW(61)
C     THIS IS A BLASIUS PROFILE OPTIMIZED FOR RE=2.E6.  THIS MUST
C     BE MODIFIED FOR MY REYNOLD'S NUMBER.  ALSO, I AM BASING THIS
C     GRID ON THE THERMAL BOUNDARY LAYER THICKNESS SO MODIFY Y WITH
C     THE PRANDTL NUMBER
C     DATA YOLD/0.,.000248,.0005,.000756,.001024,.001316,.00166,
C     &          .002,.002672,.003402,.004342,.005548,.007099,
C     &          .009092,.01165,.014945,.019174,.024609,.031593,
C     &          .040568,.0521,.06692,.085963,.11043,.14187,.18226,
C     &          .23414,.30076,.3862,.496/
C     DX=1./(IMAX-1.)
C     DO 100 I=1,IMAX
C       X(I)=DX*(I-1)
C       DO 120 J=1,JMAX
C         Y(I,J)=YOLD(J)*SQRT(2.E6)/SQRT(RE)*SQRT(X(I))/PR
C120    CONTINUE
C100   CONTINUE
C
C READ GRIDIN
```

```fortran
      DO 100 I=1,IMAX
      DO 200 J=1,JMAX
      READ(7,9999)X(I),Y(I,J)
 9999 FORMAT(2E13.5)
 200  CONTINUE
 100  CONTINUE
C  TO USE ANALTICAL METRIC FOR YXI FOR I=1 TO IMET
C  Y POINTS AT I=IMET ARE SCALED BY SQRT(X)
C  THIS WILL NOT GUARANTEE A SMOOTH GRID PAST I=IMET
      DO 110 I=1,IMET
      DO 110 J=1,JMAX
      Y(I,J)=Y(IMET,J)*SQRT(X(I)/X(IMET))
 110  CONTINUE
C
C     DEFINE THE WALL TEMPERATURES-- IF TW1=TW2 NO TEMP STEP
C                                    IF TW1<TW2 TEMP STEP
C
      DO 11 I=1,IMAX
        IF(X(I).LE.XTW2)THEN
        TW(I)=TW1
        ELSE
        TW(I)=TW2
        ENDIF
 11     CONTINUE
      HE=CP*TE/UINF**2 + (UE/UINF)**2/2.
      DO 150 I=2,IMAX
        HW=CP*TW(I)/UINF**2
        HSUB=HE - HW
        DO 130 J=1,JMAX
          DELTA=5.2/SQRT(RE)*SQRT(X(I))
          DELTAT=DELTA
          IF(Y(I,J).LE.DELTA)THEN
            U(I,J)=UE/UINF*(1.5*Y(I,J)/DELTA - .5*(Y(I,J)/DELTA)**3.)
          ELSE
          U(I,J)=UE/UINF
          ENDIF
          V(I,J)=0.0
          IF(Y(I,J).LE.DELTAT)THEN
            H(I,J)=HW + HSUB*(1.5*Y(I,J)/DELTAT - .5*(Y(I,J)/DELTAT)**3)
          ELSE
            H(I,J)=HE
          ENDIF
          TEMP=H(I,J) - U(I,J)**2/2.
          RHO(J)=GGM1*PRESS/TEMP
 130      CONTINUE
        DO 145 J=2,JMAX
          Y(I,J)=Y(I,J)*GRDFC
 145    CONTINUE
 150    CONTINUE
      DO 160 J=1,JMAX
        U(1,J)=U(2,J)
        V(1,J)=0.0
        H(1,J)=H(2,J)
 160  CONTINUE
      RETURN
      END
      SUBROUTINE TERPO(ALPHA,UINF,RINF,CP,UE,PE,HE)
C
C     THIS SUBROUTINE INTERPOLATES TO GET VELOCITY,PRESSURE,TEMPERATURE,
C     AND ENTHALPY AT A NEW ANGLE
C
      DIMENSION EVEL(14),ETEMP(14),EPRESS(14)
      DATA EVEL/0.,4843.7962,4843.7962,4834.5371,4823.7297,4811.1933,
     &          4796.8408,4780.5741,4762.3358,4742.0933,4719.8062,
     &          4695.4522,4669.00,4639.60/
```

```fortran
      DATA ETEMP/0.,65.62,65.62,73.08,81.78,91.84,103.33,116.30,130.80,
     &          146.83,164.39,183.49,204.12,227.99/
      DATA EPRESS/0.,1.3063,1.3063,1.7262,2.2334,2.8322,3.5250,4.3135,
     &          5.1985,6.1801,7.2581,8.4319,9.7010,11.060/
C
      IALPH=INT(ALPHA)
      UE=EVEL(IALPH) + (ALPHA-IALPH) * (EVEL(IALPH+1) - EVEL(IALPH))
      TE=ETEMP(IALPH) + (ALPHA-IALPH) * (ETEMP(IALPH+1) - ETEMP(IALPH))
      HE=CP*TE + UE**2/2
      PE=EPRESS(IALPH)+(ALPHA-IALPH)*(EPRESS(IALPH+1) - EPRESS(IALPH))
      RETURN
      END
C
CCCCCCCCCCCCCCCCCCCCCCCCCCCCCCCCCCCCCCCCCCCCCCCCCCCCCCCCCCCCCCCCCCCCCCCCCC
C
      SUBROUTINE THOMAS(U,I,JMAX,E,AA,D,CC,BB,EUMAX)
      DIMENSION U(61,0:60),E(60),AA(60),D(60),CC(60),BB(60)
      JMM1=JMAX-1
      DO 530 J=2,JMM1
        JM=J-1
        D(J)=D(J)-BB(J)*AA(JM)/D(JM)
        AA(J)=AA(J)-BB(J)*CC(JM)/D(JM)
        E(J)=E(J)-BB(J)*E(JM)/D(JM)
  530 CONTINUE
C
C NOW SOLVE FOR U OR H
C
      UOLD=U(I,JMM1)
      U(I,JMM1)=(E(JMM1)-AA(JMM1)*U(I,JMAX))/D(JMM1)
      EU=ABS(U(I,JMM1)-UOLD)
      IF (EU .GE. EUMAX) THEN
        EUMAX=EU
      ENDIF
      DO 540 J=JMAX-2,2,-1
        UOLD=U(I,J)
        JP=J+1
        JP2=J+2
        U(I,J)=(E(J)-AA(J)*U(I,JP)-CC(J)*U(I,JP2))/D(J)
        EU=ABS(U(I,J)-UOLD)
        IF (EU .GE. EUMAX) THEN
          EUMAX=EU
        ENDIF
  540 CONTINUE
      RETURN
      END
```

Appendix D

Mach Number Iteration Program

```
100 PRINT "What is Patm in mm Hg?"
105 GAM=1.4
110 INPUT PATM
120 PRINT "What is the number of divisions of Pt1?"
130 INPUT P1
140 PT1=(P1*755!)/10! - PATM
145 PRINT "pt1 = " PT1          ' mm of mercury
150 PRINT "What is the number of divisions of Pt0?"
160 INPUT P0
170 PRINT
180 DP=767.0/P0/100!
190 PT0=PATM-DP          ' mm of mercury
200 PR=PT0/PT1
210 N=5.999          ' initial guess
220 A=(GAM+1!)/(2!-GAM)
230 B=(1/M^2+(GAM-1)/2)/(.5*(GAM-1))
250 C=(GAM-1)/(GAM+1)
260 MACH=(A*(C+(1!/(PR^(GAM-1)*B^GAM))))^.5
270 DIFF=ABS(MACH-N)
272 IF DIFF <.001 THEN PRINT "pt0 = " PT0
275 IF DIFF <.001 THEN PRINT "pt0/pt1 = " PR
280 IF DIFF <.001 THEN PRINT "mach=" MACH ELSE N=MACH:GOTO 220
300 PRINT "Is there any more pressure data?"
310 PRINT "Type a 1 if yes, 0 if no"
320 INPUT ANS
330 IF ANS = 1 GOTO 150
```

Appendix E

Calibration of the VKI H-3 Wind Tunnel

Purpose

To determine the size of the flat plate model to construct, the scope of the Mach 6 uniform free jet must be determined. The first time the tunnel was calibrated was after its installation in 1970 (29). That previous calibration showed the existence of a small centerline disturbance and the slow streamwise growth of the outer shear layer.

This test will examine the streamwise distribution from the nozzle exit, taking measurements every 50 mm. Also the uniformity of the flow at each streamwise position will be examined by rotating the rake 30 degrees at a time from a vertical position until the entire cross-sectional area is examined.

3.3.2 Theory

To determine the uniformity of the flow, a distribution of pitot pressure is measured along various cross sections of the test chamber. The pressure in the reservoir is also monitored throughout the test. The ratio of the reservoir pressure, P_{o1}, and the test chamber total pressure, P_{o2}, gives the Mach number of the flow coming out of the nozzle exit.

The pitot pressure in the test chamber is actually the total pressure behind a normal shock. The normal shock is

present due to the presence of the pitot probe itself. Isentropic flow relations and normal shock theory can be used to find the initial Mach number (35:148). The ratio of total pressures can be written in terms of the initial Mach number.

$$\frac{P_{o1}}{P_{o2}} = \left[\frac{2\gamma}{\gamma+1} M_1^2 - \frac{\gamma-1}{\gamma+1} \right]^{1/(\gamma-1)} \left[\frac{1 + .5(\gamma-1) M_1^2}{.5(\gamma+1) M_1^2} \right]^{\gamma/(\gamma-1)} \quad (E.1)$$

This equation can be rewritten, solving for M_1, so that

$$M_1^2 = \frac{(\gamma+1)}{2\gamma} \left[\frac{(\gamma-1)}{(\gamma+1)} + (P_{o1}/P_{o2})^{\gamma-1} [.5(\gamma+1)]^{\gamma} [1/M_1^2 + .5(\gamma-1)]^{-\gamma} \right]$$

$$(E.2)$$

An iterative procedure must be used to solve for M_1 since it appears on both sides of the equation. Using an initial guess for M_1 in the equation as 5.999, the solution for the actual M_1 given the total pressure ratios will be obtained very quickly. The Mach number output is compared with the Mach number input, and then the output is used as the next iteration's input. The iteration continues until the difference between the input and output Mach numbers is less than 0.001. A computer program which does this iteration is included in Appendix D.

Description of Equipment

A pitot rake with eleven pitot tubes was used to measure the total pressure in the test chamber. The

detailed dimensions of the pitot rake are given in Figure E.1. The pitot rake tubes originally extended 50 mm ahead of the metal plate support, but due to tunnel blockage problems, the probes were shortened until only 10 mm of the pitot tube extended ahead of the plate support. The shortening of the probes had no effect on the results, but this is discussed in the section on error analysis and repeatability. The probe centerlines are 13 mm apart.

The pitot probes were connected to a Scani-Valve pressure transducer. The probes were read sequentially during each run, beginning with the number 1 probe and advancing to the number 11 probe. The data was recorded on a Graphispot recorder on advancing graph paper. The total pressure for the reservoir was measured by a pressure transducer and also recorded on a Graphispot recorder. The data acquisition system is shown in Figure E.2.

The installed pressure rake is shown in Figure E.3. This is the position the rake is in during the startup sequence of the tunnel. After the tunnel has started, the rake is injected into the free jet. Figure E.4 shows the position of the rake after injection. In this particular figure, the rake is at an orientation of 120°. Note there is a portion of the diffuser nozzle cut to permit the injection of the rake. Due to tunnel blockage problems, a
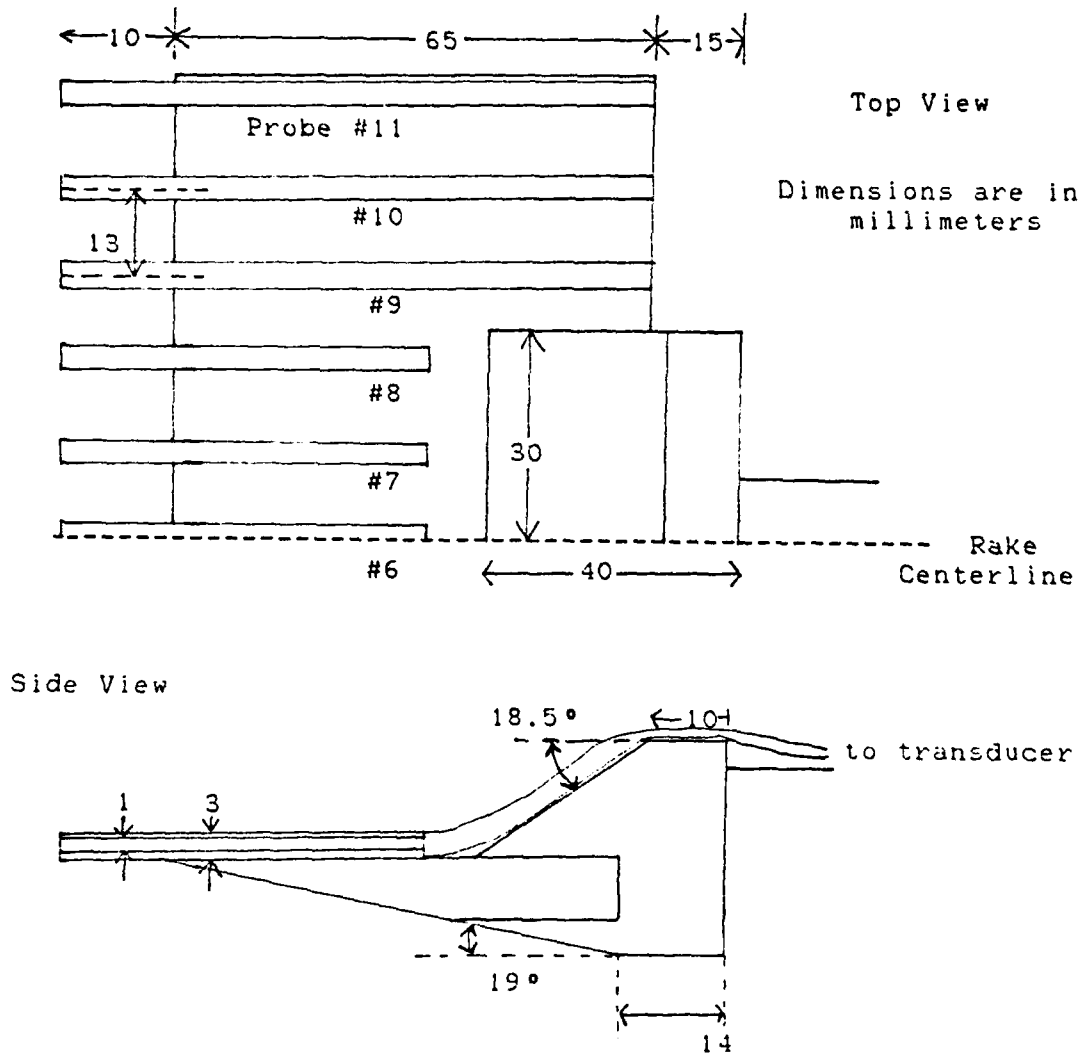
Figure E.1.   Pitot Pressure Rake
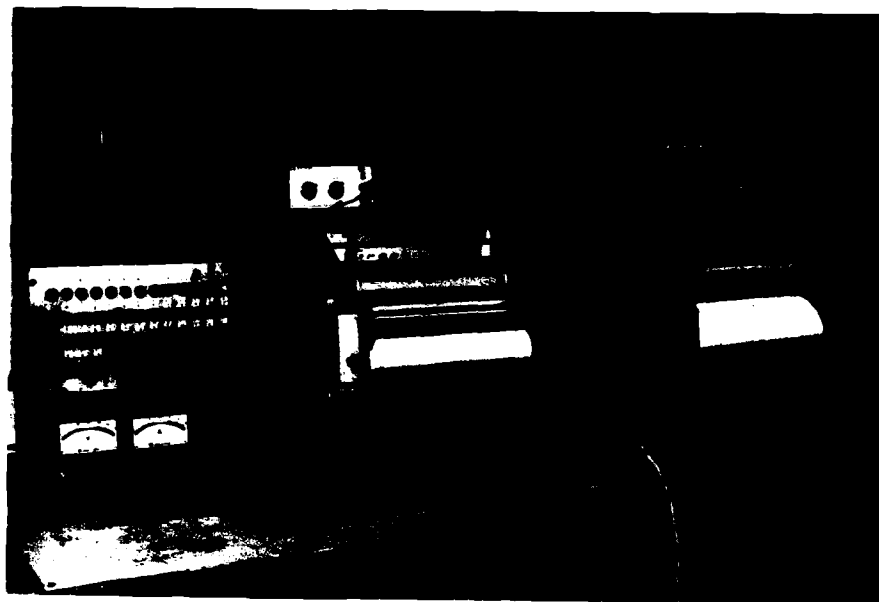
Figure E.2.   Data Acquisition System for Calibration

Figure E.3.   Pitot Rake Installed

Figure E.4   Pitot Rake in Injected Position

metal piece was constructed and attached to the rake support
to replace the cut portion of the diffuser during the test.
After injection, the additional piece fits closely to the
diffuser.

The reservoir pressure transducer was calibrated
against a manometric balance equipped with precision
weights.   During tests, the transducer was referenced
against atmospheric pressure.   The pitot rake transducer was
calibrated against a vacuum pump and a mercury manometer.
During tests, it also was referenced against atmospheric
pressure.   The atmospheric pressure was read from a mercury
manometer.

The orientation of the injected rake is 0° when the
rake is vertical and probe number 1 is on the top. The
injected rake is at 90° when it is horizontal and probe
number 1 is at the left most position when looking forward
toward the reservoir. The other angles, 30°, 60°, 120°, and
150° are defined accordingly.

Results

Data was taken in the streamwise direction up to 143.5
mm from the nozzle exit. The previous studies (1; 14; 15;
53) at VKI had used models that were 296 mm in length and
110 mm in width, so it had originally been intended to
calibrate the tunnel as far as 300 mm behind the nozzle
exit. However, the tunnel would block after injection of
the pressure rake at x = 150 mm. After several changes to
the wind tunnel and model, the farthest distance the
calibration tests were eventually run at was 143.5 mm behind
the nozzle exit. At this distance, the data set could be
fairly well completed at all the rake orientations.

Tunnel Blockage

The tunnel blockage phenomena is linked to the
complexity of the flow which has to pass through the
diffuser. The complex flow is composed of the wake of the
model, the shock waves formed from the model, and also the
distance from the nozzle exit and the diffuser nozzle
entrance. It appeared that the tunnel blockage occurrence
was primarily a function of the location of the diffuser,

but still a function of rake orientation and reservoir stagnation pressure.

When the rake was 153.5 mm behind the nozzle exit, blockage occurred at Po = 10 and 20 bars. At this time, the tests at the 90° rake orientation had already been completed. It was at this point that the pressure probes were shortened from 50 mm to 10 mm in length. That way the rake support could be moved closer toward the nozzle exit, and therefore the diffuser nozzle entrance could also be moved closer to the nozzle exit. The tunnel ran for perhaps a second after injection of the rake at 153.5 mm with Po = 20 bars, and then blocked. The rake and diffuser nozzle were moved forward 10 mm and the tunnel ran successfully. However, at 143.5 mm, blockage still occurred when the rake was at 60° and 90° for Po = 10 bars, so no data could be taken at those conditions. However, the tunnel ran for all the orientations at Po = 20 bars at x=143.5 mm.

Although blockage occurred with the rake at 90°, x = 153.5 mm and Po = 20 bars, at the end of the calibration tests it was found that the tunnel did not block when the rake was at 150° and Po = 20 bars. It was promising to see that some of the rake orientations were less disturbing to the flow and did not cause tunnel blockage. Unfortunately, time did not permit an extensive study on the tunnel blockage phenomena, so the exact cause of blockage could not be determined.

Error Analysis and Repeatability

The error analysis for the Mach number calculations was completed by examining the equation of total pressure ratio, equation (E.1). The natural logarithm was taken of the entire equation and then each term was partially differentiated with respect to P_{o1}, P_{o2}, or M_1. The resulting equation is

$$\frac{dP_{o1}}{P_{o1}} - \frac{dP_{o2}}{P_{o2}} = A \frac{dM_1}{M_1} \qquad (E.3)$$

where

$$A = \frac{4\gamma M_1^2 / [(\gamma-1)(\gamma+1)]}{[2\gamma M_1^2/(\gamma+1) - (\gamma-1)/(\gamma+1)]} + \frac{\gamma M_1^2}{[1 + .5(\gamma-1)M_1^2]}$$

$$+ \frac{\gamma(\gamma+1)M_1^2/(\gamma-1)}{[.5(\gamma+1)M_1^2]} \qquad (E.4)$$

If $M_1 = 6.0$ and $\gamma = 1.4$, then $A = 4.17$. The error in Mach number is then

$$\frac{dM_1}{M_1} = \left[\left[\frac{1}{4.17} \frac{dP_{o1}}{P_{o1}} \right]^2 + \left[\frac{1}{4.17} \frac{d P_{o2}}{P_{o2}} \right]^2 \right]^{1/2} \qquad (E.5)$$

The same type of analysis is completed on the equations used to calculate P_{o1} and P_{o2} from the graphispot recorder data, accounting for errors of ±0.2 mm in the atmospheric pressure readings. P_{o1} varied 1.3 division during a test

while P_{o2} could be read to within 0.3 division and varied 0.3 divisions during a test. This corresponds to errors of

$$dPATM/PATM = 0.000263$$

$$
\begin{aligned}
dP_{o1}/P_{o1} &= 0.0158 & \text{for } P_{o1} &= 10 \text{ bars} \\[6pt]
dP_{o2}/P_{o2} &= 0.0042 & \text{for } P_{o1} &= 10 \text{ bars} \\[6pt]
dM_1/M_1 &= 0.0039 & \text{for } P_{o1} &= 10 \text{ bars} \\[6pt]
dP_{o1}/P_{o1} &= 0.0073 & \text{for } P_{o1} &= 20 \text{ bars} \\[6pt]
dP_{o2}/P_{o2} &= 0.0070 & \text{for } P_{o1} &= 20 \text{ bars} \\[6pt]
dM_1/M_1 &= 0.0024 & \text{for } P_{o1} &= 20 \text{ bars}
\end{aligned}
\tag{E.6}
$$

The errors in the calibration tests are listed in Table E.1.

Table E.1.   Measurement Errors in Calibration

	dM	$d(P_{o2}/P_{o1})$
P_{o1} = 10 bars	±0.024	±0.00035
P_{o1} = 20 bars	±0.015	±0.00022

Several runs were repeated to verify that shortening the probe lengths had no effect on the data taken later. This is shown in Figures E.5 through E.7. Figure E.7 shows results for the probe shortening and also repetition of a test with the same probe length. All the tests are repeatable to within the measurement errors.
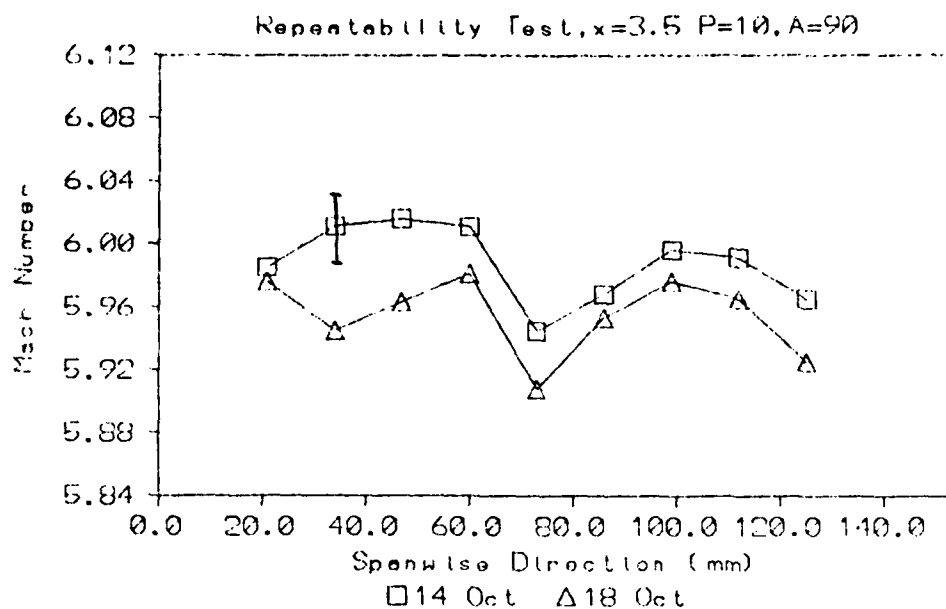
Figure E.5. Repeatability, x = 3.5 mm,
Po = 10 bar, A = 90°
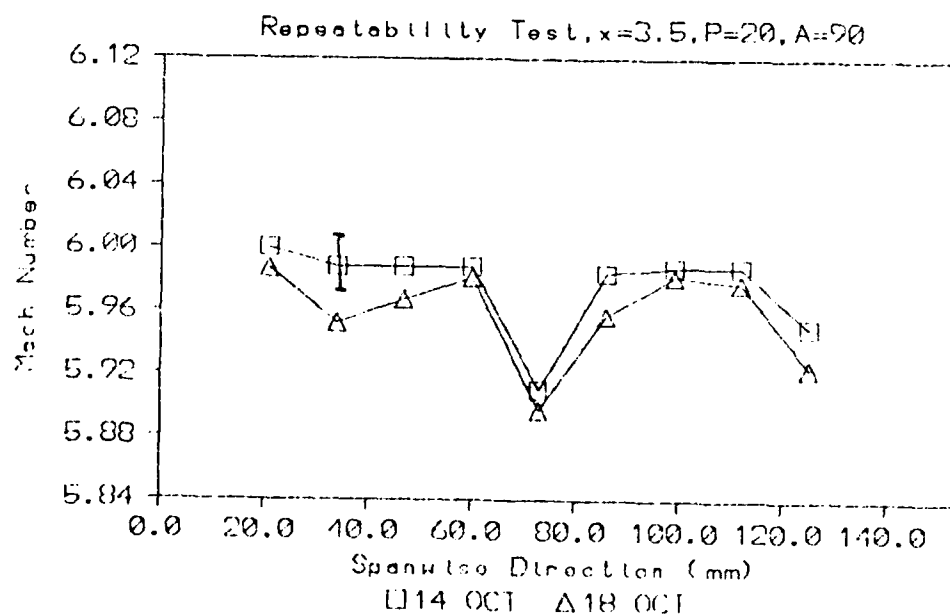
Figure E.6. Repeatability, x = 3.5 mm,
Po = 20 bar, A = 90°
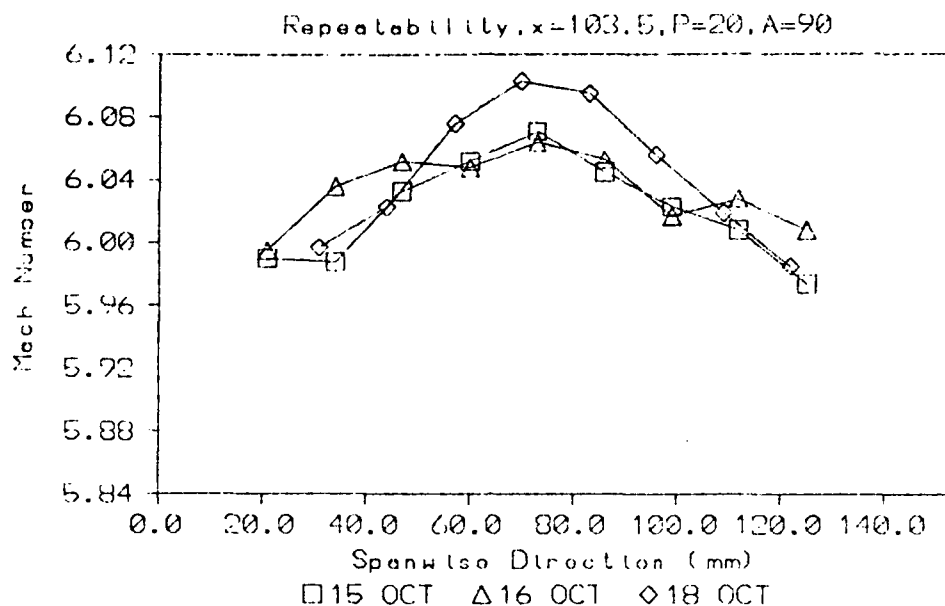
Figure E.7. Repeatability, x = 103.5 mm,
Po = 20 bar, A = 90°

Streamwise Flow

The streamwise flow at a radial distance of 39 mm from the centerline is examined by plotting the data from probes 3 and 9 versus streamwise direction, x. The trend of the streamwise flow is shown in Figures E.8 and E.9. For each angle, there are two sets of data, for viewing purposes the number 3 probe was plotted slightly ahead of the probe 9 data, although the probes were actually at the same x location. The trend is a slow rise in Mach number as the distance from the nozzle increases from a mean Mach number of 5.97 to a mean Mach number of 6.00. This is not unexpected as the flow exiting out of the nozzle continues

to expand slightly in the open test section, thereby slightly increasing the flow velocity and Mach number.

The centerline streamwise flow is examined by plotting the data from probe number 6 versus x. It can be seen in Figures E.10 and E.11. The trend of a rise in Mach number is also seen as in the $r = 39$ mm case, but the rise in Mach number is more evident on the centerline. The rise is sudden between $x = 3.5$ mm and 53.5 mm, but then the Mach number increases very slowly, perhaps even becoming constant near Mach $= 6.05$ after $x = 143.5$ mm.

Cross-sectional Variation

The Mach number is fairly constant over the cross section of the test section with variations of approximately 2 % for the flow at Po = 10 bar and 2.2% for the flow at Po = 20 bar at the center of the flow. This can be seen from Figures E.12 through E.19. The centerline disturbance will be examined in a later section. The flow has been determined to be axisymmetric and after taking into account the measurement error, there are no significant trends due to the angular orientation of the rake.

Comparing the plots at $P_{o1} = 10$ bars, and $P_{o1} = 20$ bars reveals no significant difference between the plots when taking the measurement error into account. This means there are no Reynolds numbers effects for the uniform flow at Mach 6 in the range of Reynolds numbers that have been studied.

Shear Layer

The ratio P_{o2}/P_{o1} is plotted in Figures E.20 through E.23 to illustrate the growth of the shear layer when $P_{o1} = 20$ bars. The boundaries of the shear layer/uniform flow region are shown in Table E.2. The errors in these interpretations are approximately ±2 mm.

Using the data from Table E.2, the region of uniform flow is sketched in Figure 3.2. The boundary beginning at the nozzle exit is interpolated to 143.5 mm behind the nozzle exit. After x = 143.5 mm, the region of uniform flow could be extrapolated to 300 mm behind the nozzle exit. However, the region of uniform flow resulting from the extrapolation appears unrealistic. It is difficult to believe that the shear layer would grow as fast as the extrapolation indicated. Therefore, this seems to indicate that there is not enough information available to draw a conclusion about the extent of the growth of the shear layer farther than the 143 mm after the nozzle exit.

Table E.2. Definition of Uniform Flow Regions

x location (mm)	left edge of shear layer (mm)	right edge of shear layer (mm)	diameter of uniform flow region (mm)
3.5	17 ± 2	134 ± 2	117 ± 2
53.5	16 ± 2	135 ± 2	118 ± 2
103.5	22 ± 2	133 ± 2	111 ± 2
143.5	27 ± 2	125 ± 2	98 ± 2

Centerline Disturbance

A centerline disturbance was evident in every test. This disturbance can be seen in Figures E.12 through E.19. The disturbance was, at worst, approximately 2.2% of the mean flow. The centerline disturbance only affected the center probe at the nozzle exit, but this disturbed region expanded to affect the three center probes (a width of at least 26 mm) at x = 143.5 mm from the nozzle exit. The centerline disturbance was negative at the exit and then became a positive disturbance at x = 53.5 mm. The centerline flow behaves as if it were a separate jet itself - increasing in Mach number as it expands inside the larger uniform jet of Mach 6.

Conclusions of Calibration

This study shows the presence of a slow growing shear layer and centerline disturbance. These results are similar to those found by an earlier study (29). The extent of the uniform flow has been obtained and the Mach number variations have been shown to be within 2.2% in this uniform flow region.

The flow can be considered to be a uniform axisymmetric jet of Mach 6. The uniform flow has been determined to be approximately 117 ± 2 mm in diameter at the nozzle exit and remains relatively constant until a distance of 103.5 mm downstream of the nozzle exit. The uniform flow then decreases to approximately 98 ± 2 mm in diameter at 143.5 mm

downstream of the nozzle exit. More information needs to be obtained farther downstream of the nozzle exit to determine the extent of the uniform flow. This would entail, not only conducting more tests, but designing a new pressure rake to avoid the occurrence of tunnel blockage.
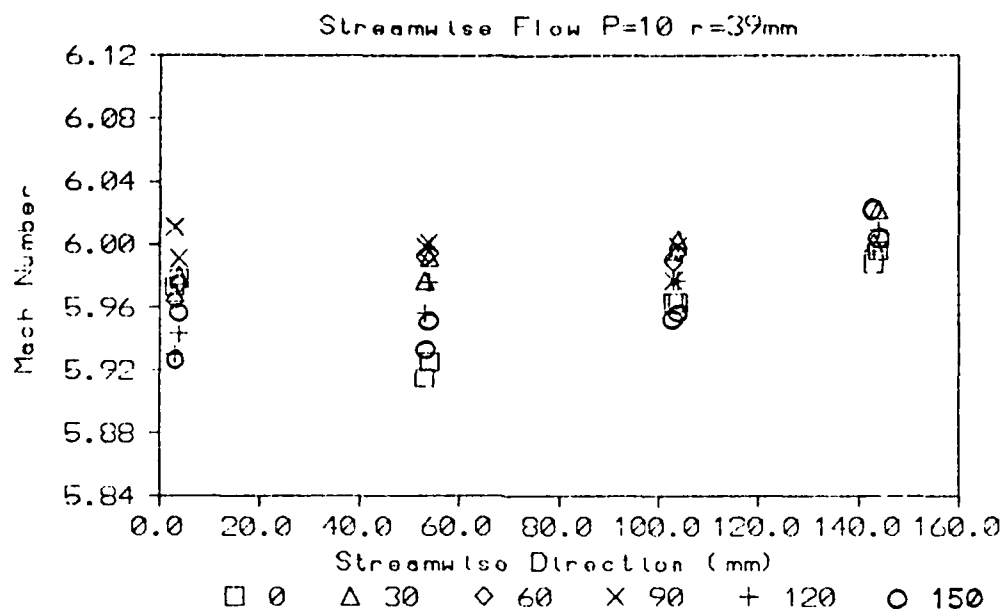
Figure E.8.   Streamwise Flow, r = 39 mm, Po = 10 bar
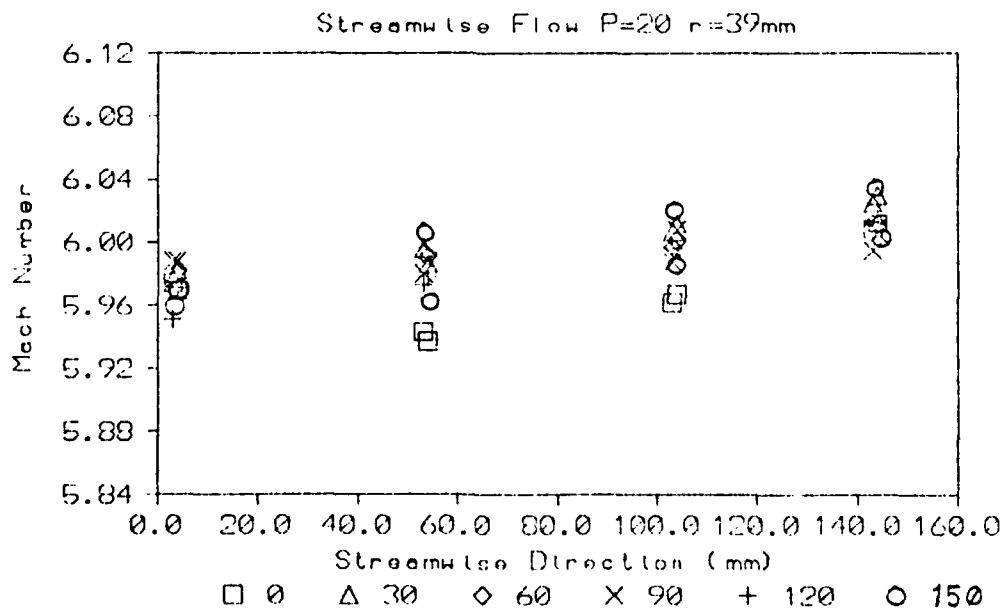
Figure E.9.   Streamwise Flow, r = 39 mm, Po = 20 bar
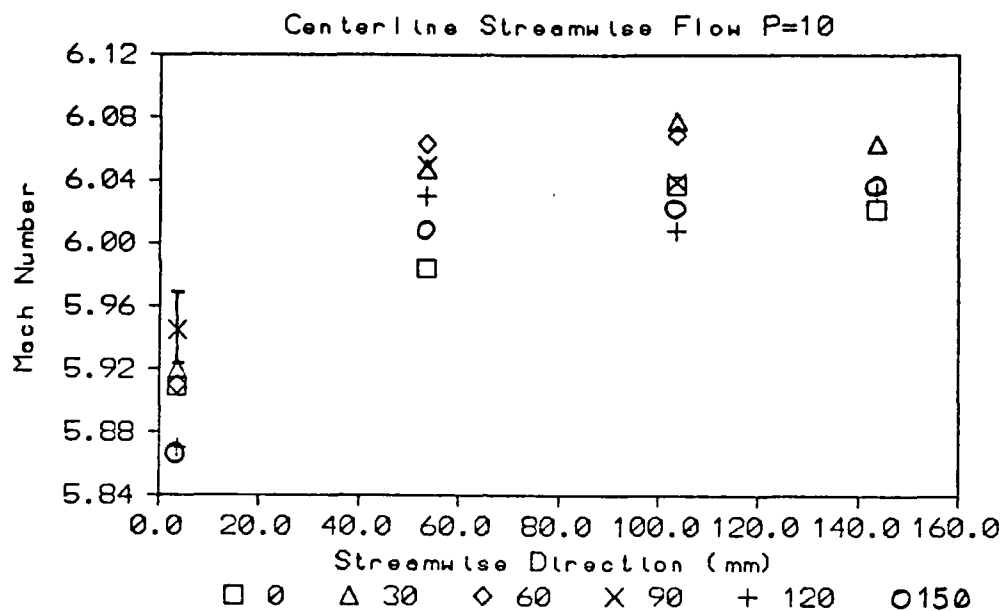
Figure E.10. Centerline Streamwise Flow, Po = 10 bar
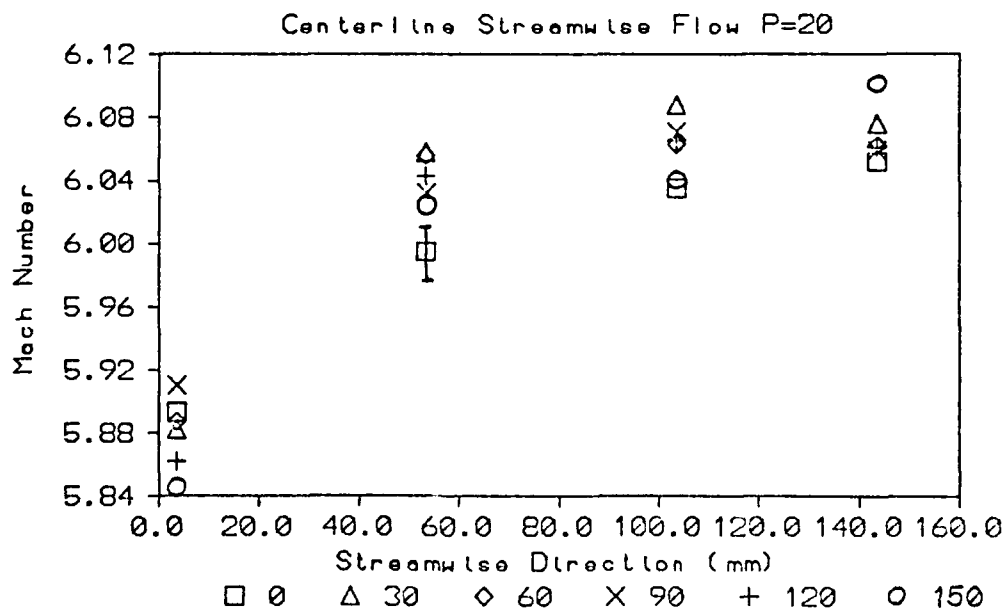
Figure E.11. Centerline Streamwise Flow, Po = 20 bar

UNIFORM FLOW X=3.5 P=10
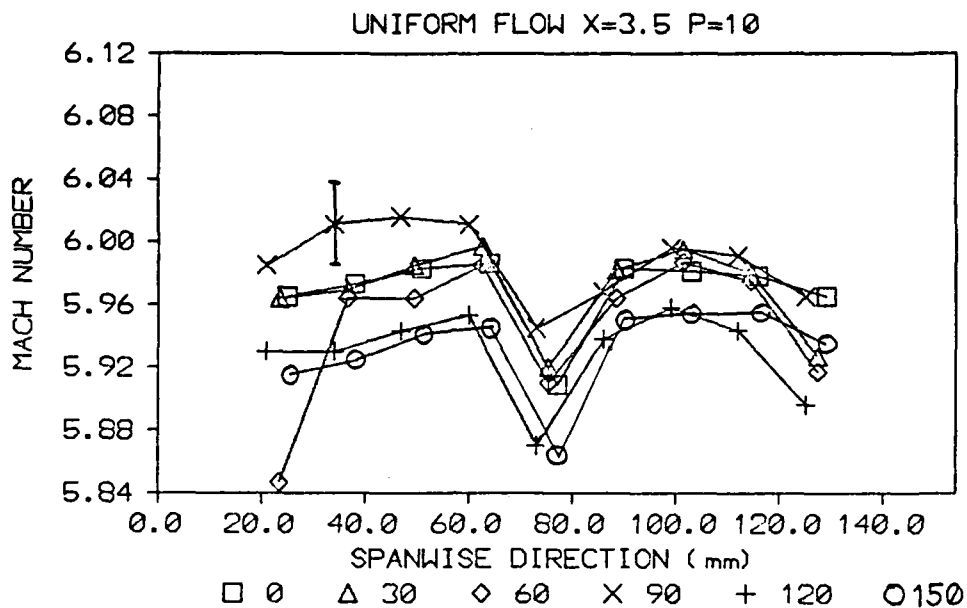
Figure E.12. Uniform Flow, x = 3.5 mm, Po = 10 bar

UNIFORM FLOW X=3.5 P=20
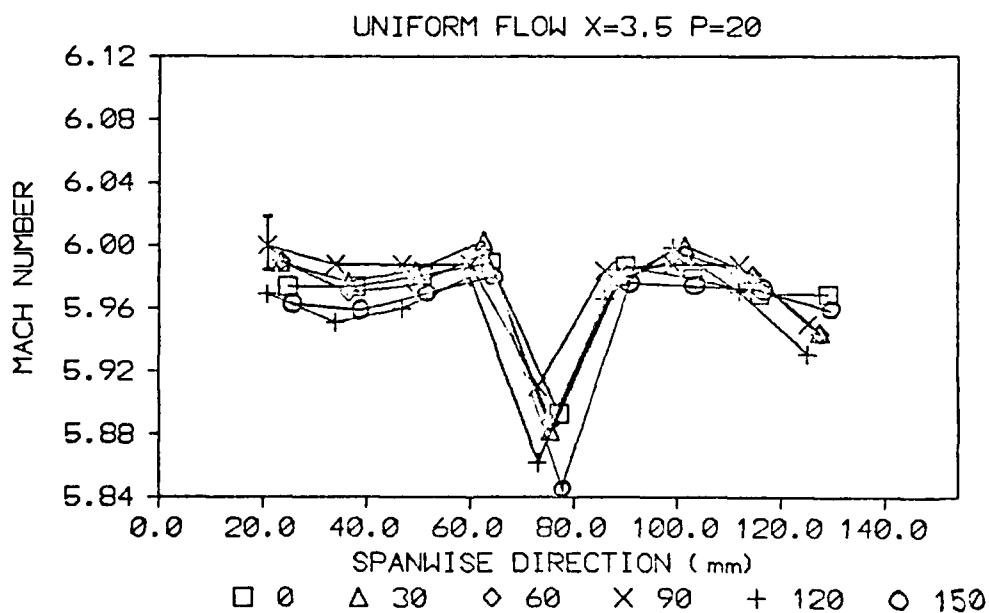
Figure E.13. Uniform Flow, x = 3.5 mm, Po = 20 bar
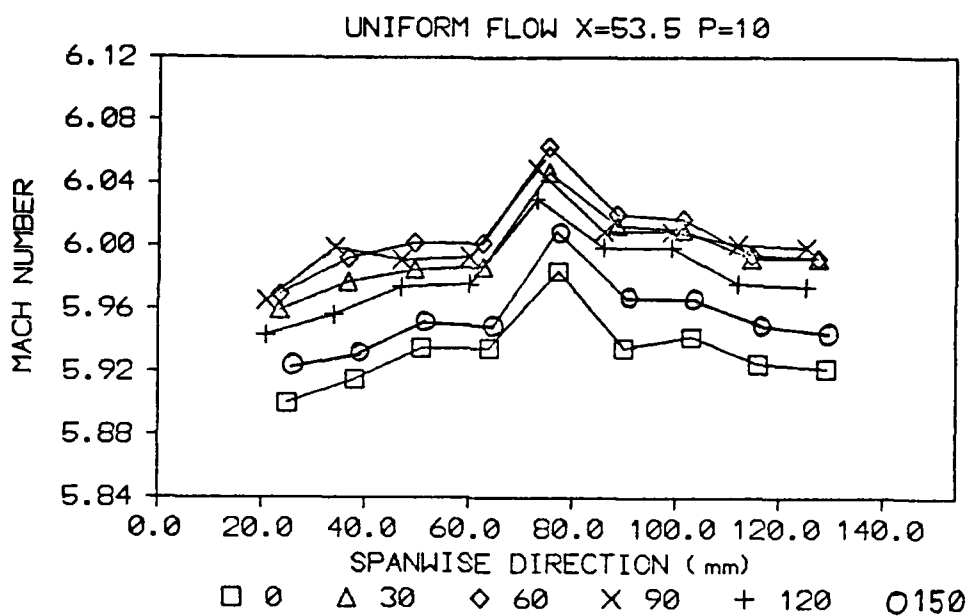
Figure E.14. Uniform Flow, x = 53.5 mm, Po = 10 bar
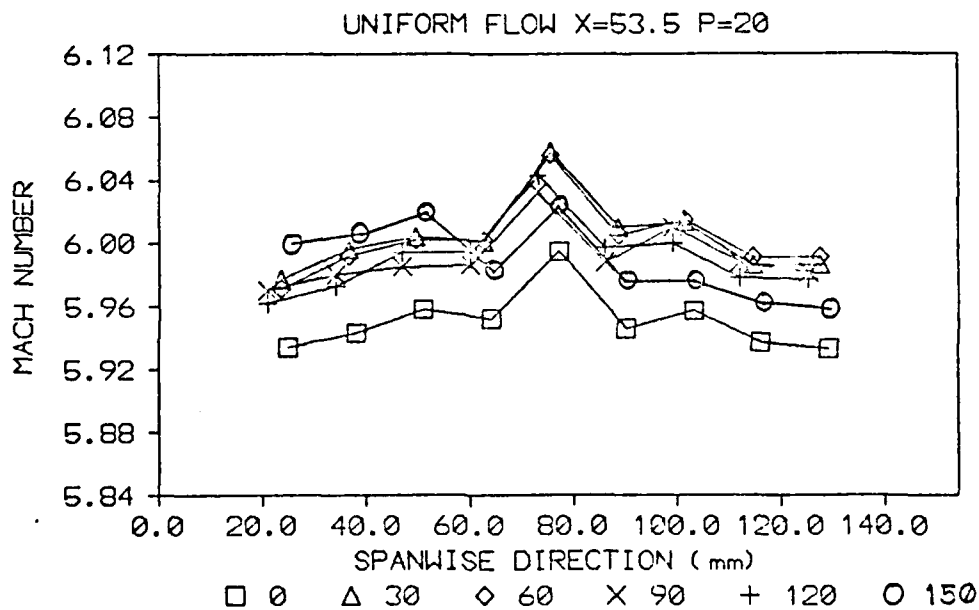
Figure E.15. Uniform Flow, x = 53.5 mm, Po = 20 bar

UNIFORM FLOW X=103.5 P=10
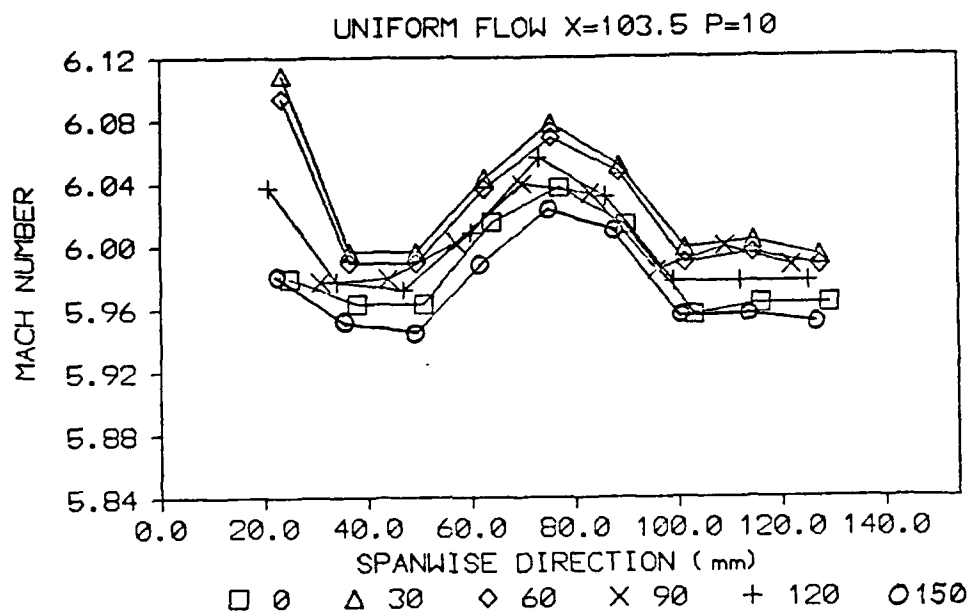
Figure E.16. Uniform Flow, x = 103.5 mm, Po = 10 bar

UNIFORM FLOW X=103.5 P=20
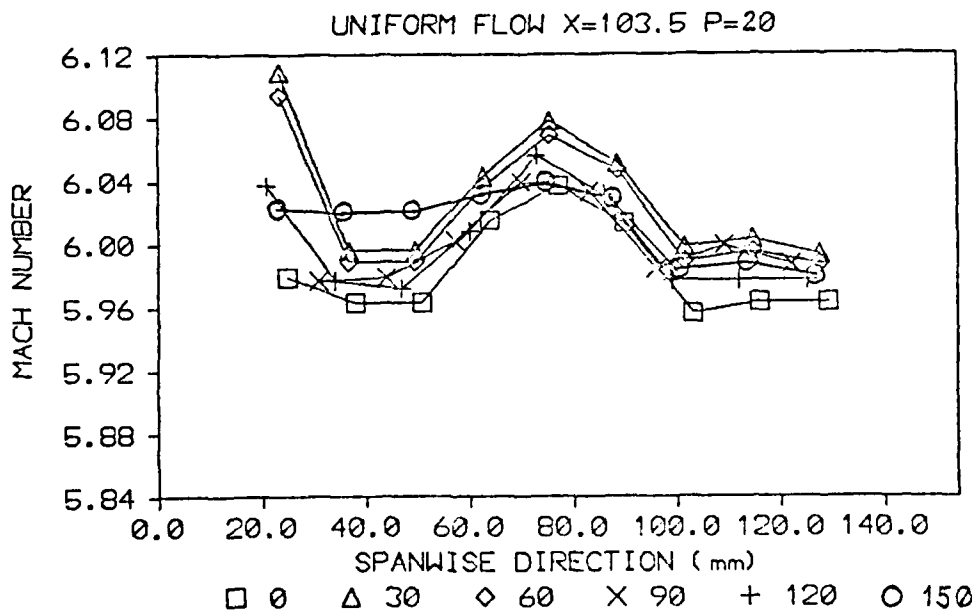
Figure E.17. Uniform Flow, x = 103.5 mm, Po = 20 bar

UNIFORM FLOW X=143.5 P=10
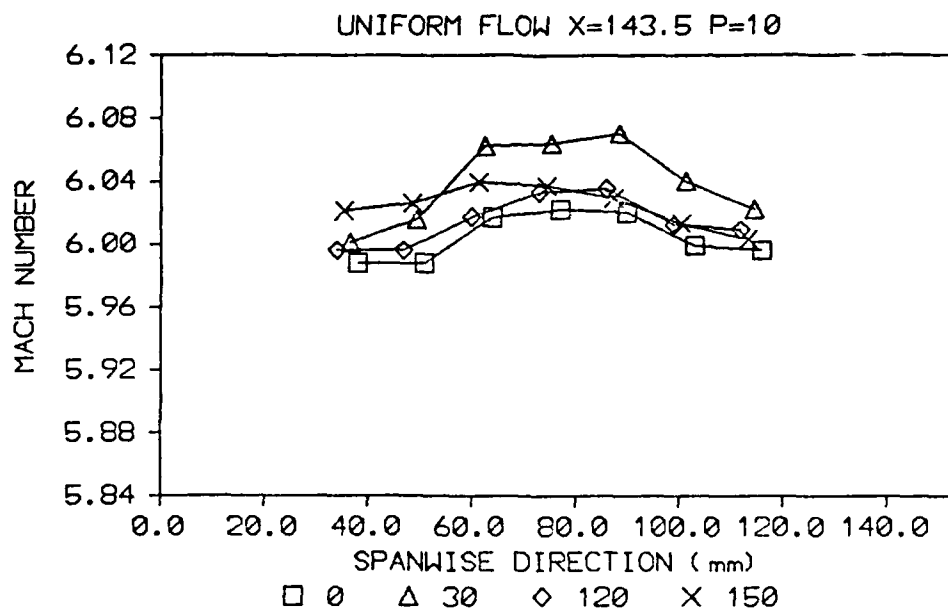
Figure E.18. Uniform Flow, x = 143.5 mm, Po = 10 bar

UNIFORM FLOW X=143.5 P=20
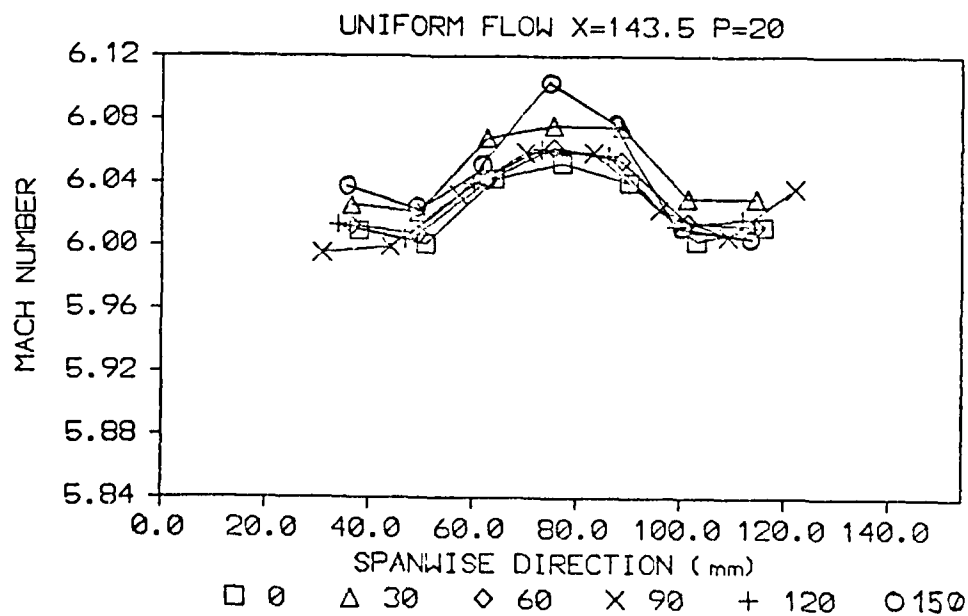
Figure E.19. Uniform Flow, x = 143.5 mm, Po = 20 bar
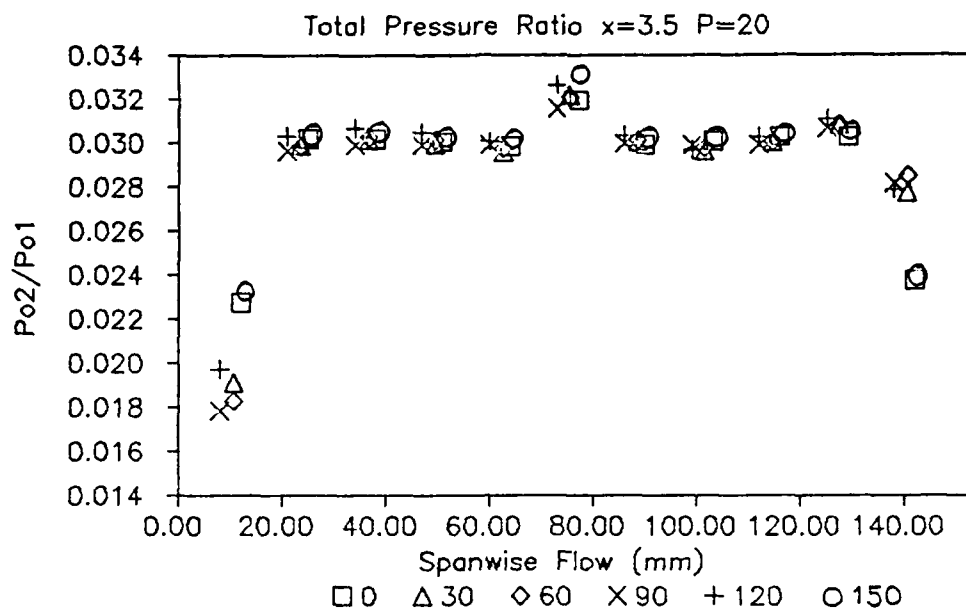
Figure E.20. Total Pressure Ratio,
x = 3.5 mm, Po = 20 bar
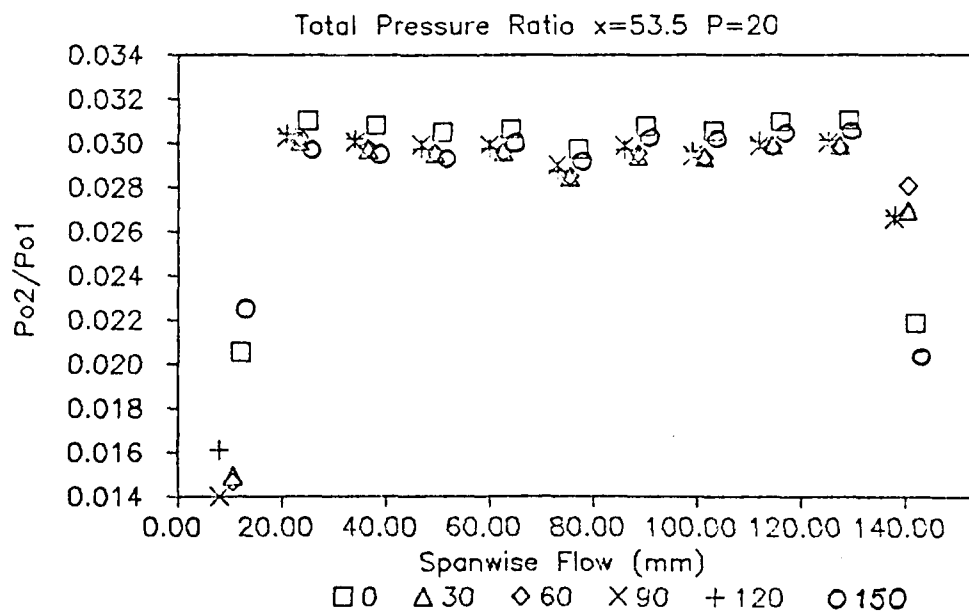
Figure E.21. Total Pressure Ratio,
x = 53.5 mm, Po = 20 bar
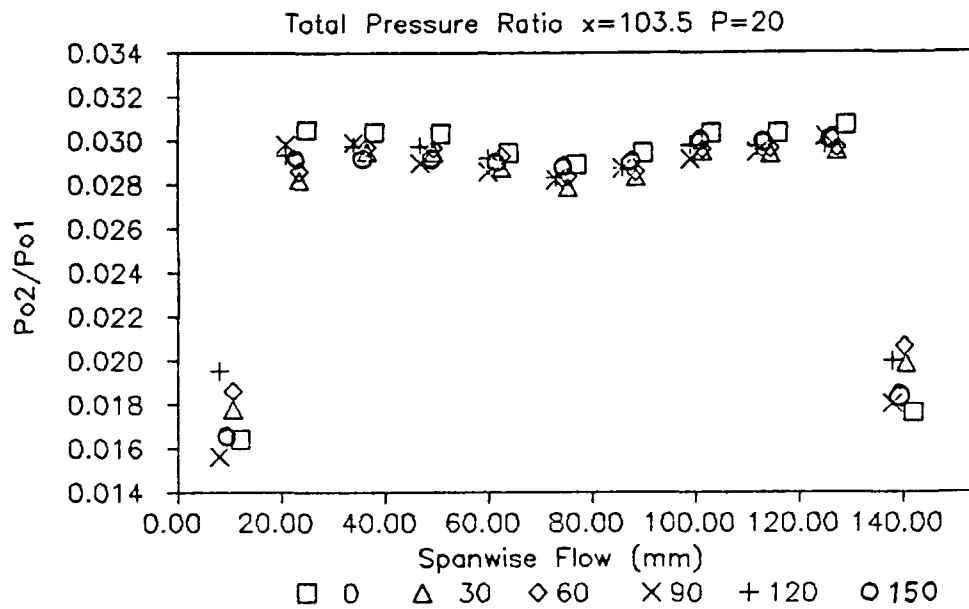
Figure E.22. Total Pressure Ratio,
x = 103.5 mm, Po = 20 bar
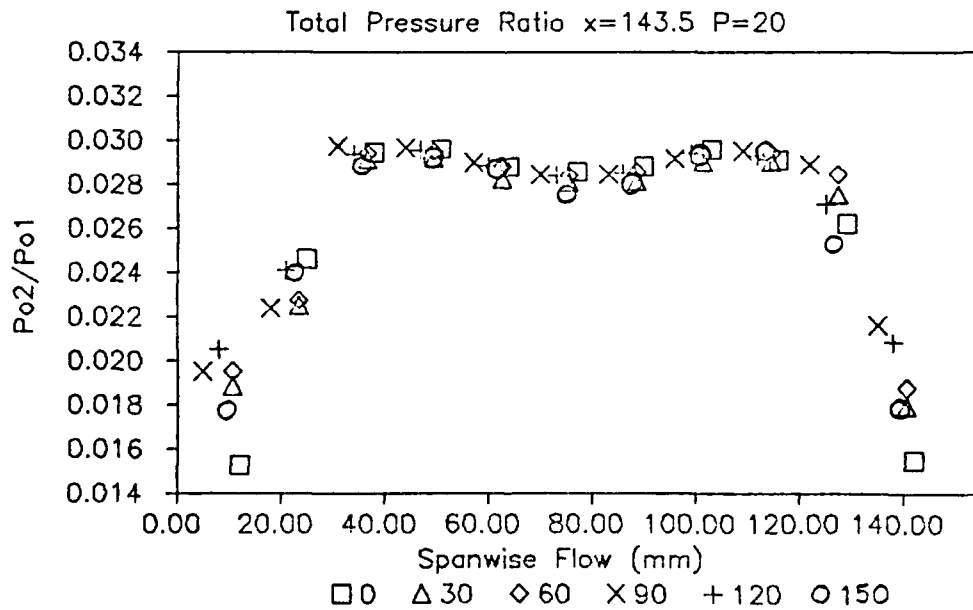
Figure E.23. Total Pressure Ratio,
x = 143.5 mm, Po = 20 bar

Appendix F

Preparation of the Liquid Crystal Model
(19:25,26; 14:37,38)

The encapsulated liquid crystals are sold as a water-based slurry. After shaking the bottle vigorously, the slurry is then diluted by addition of distilled water (50 to 150% dilution, depending on the batch of liquid crystals). After thorough mixing (several hours) with a small propeller mixer, the slurry is filtered through a thin layer of cotton. If the liquid crystals were not diluted enough, most of the liquid crystals will be trapped in the cotton, and the filtered solution will be mostly composed of water.

The model used for the liquid crystal technique should have a low thermal conductivity so that the heat is not conducted away too rapidly. The surface of the material has to be painted in dull black. This is to prevent light reflections from the underlaying model surface which would overwhelm the intensity changes due to temperature change. This is especially critical if the DIP system is used for the color/temperature correlation. Before applying the coat of liquid crystals, the surface must be degreased with a substance that will not dissolve the paint on the model.

The liquid crystals are then sprayed with an air brush onto the model's surface in very thin layers. Each layer should be at the limit between droplets and a completely wet film. The first layer should be allowed to dry thoroughly

in the surrounding air. It is the basis for all subsequent layers and has to provide the bonding to the model. The other layers can be dried quickly with a hair dryer. The hair dryer will also act as a heater, so the quality of the liquid crystal layer can be easily inspected. The most critical color is the red, and if it shows up properly, the model is ready.

A damaged coat of liquid crystals can be removed under running water by wiping with a soft cloth. The remaining particles of liquid crystals can be easily removed with a methanol soaked cloth. The gelatin of the microcapsules is destroyed by methanol.

Appendix G

Digital Image Processing

The use of the digital image processing (DIP) makes the liquid crystal technique more quantitative by taking the subjectiveness out of determining the temperature from a color picture. The system works directly from a video frame. It works with a black and white version of the frame and according to the gray intensity of a point (pixel), a "false color" is assigned to it. The VKI system distinguishes between 256 shades of gray from black (intensity 0) to white (intensity 255).

The critical link between the DIP and the liquid crystal technique is the calibration of the liquid crystals. The calibration gives the correlation between the "false color" (intensity) and the temperature.

The use of a video camera complicates this system somewhat. In order to photograph the model, a bright light must be used to illuminate the model. However, the variations in the intensity of this bright light overwhelms the intensity variations due to temperature changes. A solution to this problem is to film the model (with no temperature changes) when illuminated by the bright light. This picture represents the intensity variations due only to the lighting. The intensities of this "reference" frame are then subtracted appropriately from the calibration and test video frames.

The correlation between temperature and intensity, after correcting for the reference frame intensity, can now be used, but with a precaution. The relation of intensity to temperature is multi-valued, ie., there are two different colors for one intensity. Hence, the analysis requires a simultaneous inspection of the video image and the intensity curve of the corrected picture. Once the surface temperatures are obtained, the heat transfer rate and Stanton number can be determined.

Several computer programs are used in the processing of the liquid crystal video frames and are located in the VKI PDP computer under the account name CREUSOT. Some explanations concerning the computer programs are located in several references (14:12-14; 12:35-39).

Appendix H

Electrical Analog Circuits

The surface heat flux is deduced from temperature versus time signals using electrical analog circuits. Each of these circuits consists of a series of resistances and capacitances in which voltages and currents behave in ways similar to temperatures and heat fluxes, respectively.

The following is a comparison of the thermal and electrical equations, and is extracted from Schultz and Jones (48:37,38). Further behavior of the analog circuit is described and is extracted from Ligrani, Camci, and Grady (37:16-20).

(a)   (b)
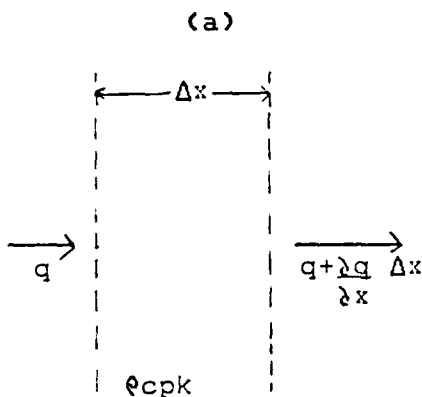
Figure H.1a.   Figure H.1b.
Thermal Circuit   Electrical Circuit

Rate of gain of energy in   Rate of gain of charge in

element Δx element Δx

$$= - \frac{\partial q}{\partial x} \Delta x \qquad\qquad = - \frac{\partial i}{\partial x} \Delta x \qquad (H.1)$$

which by conservation of   which by conservation of

energy   charge

$= \rho c_p \Delta x \dfrac{\partial T}{\partial t}$	$= C' \Delta x \dfrac{\partial V}{\partial t}$	(H.2)

Thus   Thus

$$\dfrac{\partial q}{\partial x} = - \rho c_p \dfrac{\partial T}{\partial t} \qquad\qquad \dfrac{\partial i}{\partial x} = - C' \dfrac{\partial V}{\partial t} \qquad (H.3)$$

The conduction equation is: Ohm's law is:

$$q = - k \dfrac{\partial T}{\partial x} \qquad\qquad i = -\dfrac{1}{r' \Delta x} \dfrac{\Delta V}{\Delta x} \Delta x = -\dfrac{1}{r'} \dfrac{\partial V}{\partial x} \quad (H.4)$$

Combining the above equations   Combining the above equations

and the diffusion equation   and the transmission line

is obtained   equation is obtained

$$\dfrac{\partial^2 T}{\partial x^2} = \dfrac{\rho c_p}{k} \dfrac{\partial T}{\partial t} \qquad\qquad \dfrac{\partial^2 V}{\partial x^2} = r'C' \dfrac{\partial V}{\partial t} \qquad (H.5)$$

It is evident from equations (H.5a) and (H.5b), that
the heat diffusion equation is analogous to the electrical
transmission line equation. Taking the Laplace transform of
equation (H.5b),

$$\dfrac{\partial^2 V*}{\partial x^2} = r'C' [sV* + V(t=\infty) - V(t=0)] \qquad (H.6)$$

where $V(t=\infty) = 0$.

The initial condition is

$$V* = 0 \qquad \text{at } t = 0 \qquad\qquad (H.7)$$

and the boundary conditions are

$$V* = 0 \qquad \text{at } x = \infty \qquad\qquad (H.8)$$

$$-\dfrac{1}{r'} \dfrac{\partial V*}{\partial x} = i*_{\text{input}} \qquad \text{at } x = 0 \qquad (H.9)$$

Applying the initial condition to equation (H.6) and solving
the differential equation obtained in $V*$ and x gives:

$$V* = A \exp [\ x \ (r'C's)^{1/2} \ ] + B \exp [-x(r'C's)^{1/2}] \quad (H.10)$$

where A and B are constants. The boundary condition (H.8) gives A=0, and after using the boundary condition (H.9),

$$\frac{\partial V*}{\partial x} = -(r'C's)^{1/2} \ B \exp[\ -x(r'C's)^{1/2} \ ] = - i*_{input} \ r' \quad (H.11)$$

or alternatively,

$$B = i*_{input} \ [r'/(C's)]^{1/2} \quad (H.12)$$

So when x = 0, using equations (H.10) and (H.12), the voltage ΔV at the input of the analog circuit, shown in Figure H.2, is given by

$$\Delta V* = i*_{input} \ [r'/(C's)]^{1/2} \quad (H.13)$$
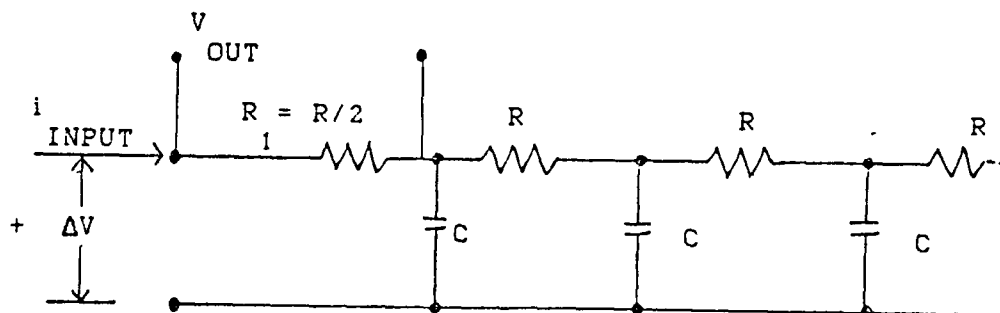
Figure H.2   Electrical Analog Using Equal Sections
            Representing a Homogeneous Heat Conductor

Using equation (3.26) which is repeated here

$$\frac{\Delta V}{\frac{\alpha\ VREF}{R}} = Ts \qquad\qquad (H.14)$$

the circuit input is now the thin film output,

$$\Delta V* = \frac{\alpha\ VREF\ Ts*}{R} \qquad\qquad (H.15)$$

Substituting equation (H.15) into (H.13) and rearranging,

$$i*_{input} = (sC'/r')^{1/2}\ \frac{\alpha\ VREF\ Ts*}{R} \qquad\qquad (H.16)$$

Now the heat conduction equation (15:57-60) analogous to equation (H.13) is

$$q_s* = (\rho cpks)^{1/2}\ Ts* \qquad\qquad (H.17)$$

So substituting into equation (H.17) for Ts* using equation (H.16) gives

$$q_s* = (\rho cpk)^{1/2}\ (r'/C')^{1/2}\ \frac{(\alpha\ VREF)^{-1}}{R}\ i*_{input} \qquad\qquad (H.18)$$

For the analog termination shown in Figure H.2, equation (H.18) after inversion then becomes

$$q_s = (\rho cpk)^{1/2}\ (r'/C')^{1/2}\ \frac{(\alpha\ VREF)^{-1}}{R}\ \frac{VOUT}{R_1} \qquad\qquad (H.19)$$

For the substrate heat transfer behavior, the values of q$_s$ obtained from equation (3.32), which is repeated here

$$q_s = \frac{1}{2}\ (\rho cpk\pi/t)^{1/2}\ \frac{\Delta V}{\frac{\alpha\ VREF}{R}} \qquad\qquad (H.20)$$

and equation (H.18) must be the same provided that q_s is a constant for t > 0 and that Ta = TREF. Thus,

$$q_s = (\rho cpk\pi/t)^{1/2} \frac{\Delta V}{2\alpha_R VREF} = (\rho cpk)^{1/2} (r'/C')^{1/2} \frac{VOUT}{\alpha_R VREF R_1} \quad (H.21)$$

If a calibration of circuits is then made with a step in heat flux, a calibration coefficient for the analog time may then be defined using

$$\frac{A*}{\beta} = (r'/C')^{1/2} (1/R_1) = \frac{\Delta V}{2VOUT} (\pi/t)^{1/2} \quad (H.22)$$

This single time dependent calibration coefficient thus defines the characteristics of the analog circuit in relation to heat flow. Heat fluxes for gages operating when Ta = TREF are obtained by substituting ΔV from equation (H.22) into equation (H.21) to give the equation

$$q_s = \frac{VOUT}{VREF} \frac{(\rho cpk)^{1/2}}{\alpha_R} \frac{A*}{\beta} \quad (H.23)$$

which is then used for heat transfer data reduction with the temperature correction on α_R, if required.

Circuit Considerations

The actual values of r' and C' in equation (H.18) required in an analog circuit are dependent on many factors. Any arrangement of resistive and capacitive components represents semi-infinite heat transfer behavior provided that the value of r'C' (which is analogous to ρcpk) is

241

constant with time. Two performance criteria by which circuits are judged are

    a) response time - the time required for the analog output to fully account for an alteration in heat transfer rate, ie., voltage input signal, and

    b) operation time - the time after the first input to the analog that the output signal represents a particular heat transfer profile to a stated accuracy.

The aim in analog circuit design is to minimize response time and maximize operation time.

The T-section analog circuit, shown in Figure H.2, has a short response time. For a circuit with all stages of identical component values, this response time is RC. The operation time for which this circuit reproduces a step input in heat transfer to within 1.4% is given by

$$0.2n^2(RC) \hspace{4cm} (H.24)$$

where n is the number of stages. When long operating times are required, arithmetically increasing component values are used, as shown in Figure H.3. For the purpose of calculating operating times from equation (H.24), h T-section analog stages of arithmetically increasing values of capacitance and resistance are equivalent to

$$h(h+1)/2 \hspace{4cm} (H.25)$$

identical stages. When using arithmetically increasing components, the first two stages must be identical if the

frequency response of the circuit is to be acceptable.
Figure H.3 shows the analog circuit used in this study, with
24 stages, R = 4099 ohms, C = 20 x 10^{-9} farads, an operating
time of 1.4 seconds and a response time of 8.2 x 10^{-5}
seconds.

Figure H.3. T-Section Analog Circuit Used in Test

Appendix I

Calibration of Thin Film Gages

The equation used for heat flux measurements is equation (3.36), but the equation will be repeated here for completeness.

$$q_s = \frac{VOUT}{VREF} \frac{(\rho cpk)^{1/2}}{\alpha_R} \frac{A*}{\beta} [1 + \alpha_R (Ta - TREF)] \qquad (I.1)$$

The determination of different parts of equation (I.1); VREF, α_R, $(\rho cpk)^{1/2}$, and $A*/\beta$, will be discussed in detail. The $[1 + \alpha_R (Ta - TREF)]$ correction term has been previously discussed. These details are extracted from Ligrani, Camci, and Grady (37:24-33).

Output Voltage: VOUT

The output voltage from the analog circuit, VOUT, is different from the other terms in equation (I.1) because it is dependent on the heat flux to a particular gage during specific flow conditions. The other terms in equation (I.1) are determined from sensor or measurement chain calibration characteristics.

Temperature Coefficient of Resistance : α_R

The temperature coefficient of resistance, α_R, of a thin film gage depends on a variety of factors including the film material, the size of the film metal deposit, and its shape. Therefore each gage film must be calibrated

245

independently since it is impossible to make each film
exactly the same.

The temperature coefficient of resistance is defined by

$$R = RREF [1 + \alpha_R (T - TREF)] \qquad (I.2)$$

This can be rewritten

$$\frac{R - RREF}{T - TREF} = \alpha_R RREF \qquad (I.3)$$

where TREF is some reference temperature. The magnitude of
(R-RREF)/(T-TREF) is found by plotting resistance versus
temperature for a given gage and then calculating the slope.
This can also be done mathematically by using a least
squares algorithm to find the slope of the line between all
the data points. The program used for this calculation is
listed in Appendix J. RREF is determined by measuring the
resistance of the gage and its connecting wires just before
input to an analog circuit bridge.

The calibration may be performed in an oil bath. A
multimeter is used to measure the film resistances at a
range of constant oil bath temperatures. The range of
temperatures to calibrate against is determined by the range
of temperatures that the gages will be used. The value of
α_R may be obtained from the experimental readings using a
least squares program.

Experience has shown that maintaining constant oil bath
temperature during readings is very critical. This is
easiest to accomplish when the oil bath is being cooled

between readings. If constant bath temperatures are maintained during readings, then the accuracy of the calibration is governed by the accuracies of the multimeter and thermometer.

Substrate Thermal Product: $(\rho cpk)^{1/2}$

The substrate thermal product is $(\rho cpk)^{1/2}$. For quartz substrates, the value of the thermal product is well known between ambient and 100 °C. However, the thermal product for machinable ceramic substrates are not well defined. The value of the thermal product depends on the history of the gage construction, in particular the high temperature baking details of the ceramic production process. Therefore, when the gages are completed, each ceramic piece must be calibrated.

The thermal product of ceramic will vary with test temperature, so calibration must be completed under the same conditions for which the gages will be used. An arrangement for calibration would consist of a quartz gage and a sample ceramic gage on a flat test plate in the VKI CT-2 tunnel at the same distance downstream of the leading edge. The sample ceramic gage must have been made at the same time as the actual test gage so as to have undergone the same production process. The heat flow is then calculated from the quartz gage readings. The value of q_s obtained is substituted into equation (I.1) to give

$$(\rho cpk)^{1/2}_{ceramic} = q_s \frac{VREF}{VOUT} \alpha_R \frac{1}{A\ast/\beta} \frac{1}{[1 + \alpha_R (Ta - TREF)]} \qquad (I.4)$$

Calibration Constant for the Electrical Analog: $A\ast/\beta$

Once the electrical analog circuits are set up to process the signals from thin film gages they are ready to be calibrated. The purpose of the analog circuit calibration is to obtain $A\ast/\beta$ in equation (I.1). Recall that the calibration constant is defined from Appendix H as

$$\frac{A\ast}{\beta} = \frac{\Delta V}{2VOUT} (\pi/t)^{1/2} \qquad (I.5)$$

If a parabolic voltage signal is inserted into the input of the analog circuit, then the output is a step in voltage, VOUT. In actual practice, VOUT is measured in digital data units in order to calibrate both the analog circuit as well as the other parts of the measurement chain before the computer: amplifier, filter, multiplexer, analog/digital converter. Therefore, equation (I.5) becomes

$$\frac{A\ast}{\beta} = \frac{\Delta V}{2NOUT} (\pi/t)^{1/2} \qquad (I.6)$$

and during an actual measurement, equation (I.1) is changed to

$$q_s = \frac{NOUT}{VREF} \frac{(\rho cpk)^{1/2}}{\alpha_R} \frac{A\ast}{\beta} \frac{[1 + \alpha_R (Ta - TREF)]}{R} \qquad (I.7)$$

where NOUT is VOUT measured in digital data units.

Appendix J

Coefficient of Resistance Program

```
100 'This program calculates the thin film gage coefficient
110 '    of resistance using a least squares method
120 '
130 DIM X(7),Y(30,7),T(30,7),T(7)
140 LPRINT"no    20.5   30.0   41.0   49.0   62.65 63.65 ao a1 f    ar"
150 LPRINT
160 LPRINT
170 'Set temperatures
180 X(1)=20.5
190 X(2)=30!
200 X(3)=41.0
210 X(4)=49!
220 X(5)=62.65
230 X(6)=63.65
240 'Set the number of temperature/resistance data points
250 TMAX=6
260 FOR I=1 TO TMAX
270 T(I)=X(I)-X(1)
280 NEXT I
290 PRINT "how many thin film gages are there?"
300 INPUT N
310 'Input data points
320 FOR J=1 TO N
330 PRINT "type in data"
340 FOR I=1 TO TMAX
350   PRINT "resistance data for gage #, at temp # ",J,I
360   INPUT Y(J,I)
370 NEXT I
380 'The data will be displayed to check for correctness
390 PRINT "the data you input is:"
400 FOR I=1 TO TMAX
410   PRINT I,X(I),Y(J,I)
420 NEXT I
430 PRINT "is the data correct?"
440 PRINT "type 1 if yes, 0 if no"
450 INPUT ANS
460 IF ANS = 1 THEN GOTO 560
470 'If one of the data points is wrong, input the correction
480 PRINT "type in the data number that is wrong"
490 INPUT M
500 PRINT "type in the correct resistance data"
```

```
510 INPUT Y(J,N)
520 GOTO 630
530 'Begin the computation of the thin film coefficient
540 '    of resistance, using a least squares
550 '     algorithm
560 SX=0
570 SY=0
580 SX2=0
590 SY2=0
600 SXY=0
610 FOR I=1 TO TMAX
620 R(J,I)=Y(J,I)-Y(J,1)
630 NEXT I
640 FOR I=1 TO TMAX
650    SX=SX+T(I)
660    SY=SY+R(J,I)
670    SX2=SX2+T(I)*T(I)
680    SY2=SY2+R(J,I)*R(J,I)
690    SXY=SXY+R(J,I)*T(I)
700 NEXT I
710 DEN=SX2-SX*SX/TMAX
720 A1=(SXY-SX*SY/TMAX)/DEN
730 A0=(SY-A1*SX)/TMAX
740 F=A1*A1*(SX2-SX*SX/TMAX)/(SY2-SY*SY/TMAX)
750 AP=A1/Y(J,1)
760   LPRINT J;A0;A1;F;AP
770 NEXT J
```

Appendix K

Read Data Program

```
        PROGRAM READAVE
C       READING OF DATA FROM DATA ACQUISITION SYSTEM
C
        LOGICAL*1 NAME4(15),YES
        DIMENSION LXX(768),LXXX(256)
        COMMON IVEC(12,1780),x(50),y(50),time(1780),IV(12,500),T(500)
     1    ,V(12,500)
        CHARACTER*1 ANSW
        CHARACTER*20 C3
C
        ISTEP=12
        NPTS=1780
        IV4=1
        TYPE 98765
98765   FORMAT(/,' DATA FILE NAME : ',$)
        CALL GETSTR (5,NAME4,14)
        CALL ASSIGN(4,NAME4)
        DEFINE FILE 4(103,256,U,IV4)
  110   FORMAT(A20)
   55   FORMAT(/,' WHAT IS THE OUTPUT FILE NAME? ',$)
        TYPE 55
        ACCEPT 110,C3
        OPEN (UNIT=10,NAME=C3,TYPE='NEW')
C
C READ THE DATA FROM THE DIRECT ACCESS FILE
C
        IV4=2
        IJ=0
        DO 900 IXY=1,28
          J=0
          DO 901 I=1,3
            READ(4'IV4)LXXX
            DO 901 II=1,256
              J=J+1
              LXX(J)=LXXX(II)
  901       CONTINUE
          DO 902 IJJ=1,64
            IJ=IJ+1
            DO 903 K=1,12
              JJ=K+(IJJ-1)*ISTEP
              IVEC(K,IJ)=LXX(JJ)
              time(ij)=ij
  903       CONTINUE
          IF (IJ .EQ. 1780) GO TO 909
  902     CONTINUE
  900   CONTINUE
  909   CONTINUE
```

```fortran
C
C SAVE ONLY EVERY FOURTH POINT IN ANOTHER FILE
C
        do 400 n=1,12
          J=3
          K=0
          do 410 i=1,npts
            J=J+1
            IF (J .EQ. 4) THEN
              K=K+1
              T(K)=time(i)
              V(N,K)=ivec(n,i)
              J=0
            ENDIF
410       continue
400     continue
C
C OPTION TO SMOOTH THE DATA
C
130     FORMAT(I3)
120     FORMAT(I1)
        NPTS=445
5       FORMAT(/,' DO YOU WANT TO smooth THE DATA? YES=1,NO=2 ',$)
        TYPE 5
        ACCEPT 120,IANS
        IF (IANS .EQ. 2) GO TO 999
        type 200
200     format(/,' enter number of points to fit: ',$)
        accept *,IFITT
        is=ifitt/2 + 1
        iend=npts-is+1
        DO 201 N=1,12
          do 210 i=is,iend
            SUM=0.0
            do 220 j=1,ifitt
              k=i-is+j
              SUM=SUM+V(N,K)
220         continue
            V(N,I)=SUM/IFITT
210       continue
201     CONTINUE
C
999     CONTINUE
C
C WRITE TO DATA FILE TO REDUCE
C
        DO 600 N=1,12
          DO 500 I=1,NPTS
            WRITE(10,*) T(I),V(N,I)
500       CONTINUE
600     CONTINUE
        stop
        end
```

252

```
c
ccccccccccccccccccccccccccccccccccccccccccccc
c
      subroutine lstsqr(yfit,ifit)
      COMMON IVEC(12,1780),x(50),y(50),time(1780),IV(12,500),T(500)
      mdpt=ifit/2+1
      a=0.0
      b=0.0
      c=0.0
      d=0.0
      e=0.0
      f=0.0
      g=0.0
      do 300 i=1,ifit
      . a=a+x(i)
        b=b+x(i)**2
        c=c+x(i)**3
        d=d+x(i)**4
        e=e+y(i)
        f=f+(x(i)*y(i))
        g=g+(x(i)*x(i)*y(i))
300   continue
      a1=(a*e-ifit*f)/(a*a-ifit*b)
      a0=(e-a1*a)/ifit
      yfit=a0+a1*x(mdpt)
      return
      END
```

Appendix L

Input Data Files

```
12  2  10  445  1
1.0   1.0   1.0   1.0
0.0   0.0   291.9   1950.0   6.0   10.0   293.65
0.0   0.00234   0.0058   0.1111   47.52
0.0   0.00221   0.0211   0.1202   54.41
0.0   0.00230   0.0175   0.1360   59.24
0.0   0.00219   0.0269   0.1255   57.30
0.0   0.00216   0.0213   0.1060   49.09
0.0   0.00206   0.0179   0.0957   46.39
0.0   0.00203   0.0299   0.1109   54.73
0.0   0.00210   0.0026   0.1208   57.41
0.0   0.00203   -.0053   0.1124   55.41
0.0   0.00205   -.0196   0.0889   40.05
9.35e-5    0.752   47.7   -273   -964
1.175e-4   0.751   54.8   -166   -1305
8.91e-5    0.752   59.3    -19   -1706
1.197e-4   0.750   57.7   -310   -2048
8.62e-5    0.754   49.6    117   -1131
1.049e-4   0.752   47.1    334   -967
2.117e-4   0.749   77.4     72   -1068
7.65e-5    0.751   60.2    -63   -2048
8.04e-5    0.752   56.7   -162   -1097
8.18e-5    0.748   41.5    365   -1632
```

```
12  2  10  445  1
1.0   1.0   1.0   1.0
0.0   0.0   291.9   1950.0   6.0   20.0   293.65
0.0   0.00234   0.0058   0.1111   47.52
0.0   0.00221   0.0211   0.1202   54.41
0.0   0.00230   0.0175   0.1360   59.24
0.0   0.00219   0.0269   0.1255   57.30
0.0   0.00216   0.0213   0.1060   49.09
0.0   0.00206   0.0179   0.0957   46.39
0.0   0.00203   0.0299   0.1109   54.73
0.0   0.00210   0.0026   0.1208   57.41
0.0   0.00203   -.0053   0.1124   55.41
0.0   0.00205   -.0196   0.0889   40.05
9.35e-5    0.752   47.8   -273   -1273
1.175e-4   0.752   54.8   -166   -994
8.91e-5    0.754   59.4    -19   -1169
1.097e-4   0.751   57.8   -310   -2048
8.62e-5    0.754   49.7    117   -1093
1.049e-4   0.753   47.1    334   -611
2.117e-4   0.750   77.4     72   -888
7.65e-5    0.752   60.3    -63   -1743
8.04e-5    0.752   56.8   -162   -566
8.18e-5    0.749   41.5    365   -1497
```

Appendix M

Data Conversion Program

```
      PROGRAM READDAT
C THIS PROGRAM READS THE DATA OBTAINED FROM THE MEDIUM SPEED
C OR HIGH SPEED DATA ACQUISITION SYSTEM
C THEN IT CONVERTS THE DIGITAL DATA UNITS INTO THE
C PHYSICAL DATA UNITS
      COMMON ALPHAR(16),CONV(16),DCAL(16),IVEC(16,2000),ZERO(16)
     1    ,VC(2,2000),VB(2,2000),Q(16,2000),RCAL(16),CONVC(2)
     2    ,VT(16,2000),TIME(2000),DATA(130),RT(16,2000),CONVB(2)
     3    ,A0(16),A1(16),VREF(16),RREF(16),dvt(16,2000),FZERO(16),R(16)
      character*20 c2,c3,c7,c8,c9
   4  FORMAT(/,' WHAT IS THE NAME OF THE INPUT DATA FILE? ',$)
   5  FORMAT(/,' WHAT IS THE NAME OF THE INFO FILE? ',$)
   6  FORMAT(/,' WHAT IS THE NAME OF THE COAX OUTPUT FILE? ',$)
   7  FORMAT(/,' WHAT IS THE NAME OF THE THIN OUTPUT FILE? ',$)
 110  FORMAT(A20)
      TYPE 5
      ACCEPT 110,C3
      OPEN(UNIT=3,NAME=C3,STATUS='OLD')
      TYPE 4
      ACCEPT 110,C2
      OPEN(UNIT=2,NAME=C2,STATUS='OLD')
      OPEN(UNIT=7,NAME=C7,STATUS='NEW')
      OPEN(UNIT=8,NAME=C8,STATUS='NEW')
      TYPE 7
      ACCEPT 110,C9
      OPEN(UNIT=9,NAME=C9,STATUS='NEW')
CCCCCCCCCCCCCCCCCCCCCCCCCCCCCCCCCCCCCCCCCCCCC
C
C  ALPHAR      RESISTANCE COEFFICIENT (/DEGREE K)
C  A0          INTERCEPT IN ALPHAR CURVE
C  A1          SLOPE OF ALPHAR CURVE
C  CONV(N)     CONVERSION BETWEEN DIGITAL UNITS TO OHMS
C                 FOR THE CHANNEL CONNECTED TO THE THIN FILM GAGE
C                 (OHMS/DIGITAL UNITS)
C  CONVB       CONVERSION BETWEEN DIGITAL UNITS TO VOLTAGE
C                 FOR THE CHANNEL CONNECTED TO BACKFACE COAX
C  CONVC       CONVERSION BETWEEN DIGITAL UNITS TO VOLTAGE
C                 FOR THE CHANNEL CONNECTED TO COAX GAGE
C                 WITH REFERENCE JUNCTION IN AN ICE BATH
C  DCAL(N)     OUTPUT IN DATA UNITS FROM CIRCUIT DURING CALIBRATION
C  DELTAV      CHANGE IN PARABOLA VOLTAGE
C  IVEC(N,J)   OUTPUT IN DIGITAL UNITS FROM CIRCUIT DURING TESTS
C  NCH         NUMBER OF DATA CHANNELS
C  NCOAX       NUMBER OF COAX GAGES
C  NTC         CHANNEL NUMBER OF FIRST COAX GAGE
C  NTHIN       NUMBER OF THIN FILM GAGES
C  NTT         CHANNEL NUMBER OF FIRST THIN FILM GAGE
C  NBF         NUMBER OF BACK FACE GAGES
```

```
C  NTB        CHANNEL NUMBER OF FIRST BACK FACE GAGE
C  PO         TUNNEL STAGNATION PRESSURE (BAR)
C  Q          HEAT TRANSFER RATE (J/M**2 SEC = WATTS/M**2)
C  RCK        SUBSTRATE THERMAL PRODUCT (SQRT(RHO CP K))
C             (J/M**2 DEGREE K SEC**1/2)
C  RCAL       RESISTANCE AT AMBIENT TEMP AT TIME OF
C             ALPHAR CALIBRATION
C  RREF       RESISTANCE OF GAGE AT AMBIENT TEMP AT TIME OF
C             ACTUAL TEST
C  TA         AMBIENT TEMPERATURE AT TEST TIME (DEGREE K)
C  TIM        TIME OF THE CHANGE IN PARABOLA VOLTAGE
C  TISO       WALL TEMPERATURE AT TIME=0 (DEGREE K)
C  TCAL       AMBIENT TEMPERATURE AT TIME OF ALPHAR
C  .          CALIBRATION (DEGREE K)
C  VREF(N)    VOLTAGE OF GAGE AT BEGINNING OF THE TEST AT TIME=0
C  XM         MACH NUMBER
C
CCCCCCCCCCCCCCCCCCCCCCCCCCCCCCCCCCCCCCCCCCCCCCCCCC
C READ IN ELECTRICAL ANALOG CIRCUIT INFO
      READ(3,*) NCH,NCOAX,NTHIN,NPTS,CASE
      READ(3,*) CONVC(1),CONVC(2),CONVB(1),CONVB(2)
      READ(3,*) DELTAV,TIM,TA,RCK,XM,PO,TCAL
      DO 600 N=1,NTHIN
        READ(3,*) DCAL(N),ALPHAR(N),A0(N),A1(N),rcal(n)
  600 continue
      do 601 n=1,nthin
        read (3,*) CONV(N),VREF(N),RREF(N),ZERO(N),FZERO(N)
  601 CONTINUE
      PI=3.14159
C
CCCCCCCCCCCCCCCCCCCCCCCCCCCCCCCCCCCCCCCCCCCCCCCCC
C SET UP DATA ARRAYS
CCCCCCCCCCCCCCCCCCCCCCCCCCCCCCCCCCCCCCCCCCCCCCCCCCC
C
      DO 155 N=1,NCH
        DO 156 I=1,NPTS
          READ(2,*) time(i),IVEC(N,I)
          time(i)=time(i)*.00032
  156   CONTINUE
  155 CONTINUE
C
CCCCCCCCCCCCC
C CONVERT TO PHYSICAL DATA UNITS
CCCCCCCCCCCCCC
C
  800 FORMAT(' DO YOU WANT TO CONVERT THE THIN FILM GAGE DATA INTO')
  810 FORMAT(' (1)oHMS TO NUMERICALLY INTEGRATE?, OR')
  820 FORMAT(' (2)hEAT TRANSFER RATES SINCE ALREADY INTEGRATED ')
  821 FORMAT('    BY ELECTRICAL ANALOG CIRCUITS?')
  830 FORMAT(' OR DO YOU WANT TO WORK WITH THE (3)cOAX DATA?')
  840 FORMAT(' OR DO YOU WANT TO (9)qUIT')
   90 PRINT 800
      PRINT 810
```

```
              PRINT 820
              PRINT 821
              PRINT 830
              PRINT 840
       10 FORMAT(A1)
              accept *,ians
              IF (iANS .EQ. 1) CALL STHIN(NTHIN,NPTS,CASE,XM,PO,TA,
       1         RCK,TISO,TCAL)
              IF (iANS .EQ. 2) CALL ATHIN(NTHIN,DELTAV,TIM,RCK,TA,TCAL,PI
       1         ,NPTS,CASE,XM,PO,TISO)
              IF (iANS .EQ. 3) CALL SCOAX(NCOAX,NPTS,NBF,XM,PO,TISO)
              IF (iANS .EQ. 9) GO TO 860
CCCCCCCCCCCCCCCCCCCC
              PRINT 850
              accept *,ians
       850 FORMAT(' DO YOU WANT TO LOOK AT THE OPTIONS AGAIN? (1)yES (2)nO')
              IF (iANS .EQ. 1) GO TO 90
       860 CONTINUE
              STOP
              END
C
CCCCCCCCCCCCCCCCCCCCCCCCCCCC
C
              SUBROUTINE SCOAX(NCOAX,NPTS,NBF,XM,PO,TISO)
              COMMON ALPHAR(16),CONV(16),DCAL(16),IVEC(16,2000),ZERO(16)
       1         ,VC(2,2000),VB(2,2000),Q(16,2000),RCAL(16),CONVC(2)
       2         ,VT(16,2000),TIME(2000),DATA(130),RT(16,2000),CONVB(2)
       3         ,A0(16),A1(16),VREF(16),RREF(16),dvt(16,2000),FZERO(16),R(16)
              dimension temp(2,2000)
C COAX GAGE DATA CONVERSION FROM VOLTAGE TO TEMPERATURE
C  IS TAKEN FROM THE CALIBRATION TABLES AND CONVERTED INTO AN
C  EQUATION USING A LEAST SQUARES METHOD
C    TEMP DEGREE C = (MILLIVOLTS + 0.036) /0.061
       195 FORMAT(3F10.4)
              DO 210 N=1,NCOAX
                DO 200 J=1,NPTS
                  VC(N,J)=IVEC(N+10,J)*CONVC(N)
                  TEMP(N,J)=(VC(N,J)+0.036)/0.061 + 273.15
       200    CONTINUE
       210 CONTINUE
C     DO 220 J=1,NPTS
C        BTEMP(1,J)=(VB(1,J) + 0.036)/0.061 + 273.15
C        BTEMP(NBF,J)=(VB(NBF,J) + 0.036)/0.061 + 273.15
C 220 CONTINUE
              WRITE(8,*) XM,PO
              WRITE(8,*) NCOAX,NPTS
              DO 300 J=1,NPTS
                WRITE(8,*) TIME(J),TEMP(1,J),TEMP(1,1)
       300 CONTINUE
              DO 400 J=1,NPTS
                WRITE(8,*) TIME(J),TEMP(2,J),TEMP(NBF,1)
       400 CONTINUE
```

```fortran
   98 RETURN
      END
C
CCCCCCCCCCCCCCCCCCCCCCCC
C
      SUBROUTINE STHIN(NTHIN,NPTS,CASE,XM,PO,TA,rck,TISO,tcal)
      COMMON ALPHAR(16),CONV(16),DCAL(16),IVEC(16,2000),ZERO(16)
     1   ,VC(2,2000),VB(2,2000),Q(16,2000),RCAL(16),CONVC(2)
     2   ,VT(16,2000),TIME(2000),DATA(130),RT(16,2000),CONVB(2)
     3   ,A0(16),A1(16),VREF(16),RREF(16),dvt(16,2000),FZERO(16),R(16)
C THIN FILM GAGE CONVERSION TO OHMS FOR
C NUMERICAL INTEGRATION
      DO 700 N=1,NTHIN
        R(N)=(FZERO(N)-ZERO(N))*CONV(N)
        DO 710 J=1,NPTS
          RT(N,J)=(IVEC(N,J)-FZERO(N))*CONV(N)
  710   CONTINUE
  700 CONTINUE
      WRITE(9,*) XM,PO,TA,RCK,TCAL
      WRITE(9,*) NTHIN,NPTS,CASE
      DO 203 N=1,NTHIN
        WRITE(9,*) ALPHAR(N),VREF(N),RREF(N)
  203 continue
      do 204 n=1,nthin
        write(9,*) A0(N),A1(N),RCAL(N),R(N)
  204 CONTINUE
      DO 200 I=1,NTHIN
        DO 210 J=1,NPTS
          WRITE(9,*) TIME(J),RT(I,J)
  210   CONTINUE
  200 CONTINUE
   97 RETURN
      END
C
CCCCCCCCCCCCCCCCCCCCCCCC
C
      SUBROUTINE ATHIN(NTHIN,DELTAV,TIM,RCK,TA,TCAL,PI,NPTS,CASE
     1    ,XM,PO,TISO)
      COMMON ALPHAR(16),CONV(16),DCAL(16),IVEC(16,2000),ZERO(16)
     1   ,VC(2,2000),VB(2,2000),Q(16,2000),RCAL(16),CONVC(2)
     2   ,VT(16,2000),TIME(2000),DATA(130),RT(16,2000),CONVB(2)
     3   ,A0(16),A1(16),VREF(16),RREF(16),dvt(16,2000),FZERO(16),R(16)
C THIN FILM GAGE CONVERSION TO HEAT TRANSFER DATA
C AFTER ELECTRICAL ANALOG INTEGRATION
      ASTAR=0
      CON=0
      PRINT*, 'THE VALUE OF ASTAR SHOULD BE AROUND .0001'
      DO 500 I=1,NTHIN
        ASTAR=DELTAV*SQRT(PI/TIM)/(2*DCAL(I))
        TYPE*, ASTAR
        CON=ASTAR*(1+ALPHAR(I)*(TA-TCAL))/(VREF(I)*ALPHAR(I))
```

```fortran
        DO 510 J=1,NPTS
          Q(I,J)=DVT(I,J)*(RCK)*CON
510     CONTINUE
        ASTAR=0
        CON=0
500 CONTINUE
    WRITE(7,*) XM,PO,RCK
    WRITE(7,*) NTHIN,NPTS,CASE
    DO 200 I=1,NTHIN
      DO 210 J=1,NPTS
        WRITE(7,*) TIME(J),Q(I,J)
210     CONTINUE
200 CONTINUE
 99 RETURN
    END
```

Appendix N

Numerical Integration Program

```
      PROGRAM THIN
C THIS PROGRAM NUMERICALLY INTEGRATES THIN FILM VOLTAGE DATA INTO
C   HEAT TRANSFER RATES
C TWO REDUCTION METHODS ARE AVAILABLE:
C   1.   AEDC REDUCTION METHOD
C            - USES SEMI-INFINITE SLAB ASSUMPTION
C            - INDIRECT METHOD, SMOOTHS THE DATA
C   2.   SHULTZ AND JONES METHOD
C            - USES SEMI-INFINITE SLAB ASSUMPTION
C            - DIRECT METHOD
      COMMON AR(16),VREF(16),TIME(2000),DV(16,2000),RREF(16)
     1      ,A0(16),A1(16),RCAL(16),TEMP(16,2000),Q(16,2000),DVFAKE(16)
     2      ,QDOT(16,2000),X(40),Y(40),R(16),RT(16,2000),DTISO(16),TW(16)
      CHARACTER*20 C2,C7,C10,C8
    4 FORMAT(/,' WHAT IS THE NAME OF THE INPUT FILE? ',$)
    5 FORMAT(/,' WHAT IS THE NAME OF THE OUTPUT FILE? ',$)
    6 FORMAT(/,' WHAT IS THE NAME OF THE PLOT FILE? ',$)
    7 FORMAT(/,' WHAT IS THE NAME OF THE TS**2 PLOT FILE? ',$)
  110 FORMAT(A20)
      TYPE 4
      ACCEPT 110,C2
      OPEN(UNIT=2,NAME=C2,STATUS='OLD')
      TYPE 6
      ACCEPT 110,C7
      OPEN(UNIT=7,NAME=C7,STATUS='NEW')
      TYPE 5
      ACCEPT 110,C10
      OPEN(UNIT=10,NAME=C10,STATUS='NEW')
      TYPE 7
      ACCEPT 110,C3
      OPEN(UNIT=8,NAME=C8,STATUS='NEW')
C ***** NOMENCLATURE ******
C    AR         FILM TEMPERATURE COEFFICIENT OF RESISTANCE
C    DV         DATA IN OHMS
C    VREF       REFERENCE VOLTAGE
C    TA         AMBIENT TEMPERATURE DURING THE TEST
C    TCAL       REFERENCE TEMPERATURE USED WHEN FINDING AR
C    RCAL       REFERENCE RESISTANCE AT AMBIENT TEMP WHEN
C                    FINDING AR
C    Q          CUMULATIVE HEATING   (WATTS SEC/M**2)
C    QDOT       HEAT TRANSFER RATE (WATTS/M**2)
C    RCK        SQRT(RHO CP K), THERMAL PRODUCT
C    XM         MACH NUMBER
C
      READ(2,*) XM,PO,TA,RCK,TCAL
      READ(2,*) NTHIN,NPTS,CASE
```

```
            DO 55 N=1,NTHIN
              READ(2,*) AR(N),VREF(N),RREF(N)
        55 CONTINUE
            DO 56 N=1,NTHIN
              READ(2,*) A0(N),A1(N),RCAL(N),R(N)
        56 CONTINUE
            DO 200 I=1,NTHIN
              DO 210 J=1,NPTS
                READ(2,*) TIME(J),RT(I,J)
       210    CONTINUE
       200 CONTINUE
            WRITE(10,*) XM,PO
            WRITE(10,*) NTHIN,NPTS,CASE
            CALL GAGEDATA(NTHIN,NPTS,TA,XM,PO,RCK,TCAL)
            STOP
            END
C
CCCCCCCCCCCCCCCCCCCCCCCCCCCCCCCCCCCCCCCCCCCCCCCCCCCCCCCCCCCCCCCC
C
            SUBROUTINE GAGEDATA(NTHIN,NPTS,TA,XM,PO,RCK,TCAL)
            COMMON AR(16),VREF(16),TIME(2000),DV(16,2000),RREF(16)
        1      ,A0(16),A1(16),RCAL(16),TEMP(16,2000),Q(16,2000),DVFAKE(16)
        2      ,QDOT(16,2000),X(40),Y(40),R(16),RT(16,2000),DTISO(16),TW(16)
        7    CONTINUE
            TYPE 104
       104 FORMAT(' DO YOU WISH TO (1)SMOOTH DATA   '/,
          &  '   (9)EXIT , (2)REDUCE DATA'/)
            ACCEPT *,IANS
            IF (IANS .EQ. 2) GO TO 20
            IF (IANS .EQ. 9) GO TO 99
C   *****   SMOOTH THE DATA *******
            TYPE 106
       106 FORMAT(' ENTER (ODD) NO. OF POINTS TO FIT,
          &   I3 FORMAT'/)
            ACCEPT *,IFITT
            IS=IFITT/2 + 1
            IEND=NPTS-IS+1
            DO 299 L=1,NTHIN
              DO 9 I=IS,IEND
                DO 8 J=1,IFITT
                  K=I-IS+J
                  X(J)=TIME(K)
                  Y(J)=RT(L,K)
        8       CONTINUE
                CALL LSTSQR(RT(L,I),DYDX,IFITT)
        9     CONTINUE
       299 CONTINUE
            GO TO 7
C ******* REDUCE THE DATA *********
        20 CONTINUE
        5    FORMAT( ' WHAT IS ISTART? ')
            TYPE 5
            ACCEPT*, ISTART
```

```
C ***** CHANGE TO TEMP AND VOLTS
      DO 297 N=1,NTHIN
        TW(N)=TCAL+(RREF(N)-RCAL(N)-A0(N))/A1(N)
        DO 296 J=1,NPTS
          TEMP(N,J)=(RT(N,J)-A0(N))/A1(N)
          DV(N,J)=RT(N,J)*VREF(N)/RREF(N)
          Q(N,J)=0.0
          QDOT(N,J)=0.0
  296   CONTINUE
        DVFAKE(N)=R(N)*VREF(N)/RREF(N)
  297 CONTINUE
      DO 211 N=1,NTHIN
        WRITE(10,*) TW(N)
  211 CONTINUE
      TIME(ISTART)=TSTART
      DO 3 I=ISTART,NPTS
        TIME(I)=TIME(I)-TSTART
  3   CONTINUE
      TYPE 300
  300 FORMAT(' CHOOSE THE METHOD OF DATA REDUCTION '/'
     &    (1)AEDC ,(3)AEDC WITH TEMP, OR (2)SHULTZ AND JONES '/)
      ACCEPT *,MET
      IF (MET .EQ. 1) THEN
        CALL AEDC(CASE,NTHIN,NPTS,TA,TCAL,RCK,XM,PO,ISTART)
      ENDIF
      IF (MET .EQ. 2) THEN
        CALL SJ(CASE,NTHIN,NPTS,TA,TCAL,RCK,XM,PO,ISTART)
      ENDIF
      IF (MET .EQ. 3) THEN
        CALL TAEDC(CASE,NTHIN,NPTS,TA,TCAL,RCK,XM,PO,ISTART)
      ENDIF
C
C SMOOTH THE RESULTING DATA
C
      TYPE 106
      ACCEPT *,IFITT
      IS=IFITT/2 + 1
      IEND=NPTS-IS+1
      DO 499 L=1,NTHIN
        DO 49 I=IS,IEND
          DO 48 J=1,IFITT
            K=I-IS+J
            X(J)=K
            Y(J)=TEMP(L,K)
  48      CONTINUE
          CALL LSTSQR(TEMP(L,I),DYDX,IFITT)
  49    CONTINUE
  499 CONTINUE
      DO 399 L=1,NTHIN
        DO 39 I=IS,IEND
          DO 38 J=1,IFITT
            K=I-IS+J
            X(J)=K
```

```
                 Y(J)=QDOT(L,K)
   38           CONTINUE
                CALL LSTSQR(QDOT(L,I),DYDX,IFITT)
   39        CONTINUE
   399 CONTINUE
        DO 331 N=1,NTHIN
          DO 221 I=1,NPTS
            WRITE(7,*) TEMP(N,I),QDOT(N,I)
            WRITE(10,*) TEMP(N,I),QDOT(N,I)
   221    CONTINUE
   331 CONTINUE
        ZERO=0.0
          WRITE(8,*) ZERO,ZERO
        DO 338 I=1,NPTS
          WRITE(8,*) TIME(I),(TEMP(1,I))**2
   338 CONTINUE
   99  RETURN
       END
C
CCCCCCCCCCCCCCCCCCCCCCCCCCCCCCCCCCCCCCCCCCCCCCCCCCCCCCCCCCCCCC
C
       SUBROUTINE AEDC(CASE,NTHIN,NPTS,TA,TREF,RCPK,XM,PO,ISTART)
       COMMON AR(16),VREF(16),TIME(2000),DV(16,2000),RREF(16)
      1      ,A0(16),A1(16),RCAL(16),TEMP(16,2000),Q(16,2000),DVFAKE(16)
      2      ,QDOT(16,2000),X(40),Y(40),R(16),RT(16,2000),TISO(16),TW(16)
C ***** NOMENCLATURE *****
C RCPK       THERMAL PARAMETER
C              R = DENSITY
C              CP = SPECIFIC HEAT CAPACITY
C              K = CONDUCTIVITY
C    Q        CUMULATIVE HEATING
C QDOT       HEAT TRANSFER RATE
C
   96  FORMAT(' AEDC REDUCTION METHOD ')
       TYPE 96
       TYPE 97
   97  FORMAT(' ******* WORKING ******' )
       DO 299 N=1,NTHIN
         DO 2 J=ISTART+1,NPTS
           J2=J-1
           SUM=0.
           DO 1 I=ISTART,J2
             SUM=SUM+((DV(N,I+1)-DV(N,ISTART))+(DV(N,I)
      &            -DV(N,ISTART))/(SQRT(TIME(J)-TIME(I))
      &            +SQRT(TIME(J)-TIME(I+1))))
   1       CONTINUE
           Q(N,J)=SQRT(1.0/3.14159)*(TIME(J)-TIME(J-1))
      &        *RCPK*SUM*(1+AR(N)*(TA-TREF))/
      &        (AR(N)*(VREF(N)+DVFAKE(N)))
   2       CONTINUE
           Q(N,ISTART)=Q(N,ISTART+1)
           IE=NPTS-8
           IS=ISTART+8
```

```
         DO 20 I=IS,IE
           QDOT(N,I)=(-2.*Q(N,I-8)-Q(N,I-4)+Q(N,I+4)+2.*Q(N,I+8))
   &               /((TIME(I)-TIME(I-1))*40.)
  20     CONTINUE
         DO 663 I=1,8
           QDOT(N,I+ISTART-1)=QDOT(N,IS)
           QDOT(N,I+IE)=QDOT(N,IE)
 663     CONTINUE
 299 CONTINUE
     RETURN
     END
C
CCCCCCCCCCCCCCCCCCCCCCCCCCCCCCCCCCCCCCCCCCCCCCCCCCCCCCCCCCCCCC
C
     SUBROUTINE TAEDC(CASE,NTHIN,NPTS,TA,TREF,RCPK,XM,PO,ISTART)
     COMMON AR(16),VREF(16),TIME(2000),DV(16,2000),RREF(16)
   1      ,A0(16),A1(16),RCAL(16),TEMP(16,2000),Q(16,2000),DVFAKE(16)
   2      ,QDOT(16,2000),X(40),Y(40),R(16),RT(16,2000),TISO(16),TW(16)
C ***** NOMENCLATURE *****
C RCPK      THERMAL PARAMETER
C             R = DENSITY
C             CP = SPECIFIC HEAT CAPACITY
C             K = CONDUCTIVITY
C   Q       CUMULATIVE HEATING
C QDOT      HEAT TRANSFER RATE
C
  96 FORMAT(' TAEDC REDUCTION METHOD ')
     TYPE 96
     TYPE 97
  97 FORMAT(' ******* WORKING ******' )
     DO 299 N=1,NTHIN
       DO 2 J=ISTART+1,NPTS
         J2=J-1
         SUM=0.
         DO 1 I=ISTART,J2
           SUM=SUM+((TEMP(N,I+1)-TEMP(N,ISTART))+(TEMP(N,I)
   &           -TEMP(N,ISTART))/(SQRT(TIME(J)-TIME(I))
   &           +SQRT(TIME(J)-TIME(I+1))))
   1     CONTINUE
         Q(N,J)=SQRT(1.0/3.14159)*(TIME(J)-TIME(J-1))
   &        *RCPK*SUM
   2     CONTINUE
         Q(N,ISTART)=Q(N,ISTART+1)
         IE=NPTS-8
         IS=ISTART+8
         DO 20 I=IS,IE
           QDOT(N,I)=(-2.*Q(N,I-8)-Q(N,I-4)+Q(N,I+4)+2.*Q(N,I+8))
   &               /((TIME(I)-TIME(I-1))*40.)
  20     CONTINUE
```

```fortran
      DO 663 I=1,8
        QDOT(N,I+ISTART-1)=QDOT(N,IS)
        QDOT(N,I+IE)=QDOT(N,IE)
663    CONTINUE
299 CONTINUE
      RETURN
      END
C
CCCCCCCCCCCCCCCCCCCCCCCCCCCCCCCCCCCCCCCCCCCCCCCCCCCCCCCCCCCCC
C
      SUBROUTINE SJ(CASE,NTHIN,NPTS,TA,TREF,RCPK,XM,PO,ISTART)
      COMMON AR(16),VREF(16),TIME(2000),DV(16,2000),RREF(16)
     1    ,A0(16),A1(16),RCAL(16),TEMP(16,2000),Q(16,2000),DVFAKE(16)
     2    ,QDOT(16,2000),X(40),Y(40),R(16),RT(16,2000),TISO(16),TW(16)
C ***** NOMENCLATURE *****
C RCPK      THERMAL PARAMETER
C             R = DENSITY
C             CP = SPECIFIC HEAT CAPACITY
C             K = CONDUCTIVITY
96  FORMAT(' SHULTZ AND JONES REDUCTION METHOD ')
      TYPE 96
      TYPE 97
97  FORMAT(' ******* WORKING ******' )
      IEND=NPTS
      J1=ISTART+1
      DO 299 N=1,NTHIN
        DO 2 J=J1,IEND
          J2=J-1
          SUM=0.
          DO 1 I=ISTART+1,J2
            SUM=SUM+((DV(N,I)-DV(N,I-1)
     &          )/(SQRT(TIME(J)-TIME(I))
     &          +SQRT(TIME(J)-TIME(I-1))))
1         CONTINUE
          QDOT(N,J)=RCPK*SQRT(1.0/3.14159)
     &          *2.0*SUM*(1+AR(N)*(TA-TREF))/
     &          (AR(N)*(VREF(N)+DVFAKE(N)))
2       CONTINUE
        QDOT(N,ISTART)=QDOT(N,ISTART+1)
101     FORMAT(I5)
299 CONTINUE
      RETURN
      END
C
```
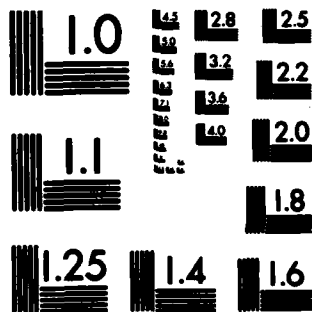
MICROCOPY RESOLUTION TEST CHART

NATIONAL BUREAU OF STANDARDS-1963-A

```
CCCCCCCCCCCCCCCCCCCCCCCCCCCCCCCCCCCCCCCCCCCCCCCCCCCCCCCCC
C
      SUBROUTINE LSTSQR(YFIT,DYDX,IFIT)
      COMMON AR(16),VREF(16),TIME(2000),DV(16,2000),RREF(16)
     1     ,A0(16),A1(16),RCAL(16),TEMP(16,2000),Q(16,2000),DVFAKE(16)
     2     ,QDOT(16,2000),X(40),Y(40),R(16),RT(16,2000),TISO(16),TW(16)
C ** FIRST ORDER LEAST SQUARES FIT OF IFIT POINTS.
C **    DYDX=F(X(MIDPT))
      MIDPT=IFIT/2 + 1
      A=0.
      B=0.
      C=0.
      D=0.
      E=0.
      F=0.
      G=0.
      DO 2 I=1,IFIT
         A=A+X(I)
         B=B+X(I)**2
         C=C+X(I)**3
         D=D+X(I)**4
         E=E+Y(I)
         F=F+(X(I)*Y(I))
         G=G+(X(I)*X(I)*Y(I))
    2    CONTINUE
      B1=(A*E-IFIT*F)/(A*A-IFIT*B)
      B0=(E-B1*A)/IFIT
      YFIT=B0+B1*X(MIDPT)
      DYDX=B1
      RETURN
      END
```

Appendix O

Temperature Reconstruction Program

```
      PROGRAM RECON
C THIS PROGRAM RECONSTRUCTS THE TEMPERATURE DATA VERSUS TIME
C    FROM THE HEAT TRANSFER VERSUS TIME DATA
C THE OUTPUT IS THEN HEAT TRANSFER VERSUS TEMP
      DIMENSION Q(16,2000),TEMP(16,2000),T(2000)
      CHARACTER*20 C7,C10
  110 FORMAT(A20)
    5 FORMAT(/,' WHAT IS THE NAME OF THE INPUT FILE? ',$)
    6 FORMAT(/,' WHAT IS THE NAME OF THE OUTPUT FILE? ',$)
      TYPE 5
      ACCEPT 110,C7
      OPEN(UNIT=7,NAME=C7,STATUS='OLD')
      TYPE 6
      ACCEPT 110,C10
      OPEN(UNIT=10,NAME=C10,STATUS='NEW')
      PI=3.14159
C RCK IS THE CERAMIC THERMAL PRODUCT
C RCK = SQRT(RCPK) UNITS OF J/M**2 K SEC**1/2
C READ IN THE Q VERSUS TIME DATA
      READ(8,*) XM,PO,RCK,TISO
      READ(8,*) NTHIN,NPTS,CASE
      DO 500 N=1,NTHIN
        DO 510 J=1,NPTS
          READ(7,*) T(J),Q(N,J)
  510   CONTINUE
  500 CONTINUE
C RECONSTRUCT THE TEMPERATURE
      DO 700 N=1,NTHIN
        DO 600 M=2,NPTS
          SUM=0.0
          TEMP(N,M)=0.0
          QDIFF=0.0
          JM=M-1
          DO 610 J=1,JM
            QDIFF=Q(N,J+1)+Q(N,J-1)-2*Q(N,J)
            SUM=SUM+SQRT(T(J)-T(J-1))*(M-J)**(3./2.)*(QDIFF)
  610     CONTINUE
          TEMP(N,M)=4.*SUM/(3.*RCK*SQRT(PI))
          TEMP(N,M)=TEMP(N,M)+TISO
  600   CONTINUE
  700 CONTINUE
C WRITE OUT THE Q VERSUS TEMPERATURE DATA
      WRITE(10,*) XM,PO,TISO
      WRITE(10,*) NTHIN,NPTS,CASE
      DO 400 N=1,NTHIN
        TEMP(N,1)=TEMP(N,2)
        DO 410 J=1,NPTS
          WRITE(10,*) TEMP(N,M),Q(N,M)
  410   CONTINUE
  400 CONTINUE
CCCCCCCCCC
      STOP
      END
```

Isothermal Heat Transfer Program

```
      PROGRAM QDOTISO
C     THIS PROGRAM DOES A LEAST SQUARES FIT OF THE
C     HEAT TRANSFER RATE VERSUS TEMPERATURE
C     CURVE BETWEEN THE TEMPERATURES T1 AND T2
C
      DIMENSION XLOC(16),ST(16),H(16),QISO(16),REX(16)
     1    ,TW(16),TEMP(16,2000),Q(16,2000)
      REAL MUFPS,MUINF
      CHARACTER*20 C8,C10,C12
  110 FORMAT(A20)
    4 FORMAT(/,' WHAT IS THE INPUT FILE NAME?',$)
      TYPE 4
      ACCEPT 110,C8
      OPEN(UNIT=8,NAME=C8,STATUS='OLD')
    5 FORMAT(/,' WHAT IS THE OUTPUT FILE NAME?',$)
      TYPE 5
      ACCEPT 110,C10
      OPEN(UNIT=10,NAME=C10,STATUS='NEW')
C READ IN THE DATA
      READ(8,*) XM,PBAR
      READ(8,*) NTHIN,NPTS,CASE
      DO 10 N=1,NTHIN
        READ(8,*) TW(N)
   10 CONTINUE
      DO 500 N=1,NTHIN
        DO 510 J=1,NPTS
          READ(8,*) TEMP(N,J),Q(N,J)
  510   CONTINUE
  500 CONTINUE
      TISO=288.95
      TSTAG=473.15
      PSTAG=PBAR*1.0E5
      PR=.72
      GC=287.0
      GAM=1.4
      FACT=1+.5*(GAM-1)*XM**2
      TINF=TSTAG/FACT
      PINF=PSTAG/FACT**(GAM/(GAM-1))
      RINF=PINF/(GC*TINF)
      AINF=SQRT(GAM*GC*TINF)
      UINF=AINF*XM
C CALCULATE MU IN FPS, THEN CONVERT TO MKS
      TF=(9./5.)*(TINF-273.15) + 32.0
      TR=459.67 + TF
      MUFPS=SQRT(TR)*2.32E-8/(1+(220./(TR*10.**(9./TR))))
      MUINF=MUFPS*3.281*14.59
```

```fortran
          CP=GC*GAM/(GAM-1)
          RREY=UINF*RINF/MUINF
C
          TYPE*,TINF,RINF,UINF,AINF,CP,MUINF,PINF,RREY
C
C LEAST SQUARES ALGORITHM
C
          DO 520 N=1,NTHIN
            TYPE*, ' WORKING ON GAGE #',N
            I=0
            SX=0
            SY=0
            SX2=0
            SY2=0
            SXY=0
            DEN=0
            A1=0
            A0=0
            QISO(N)=0
            DO 530 J=300,440
                I=I+1
                SX=SX+TEMP(N,J)
                SY=SY+Q(N,J)
                SX2=SX2+TEMP(N,J)**2
                SY2=SY2+Q(N,J)**2
                SXY=SXY+Q(N,J)*TEMP(N,J)
  530       CONTINUE
            DEN=SX2-SX*SX/I
            A1=(SXY-SX*SY/I)/DEN
            A0=(SY-A1*SX)/I
            F=A1**2*(SX2-SX**2/I)/(SY2-SY**2/I)
            QISO(N)=A0
C CALCULATE ST FROM ISOTHERMAL Q
            TAW=TINF*(1+SQRT(PR)*(GAM-1)*.5*XM**2)
            H(N)=QISO(N)/(TAW-TISO)
            ST(N)=H(N)/(CP*RINF*UINF)
  525       CONTINUE
          TYPE*,QISO(N)
  520   CONTINUE
C
C CALCULATE X POSITION OF EACH GAGE AND
C   THE LOCAL REYNOLDS NUMBER OF EACH GAGE
C
CCCCC FOR CASE NUMBER 1
C
          IF (CASE .EQ. 1) THEN
            DO 505 N=1,NTHIN
                XLOC(N)=(2*N+3)*4.0 +7.0+40.0
                REX(N)=RINF*UINF*XLOC(N)/MUINF/1000
  505       CONTINUE
          ENDIF
C
```

```
CCCCC FOR CASE NUMBER 2
C
      IF (CASE .EQ. 2) THEN
        DO 506 N=1,8
          XLOC(N)=(2*N+2)*4.0 + 7.0 + 40.0
          REX(N)=RINF*UINF*XLOC(N)/MUINF/1000
  506   CONTINUE
          XLOC(9)=22*4.0 + 7.0 + 40.0
          XLOC(10)=24*4.0 + 7.0 + 40.0
          REX(9)=RINF*UINF*XLOC(9)/MUINF/1000
          REX(10)=RINF*UINF*XLOC(10)/MUINF/1000
      ENDIF
C
CCCCC FOR CASE NUMBER 3
C
      IF (CASE .EQ. 3) THEN
        XLOC(1)=50.0
        XLOC(2)=86.0
        DO 508 N=1,NTHIN
          REX(N)=RINF*UINF*XLOC(N)/MUINF/1000
  508   CONTINUE
      ENDIF
C
CCCCCCCCCCCCCCCCCC
C
C PRINT OUT THE RESULTS TO SEE
      DO 507 N=1,NTHIN
        WRITE(10,*) N,XLOC(N),LOG10(REX(N)),ST(N),H(N)
     1        ,QISO(N),REX(N)
  507 CONTINUE
      STOP
      END
```

Appendix Q

Temperature Calibration for Coax Gage

DEG F	0	1	2	3	4	5	6	7	8	9	10	DEG F

THERMOELECTRIC VOLTAGE IN ABSOLUTE MILLIVOLTS

TYPE

E

NEW REFERENCE TABLES
SUPERSEDES N.B.S CIRCULAR #561

Reference Junction at 32°F

* CONVERTED FROM DEGREES CELSIUS 1968.

NICKEL-CHROMIUM vs. COPPER-NICKEL
(Chromel-Constantan)

TYPE E

Temperature in Degrees F

Reference Junction at 32°F

TYPE
E

THERMOELECTRIC VOLTAGE IN ABSOLUTE MILLIVOLTS

DEG F	0	1	2	3	4	5	6	7	8	9	10	DEG F
450	15.829	15.871	15.912	15.954	15.996	16.038	16.080	16.123	16.165	16.207	16.249	450
460	16.249	16.291	16.333	16.375	16.417	16.459	16.501	16.544	16.586	16.628	16.670	460
470	16.670	16.712	16.755	16.797	16.839	16.881	16.924	16.966	17.008	17.051	17.093	470
480	17.093	17.135	17.178	17.220	17.262	17.305	17.347	17.389	17.432	17.474	17.517	480
490	17.517	17.559	17.602	17.644	17.687	17.729	17.772	17.814	17.857	17.899	17.942	490
500	17.942	17.984	18.027	18.070	18.112	18.155	18.197	18.240	18.283	18.325	18.368	500
510	18.368	18.411	18.453	18.496	18.539	18.581	18.624	18.667	18.710	18.752	18.795	510
520	18.795	18.838	18.881	18.924	18.966	19.009	19.052	19.095	19.138	19.181	19.223	520
530	19.223	19.266	19.309	19.352	19.395	19.438	19.481	19.524	19.567	19.610	19.653	530
540	19.653	19.696	19.739	19.782	19.825	19.868	19.911	19.954	19.997	20.040	20.083	540
550	20.083	20.126	20.169	20.212	20.256	20.299	20.342	20.385	20.428	20.471	20.514	550
560	20.514	20.558	20.601	20.644	20.687	20.730	20.774	20.817	20.860	20.903	20.947	560
570	20.947	20.990	21.033	21.076	21.120	21.163	21.206	21.250	21.293	21.336	21.380	570
580	21.380	21.423	21.466	21.510	21.553	21.597	21.640	21.683	21.727	21.770	21.814	580
590	21.814	21.857	21.901	21.944	21.987	22.031	22.074	22.118	22.161	22.205	22.248	590
600	22.248	22.292	22.336	22.379	22.423	22.466	22.510	22.553	22.597	22.640	22.684	600
610	22.684	22.728	22.771	22.815	22.859	22.902	22.946	22.990	23.033	23.077	23.120	610
620	23.120	23.164	23.208	23.252	23.295	23.339	23.383	23.426	23.470	23.514	23.558	620
630	23.558	23.601	23.645	23.689	23.733	23.777	23.820	23.864	23.908	23.952	23.996	630
640	23.996	24.039	24.083	24.127	24.171	24.215	24.259	24.302	24.346	24.390	24.434	640
650	24.434	24.478	24.522	24.566	24.610	24.654	24.698	24.742	24.786	24.829	24.873	650
660	24.873	24.917	24.961	25.005	25.049	25.093	25.137	25.181	25.225	25.269	25.313	660
670	25.313	25.357	25.401	25.445	25.490	25.534	25.578	25.622	25.666	25.710	25.754	670
680	25.754	25.798	25.842	25.886	25.930	25.974	26.019	26.063	26.107	26.151	26.195	680
690	26.195	26.239	26.283	26.328	26.372	26.416	26.460	26.504	26.549	26.593	26.637	690
700	26.637	26.681	26.725	26.770	26.814	26.858	26.902	26.947	26.991	27.035	27.079	700
710	27.079	27.124	27.168	27.212	27.256	27.301	27.345	27.389	27.434	27.478	27.522	710
720	27.522	27.566	27.611	27.655	27.699	27.744	27.788	27.832	27.877	27.921	27.966	720
730	27.966	28.010	28.054	28.099	28.143	28.187	28.232	28.276	28.321	28.365	28.409	730
740	28.409	28.454	28.498	28.543	28.587	28.632	28.676	28.720	28.765	28.809	28.854	740
750	28.854	28.898	28.943	28.987	29.032	29.076	29.121	29.165	29.210	29.254	29.299	750
760	29.299	29.343	29.388	29.432	29.477	29.521	29.566	29.610	29.655	29.699	29.744	760
770	29.744	29.788	29.833	29.878	29.922	29.967	30.011	30.056	30.100	30.145	30.190	770
780	30.190	30.234	30.279	30.323	30.368	30.412	30.457	30.502	30.546	30.591	30.636	780
790	30.636	30.680	30.725	30.769	30.814	30.859	30.903	30.948	30.993	31.037	31.082	790
800	31.082	31.127	31.171	31.216	31.261	31.305	31.350	31.395	31.439	31.484	31.529	800
810	31.529	31.573	31.618	31.663	31.707	31.752	31.797	31.842	31.886	31.931	31.976	810
820	31.976	32.020	32.065	32.110	32.155	32.199	32.244	32.289	32.334	32.378	32.423	820
830	32.423	32.468	32.513	32.557	32.602	32.647	32.692	32.736	32.781	32.826	32.871	830
840	32.871	32.916	32.960	33.005	33.050	33.095	33.140	33.184	33.229	33.274	33.319	840
850	33.319	33.364	33.408	33.453	33.498	33.543	33.588	33.632	33.677	33.722	33.767	850
860	33.767	33.812	33.857	33.901	33.946	33.991	34.036	34.081	34.126	34.170	34.215	860
870	34.215	34.260	34.305	34.350	34.395	34.440	34.484	34.529	34.574	34.619	34.664	870
880	34.664	34.709	34.754	34.798	34.843	34.888	34.933	34.978	35.023	35.068	35.113	880
890	35.113	35.157	35.202	35.247	35.292	35.337	35.382	35.427	35.472	35.517	35.562	890
900	35.562	35.606	35.651	35.696	35.741	35.786	35.831	35.876	35.921	35.966	36.011	900
910	36.011	36.056	36.100	36.145	36.190	36.235	36.280	36.325	36.370	36.415	36.460	910
920	36.460	36.505	36.550	36.595	36.640	36.684	36.729	36.774	36.819	36.864	36.909	920
930	36.909	36.954	36.999	37.044	37.089	37.134	37.179	37.224	37.269	37.314	37.358	930
940	37.358	37.403	37.448	37.493	37.538	37.583	37.628	37.673	37.718	37.763	37.808	940
950	37.808	37.853	37.898	37.943	37.988	38.033	38.078	38.123	38.168	38.213	38.257	950
960	38.257	38.302	38.347	38.392	38.437	38.482	38.527	38.572	38.617	38.662	38.707	960
970	38.707	38.752	38.797	38.842	38.887	38.932	38.977	39.022	39.067	39.112	39.157	970
980	39.157	39.202	39.247	39.291	39.336	39.381	39.426	39.471	39.516	39.561	39.606	980
990	39.606	39.651	39.696	39.741	39.786	39.831	39.876	39.921	39.966	40.011	40.056	990
1,000	40.056	40.101	40.146	40.191	40.236	40.280	40.325	40.370	40.415	40.460	40.505	1,000
1,010	40.505	40.550	40.595	40.640	40.685	40.730	40.775	40.820	40.865	40.910	40.955	1,010
1,020	40.955	41.000	41.045	41.090	41.134	41.179	41.224	41.269	41.314	41.359	41.404	1,020
1,030	41.404	41.449	41.494	41.539	41.584	41.629	41.674	41.719	41.764	41.808	41.853	1,030
1,040	41.853	41.898	41.943	41.988	42.033	42.078	42.123	42.168	42.213	42.258	42.303	1,040
1,050	42.303	42.348	42.392	42.437	42.482	42.527	42.572	42.617	42.662	42.707	42.752	1,050
1,060	42.752	42.797	42.842	42.886	42.931	42.976	43.021	43.066	43.111	43.156	43.201	1,060
1,070	43.201	43.246	43.290	43.335	43.380	43.425	43.470	43.515	43.560	43.605	43.650	1,070
1,080	43.650	43.694	43.739	43.784	43.829	43.874	43.919	43.964	44.008	44.053	44.098	1,080
1,090	44.098	44.143	44.188	44.233	44.278	44.322	44.367	44.412	44.457	44.502	44.547	1,090
1,100	44.547	44.592	44.636	44.681	44.726	44.771	44.816	44.861	44.905	44.950	44.995	1,100
1,110	44.995	45.040	45.085	45.130	45.174	45.219	45.264	45.309	45.354	45.398	45.443	1,110
1,120	45.443	45.488	45.533	45.578	45.622	45.667	45.712	45.757	45.802	45.846	45.891	1,120
1,130	45.891	45.936	45.981	46.025	46.070	46.115	46.160	46.205	46.249	46.294	46.339	1,130
1,140	46.339	46.384	46.428	46.473	46.518	46.563	46.607	46.652	46.697	46.742	46.786	1,140
1,150	46.786	46.831	46.876	46.921	46.965	47.010	47.055	47.099	47.144	47.189	47.234	1,150
1,160	47.234	47.279	47.323	47.368	47.412	47.457	47.502	47.546	47.591	47.636	47.681	1,160
1,170	47.681	47.725	47.770	47.815	47.859	47.904	47.949	47.993	48.038	48.083	48.127	1,170
1,180	48.127	48.172	48.217	48.261	48.306	48.351	48.395	48.440	48.484	48.529	48.574	1,180
1,190	48.574	48.618	48.663	48.708	48.752	48.797	48.842	48.886	48.931	48.975	49.020	1,190
1,200	49.020	49.065	49.109	49.154	49.198	49.243	49.288	49.332	49.377	49.421	49.466	1,200
1,210	49.466	49.510	49.555	49.600	49.644	49.689	49.733	49.778	49.822	49.867	49.911	1,210
1,220	49.911	49.956	50.001	50.045	50.090	50.134	50.179	50.223	50.268	50.312	50.357	1,220
1,230	50.357	50.401	50.446	50.490	50.535	50.579	50.624	50.668	50.713	50.757	50.802	1,230
1,240	50.802	50.846	50.891	50.935	50.980	51.024	51.069	51.113	51.157	51.202	51.246	1,240
1,250	51.246	51.291	51.335	51.380	51.424	51.469	51.513	51.557	51.602	51.646	51.691	1,250
1,260	51.691	51.735	51.779	51.824	51.868	51.913	51.957	52.002	52.046	52.090	52.135	1,260
1,270	52.135	52.179	52.223	52.268	52.312	52.357	52.401	52.445	52.490	52.534	52.578	1,270
1,280	52.578	52.623	52.667	52.711	52.756	52.800	52.844	52.889	52.933	52.977	53.022	1,280
1,290	53.022	53.066	53.110	53.155	53.199	53.243	53.288	53.332	53.376	53.420	53.465	1,290
1,300	53.465	53.509	53.553	53.597	53.642	53.686	53.730	53.774	53.819	53.863	53.907	1,300
1,310	53.907	53.951	53.996	54.040	54.084	54.128	54.173	54.217	54.261	54.305	54.349	1,310
1,320	54.349	54.394	54.438	54.482	54.526	54.570	54.615	54.703	54.747	54.791	1,320	
1,330	54.791	54.835	54.880	54.924	54.968	55.012	55.056	55.100	55.145	55.189	55.233	1,330
1,340	55.233	55.277	55.321	55.365	55.409	55.453	55.498	55.542	55.586	55.630	55.674	1,340
1,350	55.674	55.718	55.762	55.806	55.850	55.894	55.938	55.982	56.026	56.071	56.115	1,350
1,360	56.115	56.159	56.203	56.247	56.291	56.335	56.379	56.423	56.467	56.511	56.555	1,360
1,370	56.555	56.599	56.643	56.687	56.731	56.775	56.819	56.863	56.907	56.951	56.995	1,370
1,380	56.995	57.039	57.083	57.127	57.171	57.215	57.259	57.303	57.346	57.390	57.434	1,380
1,390	57.434	57.478	57.522	57.566	57.610	57.654	57.698	57.742	57.786	57.830	57.873	1,390

DEG F	0	1	2	3	4	5	6	7	8	9	10	DEG F

* CONVERTED FROM DEGREES C (IPTS 1948).

—CONTINUED
TABLE X

NICKEL-CHROMIUM vs. COPPER-NICKEL   TYPE E
(Chromel-Constantan)

Temperature in Degrees F   Reference Junction at 32°F

TYPE

E

NEW REFERENCE TABLES
SUPERSEDES N B S CIRCULAR #561

DEG F	0	1	2	3	4	5	6	7	8	9	10	DEG F

THERMOELECTRIC VOLTAGE IN ABSOLUTE MILLIVOLTS

(tabular thermoelectric voltage data, largely illegible)

DEG F   0   1   2   3   4   5   6   7   8   9   10   DEG F
* CONVERTED FROM DEGREES C (IPTS 1968).

TABLE XI

COPPER vs. COPPER-NICKEL   TYPE T
(Copper-Constantan)

Temperature in Degrees F   Reference Junction at 32°F

TYPE

T

NEW REFERENCE TABLES
SUPERSEDES N B S CIRCULAR #561

DEG F	0	1	2	3	4	5	6	7	8	9	10	DEG F

THERMOELECTRIC VOLTAGE IN ABSOLUTE MILLIVOLTS

(tabular thermoelectric voltage data, largely illegible)

DEG F   0   1   2   3   4   5   6   7   8   9   10   DEG F
* CONVERTED FROM DEGREES C (IPTS 1968).

273

Coax Gage Data Reduction Program

```
      PROGRAM COAX
C THIS PROGRAM REDUCES SURFACE TEMPERATURE DATA INTO
C   HEAT TRANSFER RATES AND HEAT COEFFICIENTS
C TWO REDUCTION METHODS ARE AVAILABLE:
C   1.  AEDC REDUCTION METHOD
C           - USES SEMI-INFINITE SLAB ASSUMPTION
C   2.  NSWC REDUCTION METHOD
C           - SOLVES THE HEAT EQUATION NUMERICALLY
C           - INCLUDES THE BACK SIDE TEMPERATURE CHANGE
      COMMON H(2,2000),TBF(2,2000),QDOT(2,2000)
     1     ,TIME(2000),TW(2,2000),Q(2,2000),X(40),Y(40)
      CHARACTER*10 C8,C7,C10,C12
  110 FORMAT(A20)
    5 FORMAT(/,' WHAT IS THE INPUT FILE NAME? ',$)
    6 FORMAT(/,' WHAT IS THE OUTPUT FILE NAME? ',$)
    7 FORMAT(/,' WHAT IS THE PLOT FILE NAME? ',$)
      TYPE 5
      ACCEPT 110,C8
      OPEN(UNIT=8,NAME=C8,STATUS='OLD')
      TYPE 6
      ACCEPT 110,C7
      OPEN(UNIT=7,NAME=C7,STATUS='NEW')
      TYPE 7
      ACCEPT 110,C10
      OPEN(UNIT=10,NAME=C10,STATUS='NEW')
C ***** NOMENCLATURE ******
C   H          HEAT COEFFICIENT
C   Q          CUMULATIVE HEATING
C   QDOT       HEAT TRANSFER RATE
C
C   NCH        NUMBER OF DATA CHANNELS
C   NCOAX      NUMBER OF THERMOCOUPLE GAGES
C   NT1        CHANNEL NUMBER OF FIRST GAGE
C   NBF        NUMBER OF BACKSIDE GAGES
C
C   XM         MACH NUMBER
C   VINJ       INJECT VOLTAGE WHEN MODEL IS FULLY INJECTED
C
      CALL COAXDATA
      STOP
      END
C
CCCCCCCCCCCCCCCCCCCCCCCCCCCCCCCCCCCCCCCCCCCCCCCCCCCCCCCCCCCCCCCCCCCC
C
```

```
      SUBROUTINE COAXDATA
      COMMON H(2,2000),TBF(2,2000),QDOT(2,2000)
     1   ,TIME(2000),TW(2,2000),Q(2,2000),X(40),Y(40)
CCCCCCCCC READ IN THE DATA
      READ(8,*) XM,PO,TISO
      READ(8,*) NCOAX,NPTS
      DO 120 N=1,NCOAX
        DO 125 J=1,NPTS
          READ(8,*) TIME(J),TW(N,J),TBF(N,J)
  125    CONTINUE
  120 CONTINUE
      TSTAG=473.15
  7    CONTINUE
      TYPE 104
  104 FORMAT(' DO YOU WISH TO (1)SMOOTH TW ,'/,
     &  '(9)EXIT OR, (2)REDUCE DATA'/)
      ACCEPT *, IANSWER
  105 FORMAT(A1)
      IF (IANSWER .EQ. 2) GO TO 20
      IF (IANSWER .EQ. 9) GO TO 99
C  *****  SMOOTH THE DATA ******
      PRINT 106
  106 FORMAT(' ENTER (ODD) NO. OF POINTS TO FIT,
     &   I3 FORMAT'/)
      ACCEPT *, IFITT
      IS=IFITT/2 + 1
      IEND=NPTS-IS+1
      DO 299 N=1,NCOAX
        DO 9 I=IS,IEND
          DO 8 J=1,IFITT
            K=I-IS+J
            X(J)=TIME(K)
            Y(J)=TW(L,K)
  8         CONTINUE
          CALL LSTSQR(TW(L,I),DYDX,IFITT)
  9     CONTINUE
  299 CONTINUE
      GO TO 7
C  ******* REDUCE THE DATA *********
  20   CONTINUE
      PRINT 300
  300 FORMAT('CHOOSE THE METHOD OF DATA REDUCTION '/'
     &   (A)EDC OR (N)SWC '/)
      ACCEPT *, MET
      IF (MET .EQ. 1HA) THEN
        CALL AEDC(NCOAX,NPTS,TSTAG)
      ENDIF
      IF (MET .EQ. 1HN) THEN
        CALL NSWC(NCOAX,NPTS,TSTAG)
      ENDIF
  99  RETURN
      END
C
```

```fortran
CCCCCCCCCCCCCCCCCCCCCCCCCCCCCCCCCCCCCCCCCCCCCCCCCCCCCCCCCCC
C
      SUBROUTINE AEDC(NCOAX,NPTS,TSTAG)
      COMMON H(2,2000),TBF(2,2000),QDOT(2,2000)
     1     ,TIME(2000),TW(2,2000),Q(2,2000),X(40),Y(40)
C ***** NOMENCLATURE *****
C RCPK      THERMAL PARAMETER    BTU**2/FT**4 SEC DEGREE R**2
C              R = DENSITY
C             CP = SPECIFIC HEAT CAPACITY
C              K = CONDUCTIVITY
C    Q      CUMULATIVE HEATING    BTU/FT**2
C
      CASE=3
  96 FORMAT('COAX AEDC REDUCTION METHOD ')
      PRINT 96
      PRINT 97
  97 FORMAT(' ******* WORKING ******' )
      WRITE(10,*) XM,PO,TISO
      WRITE(10,*) NCOAX,NPTS,CASE
      ISTART=1
      IEND=NPTS
      RCPK=0.1673
C CHANGE FROM BTU**2/FT**4 SEC DEGREE R**2 TO METRIC UNITS OF
C        J**2/ M**4 SEC DEGREE K**2
      RCPK=RCPK*(1.055E3)**2/((.3048)**4*(9./5.)**2)
      DO 299 N=1,NCOAX
        Q(N,ISTART)=0.
        J1=ISTART+1
        DO 2 J=J1,IEND
          J2=J-1
          SUM=0.
          DO 1 I=ISTART,J2
            SUM=SUM+((TW(N,I+1)-TW(N,ISTART)+TW(N,I)
     &          -TW(N,ISTART))/(SQRT(TIME(J)-TIME(I))
     &          +SQRT(TIME(J)-TIME(I+1))))
  1       CONTINUE
          Q(N,J)=SQRT(RCPK/3.14159)*(TIME(J)-TIME(J-1))
     &          *SUM
  2     CONTINUE
        IS=9
        IE=IEND-8
        DO 20 I=9,IE
          QDOT(N,I)=(-2.*Q(N,I-8)-Q(N,I-4)+Q(N,I+4)+2.*Q(N,I+8))
     &          /((TIME(I)-TIME(I-1))*40.)
          TAW=.9*TSTAG
          H(N,I)=QDOT(N,I)/(TAW-TW(N,I))
          WRITE(7,*) TIME(I),TBF(N,I),TW(N,I),QDOT(N,I),H(N,I)
  20    CONTINUE
        DO 663 I=1,8
          QDOT(N,I)=QDOT(N,9)
          QDOT(N,I+IE)=QDOT(N,IE)
  663   CONTINUE
```

```
          DO 201 J=1,NPTS
            WRITE(10,*) TW(N,J),Q(N,J)
  201     CONTINUE
  299 CONTINUE
      RETURN
      END
C
CCCCCCCCCCCCCCCCCCCCCCCCCCCCCCCCCCCCCCCCCCCCCCCCCCCCCCCCCCCCCCCCC
C
      SUBROUTINE NSWC(NCOAX,NPTS,TSTAG)
      DIMENSION TT(2,10)
      COMMON H(2,2000),TBF(2,2000),QDOT(2,2000)
     1     ,TIME(2000),TW(2,2000),Q(2,2000),X(40),Y(40)
      CASE=3
      PRINT 96
  96  FORMAT(' COAX NSWC REDUCTION METHOD ')
      PRINT 97
  97  FORMAT('********  WORKING ********')
C ****** NOMENCLATURE *********
C  THICK        LENGTH OF COAX GAGE (FT)
C  CP           HEAT CAPACITY (BTU / LB DEGREE R)
C  RHO          DENSITY
C               =.322*1728 = 556.42 LB/FT**3
C               (=.322 LB/IN**3)
C  COND         CONDUCTIVITY
C               =.000267*12 = .003204 BTU/FT SEC DEGREE R
C               (=.000267 BTU/IN SEC DEGREE R)
C               (=.000267*12*3600 = 11.53 BTU/FT HR DEGREE R)
C  THET         STABILITY PARAMETER
C ****** PRELIMINARY CALCULATIONS *********
      WRITE(10,*) XM,PO,TISO
      WRITE(10,*) NCOAX,NPTS,CASE
      DO 299 N=1,NCOAX
        NODES=10
        NODEM1=NODES-1
        HIDT=TIME(2)-TIME(1)
        THICK=0.03125
        DX=THICK/NODEM1
C CHANGE CP TO J/ KG DEGREE K
        CP=0.094*1.055E3/(.4536*(9./5.))
C CHANGE RHO TO KG/ M**3
        RHO=0.322*1728.0*.4536/(.3048)**3
C CHANGE COND TO J/M SEC DEGREE K
        COND=0.267E-3 * 12.0 * 1.055E3/(.3048*(9./5.))
        CONDUX=COND/DX
        THETOT=COND/(CP*RHO*DX**2)
        M=0
        ADJUST=TBF(N,1)-TW(N,1)
        DO 52 I=1,NPTS
          TBF(N,I)=TBF(N,I)-ADJUST
  52    CONTINUE
```

```fortran
            DO 102 I=1,NODES
               TT(1,I)=TW(N,1)
   102      CONTINUE
            L1=1
            L2=2
C LOOP TIME INTERVALS
            DO 302 IHI=2,NPTS
C THET MUST BE LESS THAN 0.50 FOR PROCEDURE TO
C    BE NUMERICALLY STABLE
               THET=TIME(IHI)-TIME(IHI-1)
               DTLO=THET/THETOT
               NTLO=HIDT/DTLO
               IF (NTLO .GE. 0) GO TO 32
                  NTLO=IABS(NTLO)
   32          CONTINUE
               NTLO=NTLO+1
               DTLO=HIDT/NTLO
               THET=THETOT*DTLO
               B=1.0-(2.0*THET)
C LOOP TIME SUBINTERVALS
               DO 252 ITLO=1,NTLO
                  DO 202 INODE=2,NODEM1
                     TT(L2,INODE)=THET*(TT(L1,INODE+1)
     &                  +TT(L1,INODE-1))+B*TT(L1,INODE)
   202            CONTINUE
                  TFAC=FLOAT(ITLO)/FLOAT(NTLO)
                  TT(L2,1)=TW(N,IHI-1) + (TW(N,IHI)
     &               TW(N,IHI-1))*TFAC
                  TT(L2,NODES)=TBF(N,IHI-1)+(TBF(N,I
     &               - TBF(N,IHI-1))*TFAC
                  LHOLD=L1
                  L1=L2
                  L2=LHOLD
   252         CONTINUE
C NEW WALL TEMPERATURES NOW AT L1
C    AT THE INPUT RECORDED TIME, TIME(IHI)
               QDOT(N,IHI)=-(CONDUX/2.)*(-3.*TT(L1
     &            4.*TT(L1,2)-TT(L1,3))
               TAW=.9*TSTAG
               H(N,IHI)=QDOT(N,IHI)/(TAW-TW(N,IHI
               WRITE(7,*) TIME(IHI),TBF(N,IHI),TW
     &            QDOT(N,IHI),H(N,IHI)
   302      CONTINUE
```

278

```
       DO 201 I=1,NPTS
           WRITE(10,*) TW(N,I),Q(N,I)
  201    CONTINUE
  299 CONTINUE
      RETURN
      END
C
CCCCCCCCCCCCCCCCCCCCCCCCCCCCCCCCCCCCCCCCCCCCCCCCCCCCCCCCCC
C
      SUBROUTINE LSTSQR(YFIT,DYDX,IFIT)
      COMMON H(2,2000),TBF(2,2000),QDOT(2,2000)
     1    ,TIME(2000),TW(2,2000),Q(2,2000),X(40),Y(40)
C ** FIRST ORDER LEAST SQUARES FIT OF IFIT POINTS,
C **    DYDX=F(X(MIDPT))
      MIDPT=IFIT/2 + 1
      A=0.
      B=0.
      C=0.
      D=0.
      E=0.
      F=0.
      G=0.
      DO 2 I=1,IFIT
        A=A+X(I)
        B=B+X(I)**2
        C=C+X(I)**3
        D=D+X(I)**4
        E=E+Y(I)
        F=F+(X(I)*Y(I))
        G=G+(X(I)*X(I)*Y(I))
  2    CONTINUE
      B1=(A*E-IFIT*F)/(A*A-IFIT*B)
      A1=(E-B1*A)/IFIT
      YFIT=A1+B1*X(MIDPT)
      DYDX=B1
      RETURN
      END
```

Appendix S

Test Parameter/Photo Catalog Number

Photo No.	Photo Description	Test

85-2334 Calibration, rake in uninjected position
85-2335 Calibration, rake in injected position
85-2336 Calibration, instrumentation

85-2356 Oil flow, plexiglas flat plate, P=20 bar, α=0°
85-2357 Oil flow, plexiglas flat plate, P=10 bar, α=0°
85-2358 Oil flow, plexiglas flat plate, P=20 bar, α=-5.5°
85-2359 Oil flow, plexiglas flat plate, P=10 bar, α=-5.5°

85-2361 Oil flow, aluminum flat plate, P=20 bar, α=-5.5° O-2
85-2362 Oil flow, aluminum flat plate, P=20 bar, α=-5.5°
85-2364 Oil flow, aluminum flat plate, P=20 bar, α=0°
85-2365 Oil flow, aluminum flat plate, P=20 bar, α=0°
85-2366 Oil flow, aluminum flat plate, P=10 bar, α=0°
85-2481 Oil flow, aluminum flat plate, P=20 bar, α=0°   O-1
85-2482 Oil flow, aluminum flat plate, P=20 bar, α=0°
85-2483 Oil flow, aluminum flat plate, P=10 bar, α=0°

85-Z Double pass schlieren, P=20 bar, α=-5.5°, $\emptyset$=40°, Ω=60°
85-Y Double pass schlieren, P=10 bar, α=-5.5°, $\emptyset$=40°, Ω=60°
85-X Double pass schlieren, P=20 bar, α=0°, $\emptyset$=40°, Ω=60°
85-V Double pass schlieren, P=10 bar, α=0°, $\emptyset$=40°, Ω=60°
85-U Double pass schlieren, P=20 bar, α=0°, $\emptyset$=40°, Ω=0°
85-T Double pass schlieren, P=10 bar, α=0°, $\emptyset$=40°, Ω=0°
85-S Double pass schlieren, P=10 bar, α=0°, $\emptyset$=40°, Ω=30°
85-Q Double pass schlieren, P=10 bar, α=-5.5°, $\emptyset$=40°, Ω=30°
85-P Double pass schlieren, P=10 bar, α=-5.5°, $\emptyset$=40°, Ω=75°
85-N Double pass schlieren, P=10 bar, α=0°, $\emptyset$=40°, Ω=75°
85-M Double pass schlieren, P=10 bar, α=-5.5°, $\emptyset$=15°, Ω=0°
85-K Double pass schlieren, P=10 bar, α=0°, $\emptyset$=15°, Ω=0°
85-J Double pass schlieren, P=10 bar, α=0°, $\emptyset$=15°, Ω=30°
85-I Double pass schlieren, P=10 bar, α=-5.5°, $\emptyset$=15°, Ω=30°
85-H Double pass schlieren, P=10 bar, α=-5.5°, $\emptyset$=15°, Ω=60°
85-G Double pass schlieren, P=10 bar, α=0°, $\emptyset$=15°, Ω=60°
85-F Double pass schlieren, P=10 bar, α=0°, $\emptyset$=15°, Ω=75°
85-E Double pass schlieren, P=10 bar, α=-5.5°, $\emptyset$=15°, Ω=75°

85-2486 Sublimation, P=20 bar, α=-5.5°, $\emptyset$=15°, Ω=0°
85-2487 Sublimation, P=20 bar, α=-5.5°, $\emptyset$=15°, Ω=0°
85-2488 Sublimation, P=10 bar, α=-5.5°, $\emptyset$=15°, Ω=0°

85-2489 Sublimation, P=10 bar, $\emptyset$=15°, Ω=0°   WS-1
85-2490 Sublimation, P=20 bar, $\emptyset$=15°, Ω=0°
85-2491 Sublimation, P=20 bar, $\emptyset$=15°, Ω=30°   WS-3

```
85-2492  Sublimation, P=10 bar, Ø=15°, Ω=30°                      WS-2
85-2497  Sublimation, P=10 bar, Ø=15°, Ω=60°                      WS-4
85-2498  Sublimation, P=20 bar, Ø=15°, Ω=60°
85-2499  Sublimation, P=10 bar, Ø=15°, Ω=75°                      WS-5
85-2507  Sublimation, P=20 bar, Ø=40°, Ω=0°
85-2508  Sublimation, P=20 bar, Ø=40°, Ω=0°
85-2509  Sublimation, P=10 bar, Ø=40°, Ω=0°                       WS-6
85-2510  Sublimation, P=10 bar, Ø=40°, Ω=30°                      WS-7
85-2511  Sublimation, P=10 bar, Ø=40°, Ω=60°                      WS-8
85-2512  Sublimation, P=10 bar, Ø=40°, Ω=75°                      WS-9
85-2513  Sublimation, P=10 bar, Ø=0°,  Ω=0°
86-59    Sublimation, P=20 bar, Ø=15°, Ω=0°, h=15mm
86-78    Sublimation, P=20 bar, Ø=0°,  Ω=0°, h=15mm
86-79    Sublimation, P=10 bar, Ø=0°,  Ω=0°, h=15mm
86-80    Sublimation, P=20 bar, Ø=40°, Ω=0°, h=15mm
86-81    Sublimation, P=10 bar, Ø=40°, Ω=0°, h=15mm               WS-10


85-2514  Oil flow, P=20 bar, α=0°, Ø=0°,  Ω=0°                     WO-11
85-2515  Oil flow, P=20 bar, α=0°, Ø=15°, Ω=0°
85-2518  Oil flow, P=10 bar, α=0°, Ø=15°, Ω=0°    *               WO-1
85-2521  Oil flow, P=20 bar, α=0°, Ø=15°, Ω=0°                     WO-13
85-2522  Oil flow, P=10 bar, α=0°, Ø=15°, Ω=30°                    WO-2
85-2527  Oil flow, P=20 bar, α=0°, Ø=15°, Ω=30°                    WO-3
85-2528  Oil flow, P=20 bar, α=0°, Ø=15°, Ω=30°
85-2529  Oil flow, P=10 bar, α=0°, Ø=15°, Ω=30°
85-2530  Oil flow, P=20 bar, α=0°, Ø=15°, Ω=60°
85-2533  Oil flow, P=10 bar, α=0°, Ø=15°, Ω=60°                    WO-4
85-2534  Oil flow, P=10 bar, α=0°, Ø=15°, Ω=75°                    WO-5
85-2535  Oil flow, P=20 bar, α=0°, Ø=15°, Ω=75°
85-2536  Oil flow, P=20 bar, α=0°, Ø=40°, Ω=0°
85-2537  Oil flow, P=10 bar, α=0°, Ø=40°, Ω=0°                     WO-6
85-2538  Oil flow, P=20 bar, α=0°, Ø=40°, Ω=30°
85-2539  Oil flow, P=10 bar, α=0°, Ø=40°, Ω=30°                    WO-7
85-2540  Oil flow, P=20 bar, α=0°, Ø=40°, Ω=60°
85-2541  Oil flow, P=10 bar, α=0°, Ø=40°, Ω=60°                    WO-8
85-2542  Oil flow, P=20 bar, α=0°, Ø=40°, Ω=75°
85-2543  Oil flow, P=10 bar, α=0°, Ø=40°, Ω=75°                    WO-9
86-53    Oil flow, P=20 bar, α=0°, Ø=40°, Ω=0°, h=15mm
86-54    Oil flow, P=10 bar, α=0°, Ø=40°, Ω=0°, h=15mm WO-10
86-55    Oil flow, P=20 bar, α=0°, Ø=0°,  Ω=0°, h=15mm WO-12
86-56    Oil flow, P=10 bar, α=0°, Ø=0°,  Ω=0°, h=15mm WO-14
86-57    Oil flow, P=20 bar, α=0°, Ø=15°, Ω=0°, h=15mm
86-58    Oil flow, P=10 bar, α=0°, Ø=15°, Ω=0°, h=15mm
```

* Started using motor oil

```
86-264   Heat transfer model installed in tunnel
86-265   Heat transfer data acquisition set-up
86-266   Heat transfer data acquisition set-up
```

```
Color
Slide
No              Photograph Description

1       Liquid Crystal, L-2, P=10, time =  4.08 seconds
2       Liquid Crystal, L-2, P=10, time =  5.54 seconds
3       Liquid Crystal, L-2, P=10, time =  6.00 seconds
4       Liquid Crystal, L-2, P=10, time =  6.45 seconds
5       Liquid Crystal, L-2, P=10, time =  6.91 seconds
6       Liquid Crystal, L-2, P=10, time =  7.38 seconds
7       Liquid Crystal, L-2, P=10, time =  7.84 seconds
8       Liquid Crystal, L-2, P=10, time =  8.30 seconds
9       Liquid Crystal, L-2, P=10, time =  8.76 seconds
10      Liquid Crystal, L-2, P=10, time =  9.23 seconds
11      Liquid Crystal, L-2, P=10, time =  9.69 seconds
12      Liquid Crystal, L-2, P=10, time = 10.15 seconds
13      Liquid Crystal, L-2, P=10, time = 10.41 seconds
14      Liquid Crystal, L-1, P=20, time = 3.03 seconds
15      Liquid Crystal, L-1, P=20, time = 3.42 seconds
16      Liquid Crystal, L-1, P=20, time = 3.85 seconds
17      Liquid Crystal, L-1, P=20, time = 4.28 seconds
18      Liquid Crystal, L-1, P=20, time = 4.70 seconds
19      Liquid Crystal, L-1, P=20, time = 5.13 seconds
20      Liquid Crystal, L-1, P=20, time = 5.56 seconds
21      Liquid Crystal, L-1, P=20, time = 5.98 seconds

32      Liquid Crystal Calibration, Temperature = 24.2 °C
34      Liquid Crystal Calibration, Temperature = 23.4 °C
35      Liquid Crystal Calibration, Temperature = 24.8 °C
```

Bibliography

1. Abriat, Eric. _Etude Experimentale D'une Interaction Tridimensionnelle Entre Une Onde De Choc, Engendree Par Une Ailette, Et Une Couche Limite Turbulente A Un Nombre De Mach De 5_. ESTACA Project Report, VKI-SR-1985-10. Von Karman Institute for Fluid Dynamics, Rhode-Saint-Genese, Belgium, March 1985.

2. Ames Research Staff. _Equations, Tables, and Charts for Compressible Flow_. NACA Report 1135. Bellevue, WA: AMTEC Engineering Inc.

3. Anderson, Dale A., John C. Tannehill, and Richard H. Pletcher. _Computational Fluid Mechanics and Heat Transfer_. Washington: Hemisphere Publishing Corporation 1984.

4. Anderson, E.C. and C.H. Lewis. _Laminar or Turbulent Boundary-Layer Flows of Perfect Gases or Reacting Gas Mixtures in Chemical Equilibrium_, NASA CR-1893. Virginia Polytechnic Institute and State University. Blacksburg, VA: NASA, October 1971.

5. Arts, T. Personal Interview. Von Karman Institute for Fluid Dynamics, Rhode-Saint-Genese, Belgium. October 1985 through March 1986.

6. Bramlette, T.T., R.R. Smith and N.J. Sliski. "Fin Induced Laminar Interactions on Sharp and Spherically Blunted Cones", _AIAA Journal of Spacecraft, Vol 10, No 11_, November 1973.

7. Cebeci, T. and A.M.O. Smith. "Analysis of Turbulent Boundary Layers", _Applied Mathematics and Mechanics_, _15_. New York: Academic Press, 1974.

8. Chapman, D.R. and J.K. Hodge. Telephone conversation between Chapman and Hodge. Air Force Institute of Technology, 22 December 1985.

9. Chapman, Dean R. and Gary D. Kuhn. "Navier-Stokes Computations of Viscous Sublayer Flow and the Limiting Behavior of Turbulence Near a Wall," _AIAA 85-1487_, 1985.

10. Chen, Alice J. _A Study of Two Coax Gage Data Reduction Methods_. AE 6.99 Class Project Report. Air Force Institute of Technology, Wright-Patterson AFB OH, September 1985.

11. Coffey, Jr., D.E. _Adaptive-Grid Optimization for Minimizing Steady-State, Truncation Error_. MS Thesis, AFIT/GA/AA/85D-4. School of Engineering, Air Force Institute of Technology (AU), Wright-Patterson AFB OH, December 1985.

12. Creusot, D. and R. Thevenot. _Traitement D'Images Applique Aux Cristaux Liquides Transfert de Chaleur en Hypersonique_. Project Report. VKI-SR-1985-06. Von Karman Institute for Fluid Dynamics, Rhode-Saint-Genese, Belgium, October 1984.

13. Daum, F.L. and G. Gyarmathy. "Condensation of Air and Nitrogen in Hypersonic Wind Tunnels". _AIAA Journal_, _Vol 6_, _No 3_. March 1968. Pages 458-465.

14. DeGraef, Pierre. _Study of Kinetic Heatings in Hypersonic Flows Using Liquid Crystals_. Project Report, U-VKI-1985-07. Von Karman Institute for Fluid Dynamics, Rhode-Saint-Genese, Belgium, May 1985.

15. Degrez, Gerard. _Study of Kinetic Heating Due to a Three Dimensional Shock Wave/Turbulent Boundary Layer Interaction_. Project Report, U-VKI-1979-1. Von Karman Institute for Fluid Dynamics, Rhode-Saint-Genese, Belgium, May 1979.

16. Dolling, D.S. and S.M. Bogdonoff. "Upstream Influence in Sharp Fin-Induced Shock Wave Turbulent Boundary Layer Interaction." _AIAA Journal_, _Vol 21_, _No 1_. Jan 1983. Pages 143-145.

17. Duncan, W.J., A.S. Thom, and A.D. Young. _Mechanics of Fluids_. London: Edward Arnold Ltd., 1960.

18. Harris, Julius E. _Numerical Solution of the Equations for Compressible Laminar, Transitional, and Turbulent Boundary Layers and Comparisons with Experimental Data_. PhD dissertation. Virginia Polytechnic Institute and State University, Blacksburg, Virginia, May 1970. (NASA TR R-368).

19. Hermans, T. _Surface Temperature Measurements on a Model Placed in a Hypersonic Flow using Liquid Crystals._ Project Report, U-VKI-1984-09. Von Karman Institute for Fluid Dynamics, Rhode-Saint-Genese, Belgium, May 1984.

20. Hironimus, G.A. _Hypersonic Shock Tunnel Experiments on the W7 Flat Plate Model - Expansion Side, Turbulent Flow and Leading Edge Transpiration Data_. Cal Report No. AA-1952-Y-2, Contract No. AF 33(615)-1847. Cornell Aeronautical Laboratory, Inc. February 1966.

21. Hodge, J.K. Personal Interview. Air Force Institute of Technology, Wright-Patterson AFB, OH. Jan 1985 through March 1986.

22. Hodge, J.K., S.A. Leone, and R.L. McCarty. "Non-iterative Parabolic Grid Generation for Parabolized Equations", _AIAA 85-1528-CP_, 1985.

23. Holden, M.S. _An Experimental Investigation of Turbulent Boundary Layers at High Mach Number and Reynolds Numbers_, NASA CR-112147. Cornell Aeronautical Laboratory, Inc.: NASA. November 1972.

24. Hung C.-M., and P.G. Buning. "Simulation of Blunt-Fin Induced Shock Wave and Turbulent Boundary Layer Interaction", _AIAA 84-0457_. Jan 1984.

25. Jordan, J.L., and P.L. Kessel. "Heat Transfer Rate Measurements Obtained in a Highly Erosive Two Phase Flow Field", _AIAA 83-0584_. Jan 10-13, 1983.

26. Kaufmann II, L.G., R.H. Korkegi, and L.C. Morton. _Shock Impingement Caused by Boundary Layer Separation Ahead of Blunt Fins_, ARL 72-0118. Aerospace Research Laboratories, Wright-Patterson Air Force Base, OH. August 1972.

27. Kim, J.S. and K.S. Chang. "Calculation of Incompressible and Compressible Unsteady Boundary Layers by a Noniterative Finite Difference Method," _AIAA 84-1639_, June 1984.

28. Kipp, H.W. and V.T. Helms, III. "Some Observations on the Occurrence of Striation Heating", _AIAA 85-0324_. Jan 1985.

29. Kordulla, W. _Calibration of the Hypersonic Blowdown Wind Tunnel H-3_. Project Report 1970-264. Von Karman Institute for Fluid Dynamics, Rhode-Saint-Genese, Belgium, June 1970.

30. Korkegi, R.H. "Effect of Transition on Three-Dimensional Shock-Wave/Boundary Layer Interaction," _AIAA Journal_, _Vol 10_, _No 3_. March 1972.

31. Korkegi, R.H. Hypersonic Aerodynamics. Course Note 9, (Second Reprint). Von Karman Institute for Fluid Dynamics, Rhode-Saint-Genese, Belgium, September 1966.

32. Korkegi, R.H. "On the Structure of Three-Dimensional Shock Induced Separated Flow Regions". AIAA Journal, Vol 14, No 5. May 1976. Pages 597-600.

33. Korkegi, R.H. "Survey of Viscous Interactions Associated with High Mach Number Flight", AIAA Journal Vol 9, No 5, May 1971. Pages 771-784.

34. Lange, Karen J. Unsteady Solution of the Boundary Layer Equations with Application to Space Shuttle Tiles. MS Thesis, AFIT/GAE/ENY/84D-11. School of Engineering, Air Force Institute of Technology (AU), Wright-Patterson AFB OH, June 1985.

35. Liepmann, H.W. and A. Roshko. Elements of Gas Dynamics. New York: John Wiley and Sons, Inc., 1957.

36. Ligrani, P.M. Measurement Techniques. Course Note 108. Von Karman Institute for Fluid Dynamics, Rhode-Saint-Genese, Belgium, October 1979.

37. Ligrani, P.M., C. Camci, and M.S. Grady. Thin Film Heat Transfer Gage Construction and Measurement Details. Technical Memorandum 33. Von Karman Institute for Fluid Dynamics, Rhode-Saint-Genese, Belgium, November 1982.

38. Lorber, P.F. Turbulent Boundary Layers on an Airfoil in Unsteady Flow. PhD dissertation. Massachusetts Institute of Technology, May 1984.

39. Mechtly, E.A. The International System of Units: Physical Constants and Conversion Factors (Second Revision). Washington,D.C.: National Aeronautics and Space Administration, 1973 (NASA SP-7012).

40. Narayan, K.Y. "Leeside Flowfield and Heat Transfer of a Delta Wing at $M_\infty = 10$," AIAA Journal, Vol 16, No 2. Pages 160-165. February 1978.

41. Peake, D.J. and M. Tobak. "Three - Dimensional Separation and Reattachment", High Angle of Attack Aerodynamics, AGARD LS 121. March 1982.

42. Pope, A. and K.L. Goin. High - Speed Wind Tunnel Testing. New York: John Wiley and Sons, Inc., 1965.

43. Price E. Jr., and R. Stallings Jr. <u>Investigation of Turbulent Separated Flows in the Vicinity of Fin-Type Protuberances at Supersonic Mach Numbers</u>. NASA TND-3804. Feb 1967.

44. Reynolds, W.C., W.M. Kays and S.J. Kline. <u>Heat Transfer in the Turbulent Incompressible Boundary Layer, I - Constant Wall Temperature</u>. NASA Memorandum 12-1-58W. NASA: Washington, DC. December 1958.

45. Reynolds, W.C., W.M. Kays and S.J. Kline. <u>Heat Transfer in the Turbulent Incompressible Boundary Layer, II - Step Wall-Temperature Distribution</u>. NASA Memorandum 12-2-58W. NASA: Washington, DC. December 1958.

46. Schlichting, Hermann. <u>Boundary Layer Theory</u> (Seventh Edition). New York: McGraw-Hill Book Company, 1968.

47. Schöler, H. "The Measurement of Heat Transfer and Temperature Distributions in Hypersonic Testing", <u>Hypersonic Aerothermodynamics</u>, VKI Lecture Series 1984-01. Von Karman Institute for Fluid Dynamics, Rhode-Saint-Genese, Belgium, February 1984.

48. Schultz, D.L. and T.V. Jones. " Heat - transfer Measurements in Short-duration Hypersonic Facilities," <u>AGARDograph</u>, <u>165</u>. London: Technical Editing and Reproduction Ltd, 1973 (AGARD-AG-165).

49. Shang, J.S. <u>A Parametric Study of Hypersonic Turbulent Boundary Layers with Heat Transfer.</u> ARL TR 74-0003. Aerospace Research Laboratories, Wright-Patterson Air Force Base, OH. January 1974.

50. Shang, J.S., W.L. Hankey, and D.L. Dwoyer. "Numerical Analysis of Eddy Viscosity Models in Supersonic Turbulent Boundary Layers," <u>AIAA</u> 73-164.

51. Stock, H., and revised by J. Sandford. <u>Flow Visualization</u>. Course Note 97. Von Karman Institute for Fluid Dynamics, Rhode-Saint-Genese, Belgium.

52. Tobak, M. and D.J. Peake. "Topology of Three Dimensional Separated Flows", <u>Ann. Rev. Fluid. Mech.</u>, <u>Vol 14</u>, 1982. Pages 61-85.

53. Vaughan, D.A. <u>Three Dimensional Shock Wave/Turbulent Boundary Layer Interaction at Mach 5.4.</u> Project Report 1977-3. Von Karman Institute for Fluid Dynamics, Rhode-Saint-Genese, Belgium, June 1977.

54. Winkelman, A.E. Flow Visualization Studies of a Fin Protuberance Partially Immersed in a Turbulent Boundary Layer at Mach 5. NOL TR 70-93, Naval Ordnance Laboratory, White Oak, MD. 20 May 1970.

55. Young F., L. Kaufman II, and R. Korkegi. Experimental Investigation of Interactions Between Blunt Fin Shock Waves and Adjacent Boundary Layers at Mach Numbers 3 and 5. ARL 68-0214. Dec 1968.
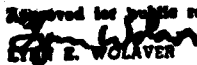
Vita

Alice J. Chen was born on 20 November 1958 in Chattanooga, Tennessee. She graduated from Carlsbad High School, Carlsbad, California in 1976 and entered the University of California; San Diego. She graduated in 1980 with a Bachelor of Arts degree in Chemistry. After graduation she received a commission in the USAF after completing training at the Air Force Officer Training School. Her first assignment was to the Air Force Institute of Technology (AFIT), Wright-Patterson Air Force Base, Ohio. She was enrolled in the Undergraduate Engineering Conversion Program and graduated in 1982 with a Bachelor of Science degree in Aeronautical Engineering. Upon graduation, she was assigned to the Air Force Armament Laboratory, Eglin AFB, Florida. She worked as an aeronautical engineer in the Weapon Separations Team, Aerodynamics Branch until May 1984 when she entered the School of Engineering at AFIT. As part of her AFIT assignment, she conducted experimental research during a six month visit at the von Karman Institute for Fluid Dynamics (VKI) in Rhode-Saint-Genese, Belgium, under the AFIT/VKI Exchange Program which was sponsored by HQ USAF, AFIT, VKI, and the Air Force Flight Dynamics Laboratory.

> Permanent address: 2091 Truesdell Lane
>
> Carlsbad, California 92008

REPORT DOCUMENTATION PAGE

1a. REPORT SECURITY CLASSIFICATION	1b. RESTRICTIVE MARKINGS
UNCLASSIFIED	

2a. SECURITY CLASSIFICATION AUTHORITY	3. DISTRIBUTION/AVAILABILITY OF REPORT
	Approved for public release:
2b. DECLASSIFICATION/DOWNGRADING SCHEDULE	distribution unlimited.

4. PERFORMING ORGANIZATION REPORT NUMBER(S)	5. MONITORING ORGANIZATION REPORT NUMBER(S)
AFIT/GAE/ENY/86M-1	

6a. NAME OF PERFORMING ORGANIZATION	6b. OFFICE SYMBOL (If applicable)	7a. NAME OF MONITORING ORGANIZATION
School of Engineering	AFIT/ENY	

6c. ADDRESS (City, State and ZIP Code)	7b. ADDRESS (City, State and ZIP Code)
Air Force Institute of Technology Wright-Patterson AFB, OH 45433	

8a. NAME OF FUNDING/SPONSORING ORGANIZATION	8b. OFFICE SYMBOL (If applicable)	9. PROCUREMENT INSTRUMENT IDENTIFICATION NUMBER
Flight Dynamics Lab	AFWAL/FIMG	

8c. ADDRESS (City, State and ZIP Code)	10. SOURCE OF FUNDING NOS.			
	PROGRAM ELEMENT NO.	PROJECT NO.	TASK NO.	WORK UNIT NO.
AFWAL/FIMG Wright-Patterson AFB, OH 45433				

11. TITLE (Include Security Classification)
See Box 19

12. PERSONAL AUTHOR(S)
Alice J. Chen, B.S., Capt, USAF

13a. TYPE OF REPORT	13b. TIME COVERED	14. DATE OF REPORT (Yr., Mo., Day)	15. PAGE COUNT
MS Thesis	FROM ___ TO ___	1986 March	320

16. SUPPLEMENTARY NOTATION

17. COSATI CODES			18. SUBJECT TERMS (Continue on reverse if necessary and identify by block number)
FIELD	GROUP	SUB. GR.	Boundary Layer Code, Turbulence, Transition, Unsteady, Viscous-Inviscid Interaction, Hypersonic Blunt Fin on Flat Plate, Striation Heating
01	01		
20	04		

19. ABSTRACT (Continue on reverse if necessary and identify by block number)

UNCLASSIFIED

Title: Numerical Solution of Laminar and Turbulent Boundary Layer
Equations including Transition, and Experimental Study of a
Blunt Fin at Incidence

Thesis Chairman: Dr. James K. Hodge, Major, USAF
Associate Professor of Aeronautical and Astronautical
Engineering

Approved for public release: IAW AFR 190-1.
LYNN E. WOLAVER   9 May 86
Dean for Research and Professional Development
Air Force Institute of Technology (ATC)
Wright-Patterson AFB OH 45433

20. DISTRIBUTION/AVAILABILITY OF ABSTRACT	21. ABSTRACT SECURITY CLASSIFICATION
UNCLASSIFIED/UNLIMITED ☒ SAME AS RPT. ☐ DTIC USERS ☐	UNCLASSIFIED

22a. NAME OF RESPONSIBLE INDIVIDUAL	22b. TELEPHONE NUMBER (Include Area Code)	22c. OFFICE SYMBOL
Dr. James K. Hodge, Major, USAF	513-255-3517	AFIT/ENY

DD FORM 1473, 83 APR   EDITION OF 1 JAN 73 IS OBSOLETE.   UNCLASSIFIED

This study combines the techniques of computational fluid dynamics and experimentation.

An unsteady laminar boundary layer code was shown to be more efficient when modified to solve the momentum and energy equations using Thomas' algorithm instead of optimized successive over-relaxation (SOR). A steady eddy viscosity turbulence model was then added to the code: two models for the inner region, Van Driest and Chapman, and two models for the outer region, a mixing length and Clauser were used. The computer code was verified against theoretical and experimental data from the literature. The code shows excellent results for laminar flow and each of the models showed very good agreement with turbulent experimental data.

The experimental study was conducted in a Mach 6 blowdown wind tunnel. Oil flow, sublimation, liquid crystals, and thin film gages were used to examine the flow structure and heat transfer on a flat plate. The heat transfer rates from these gages were lower than from the liquid crystals. The viscid-inviscid interaction flow region of flow past a blunt fin mounted on the flat plate was examined using the same flow visualization methods and possible flow interaction models are presented. Striation heating appeared when the fin incidence was 40° and the sweep was 60 or 75°.

The numerical and experimental techniques of this study were then merged. The heat transfer results from the flat plate experiment were compared with results from the computer code and were found to be in good agreement.